Stefan Schuß

C^n-continuous mortar method for Isogeometric Analysis

LNM Lehrstuhl für Numerische Mechanik

universi
UNIVERSITÄTSVERLAG SIEGEN

Stefan Schuß

C^n-continuous mortar method for Isogeometric Analysis

universi
UNIVERSITÄTSVERLAG SIEGEN

Bibliografische Information der Deutschen Nationalbibliothek

Die Deutsche Nationalbibliothek verzeichnet diese Publikation in der Deutschen Nationalbibliografie; detaillierte Daten sind im Internet über http://dnb.dnb.de abrufbar

Impressum

Druck und Bindung:
UniPrint, Universität Siegen

Gedruckt auf alterungsbeständigem holz- und säurefreiem Papier

Siegen 2024: univers*i* – Universitätsverlag Siegen
www.uni-siegen.de/universi

ISBN 978-3-96182-169-3

doi.org/10.25819/ubsi/10477

C^n-continuous mortar method for Isogeometric Analysis

DISSERTATION

zur Erlangung des Grades eines Doktors

der Ingenieurwissenschaften

vorgelegt von

M.Sc. Stefan Schuß

eingereicht bei der Naturwissenschaftlich-Technischen Fakultät

der Universität Siegen

Siegen 2023

Betreuer und erster Gutachter
Prof. Dr.-Ing. habil. Christian Hesch
Universität Siegen

Zweiter Gutachter
Prof. Dr.-Ing. habil. Peter Betsch
Karlsruhe Institute of Technology

Tag der mündlichen Prüfung
23.01.2024

Abstract

In recent years, isogeometric methods, using NURBS (Non-Uniform Rational B-Splines) as basis functions, have gained increasing attention. These methods offer exceptional flexibility in geometric modelling and the ability to adjust the smoothness of the piecewise-defined shape functions on a single patch as needed. This feature makes isogeometric analysis particularly attractive in the context of higher-order differential equations. However, to maintain this characteristic in the case of multiple patches, it must be appropriately accounted for in domain coupling.

This work addresses this challenge by presenting a novel method for implementing general non-conforming weak C^n-continuous domain couplings within the framework of isogeometric analysis. This approach builds upon the established mortar method and extends it by imposing additional constraints on derivatives up to a specified order. Within this study, the method is comprehensively elucidated using an abstract variational framework. This encompasses discretisation within the context of isogeometric analysis, selection of the dual space, efficient handling of crosspoints and wirebaskets, and the evaluation of mortar integrals. A significant emphasis is also placed on the construction of isogeometric approximation spaces which a priori fulfil the higher-order coupling conditions. Furthermore, the performance and applicability of the method are investigated in various engineering problems, including elasticity, heat conduction, diffusion and Phase-Field-Crystal modelling. This is achieved through a series of simulations that substantiate the applicability and efficiency of the approach in various technical domains.

Keywords: mortar, C^n-continuous, multi-patch, higher-order, IGA, crosspoints, wirebaskets, elasticity, Kirchhoff–Love, Cahn-Hilliard, Phase-Field-Crystal model

Kurzfassung

In den letzten Jahren haben isogeometrische Methoden, in denen NURBS (Non-Uniform Rational B-Splines) als Basisfunktionen verwendet werden, zunehmend an Aufmerksamkeit gewonnen. Diese Methoden zeichnen sich nicht nur durch ihre hohe Flexibilität bei der geometrischen Modellierung aus, sondern bieten auch die Möglichkeit die Differentiationsklasse der stückweise definierten Formfunktionen auf einem einzelnen Patch beliebig festzulegen. Das macht die isogeometrische Analyse besonders attraktiv im Zusammenhang mit Differentialgleichungen höherer Ordnung. Damit diese Eigenschaft bei der Verwendung mehrerer Patches nicht verloren geht, muss sie bei einer Gebietskopplung entsprechend berücksichtigt werden.

In diesem Zusammenhang setzt die vorliegende Arbeit an und stellt eine neue Methode zur Implementierung von allgemeinen nicht-konformen schwach C^n-stetigen Gebietskopplungen im Kontext der isogeometrischen Analyse vor. Dieser Ansatz baut auf der etablierten Mortar-Methode auf und erweitert sie durch zusätzliche Bedingungen, die Ableitungen bis zu einer vordefinierten Ordnung einbeziehen. Im Detail wird das Verfahren innerhalb eines abstrakten variationellen Frameworks erörtert. Hierbei werden mehrere Schlüsselaspekte beleuchtet, darunter die Diskretisierung im Kontext der isogeometrischen Analyse, die Wahl des dualen Raums, der effiziente Umgang mit Crosspoints und Wirebaskets, sowie die Auswertung von Mortar-Integralen. Besondere Aufmerksamkeit gilt auch der Konstruktion von isogeometrischen Approximationsräumen, die a priori den Kopplungsbedingungen genügen. Die Leistungsfähigkeit der Methode wird abschließend in verschiedenen ingenieurtechnischen Problemstellungen eingehend untersucht, darunter Elastizität, Wärmeleitung, Diffusion und dem Phasen-Feld-Kristall-Modell. Dies geschieht durch eine Reihe von Simulationen, die die Anwendbarkeit und Effizienz des Ansatzes in unterschiedlichen technischen Anwendungsgebieten untermauern.

Schlüsselwörter: Mortar, C^n, multi-patch, höhere Ordnung, IGA, Crosspoints, Wirebaskets, Elastizität, Kirchhoff–Love, Cahn-Hilliard, Phasen-Feld-Kristall-Modell

Acknowledgements

The research results presented in this thesis were obtained during my work as a research assistant at the Chair of Computational Mechanics at the University of Siegen. My work was largely funded by the Deutsche Forschungsgemeinschaft (DFG), for which I would like to take this opportunity to express my thanks.

Foremost, I wish to convey my deepest thanks to Prof. Dr Christian Hesch for his outstanding support and guidance as my PhD supervisor. His insightful feedback and encouragement have been instrumental in the successful completion of this thesis. I would also like to thank Prof. Dr Peter Betsch for his interest in my work and for acting as co-referee. I am grateful for the time and effort he put into evaluating my research. In addition, many thanks go to the other members of my examination board, Prof. Dr Peter Kraemer and Prof. Dr Oliver Nelles, for their time and commitment during the PhD process.

Special thanks go to all my colleagues for the excellent collaboration, for the pleasant working atmosphere and for many fruitful discussions: Dr Maik Dittmann, Dr Melanie Krüger, Felix Schmidt and Dr Jonathan Schulte, it has been a pleasure working together. In particular, I wish to thank Prof. Dr Barbara Wohlmuth and Dr Maik Dittmann for their valuable advice and constructive discussions about mortar methods. Their expertise contributed greatly to the depth and quality of my research. A big thank you is also due to Harald Schmitz and Annika Ippach for their kind help and support with various off-topic questions and concerns.

Finally, and most importantly, my deepest thanks to my beloved life partner Birgit for her constant support throughout the entire duration of writing this thesis. Her encouragement and understanding have been a source of strength, and I am grateful for her unwavering presence in my life.

Siegen, January 2024 Stefan Schuß

Contents

List of Figures

List of Tables

List of Symbols

Sign	Description	Definition
$\overline{M}$	Closure of a set M.	page xxi
$\prod_{i=1}^{n} M_i$	Cartesian product of the sets $M_1, \ldots, M_n$.	page xxi
M°	Interior of a set M.	page xxi
$\mathbb{N}$	Set of natural numbers.	page xxi
$\mathbb{N}_0$	Set of of natural numbers including zero.	page xxi
$\mathbb{Z}$	Set of integers.	page xxi
$\mathbb{Q}$	Set of rational numbers.	page xxi
$\mathbb{R}$	Set of real numbers.	page xxi
$\dim(V)$	Dimension of the linear space V.	page xxi
$\boldsymbol{A} : \boldsymbol{B}$	Double contraction of the tensors $\boldsymbol{A}$, $\boldsymbol{B}$.	page xxii
$\|\boldsymbol{v}\|$	Euclidean norm of $\boldsymbol{v} \in \mathbb{R}^n$.	page xxi
$\boldsymbol{v} \cdot \boldsymbol{w}$	Euclidean scalar product of $\boldsymbol{u}, \boldsymbol{v} \in \mathbb{R}^n$.	page xxi
$\delta_{i,j}$	Kronecker delta function.	page 23
$\|\bullet\|_{L^2(C)}$	L^2 norm on C.	page xxii
$\langle \bullet, \bullet \rangle_C$	L^2 scalar product on C.	page xxii
$\operatorname{span}(W)$	Linear span of W.	page xxi
$\boldsymbol{u} \otimes \boldsymbol{v}$	Tensor product of the first order tensors $\boldsymbol{u}$, $\boldsymbol{v}$.	page xxii
$\operatorname{Tr}(\boldsymbol{A})$	Trace of the tensor $\boldsymbol{A}$.	page xxii
$\boldsymbol{A}^{\mathrm{T}}$	Transpose of a matrix or a tensor $\boldsymbol{A}$.	page xxii
C^k	Differentiability classes.	page xxiii
$L^2(C)$	Class of L^2 functions on C.	page xxii
$H^k(C)$	Sobolev spaces on C.	page xxii
∇	Gradient operator.	page xxii
$\nabla_{\boldsymbol{X}}$	Gradient operator w.r.t. $\boldsymbol{X} = (X_1, \ldots, X_n)$.	page xxiii
Δ	Laplacian operator.	page xxii
$\Delta_{\boldsymbol{X}}$	Laplacian operator w.r.t. $\boldsymbol{X} = (X_1, \ldots, X_n)$.	page xxiii

Sign	Description	Definition
$\nabla \otimes \nabla$	Hessian operator.	page xxii
$\nabla_{\boldsymbol{X}} \otimes \nabla_{\boldsymbol{X}}$	Hessian operator w.r.t. $\boldsymbol{X} = (X_1, \ldots, X_n)$.	page xxiii
$\nabla \cdot$	Divergence operator.	page xxii
$\nabla_{\boldsymbol{X}} \cdot$	Divergence operator w.r.t. $\boldsymbol{X} = (X_1, \ldots, X_n)$.	page xxiii
$\partial^{\boldsymbol{m}}$	Partial derivative to the multi-index $\boldsymbol{m}$.	page xxii
∂_{X_j}	Partial derivative w.r.t. the argument X_j.	page xxiii
∂_j	Partial derivative w.r.t. the jth argument.	page xxii
$\dot{\boldsymbol{f}}$	Derivative of a function $\boldsymbol{f}$ w.r.t. the time.	page xxiii
$\operatorname{supp}(\boldsymbol{f})$	Support of a function $\boldsymbol{f}$.	page xxii
$\hat{B}_{a,\boldsymbol{p}}$	Multivariate B-spline basis functions on the parameter space.	page 10
$\hat{R}_{a,\boldsymbol{p}}$	NURBS basis functions on the parameter space.	page 11
$\hat{N}_{i,p}$	Univariate B-spline basis functions on the parameter space.	page 9
d_p	Parametric dimension.	page 10
$\hat{\Omega}$	Parameter space, parametric domain.	page 9
Ω	Physical domain.	page 7
$\Omega^{(i)}$	ith patch.	page 19
Γ	Skeleton of a multi-patch domain.	page 19
$\Gamma_{i,j}$	Interface of the patches $\Omega^{(i)}$ and $\Omega^{(j)}$.	page 19
Γ_k	kth non-empty interface.	page 28
$\hat{\Gamma}^i_j$	Pre-image of an interface $\Gamma_{i,j}$ under $\boldsymbol{\mathcal{G}}^{(i)}$.	page 19
$\hat{\Gamma}^j_i$	Pre-image of an interface $\Gamma_{i,j}$ under $\boldsymbol{\mathcal{G}}^{(j)}$.	page 19
P^i_j	Parametric assignment from $\hat{\Gamma}^i_j$ to $\hat{\Gamma}^j_i$.	page 19
P^j_i	Parametric assignment from $\hat{\Gamma}^j_i$ to $\hat{\Gamma}^i_j$.	page 19
Γ_{e}	Boundary part with prescribed essential boundary conditions.	page 27
Γ_{n}	Boundary part with prescribed natural boundary conditions.	page 63
Θ	Knot vector.	page 8
ζ_i	ith knot in a knot vector Θ.	page 8
$\tilde{\Theta}$	Breakpoint vector corresponding to a knot vector Θ.	page 9
$\hat{\mathscr{M}}$	Mesh in the parameter space.	page 9

Sign	Description	Definition
$\mathscr{M}$	Mesh in the physical space.	page 22
$\mathfrak{n}$	Number of NURBS basis functions.	page 8
$\tilde{\mathfrak{n}}$	Number of breakpoints.	page 9
$\mathbf{I}$	NURBS coordinates.	page 10
$\boldsymbol{\mathcal{G}}$	NURBS parametrization.	page 13
$\mathbb{B}_{\mathrm{h}}$	Basis of the space of admissible solutions.	page 32
$\tilde{\mathbb{B}}_{\mathrm{h}}$	Basis of the space of test functions.	page 32
B	Coupling functional.	page 29
$\boldsymbol{\mathcal{A}}$	Global coupling matrix.	page 34
$\boldsymbol{\mathcal{A}}^{k,j}$	Non-zero block of the coupling matrix containing master or slave data.	page 34
$\boldsymbol{\mathcal{B}}_{\boldsymbol{\alpha}}^{k,j}$,	Additive component of $\boldsymbol{\mathcal{A}}^{k,j}$.	page 34
$\mathfrak{C}$	Crosspoints and wirebaskets.	page 36
$\mathcal{L}^n$	Placement operator.	page 44
M	Minimisation functional.	page 28
$\mathcal{M}$	Space of Lagrange multiplier.	page 29
$\mathcal{M}_{\mathrm{h}}$	Discrete space of Lagrange multiplier.	page 33
$\boldsymbol{\mathcal{R}}^u$	Uncoupled residuum.	page 33
$\boldsymbol{\mathcal{R}}^c$	Coupled residuum.	page 35
$\mathcal{S}$	Space of admissible solutions.	page 27
$\mathcal{S}^c$	Constrained space of admissible solutions.	page 29
$\mathcal{S}_{\mathrm{h}}^c$	Discrete constrained space of admissible solutions.	page 35
$\mathcal{V}$	Space of test functions/variations.	page 27
$\mathcal{V}^c$	Constrained space of test functions/variations.	page 29
$\mathcal{V}_{\mathrm{h}}^c$	Discrete constrained space of test functions/variations.	page 35
V	Abstract variational problem.	page 27
$\mathfrak{h}$	Weighting parameter.	page 28
$\mathcal{B}$	Continuum body.	page 55
J	Jacobian.	page 57
$\boldsymbol{\varphi}$	Motion.	page 56
$\boldsymbol{\kappa}_t$	Particle map.	page 55
$\mathbf{F}$	Deformation gradient.	page 59
$\mathbf{C}$	Right Cauchy–Green strain tensor.	page 60

Sign	Description	Definition
$\mathbf{E}$	Green–Lagrange strain tensor.	page 60
$\mathbf{P}$	First Piola–Kirchhoff stress tensor.	page 62
$\mathbf{S}$	Second Piola–Kirchhoff stress tensor.	page 60
$\mathrm{I}_{\mathbf{C}}$	First invariant of the right Cauchy–Green strain tensor.	page 61
$\mathrm{II}_{\mathbf{C}}$	Second invariant of the right Cauchy–Green strain tensor.	page 61
$\mathrm{III}_{\mathbf{C}}$	Third invariant of the right Cauchy–Green strain tensor.	page 61
$\boldsymbol{J}_k$	Diffusion flows.	page 92
$\boldsymbol{Q}$	Heat flow.	page 92

Notation and conventions

The following is a summary of the terminology used in this thesis, where the three topics "Sets and set operations", "Linear spaces" and "Functions and derivatives" are covered. Please note that this overview is not complete and only contains the designations whose knowledge is assumed in the following. Further notations are introduced and discussed in the passages where they are used for the first time.

Sets and set operations. For the different number spaces, we use the common designations. Thus $\mathbb{Z}$ denotes the integers, $\mathbb{Q}$ the rational numbers and $\mathbb{R}$ the real numbers. Regarding the natural numbers, we distinguish between the set $\mathbb{N} = \{1, 2, 3, \ldots\}$ without zero and the set $\mathbb{N}_0 = \mathbb{N} \cup \{0\}$ including zero. For a subset M of a topological space, ∂M denotes its boundary, $\overline{M}$ its closure and M° its interior. Moreover, given n sets $M_1, \ldots, M_n$, the corresponding product space $M = M_1 \times \ldots \times M_n = \{(m_1, \ldots, m_n) \,|\, m_i \in M_i,\, i = 1, \ldots n\}$ is shortly written as $M = \prod_{i=1}^n M_i$, whereby in the case $M_i = M_1$, $i = 1, \ldots, n$, we write $M = M_1^n$. Eventually, elements from product spaces are marked by bold symbols. We point out that general considerations in most cases also include the case $n = 1$. For reasons of clarity, no distinction is made regarding the notation in these situations. For example, we write for $m \in \{1, 2, 3\}$, $\boldsymbol{x} \in \mathbb{R}^m$ or $\boldsymbol{f} \colon \mathbb{R}^n \to \mathbb{R}^m$, even if there is no product space in the case $m = 1$. In other words, symbols written in bold do not automatically exclude the scalar-valued case.

Linear spaces. For a linear space V over a field K and subsets $\{v_i\}_{i=1}^m, W \subset V$, $\dim(V)$ denotes the dimension of V and $\operatorname{span}(W)$ the linear span of W, recalling that $\operatorname{span}(\{v_i\}_{i=1}^m) = \{a_1 v_1 + \ldots + a_m v_m \,|\, a_1, \ldots, a_m \in K\}$. In the case $V = \mathbb{R}^n$, the underlying field are the real numbers and for $\boldsymbol{v} = (v_1, \ldots, v_n)$, $\boldsymbol{w} = (w_1, \ldots, w_n) \in \mathbb{R}^n$ we use the Euclidean scalar product $\boldsymbol{v} \cdot \boldsymbol{w} := v_1 w_1 + \cdots + v_n w_n$ and the induced Euclidean norm $\|\boldsymbol{v}\| := \sqrt{\boldsymbol{v} \cdot \boldsymbol{v}}$.

As with product spaces, we use bold symbols for matrices and round or square brackets both to represent them and to access the elements. E.g. for a matrix $\boldsymbol{A} \in \mathbb{R}^{m \times n}$ with components $A_{i,j}$, is, as usual, $(A_{i,j})_{1 \le i \le m, 1 \le j \le n} = \boldsymbol{A}$, while $(\boldsymbol{A})_{i,j}$ designates the access to the respective component, i.e. $(\boldsymbol{A})_{i,j} = A_{i,j}$. For the sake of better readability, we further refrain from stating the index bounds and briefly write $(A_{i,j})_{i,j}$ instead of $(A_{i,j})_{1 \le i \le m, 1 \le j \le n}$, if misunderstandings are excluded. For tensors, we use the same notation as for matrices, whereby in each case it is clear from the context whether it is a tensor or the associated coefficient matrix. In addition, we use the usual notations for tensor operations. Thus

for first-order tensors $\boldsymbol{u}$, $\boldsymbol{v}$ and second-order tensors $\boldsymbol{A}$, $\boldsymbol{B}$, $\boldsymbol{A}^{\mathrm{T}}$ is the transposed, $\boldsymbol{u} \otimes \boldsymbol{v}$ is the tensor product, $\mathrm{Tr}(\boldsymbol{A})$ is the trace and $\boldsymbol{A} : \boldsymbol{B}$ denotes the double contraction.

Concerning specific function-spaces, we denote by $L^2(C)$ the Hilbert space of all square-integrable functions on a domain C, i.e. $L^2(C) := \{f \colon C \to \mathbb{R} \,|\, \int_C |f(\boldsymbol{x})|^2 \,\mathrm{d}V < \infty\}$, equipped with the L^2 scalar product $\langle \bullet, \bullet \rangle_C := \int_C (\bullet) \cdot (\bullet) \,\mathrm{d}V$ and the induced L^2 norm $\| \bullet \|_{L^2(C)} = \sqrt{\langle \bullet, \bullet \rangle_C}$. Note that in the definition of the L^2 scalar product the Euclidean scalar product is used, and so it is also valid for elements from the product spaces $L^2(C)^m$. Analogously, we extend the definitions by means of the double contraction to tensor-valued functions $\boldsymbol{A}, \boldsymbol{B} \colon C \to \mathbb{R}^{m \times n}$ according to $\langle \boldsymbol{A}, \boldsymbol{B} \rangle_C := \int_C \boldsymbol{A} : \boldsymbol{B} \,\mathrm{d}V$ and $\|\boldsymbol{A}\|_{L^2(C)} = \sqrt{\langle \boldsymbol{A}, \boldsymbol{A} \rangle_C}$. Eventually, we denote the associated Sobolev spaces, containing all L^2 functions with weak derivatives up to the kth order, by $H^k(C)$.

Functions and derivatives. For sets X, Y, $M_X \subset X$, $M_Y \subset Y$ and a function $\boldsymbol{f} \colon X \to Y$, $\boldsymbol{f}(M_X) := \{\boldsymbol{f}(\boldsymbol{x}) \,|\, \boldsymbol{x} \in X\}$ denotes the image of M_X under $\boldsymbol{f}$, $\boldsymbol{f}^{-1}(M_Y) := \{\boldsymbol{x} \in X \,|\, \boldsymbol{f}(\boldsymbol{x}) \in M_Y\}$ the pre-image of M_Y under $\boldsymbol{f}$, $\mathrm{supp}(\boldsymbol{f}) := \overline{\{\boldsymbol{x} \in X \,|\, \boldsymbol{f}(\boldsymbol{x}) \neq \boldsymbol{0}\}}$ the support of $\boldsymbol{f}$ and $\boldsymbol{f}_{|M_X}$ the restriction of $\boldsymbol{f}$ to M_X, where, in the context of multi-patch theory, $\boldsymbol{f}^{(i)}$ is written to denote the restriction to the ith patch $\Omega^{(i)}$, i.e. $\boldsymbol{f}^{(i)} := \boldsymbol{f}_{|\Omega^{(i)}}$.

Especially for expressions containing partial derivatives of higher order, the usual multi-index notation is used. For any multi-index $\boldsymbol{m} = (m_1, \ldots, m_d) \in \mathbb{N}_0^d$, we define its length as the sum $|\boldsymbol{m}| = m_1 + \ldots + m_d$ and its factorial as the product $\boldsymbol{m}! = m_1! \ldots m_d!$. Moreover, we write $\boldsymbol{m} \leq \boldsymbol{n}$ or $\boldsymbol{m} < \boldsymbol{n}$ for $\boldsymbol{m}, \boldsymbol{n} \in \mathbb{N}_0^d$ if $m_j \leq n_j$ or $m_j < n_j$ for all $j = 1, \ldots, d$. With a multi-index $\boldsymbol{m} \in \mathbb{N}_0^d$ we define $\partial^{\boldsymbol{m}} := \partial_1^{m_1} \ldots \partial_d^{m_d}$, where ∂_j denotes the operation of taking the partial derivative with respect to the jth argument and $\partial_j^{m_j}$ is the m_j-times repetition of the operation. Per definition, the components of a multi-index can take the value zero. In this case we formally set $\partial_j^0 := 1$, i.e. no operation is performed. Furthermore, we use the common designations for differential operators. I.e., $\nabla(\bullet)$ is the gradient, $\nabla \otimes \nabla(\bullet)$ the Hessian, $\Delta(\bullet)$ the Laplacian and $\nabla \cdot (\bullet)$ the divergence operator. Applied to scalar-, vector- and tensor-functions, $g \colon U \to \mathbb{R}$, $\boldsymbol{f} \colon U \to \mathbb{R}^m$ and $\boldsymbol{H} \colon U \to \mathbb{R}^{m \times n}$, where $U \subset \mathbb{R}^n$, the operations are defined in the case of Cartesian coordinates by the partial derivatives as follows: $\nabla g = (\partial_1 g, \ldots, \partial_n g)$,

$$\nabla \boldsymbol{f} = \begin{pmatrix} \partial_1 f_1 & \cdots & \partial_n f_1 \\ \vdots & \ddots & \vdots \\ \partial_1 f_m & \cdots & \partial_n f_m \end{pmatrix}, \nabla \otimes \nabla g = \begin{pmatrix} \partial_1 \partial_1 g & \cdots & \partial_1 \partial_n g \\ \vdots & \ddots & \vdots \\ \partial_n \partial_1 g & \cdots & \partial_n \partial_n g \end{pmatrix}, \nabla \cdot \boldsymbol{H} = \begin{pmatrix} \sum_{j=1}^n \partial_j H_{1,j} \\ \vdots \\ \sum_{j=1}^n \partial_j H_{m,j} \end{pmatrix},$$

$\nabla \cdot \boldsymbol{f} = \partial_1 f_1 + \cdots + \partial_n f_n$, and $\Delta g = \partial_1^2 g + \cdots + \partial_n^2 g$. It should be noted that the gradient of a vector field results from the gradients of the individual components and thus corresponds to the Jacobian matrix, while the divergence of a tensor field results from the divergence of the respective rows, which are interpreted as vector fields. The operations are therefore natural extensions of the applications to scalar/vector fields to vector/tensor fields, which justifies the use of the same operator.

Often space- and time-dependent functions are considered, i.e. functions of the form $\boldsymbol{f}\colon U \times I \to \mathbb{R}^m$, $(\boldsymbol{X}, t) \mapsto \boldsymbol{f}(\boldsymbol{X}, t)$, where $U \subset \mathbb{R}^n$ and $I \subset \mathbb{R}$. To distinguish between spatial and temporal derivatives, the temporal derivative is marked by a superscript dot, $\dot{\boldsymbol{f}} := \partial \boldsymbol{f}/\partial t$, while the operators ∂_j usually refer to the spatial derivatives, i.e. $\partial_j \boldsymbol{f} := \partial \boldsymbol{f}/\partial X_j$. Nevertheless, to avoid misunderstandings, in such cases the variable in question is written as a subscript to the operator, e.g. $\partial_{X_j} \boldsymbol{f} := \partial \boldsymbol{f}/\partial X_j$. In general, the operators as the gradient or the Laplacian refer to all variables, whereby the operations in connection with space-time-dependent functions are mostly applied only to the spatial coordinates. In order to take this into account, the operators are labelled with a corresponding index analogous to the partial derivatives. E.g., for a scalar field $g\colon U \times I \to \mathbb{R}$, $\nabla_{\boldsymbol{X}} g = (\partial_{X_1} g, \ldots, \partial_{X_n} g)$ and $\Delta_{\boldsymbol{X}} g = \partial^2_{X_1} g + \cdots + \partial^2_{X_n} g$ are the gradient and the Laplacian with respect to $\boldsymbol{X} = (X_1, \ldots, X_n)$, whereby the definition for the remaining operators $\nabla_{\boldsymbol{X}} \otimes \nabla_{\boldsymbol{X}}(\bullet)$, $\nabla_{\boldsymbol{X}} \cdot (\bullet)$ is to be continued analogously.

Eventually, for $U \subset \mathbb{R}^n$, $V \subset \mathbb{R}^m$ and $k \in \mathbb{N}_0 \cup \{-1, \infty\}$, we define the differentiation class $C^k(U, V)$ as the set of all functions $\boldsymbol{f} = (f_1, \ldots, f_m)^{\mathrm{T}}\colon U \to V$ with k-times continuously differentiable components, i.e. $\partial^{\boldsymbol{\alpha}} f_i(\boldsymbol{x})$ exists and is continuous for all $\boldsymbol{x} \in U$, $i = 1, \ldots, m$ and $|\boldsymbol{\alpha}| \leq k$. Within this notation, $\boldsymbol{f}$ is of class $C^0(U, V)$ if $\boldsymbol{f}$ is continuous and $C^\infty(U, V)$ contains the infinitely differentiable functions and it holds $C^{k-1}(U, V) \supsetneq C^k(U, V)$, $k \in \mathbb{N}$. Furthermore we write "$\boldsymbol{f}$ is C^k-continuous" for short if a function $\boldsymbol{f}\colon U \to V$ is of class $C^k(U, V)$ and "$\boldsymbol{f}$ is C^k at $\boldsymbol{x}$" to emphasise that $\boldsymbol{f}$ is k-times continuously partially differentiable at the specific point $\boldsymbol{x}^*$.

*Occasionally we also use the term C^{-1} to emphasise that f is discontinuous at a specific point.

1 Introduction

In today's complex and dynamic world, humanity is faced with an ever-increasing number of challenges and questions that require a deeper knowledge and understanding of complex systems. From forecasting the weather to optimising production processes and researching biological phenomena - the pursuit of knowledge and the ability to predict future developments drive us forward. Computer simulations are a fascinating and powerful way to virtually map and explore reality. They offer us the opportunity to study the behaviour of systems that are so complex that they are difficult to capture or analyse in controlled experiments. By transferring the real world into a virtual environment, simulations allow us to explore scenarios, test hypotheses and develop solutions to real-world problems without having to conduct time-consuming, costly or potentially dangerous physical experiments.

The history of computer simulation spans several decades and marks a fascinating journey through scientific progress technological breakthroughs and the transformation of various application areas. The first steps towards computer simulation were taken in the 1940s and 1950s when the first electronic calculators were developed. These early computers were initially limited to scientific calculations, but soon the potential of these machines to recreate real processes virtually was recognised.

One of the outstanding pioneers of this era was John von Neumann, a Hungarian-American mathematician who made significant contributions not only to mathematics, quantum mechanics, and game theory but also was a visionary in terms of computer science and simulations. Von Neumann was instrumental in the development of the "Electronic Numerical Integrator and Computer" (ENIAC), the first computer powered by electronic tubes. His collaboration with other influential figures such as Alan Turing and Herman Goldstine contributed significantly to laying the foundations for modern computer architectures and functionalities.

One of the most revolutionary developments of this time was the introduction of the Monte Carlo method in the 1940s. This method, named after the famous casino in Monaco, is based on stochastic processes and statistical analysis. It was developed by Stanislaw Ulam and Nicholas Metropolis to solve complex mathematical problems that could not be handled analytically. The Monte Carlo method allows the simulation of random events using random numbers to generate statistical results. Originally developed to simulate neutron distributions in nuclear reactors, the method quickly found application in various disciplines such as physics, chemistry, engineering and finance. Its introduction was a turning point in the history of computer simulation, as it facilitated the solution of complex problems.

The development and refinement of computer simulation technology continued in the following decades. In the 1960s and 1970s, engineers and scientists began to use computer simulations increasingly in the aerospace industry. These simulations were used to test the behaviour of aircraft, rockets and spacecraft under various conditions.

During this time, the finite element method (FEM) has been established as a powerful and versatile tool. In the 1920s, Boris Galerkin [79] laid the foundation for the idea of transforming partial differential equations into a variational problem and approximating the unknown quantity (e.g. displacement, temperature) by shape functions from a finite-dimensional function space. With this approach, the search for an approximate solution for complicated differential equations could be reduced to purely algebraic problems. Early publications in the engineering literature describing what is now known as FEM are Turner et al. [161] and Argyris & Kelsey [8], whereby the term "finite elements" was coined by Clough [40]. However, the first finite element, the linear triangle, can be traced back to Courant [45]. The basic idea of FEM is to divide the physical domain on which the problem is formulated into smaller, simple geometric elements. On each element, local shape functions are defined that vanish outside and approximate the unknown physical quantity inside the element. Due to the local support of the shape functions, even complex geometries could be approximated easily, but at the expense of a reduced continuity at the element boundaries.

Probably one of the most important advancements of the FEM is the isoparametric concept (Irons [101], Zienkiewicz & Cheung [174]), which enables a more efficient and precise modelling of complex geometries and material distributions. While initially linear elements were used, representing simple geometric shapes such as triangles or tetrahedrons, the basic principle of the isoparametric approach is to use the same functions for the geometry of the element and the approximation. This opened up the possibility of designing shape functions first on regular elements, such as a rectangle or a cuboid, and then transferring them to curved elements in physical space. Thus, the design of C^0-continuous finite elements on complex geometries became a simple matter. One limitation of the isoparametric concept, however, was that it did not work for C^1-continuous or higher approximations. Primarily because of the desire to construct thin plate and shell elements for structural analysis, there was a great interest in developing C^1-continuous interpolation schemes. Many researchers sought solutions to this problem, with noteworthy successes achieved by Clough & Tocher [41], Argyris et al. [9], de Veubeke [57] and Bell [18], among others. However, these elements were complicated and expensive to use, so interest turned to alternative variational formulations to overcome the need for C^1-continuous basis functions.

In the 2000s, another important enhancement of FEM emerged in the form of isogeometric analysis (IGA). It represents an innovative method for the numerical treatment of differential equations by seamlessly combining geometric modelling and analysis. IGA uses the same basis functions that are used in computer-aided design (CAD). This enables closer integration of design and analysis within a common mathematical framework. One of the pioneers in this field is Thomas J. R. Hughes, whose work and research contributions helped to establish IGA as an independent method, [13, 100]. Since then, IGA

has been successfully applied in a wide variety of disciplines such as structural mechanics, [19, 20, 66, 67, 107, 137], fracture mechanics, [29, 63, 61, 94, 167], and generalised continua [77].

Traditionally, FEM uses different functions for geometric modelling than CAD, which can result in discrepancies between the geometric models. In contrast, IGA uses so-called Non-Uniform Rational B-Splines (NURBS) or similar basis functions*, which are also used in CAD, for both geometry and approximation and thus follows the isoparametric paradigm. This leads to higher accuracy of the results and more efficient communication between the engineers performing the design and the analysis.

NURBS are piecewise-defined rational functions with compact support, which are defined on elements similar to the FEM shape functions. In IGA, however, there are two notions of elements, the patch and the knot span. The patch may be thought of as a macro-element or subdomain. Each patch can in turn be subdivided into knot spans, which are comparable to the elements in FEM. As with FEM, the support of NURBS is limited to a small number of such elements, depending on the polynomial degree. Within an element, the basis functions are smooth, while the continuity at the element boundaries also depends on the polynomial degree but can be adjusted as desired without changing the geometry. This opens up the possibility of creating approximations with arbitrary smoothness on a single patch. Instead of expensive and complicated elements or alternative variational formulations, IGA can thus be used to solve higher-order partial differential equations such as the Cahn-Hilliard equation or Cahn-Hilliard-like problems without any detours in a unified framework, e.g. [3, 4, 82, 95, 142].

In almost all practical situations it is necessary to describe domains with several NURBS patches. For example, it may be appropriate to use separate patches if different materials or physical models are to be used in different parts of the domain, or if different subdomains are to be handled in parallel on a multiprocessor machine. The most common case, however, is that the geometry is too complex to be covered by a single parametrisation. While such cases are not a problem from a CAD point of view, the patches need to be coupled for analysis so that they respond as a coherent domain. In the case of conforming meshes or, more generally, when the mesh on one side of the interface results from a refinement of the mesh on the other side, nodes of the two patches can be identified with each other and treated as a single one, see e.g. Cottrell et al. [43, 44] and Kleiss et al. [111]. However, the conditions for such strong couplings considerably limit the possibilities of geometric modelling. To maintain flexibility, weak methods have therefore been established in which the underlying variational problem is extended by additional coupling conditions. In [5, 85, 86, 124, 141] a modification of Nitsche's method was successfully applied in the IGA framework to achieve a weak C^0 coupling in the general non-conforming case. Another possibility for the realisation of weak C^0 couplings is offered by so-called mortar methods, which, in contrast to Nitsche's method, can be formulated independently of the underlying variational problem. Mortar methods have been studied in the FEM context for almost three decades, [15, 16, 21, 23, 115], and have

*In this work we will focus on NURBS.

already been successfully transferred to the IGA framework, [30, 31, 92]. Further applications include, among others, contact problems [17, 55, 56, 62, 110, 145, 156, 171, 172, 173] and interface problems, e.g. multi-physics applications [158]. However, since these methods are designed for C^0-continuous couplings, IGA is deprived of an important property in the multi-patch case, namely the possibility of creating approximations with arbitrary smoothness.

In the last decade, different approaches have been presented to higher-continuous spline approximations on multi-patch geometries. Horger et al. [98] developed a hybrid formulation in which a C^0-continuous mortar coupling was combined with the penalty method to introduce coupling conditions on the normal derivatives. A strong implementation is discussed in Chan et al. [36], where the NURBS bases on the patches are constructed such that any interpolation is necessarily globally C^1. Further approaches based on the construction of matching spline spaces can be found for surfaces and shell elements in [26, 26, 103, 102], where in these cases the weaker geometric continuity (G^1) is implemented. A strong implementation of G^1-couplings on conforming meshes in the framework of Kirchhoff–Love shells can further be found in Kiendl et al. [107, 108] and a penalty implementation on non-conforming meshes is discussed in Herrema et al. [89].

This work aims to bridge the gap between IGA on single patches and multi-patch geometries. For this purpose, an extended mortar method is presented, which takes into account the adjustable continuity of NURBS approximations and allows arbitrary C^n couplings. The main idea is to interpret the original mortar approach as a minimisation problem represented by a special coupling functional. This functional is extended by additive components which, besides the coupling of the approximations, also take into account their derivatives. Like the original mortar method, this approach is independent of the underlying variational problem, ensuring versatility in a wide range of problems.

Organisation of the work

This thesis is structured as follows[†]:

In *Chapter 2*, the basic concepts of isogeometric analysis are discussed. For this purpose, NURBS shape functions based on B-splines are introduced, their properties are discussed in the context of isogeometric analysis and NURBS parametrisations of curves, surfaces and solids are considered. Subsequently, the notion of multi-patch geometry is clarified and the construction of isogeometric approximation spaces is discussed.

Chapter 3 is the core of this thesis and introduces a C^n-continuous mortar method. For this purpose, an abstract variational multi-patch problem is formulated, on the basis of which appropriate conditions for the implementation of weak C^n-continuous couplings are discussed. Subsequently, the discretisation of the problem in the IGA context is considered, addressing the treatment of crosspoints/wirebaskets, the evaluation of mortar integrals and the construction of isogeometric approximation spaces that satisfy the

[†]We point out, that the work summarizes several peer-revied journal articles, [64, 65, 143], which have been published by the author.

coupling conditions a priori. The chapter concludes with a series of numerical tests and convergence studies involving polyharmonic equations.

In the following chapters, the application of the extended mortar method to several engineering problems is studied. After a brief introduction to the respective topic at the beginning of each chapter, numerical investigations on different aspects of the method are presented. *Chapter 4* starts with problems in elasticity and includes the Kirchhoff–Love shell theory, in which G^1 couplings are essential. Subsequently, problems of heat conduction and diffusion are considered in *Chapter 5*. While C^0-continuous couplings are sufficient for the variational formulation of the heat equation, the Cahn-Hilliard equation used to describe the diffusion processes requires at least a C^1-continuous transition between two patches. Eventually, *Chapter 6* deals with Phase-Field-Crystal modelling. The derivation of such models is based on a functional Taylor expansion, which is truncated above a certain order. Here, a sixth-order equation whose variational formulation requires second-order couplings is considered. Finally, conclusions are drawn in *Chapter 7*.

2 The isogeometric concept

Isogeometric Analysis (IGA) is a promising concept that closely links the technologies of Computer-Aided Design (CAD) and numerical simulation via Finite Element Analysis (FEA). The IGA framework facilitates the use of NURBS (Non-uniform rational B-spline), which originated in the field of CAD. This allows the construction of finite element (FE) basis functions with adjustable continuity across the element boundaries, in contrast to classical Lagrangian shape functions which are globally at most C^0-continuous. This chapter introduces the basics of the isogeometric concept, with Section 2.1 discussing the use of NURBS in geometric design and Section 2.2 discussing the further use in IGA.

2.1 Geometric design

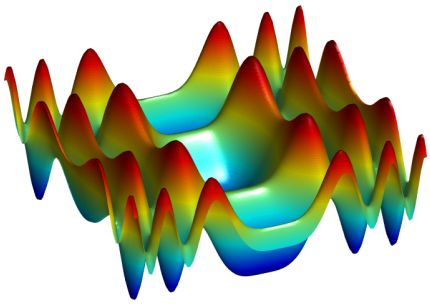

Figure 2.1: A surface explicitly defined by the function $f(x_1, x_2) = \sin(x_1^2) + \cos(x_2^2)$.

There are different ways for the description of curves, surfaces, solids, or, in general, of manifolds. An explicit representation is the simplest but also the most limited one. In this form of representation, a geometry Ω is given as graph of a function $f\colon X \to Y$, so that $\Omega = \{(\boldsymbol{x}, f(\boldsymbol{x})) \,|\, \boldsymbol{x} \in X\}$. For example, to describe a curve or a surface explicitly, a relation of the form $x_2 = f(x_1)$ (for a curve) or $x_3 = f(x_1, x_2)$ (for a surface) is needed, see Figure 2.1 for illustration. The advantages and disadvantages of this approach are obvious. It is easy to evaluate the derivatives and thus obtain geometric properties. However, by definition, a function cannot take multiple values at the same point. This means that even basic shapes such as circles or spheres cannot be represented in this way. A more flexible way of describing the points of a geometry is an implicit representation. Here, the points are defined as the roots of a function $f\colon X \to Y$, such that $\Omega = \{f(\boldsymbol{x}) = \boldsymbol{0} \,|\, \boldsymbol{x} \in X\}$, cf. Figure 2.2. Obviously, any explicit description can be converted into an implicit one,

but not vice versa. Therefore, the class of implicit geometries offers a greater variety of objects. However, this type of representation involves a root-finding problem that must be solved in order to specify the points of the object in question, which can be challenging depending on the form of f.

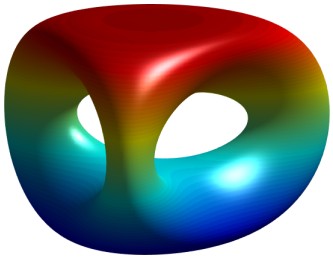

Figure 2.2: A surface implicitly defined by the function $f(x_1, x_2, x_3) = 2x_2(x_2^2 - 3x_1^2)(1 - x_3^2) + (x_1^2 + x_2^2)^2 - (9x_3^2 - 1)(1 - x_3^2)$.

The most common representation of geometries in CAD is the parametric description. Here, the coordinates are explicit functions of an independent set of parameters. In engineering design, NURBS functions in particular are used for this purpose. The following section deals with the description of complex shapes on the basis of such parametrisations. To this end, we consider in Section 2.1.1 the construction of NURBS bases and discuss the representation of curves, surfaces and solids in Section 2.1.2. Although the use of NURBS allows the description of a wide variety of complex shapes, many geometries of practical interest cannot be represented by a single parametrisation. To overcome this difficulty, such geometries are represented by using multiple patches, which is the subject of Section 2.1.4. In the context of IGA, the continuity between different patches plays a crucial role. Besides the notion of parametric continuity, there exists the notion of geometric continuity. In Section 2.1.5 we discuss this concept in the framework of surfaces for use in the Kirchhoff–Love shell theory.

2.1.1 Basis functions

NURBS are constructed on the basis of B-splines (short for Basis-splines) and multivariate functions are constructed in this framework from the tensor product of univariate functions. Therefore, a natural starting point for the investigations of NURBS is the discussion of univariate B-splines from which multivariate basis functions are constructed in order to finally define NURBS in general.

Univariate B-splines

A set of $\mathfrak{n}$ univariate B-spline functions of polynomial degree p can be defined by a non-decreasing sequence $\Theta = \{\zeta_1, \ldots, \zeta_{\mathfrak{n}+p+1}\}$, where Θ is called knot vector and $\zeta_i \in \mathbb{R}$ is called the ith knot. If the knots are equally spaced, Θ is called uniform otherwise it is

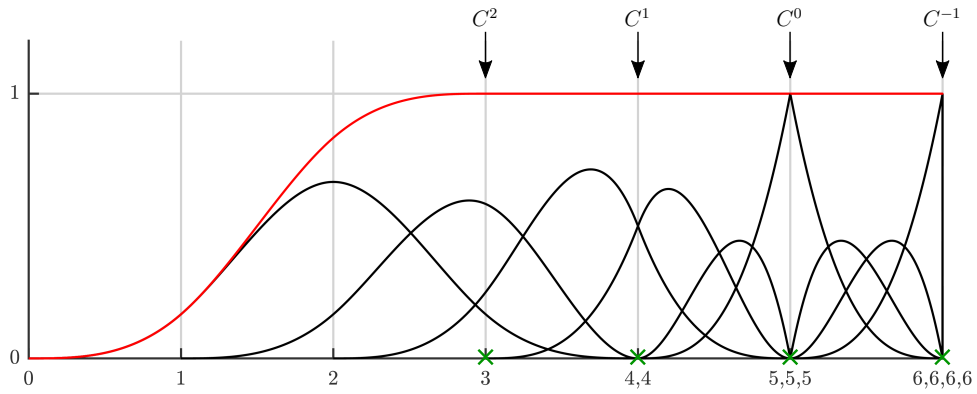

Figure 2.3: Continuity of a univariate, cubic ($p = 3$) spline basis on $\hat{\Omega} = (3, 6)$ defined by the non-uniform knot vector $\Theta = \{0, 1, 2, 3, 4, 4, 5, 5, 5, 6, 6, 6, 6\}$. The red curve represents the sum of the functions and the element boundaries are marked with green crosses.

called non-uniform. Per definition, knot values can be repeated, i.e. more than one knot can have the same value. Thereby, Θ is said to be open if its first and last knot values appear exactly $p+1$ times. The associated functions are defined recursively according to the Cox-de Boor formula, cf. [48, 51],

$$\hat{N}_{i,p}(\xi) = \frac{\xi - \zeta_i}{\zeta_{i+p} - \zeta_i} \hat{N}_{i,p-1}(\xi) + \frac{\zeta_{i+p+1} - \xi}{\zeta_{i+p+1} - \zeta_{i+1}} \hat{N}_{i+1,p-1}(\xi), \tag{2.1a}$$

where the stop function for the recursion is given by

$$\hat{N}_{i,0}(\xi) = \begin{cases} 1 & \text{if } \xi \in [\zeta_i, \zeta_{i+1}), \\ 0 & \text{otherwise.} \end{cases} \tag{2.1b}$$

As shown in Curry & Schoenberg [49], $\{\hat{N}_{i,p}\}_{i=1}^{\mathfrak{n}}$ is a spline basis on the parameter space $\hat{\Omega} = (\zeta_{p+1}, \zeta_{\mathfrak{n}+1})$, whose global continuity is determined by the knot vector and the polynomial degree. To be more precise, let $\tilde{\Theta} = \{\tilde{\zeta}_1, \dots, \tilde{\zeta}_{\tilde{\mathfrak{n}}}\}$ be the knot vector pertaining to Θ without repetitions, also called breakpoint vector. By definition, each $\hat{N}_{i,p}$ is a polynomial in $(\tilde{\zeta}_j, \tilde{\zeta}_{j+1})$, $j = 1, \dots, \tilde{\mathfrak{n}} - 1$, and thus $\hat{N}_{i,p} \in C^\infty(\tilde{\zeta}_j, \tilde{\zeta}_{j+1})$. At a breakpoint $\tilde{\zeta}_i \in \tilde{\Theta}$, however, the functions are C^{p-k_i}-continuous, where the multiplicity k_i of a breakpoint $\tilde{\zeta}_i$ is defined as its number of repetitions in Θ^*. Eventually, it should be noted that the breakpoint vector naturally defines a mesh

$$\hat{\mathscr{M}} = \{\hat{e}_i = (\tilde{\zeta}_{p+1-k_1+i}, \tilde{\zeta}_{p+2-k_1+i}) \,|\, 1 \leq i \leq \tilde{\mathfrak{n}} + k_1 + k_{\tilde{\mathfrak{n}}} - 2p - 3\}, \tag{2.2}$$

on the parameter space $\hat{\Omega}$, see Figure 2.3 for illustration.

*In case of multiplicities $k_i > 1$, the recursion (2.1) has to be augmented with the definition $\frac{0}{0} := 0$.

Multivariate B-splines

Multivariate B-spline functions are generated from d_p knot vectors $\Theta^l = \{\zeta_1^l, \dots, \zeta_{\mathfrak{n}_l+p_l+1}^l\}$, $l = 1, \dots, d_p$, where d_p is the parametric dimension, p_l indicates the polynomial degree along the parametric direction l and $\mathfrak{n}_l$ is the associated number of functions. With the resulting univariate B-splines in each direction l, written as $\hat{N}_{i_l,p_l}^l$, multivariate functions are defined by

$$\hat{B}_{a,\boldsymbol{p}}(\boldsymbol{\xi}) = \hat{B}_{\boldsymbol{i},\boldsymbol{p}}(\boldsymbol{\xi}) = \prod_{l=1}^{d_p} \hat{N}_{i_l,p_l}^l(\xi_l). \tag{2.3}$$

The multi-index (or NURBS coordinates) $\boldsymbol{i} \in \mathbf{I} := \{(i_1, \dots, i_{d_p}) \in \mathbb{N}^{d_p} \,|\, 1 \le i_l \le \mathfrak{n}_l\}$ denotes the position in the tensor product structure, the vector $\boldsymbol{p} = (p_1, \dots, p_{d_p})$ contains the polynomial degrees, $\boldsymbol{\xi} = (\xi_1, \dots, \xi_{d_p})$ are the parametric coordinates and for the global numbering of the $\mathfrak{n} = \mathfrak{n}_1\mathfrak{n}_2 \dots \mathfrak{n}_{d_p}$ multivariate functions we use the natural scheme

$$a = a(\boldsymbol{i}) = i_1 + \sum_{j=2}^{d_p} (i_j - 1) \prod_{k=1}^{j-1} \mathfrak{n}_k. \tag{2.4}$$

As in the univariate case, the functions form a spline basis on the parametric space $\hat{\Omega} = \prod_{l=1}^{d_p} (\zeta_{p_l+1}^l, \zeta_{\mathfrak{n}_l+1}^l)$ and the breakpoint vectors $\tilde{\Theta}^l$ form a mesh in $\hat{\Omega}$ given by

$$\hat{\mathscr{M}} = \left\{ \hat{e}_{\boldsymbol{i}} = \prod_{l=1}^{d_p} \hat{e}_{i_l}^l \,|\, \boldsymbol{i} = (i_1, \dots, i_{d_p}),\ 1 \le i_l \le \tilde{\mathfrak{n}}_l + k_1^l + k_{\tilde{\mathfrak{n}}_l}^l - 2p_l - 3 \right\}, \tag{2.5}$$

where $\hat{e}_{i_l}^l = (\tilde{\zeta}_{p_l+1-k_1+i}^l, \tilde{\zeta}_{p_l+2-k_1+i}^l)$ are the elements defined through $\tilde{\Theta}^l$, cf. Eq. (2.2). Furthermore, the breakpoint multiplicities k_i^l, $i = 1, \dots, \tilde{\mathfrak{n}}_l$, related to $\tilde{\Theta}^l$ determine the smoothness of the B-splines at the element boundaries. I.e. every function $\hat{B}_{\boldsymbol{i},\boldsymbol{p}}$ is $(p_l - k_i^l)$-times continuously differentiable with respect to its lth argument on any hyperplane $\mathcal{H}_i^l = \prod_{s=1}^{l-1} (\zeta_{p_s+1}^s, \zeta_{\mathfrak{n}_s+1}^s) \times \{\tilde{\zeta}_i^l\} \times \prod_{s=l+1}^{d_p} (\zeta_{p_s+1}^s, \zeta_{\mathfrak{n}_s+1}^s)$, where $l = 1, \dots, d_p$ and $i = 1, \dots, \tilde{\mathfrak{n}}_l$, see Figure 2.4 for illustration.

Eventually, in addition to the basis property and the adjustable smoothness, the following features of B-splines in the context of FEA are of importance [44, 52]:

- Non-negativity: $\hat{B}_{\boldsymbol{i},\boldsymbol{p}}(\boldsymbol{\xi}) \ge 0$ for all $\boldsymbol{\xi} \in \hat{\Omega}$.
- Compact support: $\operatorname{supp}(\hat{B}_{\boldsymbol{i},\boldsymbol{p}}) = \prod_{l=1}^{d_p} [\zeta_{i_l}^l, \zeta_{i_l+p_l+1}^l]$.
- Partition of unity: $\sum_{\boldsymbol{i} \in \mathbf{I}} \hat{B}_{\boldsymbol{i},\boldsymbol{p}}(\boldsymbol{\xi}) = 1$ for all $\boldsymbol{\xi} \in \hat{\Omega}$.

Convention 2.1.1. *When introducing B-splines, it is useful to distinguish in the notation between univariate and multivariate basis functions. In the following, this will no longer be necessary and, for the sake of clarity, both cases will be summarized under the terms* $\hat{B}_{a,\boldsymbol{p}}$ *and* $\hat{B}_{\boldsymbol{i},\boldsymbol{p}}$.

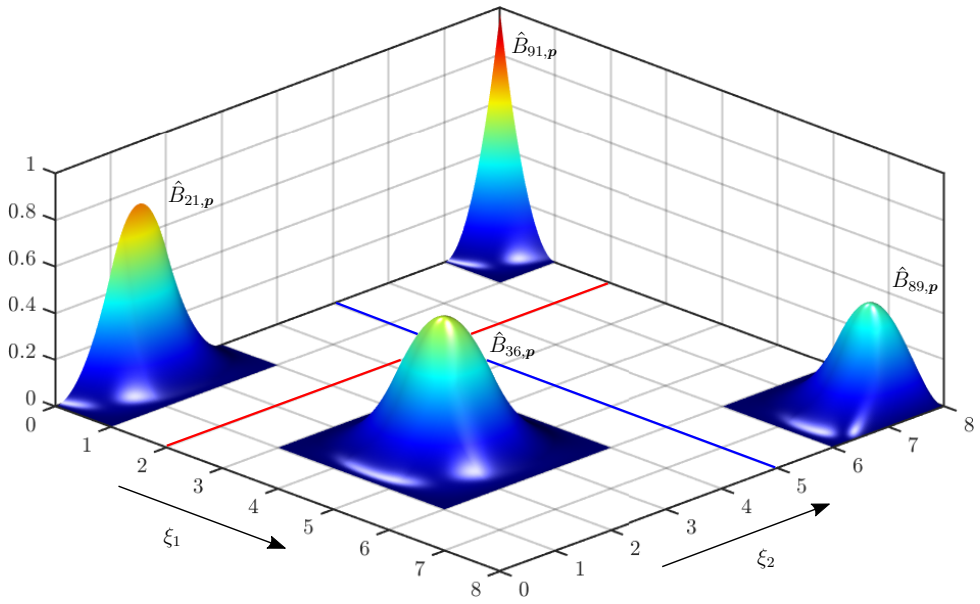

Figure 2.4: Bivariate, biquadratic ($\boldsymbol{p} = (2,2)$) basis functions defined by the two open knot vectors $\Theta^1 = \Theta^2 = \{0,0,0,1,2,3,4,5,6,7,8,8,8\}$. The grid lines on the ξ_1-ξ_2 plane represent the mesh on $\hat{\Omega} = (0,8) \times (0,8)$, which consists of the elements $\hat{e}_{(i,j)} = (\tilde{\zeta}_i, \tilde{\zeta}_{i+1}) \times (\tilde{\zeta}_j, \tilde{\zeta}_{j+1})$, $i,j = 1,\dots,8$, defined by the breakpoint vectors $\tilde{\Theta}^1 = \tilde{\Theta}^2 = \{\tilde{\zeta}_1,\dots,\tilde{\zeta}_9\} = \{0,1,2,3,4,5,6,7,8\}$. The red line marks the hyperplane $\mathcal{H}^1_3$ and the blue ones the hyperplane $\mathcal{H}^2_6$.

NURBS

NURBS basis functions associated with a B-spline basis are defined through

$$\hat{R}_{a,\boldsymbol{p}}(\boldsymbol{\xi}) = \hat{R}_{\boldsymbol{i},\boldsymbol{p}}(\boldsymbol{\xi}) = \frac{w_{\boldsymbol{i}} \hat{B}_{\boldsymbol{i},\boldsymbol{p}}(\boldsymbol{\xi})}{W(\boldsymbol{\xi})}, \quad W(\boldsymbol{\xi}) = \sum_{\boldsymbol{j} \in \mathbf{I}} w_{\boldsymbol{j}} \hat{B}_{\boldsymbol{j},\boldsymbol{p}}(\boldsymbol{\xi}), \quad \boldsymbol{\xi} \in \hat{\Omega}, \tag{2.6}$$

where W is referred to as weighting function and $w_{\boldsymbol{j}} \in \mathbb{R}$ are positive weights. As $w_{\boldsymbol{i}} \hat{B}_{\boldsymbol{i},\boldsymbol{p}}$ and W are both piecewise polynomials, $\hat{R}_{\boldsymbol{i},\boldsymbol{p}}$ is a piecewise rational function – within each element it is a polynomial divided by another polynomial. Per definition, the numerator and denominator of $\hat{R}_{\boldsymbol{i},\boldsymbol{p}}$ have the same degree, and so we refer to the "degree of $\hat{R}_{\boldsymbol{i},\boldsymbol{p}}$", meaning that of $\hat{B}_{\boldsymbol{i},\boldsymbol{p}}$. It is important to note that due to $w_{\boldsymbol{i}} > 0$ for all $\boldsymbol{i} \in \mathbf{I}$, the non-negativity of B-splines and the partition of unity, cf. Section 2.1.1, it holds

$$W(\boldsymbol{\xi}) = \sum_{\boldsymbol{j} \in \mathbf{I}} w_{\boldsymbol{j}} \hat{B}_{\boldsymbol{j},\boldsymbol{p}}(\boldsymbol{\xi}) \geq \min_{\boldsymbol{i} \in \mathbf{I}} w_{\boldsymbol{i}} \sum_{\boldsymbol{j} \in \mathbf{I}} \hat{B}_{\boldsymbol{j},\boldsymbol{p}}(\boldsymbol{\xi}) = \min_{\boldsymbol{i} \in \mathbf{I}} w_{\boldsymbol{i}} > 0 \quad \forall \boldsymbol{\xi} \in \hat{\Omega}. \tag{2.7}$$

I.e. the functions $\hat{R}_{\boldsymbol{i},\boldsymbol{p}} \colon \hat{\Omega} \to \mathbb{R}$ are well defined. The continuity of the functions, as well as their support, follows directly from the knot vectors. I.e., $\hat{R}_{\boldsymbol{i},\boldsymbol{p}}$ has the same support and continuity as $\hat{B}_{\boldsymbol{i},\boldsymbol{p}}$. Furthermore, the functions $\hat{R}_{\boldsymbol{i},\boldsymbol{p}}$ are linearly independent on the parametric space $\hat{\Omega}$, they still constitute a partition of unity and they are non-negative.

Note that if the weights $w_{\boldsymbol{i}}$ are equal, then $\hat{R}_{\boldsymbol{i},\boldsymbol{p}}(\boldsymbol{\xi}) = \hat{B}_{\boldsymbol{i},\boldsymbol{p}}(\boldsymbol{\xi})$ for all $\boldsymbol{\xi} \in \hat{\Omega}$. Thus, B-splines are a special case of NURBS.

Convention 2.1.2. *Since B-splines can be interpreted as a special case of NURBS, the terms $\hat{R}_{a,\boldsymbol{p}}$ and $\hat{R}_{\boldsymbol{i},\boldsymbol{p}}$ will be used for both NURBS and B-splines in the following. According to Convention 2.1.1, these designations thus include all kinds of basis functions considered so far. Furthermore, the index $\boldsymbol{p}$ is omitted in cases where misunderstandings are excluded.*

Derivatives of B-splines and NURBS

The derivatives of univariate B-spline basis functions can be expressed in terms of B-spline lower-degree bases. For a given order p and a knot vector Θ, the derivative of the ith basis function is given by

$$\frac{\mathrm{d}}{\mathrm{d}\xi}\hat{N}_{i,p}(\xi) = \frac{p}{\zeta_{i+p}-\zeta_i}\hat{N}_{i,p-1}(\xi) - \frac{p}{\zeta_{i+p+1}-\zeta_{i+1}}\hat{N}_{i+1,p-1}(\xi), \tag{2.8}$$

which can be generalized to higher order derivatives by simply differentiating each side $m-1$ times

$$\frac{\mathrm{d}^m}{\mathrm{d}\xi^m}\hat{N}_{i,p}(\xi) = \frac{p}{\zeta_{i+p}-\zeta_i}\frac{\mathrm{d}^{m-1}}{\mathrm{d}\xi^{m-1}}\hat{N}_{i,p-1}(\xi) - \frac{p}{\zeta_{i+p+1}-\zeta_{i+1}}\frac{\mathrm{d}^{m-1}}{\mathrm{d}\xi^{m-1}}\hat{N}_{i+1,p-1}(\xi). \tag{2.9}$$

Expanding Eq. (2.9) by means of Eq. (2.8) also gives an expression of the mth derivative of $\hat{N}_{i,p}$ purely in terms of lower order functions $\hat{N}_{i,p-m},\ldots,\hat{N}_{i+m,p-m}$

$$\frac{\mathrm{d}^m}{\mathrm{d}\xi^m}\hat{N}_{i,p}(\xi) = \frac{p!}{(p-m)!}\sum_{j=0}^{m}\alpha_{m,j}\hat{N}_{i+j,p-m}(\xi), \tag{2.10a}$$

where the coefficients $\alpha_{m,j}$ are given by the recursion

$$\alpha_{m,0} = \frac{\alpha_{m-1,0}}{\zeta_{i+p-m+1}-\zeta_i}, \quad \alpha_{m,j} = \frac{\alpha_{m-1,j}-\alpha_{m-1,j-1}}{\zeta_{i+p+j-m+1}-\zeta_{i+j}}, \quad \alpha_{m,m} = \frac{-\alpha_{m-1,m-1}}{\zeta_{i+p+1}-\zeta_{i+m}}, \tag{2.10b}$$

with $\alpha_{0,0} = 1$. Note that in case of knot multiplicities greater than one, the dominator of several of these quotients may become zero. Whenever this happens the quotient is defined to be zero. Due to the tensor product structure of multivariate B-splines, the formulas can be applied in a straightforward manner since it holds for any $\boldsymbol{m} \in \mathbb{N}_0^{d_p}$

$$\partial^{\boldsymbol{m}}\hat{B}_{\boldsymbol{i},\boldsymbol{p}}(\boldsymbol{\xi}) = \prod_{l=1}^{d_p}\frac{\mathrm{d}^{m_l}}{\mathrm{d}\xi_l^{m_l}}\hat{N}^l_{i_l,p_l}(\xi_l), \tag{2.11}$$

cf. Eq. (2.3). Eventually, a formula for NURBS basis function is given by

$$\partial^{\boldsymbol{m}}\hat{R}_{\boldsymbol{i},\boldsymbol{p}}(\boldsymbol{\xi}) = \frac{w_{\boldsymbol{i}}\partial^{\boldsymbol{m}}\hat{R}_{\boldsymbol{i},\boldsymbol{p}}(\boldsymbol{\xi}) - \sum_{\boldsymbol{n}<\boldsymbol{m}}\binom{\boldsymbol{m}}{\boldsymbol{n}}\partial^{\boldsymbol{n}}\hat{R}_{\boldsymbol{i},\boldsymbol{p}}(\boldsymbol{\xi})\partial^{\boldsymbol{m}-\boldsymbol{n}}W(\boldsymbol{\xi})}{W(\boldsymbol{\xi})}, \tag{2.12}$$

with $\boldsymbol{m}$, $\boldsymbol{n} \in \mathbb{N}_0^{d_p}$ and the binomial coefficient

$$\binom{\boldsymbol{m}}{\boldsymbol{n}} = \frac{\boldsymbol{m}!}{\boldsymbol{n}!(\boldsymbol{m}-\boldsymbol{n})!} = \binom{m_1}{n_1} \dots \binom{m_{d_p}}{n_{d_p}}. \tag{2.13}$$

Efficient algorithms for these calculations and the proofs of the formulas can be found in Piegl and Tiller [130].

2.1.2 NURBS geometries

In the following, we present parametric descriptions of curves, surfaces and three dimensional solids based on NURBS. The aim is to provide a basic understanding of the modelling of such geometries. For this purpose, the influence of different parameters such as the knot vector and the NURBS weights is explained using various examples. In addition, a summary of the most important properties of NURBS geometries with regard to IGA is given. We point out that the considerations here include both NURBS and B-spline parametrisations according to Convention 2.1.2. For a deeper insight into this topic and efficient geometric algorithms, the reader is referred to the works of Piegl & Tiller [129, 130, 157] and the references therein.

NURBS Curves

A pth-degree NURBS curve in $\mathbb{R}^d$ is defined as a linear combination of the form

$$\boldsymbol{\mathcal{G}}(\xi) = \sum_{a=1}^{\mathrm{n}} \boldsymbol{P}_a \hat{R}_{a,p}(\xi), \quad \xi \in \hat{\Omega}, \tag{2.14}$$

where the vector valued coefficients $\boldsymbol{P}_a \in \mathbb{R}^d$ are referred to as control points and the functions $\hat{R}_{a,p}$ are pth-degree univariate ($d_p = 1$) NURBS basis functions defined by a knot vector $\Theta = \{\zeta_1, \dots, \zeta_{\mathrm{n}+p+1}\}$ and a set of weights $\boldsymbol{w}$. The piecewise interpolation of the control points gives the so-called control polygon.

The example shown in Figure 2.5 is constructed from an open knot vector with an internal knot repetition. Note that the curve interpolates the first and last control points and is tangent to the control polygon at these points, which are general features of a curve built from an open knot vector, cf. [130]. Moreover, it can be observed, that the curve also interpolates the sixth control point. This is due to the fact, that the multiplicity of the breakpoint $\tilde{\zeta}_5 = 4$ is equal to the polynomial degree. The curve is $C^{p-1} = C^1$-continuous everywhere except at this location, where it is reduced to $C^{p-2} = C^0$. In such a case, all the basis functions vanish at this breakpoint, except one which takes the value 1 as shown in the lower picture in Figure 2.5. The effect of the NURBS weights on the curve can be seen in the upper image in Figure 2.5. All weights are 1 except of $w_4 = 3$ and $w_7 = 2$. Due to the greater weighting, the curve is "pulled" towards the corresponding control points $\boldsymbol{P}_4$, $\boldsymbol{P}_7$. In general, when a weight w_i increases (decreases), the curve

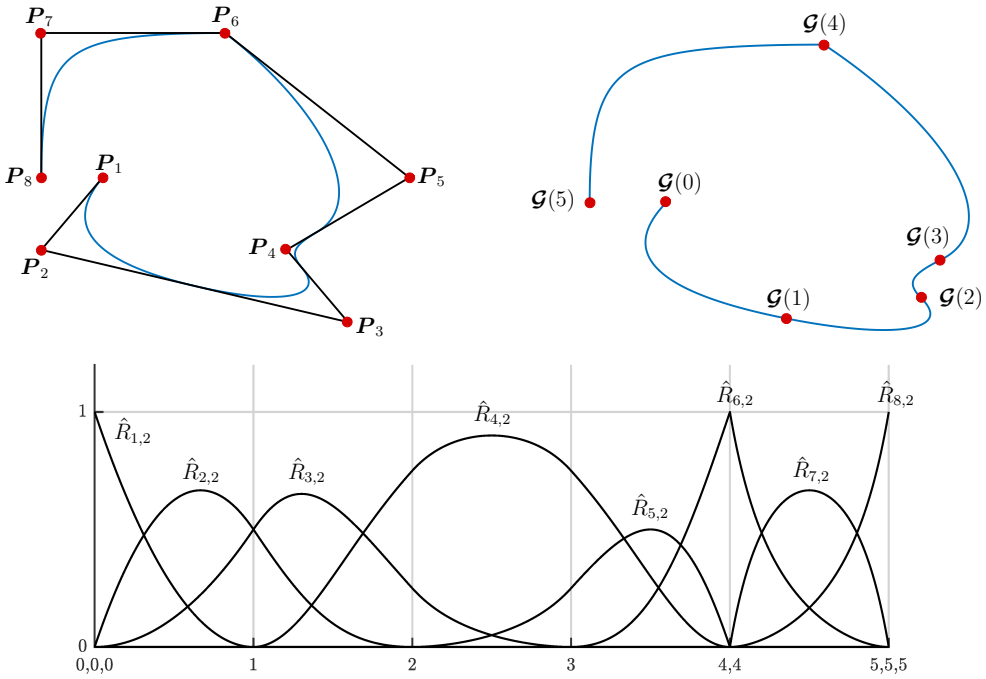

Figure 2.5: A quadratic NURBS curve ($p = 2$) in $\mathbb{R}^2$. The upper left picture shows the curve (blue line) together with the control polygon (black line). The upper right picture shows the segmentation of the curve into elements by the images of the breakpoints. The lower picture shows the corresponding NURBS basis defined by the knot vector $\Theta = \{\zeta_1, \dots, \zeta_{11}\} = \{0, 0, 0, 1, 2, 3, 4, 4, 5, 5, 5\}$ and the NURBS weights $\boldsymbol{w} = (w_1, \dots, w_8) = (1, 1, 1, 3, 1, 1, 2, 1)$.

moves closer (further) to $\boldsymbol{P}_i$, which also holds for other NURBS geometries like surfaces and solids. Note further the difference between the control points $\boldsymbol{P}_i$ and the images $\boldsymbol{\mathcal{G}}(\tilde{\zeta}_i)$ of the breakpoints. Just as the breakpoints partition the parameter space $\hat{\Omega}$ into elements, their images under the parametrisation $\boldsymbol{\mathcal{G}}$ divide the curve into elements. Conversely, the control points are, in general, not located on the curve.

Eventually, in addition to the above discussed properties, the following geometric characteristics of NURBS curves are of importance [44, 130]:

- $\boldsymbol{\mathcal{G}}$ is infinitely differentiable between two breakpoints and $(p-k)$-times continuously differentiable at a breakpoint of multiplicity k.

- Local approximation: if the control point $\boldsymbol{P}_a$ is moved, or the weight w_a is changed, it only affects the portion $\boldsymbol{\mathcal{G}}([\zeta_a, \zeta_{a+p+1}))$ of the curve. This is a consequence of the compact support of the NURBS basis functions.

- Affine invariance: an affine transformation is applied by the curve by applying it to the control points. This is due to the fact, that a NURBS basis provides a partition of unity.

NURBS Surfaces

As with curves, a NURBS surface in $\mathbb{R}^d$, $d \in \{2,3\}$, is given as a linear combination

$$\boldsymbol{\mathcal{G}}(\boldsymbol{\xi}) = \sum_{\boldsymbol{i}\in\mathbf{I}} \boldsymbol{P}_{\boldsymbol{i}} \hat{R}_{\boldsymbol{i},\boldsymbol{p}}(\boldsymbol{\xi}), \quad \boldsymbol{\xi} \in \hat{\Omega}, \tag{2.15}$$

where the bivariate ($d_p = 2$) basis functions $\hat{R}_{\boldsymbol{i},\boldsymbol{p}}$ are defined by the polynomial degree $\boldsymbol{p} = (p_1, p_2)$, two knot vectors $\Theta^l = \{\zeta^l_1, \ldots, \zeta^l_{\mathfrak{n}_l+p_l+1}\}$, $l = 1,2$, and a set of NURBS weights. The piecewise linear interpolation of the control points $\boldsymbol{P}_{(i_1,i_2)} \in \mathbb{R}^d$ gives here the so-called control net. The upper picture in Figure 2.6 shows an example of a $\boldsymbol{p} = (4,3)$ degree NURBS surface in $\mathbb{R}^3$ build from the two open knot vectors $\Theta^1 = \{0,0,0,0,0,1,2,2,2,2,2\}$, $\Theta^2 = \{0,0,0,0,1,2,2,2,2\}$ together with the corresponding control net. Due to the use of open knot vectors, the boundary of the surface is solely

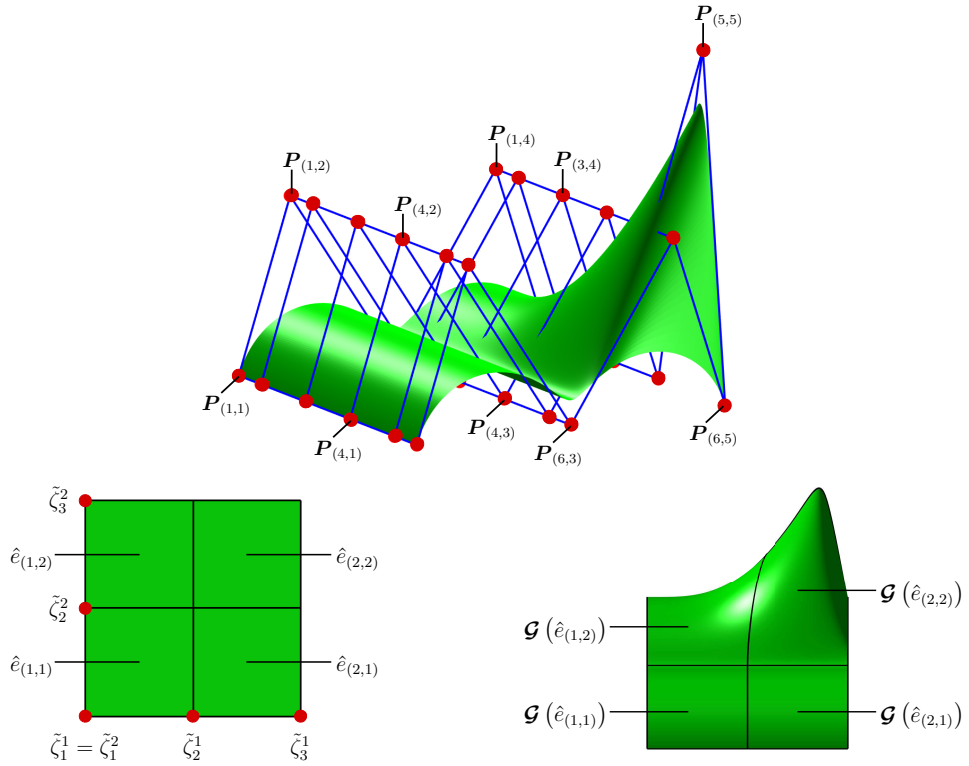

Figure 2.6: A NURBS surface of degree $\boldsymbol{p} = (4,3)$. The upper picture shows the surface together with the control net. The lower left picture shows the corresponding parameter space and the mesh consisting of the four elements $\hat{e}_{(i_1,i_2)}$, $i_1, i_2 \in \{1,2\}$, defined by the breakpoint vectors $\tilde{\Theta}^l = \{\tilde{\zeta}^l_1, \tilde{\zeta}^l_2, \tilde{\zeta}^l_3\} = \{0,1,2\}$, $l = 1,2$. The lower right picture shows the surface from a different perspective and the mesh given by the images of $\hat{e}_{(i_1,i_2)}$ under $\boldsymbol{\mathcal{G}}$.

determined by the control points $M_1 = \{\boldsymbol{P}_{(i_1,i_2)} \,|\, i_1 = 1 \vee i_1 = 6 \vee i_2 = 1 \vee i_2 = 5\}$, forming the first and last row, respectively, in the underlying tensor product structure, and the corner points are interpolated, i.e. $\boldsymbol{\mathcal{G}}(\tilde{\zeta}^1_{i_1}, \tilde{\zeta}^2_{i_2}) = \boldsymbol{P}_{(i_1,i_2)}$, if $(i_1,i_2) \in \{(1,1),(1,5),(6,1),(6,5)\}$.

In addition, the slope along the boundary is determined only by the first, second, last and penultimate rows of control points given by $M_1 \cup \{\boldsymbol{P}_{(i_1,i_2)} \,|\, i_1 = 2 \vee i_1 = 5 \vee i_2 = 2 \vee i_2 = 4\}$, which is also a direct consequence of the use of open knot vectors.

Analogously to NURBS curves, the images of the elements $\hat{e}_{(i_1,i_2)} \in \hat{\mathscr{M}}$, cf. Eq. (2.5), under $\boldsymbol{\mathcal{G}}$ form in a natural way a mesh on the surface as illustrated by the two lower pictures in Figure 2.6. Furthermore, $\boldsymbol{\mathcal{G}}$ is C^∞-continuous in every element $\hat{e}_{(i_1,i_2)}$ and $(p_l - k_i^l)$-times continuously differentiable with respect to its lth argument on every mesh line $\mathcal{H}_i^l$, $l = 1, 2$, $i = 1, \ldots \tilde{\mathfrak{n}}_l$, cf. Section 2.1.1. Eventually, $\boldsymbol{\mathcal{G}}$ is affine invariant and local, in the sense that if the control point $\boldsymbol{P}_{(i_1,i_2)}$ is moved, or the weight $w_{(i_1,i_2)}$ is changed, it only affects the part $\boldsymbol{\mathcal{G}}([\zeta_{i_1}^1, \zeta_{i_1+p_1+1}^1) \times [\zeta_{i_2}^2, \zeta_{i_2+p_2+1}^2))$.

NURBS Solids

In $\mathbb{R}^3$, NURBS solids are defined in the same manner as NURBS surfaces and curves by extending the tensor product structure accordingly. They are given by linear combinations of the form

$$\boldsymbol{\mathcal{G}}(\boldsymbol{\xi}) = \sum_{\boldsymbol{i} \in \mathbf{I}} \boldsymbol{P}_{\boldsymbol{i}} \hat{R}_{\boldsymbol{i},\boldsymbol{p}}(\boldsymbol{\xi}), \quad \boldsymbol{\xi} \in \hat{\Omega}, \tag{2.16}$$

where the trivariate ($d_p = 3$) basis functions $\hat{R}_{\boldsymbol{i},\boldsymbol{p}}$ are defined by the polynomial degree $\boldsymbol{p} = (p_1, p_2, p_3)$, three knot vectors $\Theta^l = \{\zeta_1^l, \ldots, \zeta_{\mathfrak{n}_l+p_l+1}^l\}$, $l = 1, 2, 3$, and a set of weights. The piecewise linear interpolation of the control points $\boldsymbol{P}_{(i_1,i_2,i_3)} \in \mathbb{R}^3$ gives here the so-called control lattice.

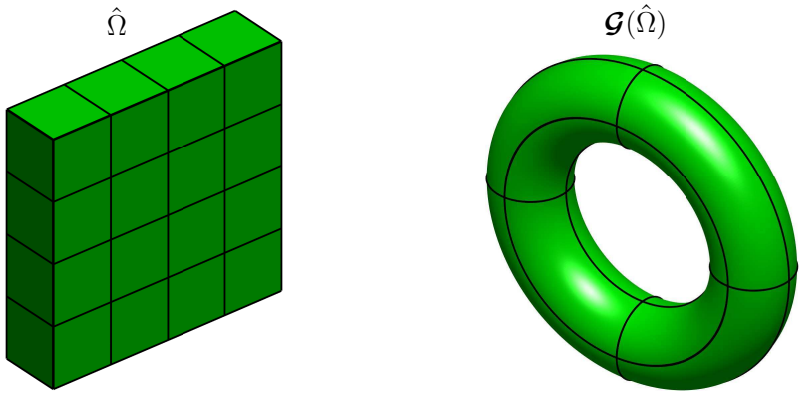

Figure 2.7: A NURBS solid of degree $\boldsymbol{p} = (2, 1, 2)$ built from the three open knot vectors $\Theta^1 = \Theta^3 = \{0, 0, 0, 1, 1, 2, 2, 3, 3, 4, 4, 4\}$, $\Theta^2 = \{0, 0, 1, 1\}$ and a set of 162 weights the specification of which is omitted here for reasons of clarity. Left: parameter space $\hat{\Omega}$ decomposed into elements. Right: the image of $\hat{\Omega}$ under $\boldsymbol{\mathcal{G}}$, a hollow torus, and the mesh on $\boldsymbol{\mathcal{G}}(\hat{\Omega})$ given by the images of the element boundaries in $\hat{\Omega}$ under $\boldsymbol{\mathcal{G}}$.

Figure 2.7 shows a hollow torus and the underlying parameter space with the respective meshes induced by the corresponding breakpoint vectors. The geometric properties of

NURBS solids are trivariate generalisations of those of NURBS surfaces. In brief, $\boldsymbol{\mathcal{G}}$ is local, affine invariant, C^∞-continuous in the elements and C^m-continuous on the element boundaries, where $m = \min\{p_l - k_i^l \,|\, l = 1,2,3,\ i = 1,\dots,\tilde{\mathfrak{n}}_l\}$ and k_i^l are the multiplicities with respect to $\tilde{\Theta}^l$.

2.1.3 Refinement

The breakpoint vectors naturally provide a mesh in the parameter space, which is mapped onto the physical space by the respective NURBS parametrisation. Thereby, the mesh as well as the number of basis functions are initially determined by the shape of the corresponding geometry. For IGA, however, it is necessary to refine the mesh resp. to enrich the approximation space while leaving the underlying geometry and its parametrisation intact. Two basic methods used for this purpose, namely knot insertion and degree elevation, are presented below. Both originate from the CAD field and were developed for application to B-spline geometries. However, the latter is not really a limitation, since the application to general NURBS geometries can be done via an argument from projective geometry. The idea is to represent a NURBS entity in $\mathbb{R}^d$ with homogeneous coordinates as a B-spline geometry in $\mathbb{R}^{d+1}$, apply the appropriate procedure to it and then return to a NURBS representation in $\mathbb{R}^d$ with the new data. To this end, each control point $\boldsymbol{P}_a \in \mathbb{R}^d$ of the NURBS geometry, together with the corresponding weight w_a, are mapped into the space $\mathbb{R}^{d+1}$ via

$$\mathbb{R}^d \times \mathbb{R} \ni (\boldsymbol{P}_a, w_a) \mapsto \boldsymbol{P}_a^w := (w_a \boldsymbol{P}_a, w_a) \in \mathbb{R}^{d+1}. \tag{2.17}$$

The corresponding B-spline parametrisation in $\mathbb{R}^{d+1}$ then results as linear combination of the points $\boldsymbol{P}_a^w$ and the B-spline basis functions underlying the basis of the NURBS entity. Eventually, after applying the respective procedure, the control points $\bar{\boldsymbol{P}}_a^w = (\bar{P}_{a,1}^w, \dots, \bar{P}_{a,d+1}^w)^{\mathrm{T}} \in \mathbb{R}^{d+1}$ of the modified parametrisation are transformed back via

$$\mathbb{R}^{d+1} \ni \bar{\boldsymbol{P}}_a^w = (\bar{P}_{a,1}^w, \dots, \bar{P}_{a,d+1}^w) \mapsto (\bar{\boldsymbol{P}}_a, \bar{w}_a) \in \mathbb{R}^d \times \mathbb{R}, \tag{2.18}$$

where $\bar{w}_a := \bar{P}_{a,d+1}^w$ and $\bar{\boldsymbol{P}}_a := (P_{a,1}^w/\bar{w}_a, \dots, P_{a,d}^w/\bar{w}_a)^{\mathrm{T}}$, to obtain the control points and weights of the corresponding NURBS geometry in $\mathbb{R}^d$. More details concerning projective geometry in the context of NURBS can be found in Farin [75].

For the description of the two methods, let for the remainder of this section $\boldsymbol{\mathcal{G}}\colon \hat{\Omega} \to \mathbb{R}^d$ be a B-spline parametrisation of order $\boldsymbol{p} = (p_1, \dots, p_{d_p})$, defined through the knot vectors $\Theta^1, \dots, \Theta^{d_p}$, $d_p \geq 1$, such that the corresponding B-spline basis consists of $\mathfrak{n} = \mathfrak{n}_1 \mathfrak{n}_2 \dots \mathfrak{n}_{d_p}$ functions, where $\mathfrak{n}_l$ as usual denotes the number of univariate basis functions in the lth parametric direction.

Knot insertion. As the name suggests, in this method the number of basis functions is increased by adding knots to the underlying knot vectors. For example, by adding a knot $\bar{\zeta}$ in Θ^l, a new univariate basis is obtained based on the resulting knot vector $\bar{\Theta}^l$ according

to recursion (2.1). Due to the underlying tensor product structure, this also yields a new multivariate basis $\{\hat{R}_{a,\boldsymbol{p}}\}_{a=1}^{\mathfrak{r}}$ consisting of $\mathfrak{r} = \mathfrak{n} + \mathfrak{n}/\mathfrak{n}_l$ functions. The actual task of knot insertion is now to find suitable control points $\{\bar{\boldsymbol{P}}_a\}_{a=1}^{\mathfrak{r}}$ so that the geometry and the parametrisation remain unchanged, i.e. points that fulfil $\sum_{a=1}^{\mathfrak{r}} \bar{\boldsymbol{P}}_a \hat{R}_{a,\boldsymbol{p}}(\boldsymbol{\xi}) = \boldsymbol{\mathcal{G}}(\boldsymbol{\xi})$, for all $\boldsymbol{\xi} \in \hat{\Omega}$. The latter problem can be solved, for example, by substituting $\mathfrak{r}$ suitable values of $\boldsymbol{\xi}$ into the equation and solving the resulting system of linear equations. However, there are much more efficient methods, which are described in Piegl & Tiller [130]. In particular, a proof for the existence of the points $\{\bar{\boldsymbol{P}}_a\}_{a=1}^{\mathfrak{r}}$ can also be found there.

Degree elevation. In this method, the approximation space is enriched by increasing the polynomial degree in a selected direction l. Since the parametrisation in each element is a polynomial of order p_l, the order elevation is trivial there. From a vector space point of view, the space of polynomials of order p_l is embedded in the space of polynomials of order $p_l + 1$ via the map $s(\xi) \mapsto s(\xi) + 0 \cdot \xi^{p_l+1}$, where s denotes a polynomial in ξ of order p_l. The element boundaries, however, require more attention, as the continuity of $\boldsymbol{\mathcal{G}}$ must be maintained. To increase the order in direction l by one, a new knot vector is formed based on the breakpoint vector $\tilde{\Theta}^l = \{\tilde{\zeta}_1, \dots, \tilde{\zeta}_{\tilde{\mathfrak{n}}_l}\}$ according to

$$\bar{\Theta}^l = \{\bar{\zeta}_1, \dots, \bar{\zeta}_{\bar{\mathfrak{n}}_l+\bar{p}_l+1}\} = \{\underbrace{\tilde{\zeta}_1, \dots, \tilde{\zeta}_1}_{k_1^l+1}, \underbrace{\tilde{\zeta}_2, \dots, \tilde{\zeta}_2}_{k_2^l+1}, \dots \underbrace{\tilde{\zeta}_{\tilde{\mathfrak{n}}_l}, \dots, \tilde{\zeta}_{\tilde{\mathfrak{n}}_l}}_{k_{\tilde{\mathfrak{n}}_l}^l+1}\}, \tag{2.19}$$

where k_i^l is the multiplicity of $\tilde{\zeta}_i$ in Θ^l and $\bar{\mathfrak{n}}_l := \mathfrak{n}_l + \tilde{\mathfrak{n}}_l - 1$ the number of the univariate basis function corresponding to $\bar{\Theta}^l$ and the elevated order $\bar{p}_l := p_l + 1$. In other words, the knot vector $\bar{\Theta}^l$ to the elevated order $\bar{p}_l$ results from Θ^l by increasing the multiplicity of each knot by 1. Eventually, together with the remaining knot vectors, Θ^i, $i = 1, \dots d_p$, $i \neq l$, one obtains a new multivariate basis $\{\hat{R}_{a,\bar{\boldsymbol{p}}}\}_{a=1}^{\mathfrak{r}}$ of order $\bar{\boldsymbol{p}} = (p_1, \dots, p_{l-1}, \bar{p}_l, p_{l+1}, \dots p_{d_p})$, consisting of $\mathfrak{r} = \mathfrak{n} + \mathfrak{n}(\tilde{\mathfrak{n}}_l - 1)/\mathfrak{n}_l$ functions, where the corresponding control points $\{\bar{\boldsymbol{P}}_a\}_{a=1}^{\mathfrak{r}}$ are characterized by $\sum_{a=1}^{\mathfrak{r}} \bar{\boldsymbol{P}}_a \hat{R}_{a,\bar{\boldsymbol{p}}}(\boldsymbol{\xi}) = \boldsymbol{\mathcal{G}}(\boldsymbol{\xi})$, $\boldsymbol{\xi} \in \hat{\Omega}$. As with knot insertion, the last equation can be used to construct a linear system of equations to determine the unknowns $\{\bar{\boldsymbol{P}}_a\}_{a=1}^{\mathfrak{r}}$. However, more efficient methods are given by [42, 130, 132, 133].

2.1.4 Multiple patches

NURBS offer a wide range of parametric descriptions but are limited to shapes that are topologically equivalent to lines ($d_p = 1$), rectangles ($d_p = 2$) or cuboids ($d_p = 3$). To increase the number of possibilities, in practice multi-patch descriptions are used. This involves the use of multiple parametrisations whose respective geometries, embedded in a common coordinate system, together yield a more complex shape. For example, as shown in Figure 2.8, an L-shaped three-dimensional body can be described by placing two cuboids of different sizes side by side. While from a graphical point of view, nothing else needs to be considered, such geometries require special treatment in the analysis because, according to the representation, it is a matter of many individual objects and

not a coherent entity. Therefore, the concept of multi-patch geometries is explained in more detail below.

Let $\Omega \subset \mathbb{R}^d$ be an open, bounded and connected domain, given by the union of N open subdomains $\Omega^{(1)}, \dots, \Omega^{(N)} \subset \mathbb{R}^d$ such that

$$\bar{\Omega} = \bigcup_{j=1}^{N} \bar{\Omega}^{(j)}, \quad \Omega^{(i)} \cap \Omega^{(j)} = \emptyset, \text{ if } i \neq j, \tag{2.20}$$

and for each part $\Omega^{(i)}$ there exists a NURBS parametrisation $\boldsymbol{\mathcal{G}}^{(i)} \colon \hat{\Omega}^{(i)} \to \mathbb{R}^d$ with $\Omega^{(i)} = \boldsymbol{\mathcal{G}}^{(i)}(\hat{\Omega}^{(i)})$[†]. Then, Ω is called a multi-patch domain and the subdomains $\Omega^{(1)}, \dots, \Omega^{(N)}$ are called patches. For $1 \leq i < j \leq N$, the interface of two patches is defined as the interior of the intersection of the boundaries, i.e. $\overline{\Gamma}_{i,j} = \partial\Omega^{(i)} \cap \partial\Omega^{(j)}$ where $\Gamma_{i,j}$ is open, and we define the skeleton Γ as the union of all interfaces,

$$\Gamma := \bigcup_{1 \leq i < j \leq N} \Gamma_{i,j}. \tag{2.21}$$

Furthermore, we denote the pre-images of an interface $\Gamma_{i,j} \neq \emptyset$ under the parametrisation $\boldsymbol{\mathcal{G}}^{(i)}$ or $\boldsymbol{\mathcal{G}}^{(j)}$ with $\hat{\Gamma}_j^i$ or $\hat{\Gamma}_i^j$, respectively, and specify assignments $\mathrm{P}_j^i \colon \hat{\Gamma}_j^i \to \hat{\Gamma}_i^j$, $\mathrm{P}_i^j \colon \hat{\Gamma}_i^j \to \hat{\Gamma}_j^i$ of the parametric coordinates by a closest point projection through

$$\begin{aligned} \mathrm{P}_j^i\, \boldsymbol{\xi}^{(i)} = \boldsymbol{\xi}^{(j)} \quad &:\Longleftrightarrow \quad \|\boldsymbol{\mathcal{G}}^{(i)}(\boldsymbol{\xi}^{(i)}) - \boldsymbol{\mathcal{G}}^{(j)}(\boldsymbol{\xi}^{(j)})\| = \min_{\boldsymbol{\xi} \in \hat{\Gamma}_i^j} \|\boldsymbol{\mathcal{G}}^{(i)}(\boldsymbol{\xi}^{(i)}) - \boldsymbol{\mathcal{G}}^{(j)}(\boldsymbol{\xi})\|, \\ \mathrm{P}_i^j\, \boldsymbol{\xi}^{(j)} = \boldsymbol{\xi}^{(i)} \quad &:\Longleftrightarrow \quad \|\boldsymbol{\mathcal{G}}^{(i)}(\boldsymbol{\xi}^{(i)}) - \boldsymbol{\mathcal{G}}^{(j)}(\boldsymbol{\xi}^{(j)})\| = \min_{\boldsymbol{\xi} \in \hat{\Gamma}_j^i} \|\boldsymbol{\mathcal{G}}^{(i)}(\boldsymbol{\xi}) - \boldsymbol{\mathcal{G}}^{(j)}(\boldsymbol{\xi}^{(j)})\|. \end{aligned} \tag{2.22}$$

By means of P_i^j and P_j^i the parametric coordinates of a common point in $\Gamma_{i,j}$ are linked in such a way that $\boldsymbol{\mathcal{G}}^{(i)} = \boldsymbol{\mathcal{G}}^{(j)} \circ \mathrm{P}_j^i$ on $\hat{\Gamma}_j^i$ and $\boldsymbol{\mathcal{G}}^{(i)} \circ \mathrm{P}_i^j = \boldsymbol{\mathcal{G}}^{(j)}$ on $\hat{\Gamma}_i^j$. In particular, for surfaces in $\mathbb{R}^3$, P_i^j and P_j^i are used in the following to formulate coupling conditions in a clear way. However, it is important to note that the parametric mappings defined by (2.22) are not well-defined for arbitrary NURBS parametrisations. Especially, if $\boldsymbol{\mathcal{G}}^{(i)}$ or $\boldsymbol{\mathcal{G}}^{(j)}$ is not an injection, minima according to (2.22) can be taken at several points in the parameter spaces. To ensure well-definiteness, a suitable regularity assumption on the NURBS parametrisations is needed, which will be formulated in Section 2.2 (Assumption 2.2.1) in connection with the construction of isogeometric approximation spaces. Until then, we tacitly assume that the parametrisations are sufficiently good-natured so that P_j^i and P_i^j are well-defined. We also note that the definition through a closest point projection is closely related to the problem of point inversion. Therefore, algorithms from this field can be used directly for implementation to a large extent. Further details on this topic can be found in Section 6.1 in [130]. Finally, an illustration of the multi-patch entities introduced is given in Figure 2.8, and we conclude with the following agreement in order to achieve a better representation of the further issues.

[†]Superscripts in round brackets, e.g. (i), are generally used to refer to the ith patch. Especially for functions $\boldsymbol{f}$ defined on Ω, the notation corresponds to the restriction of $\boldsymbol{f}$ to $\Omega^{(i)}$, i.e. $\boldsymbol{f}^{(i)} = \boldsymbol{f}_{|\Omega^{(i)}}$. This convention will be maintained throughout the rest of the work.

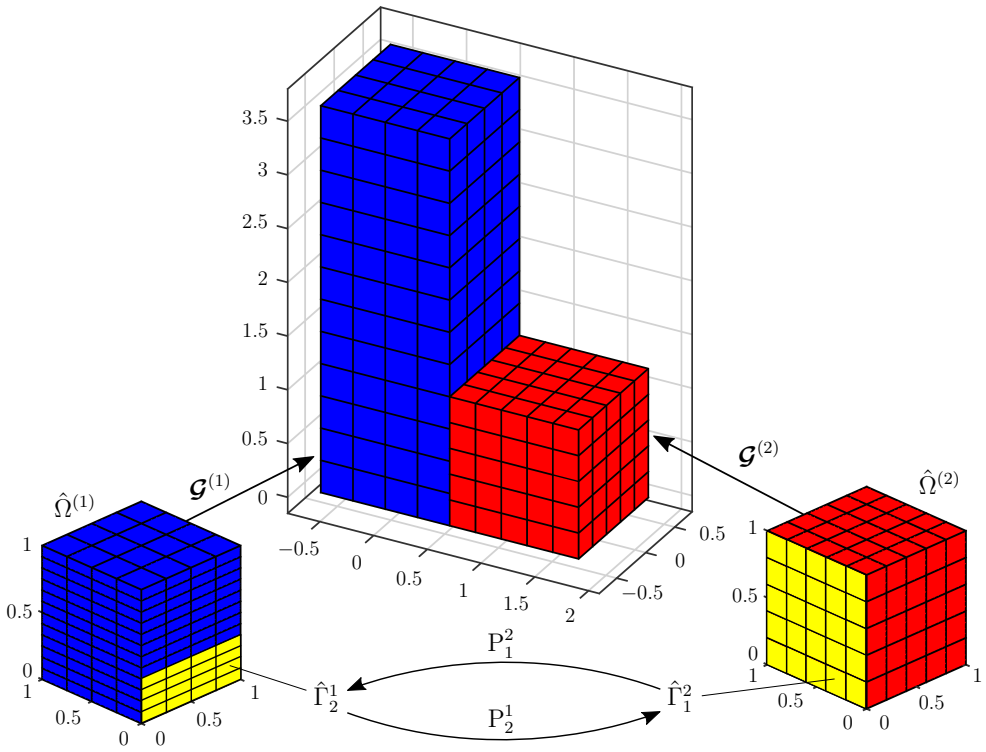

Figure 2.8: A two-patch geometry. The pre-images of the interface $\Gamma_{1,2}$ under $\boldsymbol{\mathcal{G}}^{(1)}$ and $\boldsymbol{\mathcal{G}}^{(2)}$, respectively, are marked in yellow.

Assumption 2.1.1. *For the remainder of this work, we assume that each parametric space $\hat{\Omega} \subset \mathbb{R}^{d_p}$ is given by the unit cube $(0,1)^{d_p}$. Accordingly, we omit the superscripts (i) at the parameter spaces in the case of multi-patch geometries.*

We point out that Assumption 2.1.1 is not a significant restriction. A suitable NURBS representation with the unit cube as parameter space can always be obtained by an appropriate reparametrisation, cf. Section 6.4 in Piegel & Tiller [130].

2.1.5 Geometric Continuity for surfaces

For the purposes of analysis, the continuity between patches plays a crucial role. While the continuity of each patch is determined by the underlying parametrisation, each non-empty interface must be considered separately. For parametric geometries, there are two types of continuity, parametric continuity C and geometric continuity G. Thereby, the geometric continuity measures the relative smoothness with which two patches meet, while parametric continuity is defined as usual through the derivatives of the corresponding parametrisations. For example, two patches with a common boundary are said to meet with geometric continuity of order zero, which is equivalent to C^0-continuity. However, C^n- and G^n-continuity differ from each other in the case $n > 0$. Since, in the framework

of multi-patch Kirchhoff-Love shell theory, we need the notion of first-order geometric continuity, the difference between G^1 and C^1 is briefly discussed below. More general considerations on geometric continuity can be found in [59, 60, 76, 80].

For $d \in \{2, 3\}$ let $\boldsymbol{\mathcal{G}}^{(i)} \colon (0,1)^2 \to \mathbb{R}^d$, $i = 1, 2$, be parametric descriptions of two surfaces with a common edge $\Gamma_{1,2}$, i.e.

$$\boldsymbol{\mathcal{G}}^{(1)}(\boldsymbol{\xi}^{(1)}) = \boldsymbol{\mathcal{G}}^{(2)}(\mathrm{P}_2^1\, \boldsymbol{\xi}^{(1)}), \quad \forall \boldsymbol{\xi}^{(1)} \in \hat{\Gamma}_2^1. \tag{2.23}$$

The surfaces meet C^1-continuously along this edge if additionally their first derivatives at the interface are equal, i.e.

$$\partial_i \boldsymbol{\mathcal{G}}^{(1)}(\boldsymbol{\xi}^{(1)}) = [\partial_i \boldsymbol{\mathcal{G}}^{(2)}](\mathrm{P}_2^1\, \boldsymbol{\xi}^{(1)}), \quad \forall \boldsymbol{\xi}^{(1)} \in \hat{\Gamma}_2^1, \quad i = 1, 2. \tag{2.24}$$

Geometrically, this means that the tangent vectors of the two surfaces are parallel and have the same magnitude at each point of the interface. In contrast, for G^1-continuity the tangent vectors only have to be coplanar at every interface point, which in turn means the tangent spaces of the two surfaces coincide at every point $\boldsymbol{x} \in \Gamma_{1,2}$. More formally, the two surfaces are G^1-continuous along the interface, if there are four functions $\gamma_j^i \colon \hat{\Gamma}_1^2 \to \mathbb{R}$, $i, j = 1, 2$, such that

$$\partial_i \boldsymbol{\mathcal{G}}^{(1)}(\boldsymbol{\xi}^{(1)}) = \sum_{j=1}^{2} \gamma_j^i(\mathrm{P}_2^1\, \boldsymbol{\xi}^{(1)})[\partial_j \boldsymbol{\mathcal{G}}^{(2)}](\mathrm{P}_2^1\, \boldsymbol{\xi}^{(1)}), \quad \forall \boldsymbol{\xi}^{(1)} \in \hat{\Gamma}_2^1, \quad i = 1, 2. \tag{2.25}$$

Note that if two surfaces meet C^1-continuously they also meet G^1-continuously but not vice versa, i.e. C^1-continuity is a special case of G^1-continuity.

2.2 Construction of isogeometric approximation spaces

It is common practice in FEA to use the same basis for both geometry representation and analysis. This is known as the isoparametric concept. In classical FEA, the basis chosen to approximate the unknown solution fields is then used to approximate the known geometry. This can lead to an additional error contribution if the geometry cannot be accurately represented by the basis chosen for analysis. The basic idea behind IGA is to turn this idea around. In IGA the basis used to accurately model the geometry is then used to approximate the unknown solution fields. This approach avoids the need to approximate a CAD model for the purpose of analysis so that the CAD and FEA packages can use a common data set. Apart from the fact that NURBS are widely used in CAD, we have seen in the preceding sections that they have a number of properties that are useful for analytical purposes. Based on the previous results, the construction of suitable approximation spaces will be discussed in the following. To this end, single-patch domains are first considered in Section 2.2.1 and these approaches are extended to multi-patch domains in Section 2.2.2. For the latter, bases of product spaces are needed, the construction of which is covered within Section 2.2.3.

2.2.1 Isogeometric spaces in a single-patch domain

Let $\Omega \subset \mathbb{R}^d$ be a computational domain represented by a NURBS parametrisation $\boldsymbol{\mathcal{G}}\colon \hat{\Omega} = (0,1)^{d_p} \to \mathbb{R}^d$, $\boldsymbol{\mathcal{G}}(\boldsymbol{\xi}) = \sum_{a=1}^{\mathfrak{n}} \boldsymbol{P}_a \hat{R}_a(\boldsymbol{\xi})$, where the basis $\{\hat{R}_a\}_{a=1}^{\mathfrak{n}}$ is specified through the knot vectors $\Theta^1, \dots, \Theta^{d_p}$. As shown in Section 2.1.1, the associated breakpoint vectors $\tilde{\Theta}^1, \dots, \tilde{\Theta}^{d_p}$ naturally provide a mesh $\hat{\mathscr{M}}$ in the parameter space, which is mapped into the physical space Ω by $\boldsymbol{\mathcal{G}}$. To be more specific, we define the physical mesh as

$$\mathscr{M} := \{e \subset \Omega \,|\, e = \boldsymbol{\mathcal{G}}(\hat{e}),\, \hat{e} \in \hat{\mathscr{M}}\} \tag{2.26}$$

and further introduce the element sizes $\hat{h}_{\hat{e}} = \operatorname{diam}(\hat{e})$ and $h_e = \operatorname{diam}(e)$ for each element $\hat{e} \in \hat{\mathscr{M}}$ and $e \in \mathscr{M}$, respectively. Before we proceed to the construction of a proper approximation space, it is important to note that not every NURBS parametrisation is suitable for IGA. For example, in Section 2.1.4, when introducing the parametric assignments (2.22), we noted that problems arise when the parametrisations are not injective. In fact, we need even stricter conditions for the construction of suitable approximation spaces. To this end, we take our cue from Beirão da Veiga et al. [14] and make use of the following regularity assumption on $\boldsymbol{\mathcal{G}}$.

Assumption 2.2.1. *The parametrisation $\boldsymbol{\mathcal{G}}\colon \hat{\Omega} \to \Omega$ is a bi-Lipschitz homeomorphism[‡]. Moreover, $\boldsymbol{\mathcal{G}}_{|\bar{\hat{e}}}$ is in $C^\infty(\bar{\hat{e}})$ for all $\hat{e} \in \hat{\mathscr{M}}$ and $\boldsymbol{\mathcal{G}}_{|\bar{e}}^{-1}$ is in $C^\infty(\bar{e})$ for all $e \in \mathscr{M}$.*

Apart from ensuring that the mappings (2.22) are well defined, the assumption prevents the existence of singularities. In the two-dimensional case, for instance, the most common singularity occurs when a rectangular element in $\hat{\mathscr{M}}$ is mapped by $\boldsymbol{\mathcal{G}}$ to a curvilinear triangular element, see Figure 2.9 for illustration. We point out that the existence of singularities is not a problem per se but needs specific attention which is out of the scope of this work, see, e.g., Takacs and Jüttler [154, 155] for more details on this topic.

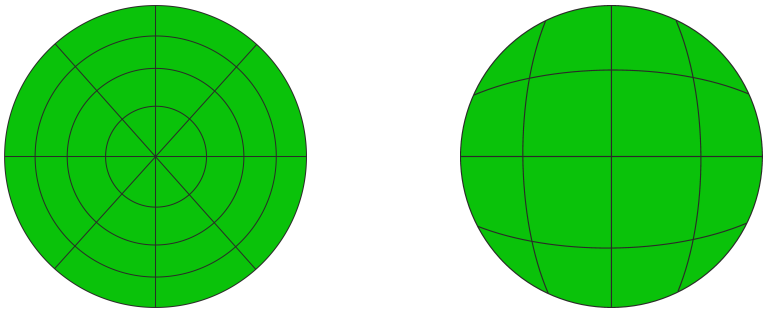

Figure 2.9: Two possible singular parametrisations of the circle. One singularity at the origin (left) and four singularities on the boundary (right).

[‡]A function is called bi-Lipschitz if it is bijective and both the function itself and its inverse are Lipschitz. Thereby, a function $\boldsymbol{f}\colon \mathbb{R}^m \supset X \to Y \subset \mathbb{R}$ is called Lipschitz (or Lipschitz continuous) if there exists a real constant $L > 0$ such that $\|\boldsymbol{f}(\boldsymbol{x}_1) - \boldsymbol{f}(\boldsymbol{x}_2)\| \leq L\|\boldsymbol{x}_1 - \boldsymbol{x}_2\|$ for all $\boldsymbol{x}_1, \boldsymbol{x}_2 \in X$.

From these preliminary considerations, the corresponding approximation spaces are obtained on the basis of the parametrisation. In the following, let $l \in \mathbb{N}$ be the dimension of the problem at hand, i.e. we assume that an unknown function of the form $\boldsymbol{v}\colon \tilde{\Omega} \to \mathbb{R}^l$, $\tilde{\Omega} \in \{\hat{\Omega}, \Omega\}$, is to be approximated within the IGA framework. Therefore we introduce on the parameter space the discrete NURBS space

$$\hat{V}_{\mathrm{h},l} := \left\{ \sum_{a=1}^{\mathfrak{n}} \boldsymbol{v}_a \hat{R}_a \,|\, \boldsymbol{v}_a \in \mathbb{R}^l \right\} = \operatorname{span} \left\{ \hat{\boldsymbol{R}}_{r,l} \right\}_{r=1}^{l\mathfrak{n}}, \tag{2.27}$$

where the basis functions $\hat{\boldsymbol{R}}_{r,l}\colon \hat{\Omega} \to \mathbb{R}^l$ are defined by $\hat{\boldsymbol{R}}_{r,l}(\boldsymbol{\xi}) = \boldsymbol{e}_i \hat{R}_a(\boldsymbol{\xi})$, $\boldsymbol{e}_i := (\delta_{i,j})_{1\le j\le l}$, $r = l(a-1)+i$, $i = 1,\dots,l$, $a = 1,\dots,\mathfrak{n}$[§]. Furthermore, we introduce analogously on the physical space the corresponding NURBS space

$$V_{\mathrm{h},l} := \left\{ \sum_{a=1}^{\mathfrak{n}} \boldsymbol{v}_a R_a \,|\, \boldsymbol{v}_a \in \mathbb{R}^l \right\} = \operatorname{span} \left\{ \boldsymbol{R}_{r,l} \right\}_{r=1}^{l\mathfrak{n}}, \tag{2.28}$$

where $R_a := \hat{R}_a \circ \boldsymbol{\mathcal{G}}^{-1}$ and the basis functions $\boldsymbol{R}_{r,l}\colon \Omega \to \mathbb{R}^l$ are defined analogue to $\hat{\boldsymbol{R}}_{r,l}$. Eventually, we point out that Assumption 2.2.1 ensures $\hat{h}_{\hat{e}} \simeq h_e$ for all $\hat{e} \in \hat{\mathscr{M}}$ and $e = \boldsymbol{\mathcal{G}}(\hat{e})$, such that no distinction is required any more, [14]. In the following, therefore, only the notation h_e is used for the element size and we introduce the mesh size $h = \max_{e\in\mathscr{M}} h_e$. Furthermore, Assumption 2.2.1 ensures, that the functions $\boldsymbol{R}_{r,l}$ are linearly independent and have the same continuity as $\hat{\boldsymbol{R}}_{r,l}$, cf. [14, 155].

2.2.2 Isogeometric spaces in a multi-patch domain

Let $\Omega \subset \mathbb{R}^d$ be a multi-patch domain consisting of the patches $\Omega^{(1)},\dots,\Omega^{(N)}$, which are parametrised by $\boldsymbol{\mathcal{G}}^{(i)}\colon (0,1)^{d_p} \to \Omega^{(i)}$, $\boldsymbol{\mathcal{G}}^{(i)} = \sum_{a=1}^{\mathfrak{n}} \boldsymbol{P}_a^{(i)} \hat{R}_a^{(i)}$. For each sub-domain $\Omega^{(i)}$, we introduce according to Section 2.2.1 the NURBS spaces on the parametric and physical domain

$$\hat{V}_{\mathrm{h},l}^{(i)} = \operatorname{span} \left\{ \hat{\boldsymbol{R}}_{r,l}^{(i)} \right\}_{r=1}^{l\mathfrak{n}^{(i)}}, \qquad V_{\mathrm{h},l}^{(i)} = \operatorname{span} \left\{ \boldsymbol{R}_{r,l}^{(i)} \right\}_{r=1}^{l\mathfrak{n}^{(i)}}, \tag{2.29}$$

and define the global approximation spaces as the products

$$\hat{V}_{\mathrm{h},l} = \prod_{i=1}^{N} \hat{V}_{\mathrm{h},l}^{(i)}, \qquad V_{\mathrm{h},l} = \prod_{i=1}^{N} V_{\mathrm{h},l}^{(i)}, \tag{2.30}$$

where we specify the mesh size h as the maximum of the mesh sizes $h^{(i)}$ corresponding to $\Omega^{(i)}$, i.e. $h := \max_{i=1,\dots N} h^{(i)}$. In this context, each component $\boldsymbol{v}_{\mathrm{h}}^{(i)}$ of a function

[§]The Kronecker delta function is defined here as usual as

$$\delta_{i,j} = \begin{cases} 1, & \text{if } i = j, \\ 0, & \text{otherwise.} \end{cases}$$

$\boldsymbol{v}_\mathrm{h} = (\boldsymbol{v}_\mathrm{h}^{(i)})_{1\leq i\leq N}$ from the space $\hat{V}_\mathrm{h,l}$ or $V_\mathrm{h,l}$ can be interpreted as an approximation of an unknown field restricted to the ith patch. To be more precise, by means of $\boldsymbol{v}_\mathrm{h} \in V_\mathrm{h,l}$, a function $\boldsymbol{v}$ on $\Omega\backslash\Gamma$ is initially obtained by $\boldsymbol{v}(\boldsymbol{x}) := \boldsymbol{v}_\mathrm{h}^{(i)}(\boldsymbol{x})$, if $\boldsymbol{x} \in \Omega^{(i)}$, where for an extension of the definition range to the entire domain Ω, $\boldsymbol{v}$ is still to be defined on the skeleton. For each point $\boldsymbol{x} \in \Gamma_{i,j} \neq \emptyset$, both components $\boldsymbol{v}_\mathrm{h}^{(i)}$ and $\boldsymbol{v}_\mathrm{h}^{(j)}$ provide a possible value, so that one of the two sides can be selected for the extension, i.e. either $\boldsymbol{v}(\boldsymbol{x}) := \boldsymbol{v}_\mathrm{h}^{(i)}(\boldsymbol{x})$ or $\boldsymbol{v}(\boldsymbol{x}) := \boldsymbol{v}_\mathrm{h}^{(j)}(\boldsymbol{x})$, if $\boldsymbol{x} \in \Gamma_{i,j}$. Note, however, that according to the construction of $V_\mathrm{h,l}$, it is not ensured that the values of the components at the interfaces match, so a function constructed in this way is generally discontinuous at the skeleton, cf. Remark 2.2.1. The formulation and implementation of suitable coupling conditions to achieve the desired continuity are addressed in Chapter 3. Note also that a similar interpretation applies to functions from the approximation space $\hat{V}_\mathrm{h,l}$, which is used when the underlying problem is transformed into the parameter space by an appropriate coordinate transformation. The concepts needed to see the relationships between the components $\boldsymbol{v}_\mathrm{h}^{(i)}$ and the connection with the overall solution of the problem are provided in Chapter 4. Especially in the Kirchhoff–Love shell theory introduced in Section 4.6, the unknown quantities are defined on the parameter space. Eventually, for the sake of clarity, the subscript l is omitted below where it is not relevant or clear from the context.

Remark 2.2.1. *In multi-patch theory, instead of a product space as introduced in Eq.* $(2.30)_2$*, the space*

$$V'_{\mathrm{h},l} = \left\{ \boldsymbol{f} \colon \Omega \to \mathbb{R}^l \mid \boldsymbol{f}_{|\Omega^{(i)}} \in V_{\mathrm{h},l}^{(i)},\, i = 1, \ldots, N \right\}, \tag{2.31}$$

is often used as global approximation space on the physical domain. Here it should be noted that the spaces $V_{\mathrm{h},l}$ and $V'_{\mathrm{h},l}$ are isomorph, so that the two approaches are essentially identical, cf. Kleiss et al. [111].

2.2.3 Bases of product spaces

Since the isogeometric multi-patch framework is based on product spaces, we will finally discuss the construction of suitable bases. The construction itself is not difficult, but the representation quickly becomes confusing in the general case. Therefore, the concept is first explained with an introductory example and then the general construction is outlined.

Let $V^{(1)}, V^{(2)}, V^{(3)}$ be function spaces and $\{\boldsymbol{h}_1^{(1)}\}$, $\{\boldsymbol{h}_j^{(2)}\}_{j=1}^2$, $\{\boldsymbol{h}_j^{(3)}\}_{j=1}^3$ be associated bases, where $\boldsymbol{h}_j^{(i)} \colon X^{(i)} \to \mathbb{R}^m$, $X^{(i)} \subset \mathbb{R}^n$. The aim is to construct a basis of the product space $V = \prod_{i=1}^3 V^{(i)}$ from the bases of the respective components. To this end, the possibility that the three domains $X^{(i)}$ may be different is first taken into account by introducing the common domain $X = X^{(1)} \cup X^{(2)} \cup X^{(3)}$ and the trivial extensions $\bar{\boldsymbol{h}}_j^{(i)} \colon X \to \mathbb{R}^n$ of the

basis functions $\boldsymbol{h}_j^{(i)}$ onto X[¶]. With the extensions, a basis $\{\boldsymbol{f}_r\colon X \to \mathbb{R}^m \times \mathbb{R}^m \times \mathbb{R}^m\}_{r=1}^6$ for V is given by

$$\{\boldsymbol{f}_1, \boldsymbol{f}_2, \dots, \boldsymbol{f}_6\} = \left\{ \begin{pmatrix} \bar{\boldsymbol{h}}_1^{(1)} \\ \boldsymbol{0} \\ \boldsymbol{0} \end{pmatrix}, \begin{pmatrix} \boldsymbol{0} \\ \bar{\boldsymbol{h}}_1^{(2)} \\ \boldsymbol{0} \end{pmatrix}, \begin{pmatrix} \boldsymbol{0} \\ \bar{\boldsymbol{h}}_2^{(2)} \\ \boldsymbol{0} \end{pmatrix}, \begin{pmatrix} \boldsymbol{0} \\ \boldsymbol{0} \\ \bar{\boldsymbol{h}}_1^{(3)} \end{pmatrix}, \begin{pmatrix} \boldsymbol{0} \\ \boldsymbol{0} \\ \bar{\boldsymbol{h}}_2^{(3)} \end{pmatrix}, \begin{pmatrix} \boldsymbol{0} \\ \boldsymbol{0} \\ \bar{\boldsymbol{h}}_3^{(3)} \end{pmatrix} \right\}, \quad (2.32)$$

where $\boldsymbol{0} \in \mathbb{R}^m$ is to be interpreted as the zero function on the respective domain. According to the construction, each basis function $\boldsymbol{h}_j^{(i)}$ receives a counterpart $\boldsymbol{f}_r$ in the product basis, where its extension is appropriately placed in the 3-tuple. Furthermore, for the numbering of the base, we use a natural scheme in which the functions are assigned to each other $\boldsymbol{h}_j^{(i)} \leftrightarrow \boldsymbol{f}_r$ by numbering the functions consecutively from base $\{\boldsymbol{h}_1^{(1)}\}$ to base $\{\boldsymbol{h}_j^{(3)}\}_{j=1}^3$ as follows

$$\begin{array}{cccccc} \boldsymbol{h}_1^{(1)}, & \boldsymbol{h}_1^{(2)}, & \boldsymbol{h}_2^{(2)}, & \boldsymbol{h}_1^{(3)}, & \boldsymbol{h}_2^{(3)}, & \boldsymbol{h}_3^{(3)} \\ \updownarrow & \updownarrow & \updownarrow & \updownarrow & \updownarrow & \updownarrow \\ \boldsymbol{f}_1, & \boldsymbol{f}_2, & \boldsymbol{f}_3, & \boldsymbol{f}_4, & \boldsymbol{f}_5, & \boldsymbol{f}_6 \end{array}$$

	$j=1$	$j=2$	$j=3$
$i=1$	$r=1$	–	–
$i=2$	$r=2$	$r=3$	–
$i=3$	$r=4$	$r=5$	$r=6$

After these considerations, we now come to the general case. Let $V^{(1)}, \dots, V^{(N)}$ be function spaces and $\{\boldsymbol{h}_j^{(1)}\}_{j=1}^{\mathfrak{n}^{(1)}}, \dots, \{\boldsymbol{h}_j^{(N)}\}_{j=1}^{\mathfrak{n}^{(N)}}$ be associated bases, where $\boldsymbol{h}_j^{(i)}\colon X^{(i)} \to \mathbb{R}^m$, $X^{(i)} \subset \mathbb{R}^n$ and $\bar{\boldsymbol{h}}_j^{(i)}\colon X \to \mathbb{R}^m$ denotes the trivial extension onto $X = \bigcup_{i=1}^N X^{(i)}$. As before, the aim is to construct a suitable basis of the space $V = \prod_{i=1}^N V^{(i)}$. The numbering scheme used in the example reads for the actual case

$$r = r(i,j) = \sum_{s=1}^{i-1} \mathfrak{n}^{(s)} + j, \quad j = 1, \dots, \mathfrak{n}^{(i)}, \quad i = 1, \dots, N, \quad (2.33)$$

and the components $\boldsymbol{f}_r^{(k)}\colon X \to \mathbb{R}^m$ of the basis function $\boldsymbol{f}_r = (\boldsymbol{f}_r^{(1)}, \dots, \boldsymbol{f}_r^{(N)})\colon X \to \prod_{i=1}^N \mathbb{R}^m$, $r = 1, \dots, \mathfrak{n} := \sum_{i=1}^N \mathfrak{n}^{(i)}$ associated with $\boldsymbol{h}_j^{(i)}$ are given by

$$\boldsymbol{f}_r^{(k)} = \boldsymbol{f}_{r(i,j)}^{(k)} = \begin{cases} \boldsymbol{0}, & \text{if } k \neq i, \\ \bar{\boldsymbol{h}}_j^{(i)}, & \text{otherwise.} \end{cases} \quad (2.34)$$

Remark 2.2.2. *We note that according to the definition in Section 2.1.4, the patches are open and the skeleton is formally not included in the domains of the respective bases. In order to take this into account in the construction of isogeometric product spaces, the closure of the corresponding domains should be used in each case. I.e. for a base of $\hat{V}_{\mathrm{h},l}$ use, according to the notation above, $X^{(i)} = [0,1]^{d_p}$ instead of $(0,1)^{d_p}$ and for a basis of $V_{\mathrm{h},l}$ accordingly $X^{(i)} = \bar{\Omega}^{(i)}$ instead of $\Omega^{(i)}$.*

[¶]The trivial extension of a function $\boldsymbol{h}\colon X \to \mathbb{R}^m$ to a larger domain $X' \supset X$ is given by

$$\bar{\boldsymbol{h}}\colon X' \to \mathbb{R}^m, \quad \bar{\boldsymbol{h}}(\boldsymbol{x}) = \begin{cases} \boldsymbol{h}(\boldsymbol{x}), & \text{if } \boldsymbol{x} \in X, \\ \boldsymbol{0}, & \text{otherwise.} \end{cases}$$

3 Extended mortar method

The mortar method, firstly proposed in [23] for C^0-continuous couplings between non-overlapping domains, can be interpreted as a minimization of a specific coupling functional. In this chapter, we present the results of several studies done on the extension of this functional to higher continuous coupling problems in the IGA framework, [64, 65, 143]. In Section 3.1, we formulate an abstract variational problem and derive weak higher order coupling conditions in a continuous setting. Subsequently, we discuss the isogeometric mortar discretization by means of this framework in Section 3.2 and conclude with several numerical studies in Section 3.3.

3.1 Abstract framework

3.1.1 Uncoupled problem

We consider an abstract variational setting on an open bounded multi-patch domain $\Omega \subset \mathbb{R}^d$ consisting of N subdomains $\Omega^{(1)}, \dots, \Omega^{(N)}$. For this purpose, we assume that on each patch $\Omega^{(i)}$ a variational problem is formulated as follows: find $\boldsymbol{v}^{(i)} \in \mathcal{S}^{(i)}$ such that

$$\mathrm{V}^{(i)}(\boldsymbol{v}^{(i)}, \delta\boldsymbol{v}^{(i)}) = 0 \quad \forall \delta\boldsymbol{v}^{(i)} \in \mathcal{V}^{(i)}, \tag{3.1}$$

where the functional $\mathrm{V}^{(i)}$ represents the corresponding problem and is assumed to be linear at least in its second argument. $\mathcal{S}^{(i)}$ and $\mathcal{V}^{(i)}$ designate suitable spaces of admissible solutions and test functions, respectively, which comply with possible essential boundary conditions stated on a subset $\Gamma_\mathrm{e} \subset \partial\Omega$. Thereby, we refer to a boundary condition as essential if it is not covered by the variational formulation and must be explicitly demanded by the elements of the space of admissible solutions. Accordingly, the spaces $\mathcal{S}^{(i)}$ and $\mathcal{V}^{(i)}$ respect an essential condition if all elements from $\mathcal{S}^{(i)}$ satisfy the constraint and the elements from $\mathcal{V}^{(i)}$ vanish on the corresponding boundary part. On the other hand, we speak of natural boundary conditions when they are included in the variational formulation in the sense that any solution of the problem satisfies the boundary condition without further restrictions on the solution space. To obtain a global functional framework on Ω, we introduce the product spaces

$$\mathcal{S} = \prod_{i=1}^{N} \mathcal{S}^{(i)}, \quad \mathcal{V} = \prod_{i=1}^{N} \mathcal{V}^{(i)} \tag{3.2}$$

and specify the global uncoupled problem as follows: find $\boldsymbol{v} = (\boldsymbol{v}^{(1)}, \dots, \boldsymbol{v}^{(N)}) \in \mathcal{S}$ such that

$$\mathrm{V}(\boldsymbol{v}, \delta\boldsymbol{v}) := \sum_{i=1}^{N} \mathrm{V}^{(i)}(\boldsymbol{v}^{(i)}, \delta\boldsymbol{v}^{(i)}) = 0, \tag{3.3}$$

for all $\delta\boldsymbol{v} = (\delta\boldsymbol{v}^{(1)}, \dots, \delta\boldsymbol{v}^{(N)}) \in \mathcal{V}$. Note that a solution of (3.3) is to be understood as outlined in Section 2.2.2 for the discrete case. Since there are no further conditions on the transitions at the interfaces within the current framework, a function characterised by (3.3) is generally discontinuous at the skeleton. In the following, we extend the variational formulation by suitable conditions in order to control the continuity of the solution.

3.1.2 Coupling conditions

Let us assume that the non-empty interfaces are enumerated by Γ_k, $k = 1, \dots, K$, so that the skeleton is given by $\Gamma = \bigcup_{k=1}^{K} \Gamma_k$. For each interface Γ_k we choose one of the adjacent subdomains as the master side and one as the slave side, where we denote the index of the former one by $m(k)$ and the index of the latter one by $s(k)$, i.e. $\overline{\Gamma}_k = \partial\Omega^{(m(k))} \cap \partial\Omega^{(s(k))}$. Since the coupling conditions must be satisfied equally at each interface, for the sake of clarity, we will first consider a two-patch situation and formulate the conditions for a general multi-patch situation at the end of this section.

Two-patch coupling

The idea to obtain a weak coupling of the patches is based on the minimization of a functional $\mathrm{M}\colon \mathcal{S}^{(1)} \times \mathcal{S}^{(2)} \to \mathbb{R}$, which describes the desired coupling conditions. To be more precise, we restrict the solution space for the uncoupled problem (3.3) to those functions $\boldsymbol{v} = (\boldsymbol{v}_1, \boldsymbol{v}_2) \in \mathcal{S}^{(1)} \times \mathcal{S}^{(2)}$ that additionally fulfil $\mathrm{M}(\boldsymbol{v}^{(1)}, \boldsymbol{v}^{(2)}) = \inf_{\boldsymbol{w} \in \mathcal{S}^{(1)}} \mathrm{M}(\boldsymbol{w}, \boldsymbol{v}^{(2)})$, where we assume here that $s(1) = 1$, $m(1) = 2$. I.e. for a given function $\boldsymbol{v}^{(2)}$ on the master side, only those functions on the slave side are accepted that optimally satisfy the conditions given by M. For a weak C^n coupling, we specify

$$\mathrm{M}(\boldsymbol{v}^{(1)}, \boldsymbol{v}^{(2)}) = \sum_{|\boldsymbol{\alpha}| \le n} \mathfrak{h}^{|\boldsymbol{\alpha}|} \| \partial^{\boldsymbol{\alpha}} (\boldsymbol{v}^{(1)} - \boldsymbol{v}^{(2)}) \|^2_{L^2(\Gamma)}, \tag{3.4}$$

where $\mathfrak{h} \in \mathbb{R}_{>0}$ is a weighting parameter which will be related in the discrete framework to the mesh size h, cf. Section 3.3. Similarly, we specify

$$\mathrm{M}(\boldsymbol{v}^{(1)}, \boldsymbol{v}^{(2)}) = \| \boldsymbol{v}^{(1)} - \boldsymbol{v}^{(2)} \circ \mathrm{P}_2^1 \|^2_{L^2(\hat{\Gamma}_2^1)} + \mathfrak{h} \sum_{i=1}^{2} \| \partial_i \boldsymbol{v}^{(1)} - \sum_{j=1}^{2} (\gamma_j^i \partial_j \boldsymbol{v}^{(2)}) \circ \mathrm{P}_2^1 \|^2_{L^2(\hat{\Gamma}_2^1)}, \tag{3.5}$$

for a weak G^1 coupling, with the conditions for the partial derivatives weakened according to Section 2.1.5. The parametric assignment P_2^1 introduced in Eq. (2.22) is used here to define the coupling integrals on the parameter space of the slave side. We point out that this definition is not mandatory. Analogously, the integrals could be defined on

the parameter space of the master side using P_1^2. Introduction of a suitable space $\mathcal{M}$ of Lagrange multipliers at the interface, standard variational calculus provides the coupling condition

$$\mathrm{B}(\boldsymbol{v}, \delta\boldsymbol{\lambda}) = \sum_{|\boldsymbol{\alpha}|\leq n} \mathfrak{h}^{|\boldsymbol{\alpha}|} \langle \partial^{\boldsymbol{\alpha}}(\boldsymbol{v}^{(1)} - \boldsymbol{v}^{(2)}), \partial^{\boldsymbol{\alpha}} \delta\boldsymbol{\lambda} \rangle_{\Gamma} = 0 \quad \forall \delta\boldsymbol{\lambda} \in \mathcal{M} \tag{3.6}$$

for a weak C^n-continuous patch coupling and the condition

$$\begin{aligned} \mathrm{B}(\boldsymbol{v}, \delta\boldsymbol{\lambda}) = {} & \langle \boldsymbol{v}^{(1)} - \boldsymbol{v}^{(2)} \circ \mathrm{P}_2^1, \delta\boldsymbol{\lambda} \rangle_{\hat{\Gamma}_2^1} \\ & + \mathfrak{h} \sum_{i=1}^{2} \langle \partial_i \boldsymbol{v}^{(1)} - \sum_{j=1}^{2} (\gamma_j^i \partial_j \boldsymbol{v}^{(2)}) \circ \mathrm{P}_2^1, \partial_i \delta\boldsymbol{\lambda} \rangle_{\hat{\Gamma}_2^1} = 0 \quad \forall \delta\boldsymbol{\lambda} \in \mathcal{M}, \end{aligned} \tag{3.7}$$

in the case of a weak G^1-continuous patch coupling. These considerations now allow us to formulate two equivalent coupled problems corresponding to (3.3). The first problem is formulated in the form of a saddle-point system, and reads as follows: find $(\boldsymbol{v}, \boldsymbol{\lambda}) \in \mathcal{S} \times \mathcal{M}$ such that

$$\begin{aligned} \mathrm{V}(\boldsymbol{v}, \delta\boldsymbol{v}) + \mathrm{B}(\delta\boldsymbol{v}, \boldsymbol{\lambda}) = 0, \quad \forall \delta\boldsymbol{v} \in \mathcal{V}, \\ \mathrm{B}(\boldsymbol{v}, \delta\boldsymbol{\lambda}) = 0, \quad \forall \delta\boldsymbol{\lambda} \in \mathcal{M}, \end{aligned} \tag{3.8}$$

where in the second formulation the constrained spaces

$$\begin{aligned} \mathcal{S}^c &:= \{ \boldsymbol{v} \in \mathcal{S} \mid \mathrm{B}(\boldsymbol{v}, \delta\boldsymbol{\lambda}) = 0, \ \forall \delta\boldsymbol{\lambda} \in \mathcal{M} \}, \\ \mathcal{V}^c &:= \{ \delta\boldsymbol{v} \in \mathcal{V} \mid \mathrm{B}(\delta\boldsymbol{v}, \delta\boldsymbol{\lambda}) = 0, \ \forall \delta\boldsymbol{\lambda} \in \mathcal{M} \} \end{aligned} \tag{3.9}$$

are used, such that the problem simply reads: find $\boldsymbol{v} \in \mathcal{S}^c$ such that

$$\mathrm{V}(\boldsymbol{v}, \delta\boldsymbol{v}) = 0, \quad \forall \delta\boldsymbol{v} \in \mathcal{V}^c. \tag{3.10}$$

The construction of constrained spaces in a discrete setting is covered in Section 3.2.4.

Multi-patch coupling

In order to consider the general case of multiple interfaces, the bilinear form B and the multiplier space $\mathcal{M}$ in the problems (3.8)-(3.10) have to be extended to the whole skeleton as follows. For each interface Γ_k we specify a suitable multiplier space $\mathcal{M}^k$ and a corresponding functional $\mathrm{B}^{(k)}$, which takes the form

$$\mathrm{B}^{(k)}(\boldsymbol{v}, \delta\boldsymbol{\lambda}^{(k)}) = \sum_{|\boldsymbol{\alpha}|\leq n} \mathfrak{h}^{|\boldsymbol{\alpha}|} \langle \partial^{\boldsymbol{\alpha}}(\boldsymbol{v}^{(s(k))} - \boldsymbol{v}^{(m(k))}), \partial^{\boldsymbol{\alpha}} \delta\boldsymbol{\lambda}^{(k)} \rangle_{\Gamma_k} \tag{3.11}$$

in the case of weak C^n conditions and the form

$$\begin{aligned} \mathrm{B}^{(k)}(\boldsymbol{v}, \delta\boldsymbol{\lambda}^{(k)}) = {} & \langle \boldsymbol{v}^{(s(k))} - \boldsymbol{v}^{(m(k))} \circ \mathrm{P}_{m(k)}^{s(k)}, \delta\boldsymbol{\lambda}^{(k)} \rangle_{\hat{\Gamma}_{m(k)}^{s(k)}} \\ & + \mathfrak{h} \sum_{i=1}^{2} \langle \partial_i \boldsymbol{v}^{(s(k))} - \sum_{j=1}^{2} (\gamma_j^{i,k} \partial_j \boldsymbol{v}^{(m(k))}) \circ \mathrm{P}_{m(k)}^{s(k)}, \partial_i \delta\boldsymbol{\lambda}^{(k)} \rangle_{\hat{\Gamma}_{m(k)}^{s(k)}} \end{aligned} \tag{3.12}$$

in the case of weak G^1 conditions. Based on the individual contributions of the interfaces, we eventually define the global multiplier space on Γ as the product $\mathcal{M} := \prod_{k=1}^{K} \mathcal{M}^k$ and the associated global coupling functional by

$$\mathrm{B}(\boldsymbol{v}, \delta\boldsymbol{\lambda}) = \sum_{k=1}^{K} \mathrm{B}^{(k)}(\boldsymbol{v}, \delta\boldsymbol{\lambda}^{(k)}). \tag{3.13}$$

3.1.3 Generalised couplings

In multi-patch systems, the coupling conditions arise naturally at the interfaces, i.e. in the areas where the patches occupy a common space. By the coincidence of the patches, one obtains through the identity $\phi(\boldsymbol{x}) = \boldsymbol{x}$ a simple assignment of the points in which the components of the field $\boldsymbol{v}$ should satisfy the coupling conditions. However, in some cases, it is necessary to couple arbitrary boundary parts, i.e. spatially separated areas. Well-known applications are for instant periodic boundary conditions. To realise such general couplings within the framework of the extended mortar method, only slight modifications are required. Thereby, the basic idea is to adjust the assignment ϕ appropriately. The procedure is described in the following by means of a weak C^n coupling, where again a single coupling is considered and the results are used to describe the general case.

As before, let the computational domain Ω consists of* $N \geq 1$ subdomains $\Omega^{(i)}$, $i = 1, \ldots, N$. Moreover, let $\gamma \subset \partial\Omega^{(i)}$, $\gamma^\phi \subset \partial\Omega^{(j)}$ be two open boundary parts whose elements are connected through a diffeomorphism $\phi\colon \gamma \to \gamma^\phi$. The aim is to couple the components $\boldsymbol{v}^{(i)}$, $\boldsymbol{v}^{(j)}$ and their derivatives of the unknown field $\boldsymbol{v} = (\boldsymbol{v}^{(1)}, \ldots, \boldsymbol{v}^{(N)}) \in \mathcal{S}$ such that they coincide on γ and γ^ϕ according to ϕ. By analogy with Section 3.1.2, the derivation of appropriate conditions is based on the minimisation of the functional

$$\mathrm{M}(\boldsymbol{v}) = \sum_{|\boldsymbol{\alpha}| \leq n} \mathfrak{h}^{|\boldsymbol{\alpha}|} \| \partial^{\boldsymbol{\alpha}} \boldsymbol{v}^{(i)} - (\partial^{\boldsymbol{\alpha}} \boldsymbol{v}^{(j)}) \circ \phi \|^2_{L^2(\gamma)}, \tag{3.14}$$

which leads to the generalised coupling condition

$$\mathrm{B}(\boldsymbol{v}, \delta\boldsymbol{\lambda}) = \sum_{|\boldsymbol{\alpha}| \leq n} \mathfrak{h}^{|\boldsymbol{\alpha}|} \langle \partial^{\boldsymbol{\alpha}} \boldsymbol{v}^{(i)} - (\partial^{\boldsymbol{\alpha}} \boldsymbol{v}^{(j)}) \circ \phi, \partial^{\boldsymbol{\alpha}} \delta\boldsymbol{\lambda} \rangle_\gamma = 0 \quad \forall \delta\boldsymbol{\lambda} \in \mathcal{M}. \tag{3.15}$$

Note that the slave and master sides are already defined by the assignment ϕ, where its domain is slave and its codomain is master. The treatment of multiple generalised couplings is now straightforward. Starting from $K \geq 1$ virtual interfaces defined through $(\gamma_1, \phi_1), \ldots, (\gamma_K, \phi_K)$, we specify for each pair (γ_k, ϕ_k) a multiplier space $\mathcal{M}^k$ and a corresponding functional

$$\mathrm{B}^{(k)}(\boldsymbol{v}, \delta\boldsymbol{\lambda}^{(k)}) = \sum_{|\boldsymbol{\alpha}| \leq n} \mathfrak{h}^{|\boldsymbol{\alpha}|} \langle \partial^{\boldsymbol{\alpha}} \boldsymbol{v}^{(s(k))} - (\partial^{\boldsymbol{\alpha}} \boldsymbol{v}^{(m(k))}) \circ \phi_k, \partial^{\boldsymbol{\alpha}} \delta\boldsymbol{\lambda}^{(k)} \rangle_{\gamma_k}. \tag{3.16}$$

*We point out that the case $N = 1$ is explicitly taken into account here since generalised couplings can also be usefully formulated in single-patch domains.

The global bilinear form B belonging to the product space $\mathcal{M} := \prod_{k=1}^{K} \mathcal{M}^k$ again results from the summation of the individual contributions $\mathrm{B}^{(k)}$, cf. Eq. (3.13). If there are both real and virtual interfaces in the system under consideration, B is composed of mixed summands of the forms (3.11) and (3.16). We point out that the generalized coupling conditions are a genuine generalisation in the sense that if $\bar{\gamma}_k = \partial\Omega^{(s(k))} \cap \partial\Omega^{(m(k))} \neq \emptyset$ and $\phi_k(\boldsymbol{x}) = \boldsymbol{x}$, $\boldsymbol{x} \in \bar{\gamma}_k$, (3.16) takes the form of (3.11). I.e. a real interface can be understood as a special case of a virtual interface. In order to establish a strict separation between these types of interfaces, we refer to a pair (γ_k, ϕ_k) as a virtual interface only if $\gamma_k \cap \phi_k(\gamma_k) = \emptyset$. In particular, with this definition, we avoid that a boundary part can be assigned to both a real and a virtual interface. Eventually, analogous to (2.21), we define the virtual skeleton as the union $\gamma' = \bigcup_{k=1}^{K} (\gamma_k \cup \phi_k(\gamma_k))$ and introduce the full skeleton $\Gamma_\gamma := \Gamma \cup \gamma'$.

Remark 3.1.1. *In the case of a single-patch system $\Omega = \Omega^{(1)}$, it holds $\gamma_k, \phi_k(\gamma_k) \subset \partial\Omega$ and the coupling functional* (3.16) *becomes*

$$\mathrm{B}^{(k)}(\boldsymbol{v}, \delta\boldsymbol{\lambda}) = \sum_{|\boldsymbol{\alpha}| \leq n} \mathfrak{h}^{|\boldsymbol{\alpha}|} \langle \partial^{\boldsymbol{\alpha}} \boldsymbol{v} - (\partial^{\boldsymbol{\alpha}} \boldsymbol{v}) \circ \phi_k, \partial^{\boldsymbol{\alpha}} \delta\boldsymbol{\lambda}^{(k)} \rangle_{\gamma_k}, \tag{3.17}$$

so that the case $N = 1$ is also covered. Finally, we point out that we have omitted graphics and examples here, as the topic is taken up again in detail in the application examples in Sections 5.3.2 and 6.3.1.

3.2 Isogeometric mortar discretization

In this section, we consider several aspects concerning the discretization of the coupling problem introduced in Section 3.1. Therefore, we first derive the corresponding discrete framework in Section 3.2.1. Within this framework, the space of the Lagrange multiplier is specified as the space of traces from the slave side, where it is known that this natural choice gives rise to problems in the presence of crosspoints and wirebaskets. In Section 3.2.2 we discuss this issue and present a modification of the involved IGA base to avoid these problems. Another particular challenge in the realisation of a mortar method is the evaluation of the interface integrals, which is addressed in Section 3.2.3. Finally, we discuss the construction of constrained IGA approximation spaces which a-priori satisfy the weak coupling conditions.

3.2.1 Discrete abstract framework

According to the definition of multi-patch domains in Section 2.1.4 and Assumption 2.1.1, each patch $\Omega^{(i)}$ in the abstract problem in Section 3.1.1 is described by a NURBS parametrisation $\boldsymbol{\mathcal{G}}^{(i)} \colon \hat{\Omega} \to \mathbb{R}^d$, $\hat{\Omega} = (0,1)^{d_p}$, which leads, according to Section 2.2.2, to approximation spaces $\hat{V}_{\mathrm{h},l}^{(i)}$ and $V_{\mathrm{h},l}^{(i)}$ on the parameter space and the physical domain, cf.

Eq. (2.29). For the further description, let $W_\mathrm{h}^{(i)} \in \{\hat{V}_{\mathrm{h},l}^{(i)}, V_{\mathrm{h},l}^{(i)}\}$ be the space to be used for approximation and $\{\boldsymbol{B}_r^{(i)}\}_{r=1}^{l\mathfrak{n}^{(i)}}$ be the associated basis, i.e.

$$\{\boldsymbol{B}_r^{(i)}\}_{r=1}^{l\mathfrak{n}^{(i)}} = \begin{cases} \{\hat{\boldsymbol{R}}_{r,l}^{(i)}\}_{r=1}^{l\mathfrak{n}^{(i)}}, & \text{if } W_\mathrm{h}^{(i)} = \hat{V}_{\mathrm{h},l}^{(i)}, \\ \{\boldsymbol{R}_{r,l}^{(i)}\}_{r=1}^{l\mathfrak{n}^{(i)}}, & \text{if } W_\mathrm{h}^{(i)} = V_{\mathrm{h},l}^{(i)}. \end{cases} \tag{3.18}$$

Note that we do not consider mixed approaches so in the following it is assumed that either $W_\mathrm{h}^{(i)} = \hat{V}_{\mathrm{h},l}^{(i)}$ or $W_\mathrm{h}^{(i)} = V_{\mathrm{h},l}^{(i)}$ is used for all $i = 1, \dots, N$. For the sake of clarity, we will further assume that it is possible to impose any essential boundary condition on $\Gamma_\mathrm{e}^{(i)} := \Gamma_\mathrm{e} \cap \partial\Omega^{(i)}$ into the discrete space by using appropriate subsets $\mathbb{B}_\mathrm{h}{}^{(i)} := \{\boldsymbol{N}_j^{(i)}\}_{j=1}^{\mathfrak{m}^{(i)}}$, $\tilde{\mathbb{B}}_\mathrm{h}{}^{(i)} := \{\tilde{\boldsymbol{N}}_j^{(i)}\}_{j=1}^{\mathfrak{m}^{(i)}}$, of $\{\boldsymbol{B}_r^{(i)}\}_{r=1}^{l\mathfrak{n}^{(i)}}$ so that the spaces $\mathcal{S}_\mathrm{h}^{(i)} := \operatorname{span} \mathbb{B}_\mathrm{h}^{(i)}$ and $\mathcal{V}_\mathrm{h}^{(i)} := \operatorname{span} \tilde{\mathbb{B}}_\mathrm{h}^{(i)}$ respect the condition in the sense outlined in Section 3.1.1. We point out that this is not possible in every case and depends on the respective boundary data. If, for example, an essential condition is described by a function $\boldsymbol{g}^{(i)} \colon \Gamma_\mathrm{e}^{(i)} \to \mathbb{R}^l$, an incorporation into the discrete space is possible if $\boldsymbol{g}^{(i)}$ is contained in $W_\mathrm{h}^{(i)}$. If this is not the case, one possibility is to approximate $\boldsymbol{g}^{(i)}$ by a function $\boldsymbol{g}_\mathrm{h}^{(i)} \in W_\mathrm{h}^{(i)}$ and to use $\boldsymbol{g}_\mathrm{h}^{(i)}$ instead of $\boldsymbol{g}^{(i)}$ to model the condition on $\Gamma_\mathrm{e}^{(i)}$, cf. Cottrell et al. [44]. Another way of implementing essential conditions is to use spaces that do not respect the essential condition and extend the variational framework in such a way that every solution of the problem also satisfies the boundary conditions. Common methods for this are, for example, the penalty method or the use of Lagrangian multipliers, where the latter leads to a saddle point system of the form (3.8). Further details on the implementation of boundary conditions can be found in the textbook by Zienkiewicz et al. [175]. All of these techniques can easily be used in combination with the extended mortar method. However, including the different approaches in the abstract framework would unnecessarily complicate the presentation and distract from the essentials. Eventually, analogous to the continuous case, we define the global space of admissible solutions and the global space of test functions as the products $\mathcal{S}_\mathrm{h} = \prod_{i=1}^N \mathcal{S}_\mathrm{h}^{(i)}$ and $\mathcal{V}_\mathrm{h} = \prod_{i=1}^N \mathcal{V}_\mathrm{h}^{(i)}$ and denote the associated bases by $\{\boldsymbol{N}_r\}_{r=1}^{\mathfrak{m}}$ and $\{\tilde{\boldsymbol{N}}_r\}_{r=1}^{\mathfrak{m}}$, respectively.

Bearing in mind the construction of product bases, see Section 2.2.3, each $\boldsymbol{v}_\mathrm{h} = (\boldsymbol{v}_\mathrm{h}^{(i)})_{1 \le i \le N}$ from the discrete space $\mathcal{S}_\mathrm{h}$ of admissible solutions has a unique representation of the form

$$\boldsymbol{v}_\mathrm{h} = \sum_{r=1}^{\mathfrak{m}} \bar{v}_r \boldsymbol{N}_r = \left(\sum_{j=1}^{\mathfrak{m}^{(1)}} \bar{v}_j^{(1)} \boldsymbol{N}_j^{(1)}, \dots, \sum_{j=1}^{\mathfrak{m}^{(N)}} \bar{v}_j^{(N)} \boldsymbol{N}_j^{(N)} \right) = \left(\boldsymbol{v}_\mathrm{h}^{(1)}, \dots, \boldsymbol{v}_\mathrm{h}^{(N)} \right), \tag{3.19}$$

where the global degrees of freedom (dof) $\bar{\boldsymbol{v}} := (\bar{v}_r)_{1 \le r \le \mathfrak{m}} \in \mathbb{R}^{\mathfrak{m}}$ and the local dof $\bar{\boldsymbol{v}}^{(i)} := (\bar{v}_j^{(i)})_{1 \le j \le \mathfrak{m}} \in \mathbb{R}^{\mathfrak{m}^{(i)}}$, $i = 1, \dots, N$, are assigned to each other by the numbering scheme (2.33), such that $\bar{\boldsymbol{v}} = (\bar{\boldsymbol{v}}^{(1)}, \dots, \bar{\boldsymbol{v}}^{(N)})$. Through these considerations, we first obtain the discrete uncoupled problem by substituting the discrete quantities into Eq. (3.3): find

$\bar{\boldsymbol{v}} \in \mathbb{R}^{\mathfrak{m}}$ such that

$$\mathrm{V}(\sum_{i=1}^{\mathfrak{m}} \bar{v}_i \boldsymbol{N}_i, \tilde{\boldsymbol{N}}_r) = 0, \quad r = 1, \dots, \mathfrak{m} \iff \boldsymbol{\mathcal{R}}^u(\bar{\boldsymbol{v}}) = \begin{pmatrix} \boldsymbol{\mathcal{R}}_1^u(\bar{\boldsymbol{v}}^{(1)}) \\ \vdots \\ \boldsymbol{\mathcal{R}}_N^u(\bar{\boldsymbol{v}}^{(N)}) \end{pmatrix} = \boldsymbol{0}, \tag{3.20}$$

where we have taken into account the relation $\mathrm{V}(\boldsymbol{v}_\mathrm{h}, \delta\boldsymbol{v}_\mathrm{h}) = 0 \, \forall \delta\boldsymbol{v}_\mathrm{h} \in \mathcal{V}_\mathrm{h} \Leftrightarrow \mathrm{V}(\boldsymbol{v}_\mathrm{h}, \tilde{\boldsymbol{N}}_r) = 0 \, \forall r \in \{1, \dots, \mathfrak{m}\}$, which directly follows from the assumed linearity of V with respect to its second argument, and the blocks $\boldsymbol{\mathcal{R}}_k^u \colon \mathbb{R}^{\mathfrak{m}^{(k)}} \to \mathbb{R}^{\mathfrak{m}^{(k)}}$ of the uncoupled residual $\boldsymbol{\mathcal{R}}^u \colon \mathbb{R}^{\mathfrak{m}} \to \mathbb{R}^{\mathfrak{m}}$ are given by

$$\boldsymbol{\mathcal{R}}_k^u(\bar{\boldsymbol{v}}^{(k)}) = \left(\mathrm{V}^{(k)}(\sum_{i=1}^{\mathfrak{m}^{(k)}} \bar{v}_i^{(k)} \boldsymbol{N}_i^{(k)}, \tilde{\boldsymbol{N}}_j^{(k)}) \right)_{1 \le j \le \mathfrak{m}^{(k)}} . \tag{3.21}$$

In order to establish a patch coupling in the next step, we first need a suitable discrete space of Lagrangian multipliers. Different approaches for mortar couplings are presented, e.g., in [22, 31, 87, 116, 153, 169]. In this work, we use a $\boldsymbol{p}/\boldsymbol{p}$ pairing with boundary modification as discussed in detail in Brivadis et al. [31] for a weak C^0 coupling, where we extend the modification approach presented there for the general case of a weak C^n/G^1 coupling in Section 3.2.2. To be specific, we use the product space $\mathcal{M}_\mathrm{h} = \prod_{k=1}^K \mathcal{M}_\mathrm{h}^k$, where the components $\mathcal{M}_\mathrm{h}^k$ are linear spaces spanned by the basis functions of the slave side with influence on the interface Γ_k. In other words, for a C^n coupling we use the space

$$\mathcal{M}_\mathrm{h}^k = \mathrm{span} \left\{ \boldsymbol{N}_j^{(s(k))} \in \mathbb{B}_\mathrm{h}^{(s(k))} \mid \bigcup_{|\boldsymbol{\alpha}| \le n} \left(\mathrm{supp}(\partial^{\boldsymbol{\alpha}} \boldsymbol{N}_j^{(s(k))}) \right)^\circ \cap \Gamma_k \neq \emptyset \right\}, \tag{3.22}$$

for each interface, while in the case of a G^1 coupling, we work on the parameter space and the multipliers are given by

$$\mathcal{M}_\mathrm{h}^k = \mathrm{span} \left\{ \boldsymbol{N}_j^{(s(k))} \in \mathbb{B}_\mathrm{h}^{(s(k))} \mid \bigcup_{|\boldsymbol{\alpha}| \le 1} \left(\mathrm{supp}(\partial^{\boldsymbol{\alpha}} \boldsymbol{N}_j^{(s(k))}) \right)^\circ \cap \hat{\Gamma}_{m(k)}^{s(k)} \neq \emptyset \right\}. \tag{3.23}$$

Let $\mathcal{J}_k = \{j_1^k, \dots, j_{\mathfrak{l}^k}^k\} \subset \{1, \dots, \mathfrak{m}^{(s(k))}\}$, $k = 1, \dots, K$, be the index sets containing the indices of the basis functions spanning the discrete spaces $\mathcal{M}_\mathrm{h}^k$, i.e. $\mathcal{M}_\mathrm{h}^k = \mathrm{span}\{\boldsymbol{N}_{j_\nu^k}^{(s(k))}\}_{\nu=1}^{\mathfrak{l}^k}$, and let us introduce the corresponding product space $\mathcal{M}_\mathrm{h} = \prod_{k=1}^K \mathcal{M}_\mathrm{h}^k = \mathrm{span}\{\boldsymbol{M}_r\}_{r=1}^{\mathfrak{l}}$, where $\mathfrak{l} = \sum_{k=1}^K \mathfrak{l}^k$ and the base $\{\boldsymbol{M}_r\}_{r=1}^{\mathfrak{l}}$ results from $\{\boldsymbol{N}_{j_\nu^k}^{(s(k))}\}_{\nu=1}^{\mathfrak{l}^k}$, $k = 1, \dots, K$, according to Section 2.2.3. Then, the weak coupling condition for the discrete solution is obtained by substituting the discrete quantities into Eq. (3.13) which results in a linear system,

$$\mathrm{B}(\sum_{i=1}^{\mathfrak{m}} \bar{v}_i \boldsymbol{N}_i, \boldsymbol{M}_r) = 0, \quad r = 1, \dots, \mathfrak{l} \iff \underbrace{\begin{pmatrix} \boldsymbol{A}_{1,1} & \dots & \boldsymbol{A}_{1,N} \\ \vdots & \ddots & \vdots \\ \boldsymbol{A}_{K,1} & \dots & \boldsymbol{A}_{K,N} \end{pmatrix}}_{=:\boldsymbol{\mathcal{A}}} \begin{pmatrix} \bar{\boldsymbol{v}}^{(1)} \\ \vdots \\ \bar{\boldsymbol{v}}^{(N)} \end{pmatrix} = \boldsymbol{0}. \tag{3.24}$$

Table 3.1: Entries of the coupling matrices for C^n/G^1 coupling conditions.

Weak C^n-continuous conditions

$$\left[\boldsymbol{\mathcal{B}}_{\boldsymbol{\alpha}}^{k,\mathtt{m}}\right]_{\mu,\nu} = \mathfrak{h}^{|\boldsymbol{\alpha}|}\langle\partial^{\boldsymbol{\alpha}}\boldsymbol{N}_{\nu}^{(m(k))},\partial^{\boldsymbol{\alpha}}\boldsymbol{N}_{j_\mu^k}^{(s(k))}\rangle_{\Gamma_k},\quad \left[\boldsymbol{\mathcal{B}}_{\boldsymbol{\alpha}}^{k,\mathtt{s}}\right]_{\mu,\nu} = \mathfrak{h}^{|\boldsymbol{\alpha}|}\langle\partial^{\boldsymbol{\alpha}}\boldsymbol{N}_{\nu}^{(s(k))},\partial^{\boldsymbol{\alpha}}\boldsymbol{N}_{j_\mu^k}^{(s(k))}\rangle_{\Gamma_k},$$
$$\left[\tilde{\boldsymbol{\mathcal{B}}}_{\boldsymbol{\alpha}}^{k,\mathtt{m}}\right]_{\mu,\nu} = \mathfrak{h}^{|\boldsymbol{\alpha}|}\langle\partial^{\boldsymbol{\alpha}}\tilde{\boldsymbol{N}}_{\nu}^{(m(k))},\partial^{\boldsymbol{\alpha}}\boldsymbol{N}_{j_\mu^k}^{(s(k))}\rangle_{\Gamma_k},\quad \left[\tilde{\boldsymbol{\mathcal{B}}}_{\boldsymbol{\alpha}}^{k,\mathtt{s}}\right]_{\mu,\nu} = \mathfrak{h}^{|\boldsymbol{\alpha}|}\langle\partial^{\boldsymbol{\alpha}}\tilde{\boldsymbol{N}}_{\nu}^{(s(k))},\partial^{\boldsymbol{\alpha}}\boldsymbol{N}_{j_\mu^k}^{(s(k))}\rangle_{\Gamma_k}.$$

Weak G^1-continuous conditions

$$\left[\boldsymbol{\mathcal{B}}_{0}^{k,\mathtt{m}}\right]_{\mu,\nu} = \langle\boldsymbol{N}_{\nu}^{(m(k))}\circ\mathrm{P}_{m(k)}^{s(k)},\boldsymbol{N}_{j_\mu^k}^{(s(k))}\rangle_{\hat{\Gamma}_{m(k)}^{s(k)}},\quad \left[\boldsymbol{\mathcal{B}}_{0}^{k,\mathtt{s}}\right]_{\mu,\nu} = \langle\boldsymbol{N}_{\nu}^{(s(k))},\boldsymbol{N}_{j_\mu^k}^{(s(k))}\rangle_{\hat{\Gamma}_{m(k)}^{s(k)}},$$
$$\left[\tilde{\boldsymbol{\mathcal{B}}}_{0}^{k,\mathtt{m}}\right]_{\mu,\nu} = \langle\tilde{\boldsymbol{N}}_{\nu}^{(m(k))}\circ\mathrm{P}_{m(k)}^{s(k)},\boldsymbol{N}_{j_\mu^k}^{(s(k))}\rangle_{\hat{\Gamma}_{m(k)}^{s(k)}},\quad \left[\boldsymbol{\mathcal{B}}_{0}^{k,\mathtt{s}}\right]_{\mu,\nu} = \langle\tilde{\boldsymbol{N}}_{\nu}^{(s(k))},\boldsymbol{N}_{j_\mu^k}^{(s(k))}\rangle_{\hat{\Gamma}_{m(k)}^{s(k)}},$$
$$\left[\boldsymbol{\mathcal{B}}_{i}^{k,\mathtt{m}}\right]_{\mu,\nu} = \mathfrak{h}\langle\sum_{l=1}^{2}(\gamma_l^{i,k}\partial_l\boldsymbol{N}_{\nu}^{(m(k))})\circ\mathrm{P}_{m(k)}^{s(k)},\partial_i\boldsymbol{N}_{j_\mu^k}^{(s(k))}\rangle_{\hat{\Gamma}_{m(k)}^{s(k)}},\quad i=1,2,$$
$$\left[\tilde{\boldsymbol{\mathcal{B}}}_{i}^{k,\mathtt{m}}\right]_{\mu,\nu} = \mathfrak{h}\langle\sum_{l=1}^{2}(\gamma_l^{i,k}\partial_l\tilde{\boldsymbol{N}}_{\nu}^{(m(k))})\circ\mathrm{P}_{m(k)}^{s(k)},\partial_i\boldsymbol{N}_{j_\mu^k}^{(s(k))}\rangle_{\hat{\Gamma}_{m(k)}^{s(k)}},\quad i=1,2,$$
$$\left[\boldsymbol{\mathcal{B}}_{i}^{k,\mathtt{s}}\right]_{\mu,\nu} = \mathfrak{h}\langle\partial_i\boldsymbol{N}_{\nu}^{(s(k))},\partial_i\boldsymbol{N}_{j_\mu^k}^{(s(k))}\rangle_{\hat{\Gamma}_{m(k)}^{s(k)}},\quad \left[\tilde{\boldsymbol{\mathcal{B}}}_{i}^{k,\mathtt{s}}\right]_{\mu,\nu} = \mathfrak{h}\langle\partial_i\tilde{\boldsymbol{N}}_{\nu}^{(s(k))},\partial_i\boldsymbol{N}_{j_\mu^k}^{(s(k))}\rangle_{\hat{\Gamma}_{m(k)}^{s(k)}},\quad i=1,2.$$

Generalized weak C^n-continuous conditions

$$\left[\boldsymbol{\mathcal{B}}_{\boldsymbol{\alpha}}^{k,\mathtt{m}}\right]_{\mu,\nu} = \mathfrak{h}^{|\boldsymbol{\alpha}|}\langle(\partial^{\boldsymbol{\alpha}}\boldsymbol{N}_{\nu}^{(m(k))})\circ\phi_k,\partial^{\boldsymbol{\alpha}}\boldsymbol{N}_{j_\mu^k}^{(s(k))}\rangle_{\gamma_k},\quad \left[\boldsymbol{\mathcal{B}}_{\boldsymbol{\alpha}}^{k,\mathtt{s}}\right]_{\mu,\nu} = \mathfrak{h}^{|\boldsymbol{\alpha}|}\langle\partial^{\boldsymbol{\alpha}}\boldsymbol{N}_{\nu}^{(s(k))},\partial^{\boldsymbol{\alpha}}\boldsymbol{N}_{j_\mu^k}^{(s(k))}\rangle_{\gamma_k},$$
$$\left[\tilde{\boldsymbol{\mathcal{B}}}_{\boldsymbol{\alpha}}^{k,\mathtt{m}}\right]_{\mu,\nu} = \mathfrak{h}^{|\boldsymbol{\alpha}|}\langle(\partial^{\boldsymbol{\alpha}}\tilde{\boldsymbol{N}}_{\nu}^{(m(k))})\circ\phi_k,\partial^{\boldsymbol{\alpha}}\boldsymbol{N}_{j_\mu^k}^{(s(k))}\rangle_{\gamma_k},\quad \left[\tilde{\boldsymbol{\mathcal{B}}}_{\boldsymbol{\alpha}}^{k,\mathtt{s}}\right]_{\mu,\nu} = \mathfrak{h}^{|\boldsymbol{\alpha}|}\langle\partial^{\boldsymbol{\alpha}}\tilde{\boldsymbol{N}}_{\nu}^{(s(k))},\partial^{\boldsymbol{\alpha}}\boldsymbol{N}_{j_\mu^k}^{(s(k))}\rangle_{\gamma_k}.$$

The blocks $\boldsymbol{A}_{k,j}\in\mathbb{R}^{\mathfrak{l}^k\times\mathfrak{m}^{(j)}}$ of the coupling matrix $\boldsymbol{\mathcal{A}}\in\mathbb{R}^{\mathfrak{l}\times\mathfrak{m}}$ describe the respective role of the jth patch in the coupling at the kth interface and are defined by

$$\boldsymbol{A}_{k,j} = \begin{cases}\boldsymbol{\mathcal{A}}^{k,\mathtt{s}}, & \text{if } s(k)=j,\\ -\boldsymbol{\mathcal{A}}^{k,\mathtt{m}}, & \text{if } m(k)=j,\\ \boldsymbol{0}, & \text{otherwise,}\end{cases} \tag{3.25}$$

where in the case of weak C^n coupling conditions or generalised couplings the matrices $\boldsymbol{\mathcal{A}}^{k,\mathtt{s}}$, $\boldsymbol{\mathcal{A}}^{k,\mathtt{m}}$ are of the form $\boldsymbol{\mathcal{A}}^{k,j}=\sum_{|\boldsymbol{\alpha}|\le n}\boldsymbol{\mathcal{B}}_{\boldsymbol{\alpha}}^{k,j}$, and in the case of a weak G^1 coupling they read $\boldsymbol{\mathcal{A}}^{k,j}=\sum_{l=0}^{1}\boldsymbol{\mathcal{B}}_{l}^{k,j}$, $j\in\{\mathtt{s},\mathtt{m}\}$. For clarity, the entries of the matrices $\boldsymbol{\mathcal{B}}_{\boldsymbol{\alpha}}^{k,\mathtt{m}}$, $\boldsymbol{\mathcal{B}}_{\boldsymbol{\alpha}}^{k,\mathtt{s}}$, $\boldsymbol{\mathcal{B}}_{l}^{k,\mathtt{m}}$ and $\boldsymbol{\mathcal{B}}_{l}^{k,\mathtt{s}}$ are listed among other quantities in Table 3.1. A block-row of $\boldsymbol{\mathcal{A}}$ thus contains the coupling data for the kth interface, while the block columns are each assigned to a patch. Thereby, all blocks in a block-row are $\boldsymbol{0}$ except of the two blocks that are assigned to the master or slave side of the corresponding interface. In the case of a (generalised) C^n coupling, the summands of the non-zero blocks contain the coupling conditions for the partial derivatives of $|\boldsymbol{\alpha}|$th order, while in the case of a G^1 coupling, $\boldsymbol{\mathcal{B}}_{0}^{k,\mathtt{m}}$, $\boldsymbol{\mathcal{B}}_{0}^{k,\mathtt{s}}$ and $\boldsymbol{\mathcal{B}}_{i}^{k,\mathtt{m}}$, $\boldsymbol{\mathcal{B}}_{i}^{k,\mathtt{s}}$, $i=1,2$, contain the conditions for the function values and the

tangent spaces, respectively. Due to the compact support of the NURBS basis functions, it should be noted that $\boldsymbol{A}_{k,j}$ and thus the matrix $\boldsymbol{\mathcal{A}}$ itself are sparse. In order to keep the computational effort low, it is therefore reasonable to include only those entries in the implementation that make an effective contribution. These can be easily identified by considering the tensor product structure of the NURBS basis functions.

Finally, we obtain two equivalent discrete problems corresponding to the continuous problems discussed in Section 3.1. Introducing the constrained spaces

$$\begin{aligned} \mathcal{S}_{\mathrm{h}}^{c} &= \left\{ \sum_{i=1}^{\mathtt{m}} \bar{w}_i \boldsymbol{N}_i \in \mathcal{S}_{\mathrm{h}} \,|\, \boldsymbol{\mathcal{A}}(\bar{w}_i)_{1\le i\le \mathtt{m}} = \boldsymbol{0} \right\} = \operatorname{span}\{\boldsymbol{N}_r^c\}_{r=1}^{\mathtt{m}_c}, \\ \mathcal{V}_{\mathrm{h}}^{c} &= \left\{ \sum_{i=1}^{\mathtt{m}} \bar{w}_i \tilde{\boldsymbol{N}}_i \in \mathcal{V}_{\mathrm{h}} \,|\, \boldsymbol{\mathcal{A}}(\bar{w}_i)_{1\le i\le \mathtt{m}} = \boldsymbol{0} \right\} = \operatorname{span}\{\tilde{\boldsymbol{N}}_r^c\}_{r=1}^{\mathtt{m}_c}, \end{aligned} \tag{3.26}$$

the first reads: find $\bar{\boldsymbol{v}} \in \mathbb{R}^{\mathtt{m}_c}$ such that $\boldsymbol{\mathcal{R}}^c(\bar{\boldsymbol{v}}) = \boldsymbol{0}$, where the coupled residual $\boldsymbol{\mathcal{R}}^c = (\boldsymbol{\mathcal{R}}_k^c)_{1\le k\le N} \colon \mathbb{R}^{\mathtt{m}_c} \to \mathbb{R}^{\mathtt{m}_c}$ is defined through

$$\boldsymbol{\mathcal{R}}_k^c \colon \mathbb{R}^{\mathtt{m}_c^{(k)}} \to \mathbb{R}^{\mathtt{m}_c^{(k)}}, \quad \boldsymbol{\mathcal{R}}_k^c(\bar{\boldsymbol{v}}^{(k)}) = \left(\mathrm{V}^{(k)}\Big(\sum_{i=1}^{\mathtt{m}_c^{(k)}} \bar{v}_i^{(k)} \boldsymbol{N}_i^{c,(k)}, \tilde{\boldsymbol{N}}_j^{c,(k)}\Big) \right)_{1\le j\le \mathtt{m}_c^{(k)}}, \tag{3.27}$$

c.f. Eqs. (3.20), (3.21). Note that the construction of suitable bases $\{\boldsymbol{N}_r^c\}_{r=1}^{\mathtt{m}_c}$, $\{\tilde{\boldsymbol{N}}_r^c\}_{r=1}^{\mathtt{m}_c}$ of the spaces (3.26) is dealt with in Section 3.2.4. The second problem is the discrete analogue to the saddle point system (3.8) and reads: find $(\bar{\boldsymbol{v}}, \bar{\boldsymbol{\lambda}}) \in \mathbb{R}^{\mathtt{m}} \times \mathbb{R}^{\mathtt{l}}$ such that

$$\boldsymbol{\mathcal{R}}^c(\bar{\boldsymbol{v}}, \bar{\boldsymbol{\lambda}}) = \begin{pmatrix} \boldsymbol{\mathcal{R}}^u(\bar{\boldsymbol{v}}) + \tilde{\boldsymbol{\mathcal{A}}}^{\mathrm{T}} \bar{\boldsymbol{\lambda}} \\ \boldsymbol{\mathcal{A}} \bar{\boldsymbol{v}} \end{pmatrix} = \begin{pmatrix} \boldsymbol{0} \\ \boldsymbol{0} \end{pmatrix}, \tag{3.28}$$

where the matrix $\tilde{\boldsymbol{\mathcal{A}}} \in \mathbb{R}^{\mathtt{l}\times\mathtt{m}}$ is defined analogous to the coupling matrix introduced in Eq. (3.24), i.e. $\tilde{\boldsymbol{\mathcal{A}}} = (\tilde{\boldsymbol{A}}_{k,j})_{k,j}$,

$$\tilde{\boldsymbol{A}}_{i,j} = \begin{cases} \tilde{\boldsymbol{\mathcal{A}}}^{k,\mathtt{s}}, & \text{if } s(k) = j, \\ -\tilde{\boldsymbol{\mathcal{A}}}^{k,\mathtt{m}}, & \text{if } m(k) = j, \\ \boldsymbol{0}, & \text{otherwise}, \end{cases} \qquad \tilde{\boldsymbol{\mathcal{A}}}^{k,i} = \begin{cases} \displaystyle\sum_{|\boldsymbol{\alpha}|\le n} \tilde{\boldsymbol{\mathcal{B}}}_{\boldsymbol{\alpha}}^{k,i}, & \text{(weak } C^n \text{ coupling)}, \\ \displaystyle\sum_{l=0}^{1} \tilde{\boldsymbol{\mathcal{B}}}_{l}^{k,i}, & \text{(weak } G^1 \text{ coupling)}, \end{cases} \tag{3.29}$$

where $i \in \{\mathtt{s}, \mathtt{m}\}$ in the right equation, see also Table 3.1. Note that the blocks $\boldsymbol{\mathcal{A}}^{k,i}$, $\tilde{\boldsymbol{\mathcal{A}}}^{k,i}$, $i \in \{\mathtt{s}, \mathtt{m}\}$, of the coupling matrices $\boldsymbol{\mathcal{A}}$ and $\tilde{\boldsymbol{\mathcal{A}}}$ generally differ, as we consider here the possibility that the bases of the space of admissible solutions and test functions differ. If the bases coincide, it holds $\boldsymbol{\mathcal{A}} = \tilde{\boldsymbol{\mathcal{A}}}$.

3.2.2 Crosspoints and wirebaskets

In the finite element context, it is well known that the natural choice of the space of Lagrange multipliers as the trace space from the slave side leads to problems at the so-called crosspoints for $d = 2$ and wirebaskets for $d = 3$. These are regions where more

than two patches meet or a boundary of an interface meets Γ_e, where Γ_e denotes the boundary part of $\partial\Omega$ on which essential boundary conditions are specified, see Figure 3.1 for illustration. To be more precise, given $K \geq 0$ real interfaces $\Gamma_1, \ldots, \Gamma_K$ and $K' \geq 0$

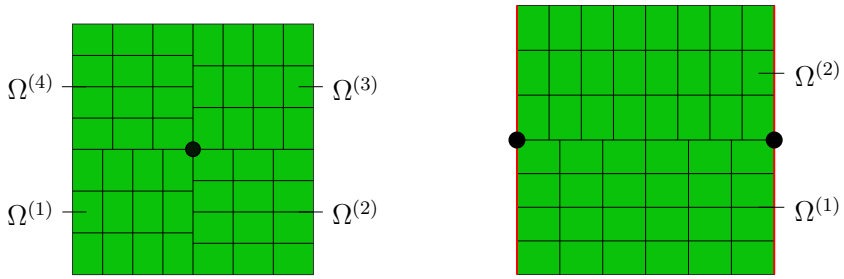

Figure 3.1: Two typical crosspoint situations. Left: a four-patch geometry where the interior corners of the four patches belong to each interface. Right: a two-patch geometry where the left and right ends of the interface meet Γ_e. Crosspoints are marked with black bullets and the exterior boundary part Γ_e with prescribed essential conditions is marked in red.

virtual interfaces $(\gamma_1, \phi_1), \ldots, (\gamma_{K'}, \phi_{K'})$, the set of all crosspoints/wirebaskets is given by the union

$$\mathfrak{C} = \left(\bigcup_{1 \leq k < j \leq K+K'} \partial\tilde{\Gamma}_k \cap \partial\tilde{\Gamma}_j \right) \cup \left(\bigcup_{k=1}^{K+K'} \partial\tilde{\Gamma}_k \cap \Gamma_e \right), \tag{3.30}$$

where $\tilde{\Gamma}_k := \Gamma_k$ for $k = 1, \ldots, K$ and $\tilde{\Gamma}_k := \gamma_k \cup \phi_k(\gamma_k)$ for $k = K+1, \ldots, K+K'$. To ensure uniform inf-sup stability and an optimal approximation order of the method also in this case, in the finite element method a modification of the multiplier space is performed, see [16, 170], which is adapted in Brivadis et al. [31] to isogeometric analysis for C^0 mortar couplings. Each of these modifications aims to reduce the dimension of the dual space. Roughly speaking, there are two ways to achieve this. On the one hand, the mesh for the Lagrange multipliers can be locally coarsened in the vicinity of a crosspoint (wirebasket) and, on the other hand, the order of the multipliers can be reduced there. In this section we, adopt the second strategy and extend it to higher order couplings. Thereby we focus our attention on the univariate case, since the construction for the bivariate case can be done as a tensor product in accordance with the tensor product structure of isogeometric approximation functions.

Let us consider a weak C^{l-1}-coupling, $l = 1, \ldots, p$, where p is the polynomial degree of the isogeometric approximation space concerning the affected direction. Our modification will be carried out on the parametric space and only in a region of the order of magnitude $\mathcal{O}(h)$ in the neighbourhood of the crosspoint on the slave side of each interface separately. For this reason, it is sufficient to consider one interface and one crosspoint at a time. Furthermore, we modify the univariate functions used to parametrise the geometry and then use the modified functions to construct the associated isogeometric approximation space according to Section 2.2. I.e. the underlying parametrisation $\boldsymbol{\mathcal{G}}$ remains unaffected by the modification. Without loss of generality, we can assume the pre-image $\hat{\Gamma}$ of the

interface Γ to be given as the unit interval, $\hat{\Gamma} = (0,1)$. Furthermore, we assume that the crosspoint we consider is the left endpoint and that the corresponding knots are ordered such that $0 = \zeta_1 = \ldots = \zeta_{p+1} < \ldots < \zeta_{p+1+l} < \ldots < \zeta_{\mathfrak{n}+1} = \ldots = \zeta_{\mathfrak{n}+p+1} = 1$, i.e. we assume an open knot vector in the affected direction. The associated univariate basis functions of maximal regularity are in the following denoted by $\hat{R}_i$, $i = 1, \ldots, \mathfrak{n}$.

For low-order mortar finite elements, only one basis function has to be removed and one has to be modified, cf. Maday et al. [119]. It is shown in Brivadis et al. [31] that p basis functions have to be modified in the IGA context while still only one basis function has to be removed. This results from the fact that only one basis function interacts with the crosspoint in case of a weak C^0 coupling. However, this is not the case for a higher continuity coupling. From a best approximation point of view, we want that our reduced Lagrange multiplier space can still reproduce polynomials of degree $p-1$. Additionally, no coupling across the crosspoint should occur. In case of a weak C^{l-1} coupling, where $1 \leq l \leq p$, this means that we have to remove the first l basis functions on the interface but also functions associated with the interior of the subdomain. While the interior basis functions are affected by normal derivatives, the functions at the interface are affected by tangential derivatives. Now we want to modify the following next p such that the new reduced basis functions are given as

$$\hat{R}_i^m = \sum_{j=1}^{l} c_{i,j}\hat{R}_j + \hat{R}_{i+l}, \quad i = 1, \ldots, p, \quad \hat{R}_i^m = \hat{R}_{i+l}, \quad p+1 \leq i \leq \mathfrak{n} - l. \tag{3.31}$$

Obviously, the new $\hat{R}_i^m$ are linearly independent, and in case of maximal continuity $\boldsymbol{C} := (c_{i,j})_{i,j} \in \mathbb{R}^{p\times l}$ forms a square matrix. Let $\Gamma_{l;p} := (0, \zeta_{p+l+1})$ and q_i, $1 \leq i \leq p$, be a basis of the polynomial space of degree $p-1$ on $\Gamma_{l;p}$. Then we can represent q_i in terms of $\hat{R}_j$, $j = 1, \ldots, p+l$, i.e. there exist $a_{i,j} \in \mathbb{R}$ such that on $\Gamma_{l;p}$ we have

$$q_i = \sum_{j=1}^{p+l} a_{i,j}\hat{R}_j. \tag{3.32}$$

Let us now introduce the two matrices $\boldsymbol{A}_1 = (a_{i,j})_{i,j} \in \mathbb{R}^{p\times l}$ and $\boldsymbol{A}_2 = (a_{i,j+l})_{i,j} \in \mathbb{R}^{p\times p}$. This gives us the following relationships.

Lemma 3.2.1. *If and only if the matrix $\boldsymbol{C}$ is defined through $\boldsymbol{C} = \boldsymbol{A}_2^{-1}\boldsymbol{A}_1$ the reduced basis $\hat{R}_i^m$ reproduces polynomials of degree at most $p-1$.*

Proof. We assume that q_i can also be represented by $\hat{R}_j^m$, $j = 1, \ldots, p$. Then for some coefficients $b_{i,j}$ we have

$$q_i = \sum_{j=1}^{p} b_{i,j}\hat{R}_j^m, \quad i = 1, \ldots, p. \tag{3.33}$$

Inserting the definition (3.31) into (3.33) yields

$$q_i = \sum_{j=1}^{p} b_{i,j}\left(\sum_{k=1}^{l} c_{j,k}\hat{R}_k + \hat{R}_{j+l}\right) = \sum_{k=1}^{l}\sum_{j=1}^{p} b_{i,j}c_{j,k}\hat{R}_k + \sum_{k=l+1}^{l+p} b_{i,k-l}\hat{R}_k. \tag{3.34}$$

Since the presentation (3.32) is unique a comparison of the coefficients yields $\boldsymbol{B} = \boldsymbol{A}_2$ and $\boldsymbol{BC} = \boldsymbol{A}_1$, where $\boldsymbol{B}$ denotes the matrix containing the coefficients $b_{i,j}$. This is obviously the case if and only if $\boldsymbol{C}$ is defined by $\boldsymbol{C} = \boldsymbol{A}_2^{-1}\boldsymbol{A}_1$. Here, we have assumed that $\boldsymbol{A}_2$ is non-singular. □

Lemma 3.2.1 shows us that the matrix $\boldsymbol{C}$ can be formally computed from $\boldsymbol{A}_1$ and $\boldsymbol{A}_2$. These two matrices can in turn be obtained from computing the L^2 scalar products $[\boldsymbol{Q}]_{i,j} := \langle q_i, \hat{R}_j \rangle_{\Gamma_{l;p}}$, $i = 1, \dots, p$, $j = 1, \dots, p+l$, $[\boldsymbol{M}]_{i,j} := \langle \hat{R}_i, \hat{R}_j \rangle_{\Gamma_{l;p}}$, $i, j = 1, \dots, p+l$, and setting $(\boldsymbol{A}_1, \boldsymbol{A}_2) = \boldsymbol{QM}^{-1}$. As an example, the modification matrices $\boldsymbol{C}$ for B-spline bases of order $p = 2, 3$ are listed in Table 3.2 and for $p = 3$ modificated Lagrange multiplier basis functions are shown in Figure 3.2.

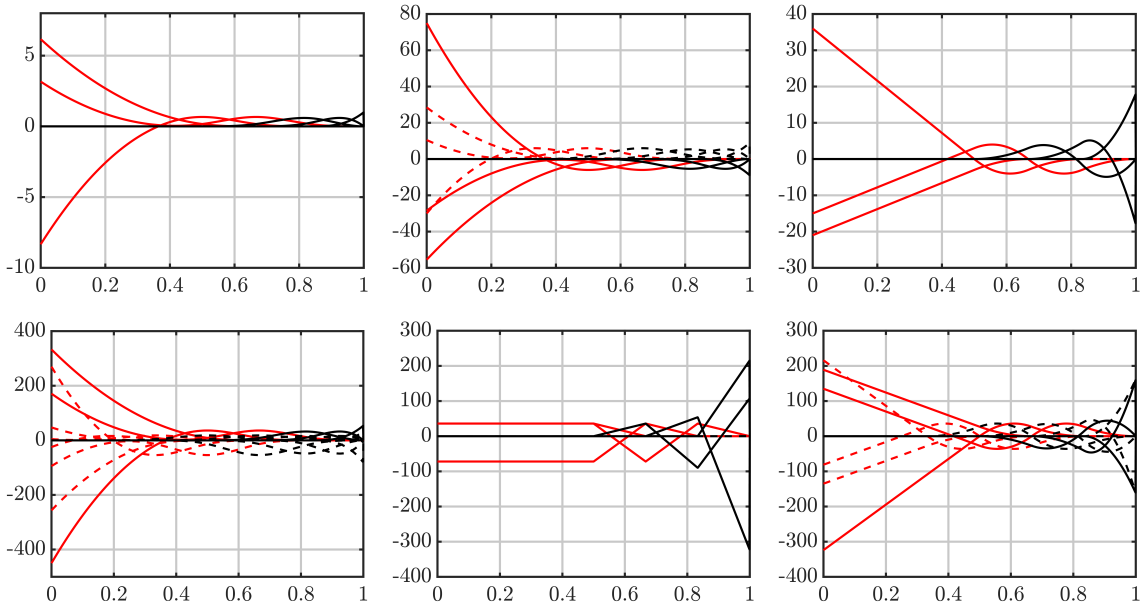

Figure 3.2: Modified cubic B-spline basis ($\boldsymbol{p} = (3, 3)$) associated to a weak C^2 coupling on the pre-image of the interface. First row: basis functions and their first derivatives in normal and tangential directions (from left to right). Second row: second derivatives in normal and tangential direction as well as mixed derivatives in normal and tangential (from left to right). Modified functions and their derivatives are coloured in red. The dashed curves denote derivatives associated with the interior of the slave patch.

So far, we have tacitly assumed that the choice of the polynomial basis $\{q_i\}$ has no influence on $\boldsymbol{C}$. In fact, the following holds.

Lemma 3.2.2. *The matrix $\boldsymbol{C} = \boldsymbol{A}_2^{-1}\boldsymbol{A}_1$ is invariant with respect to the choice of the polynomial basis $\{q_i\}$. Moreover, for all combinations of p and possible l, we have $\sum_{i=1}^{p} c_{i,j} = 1$ for all $j \in \{1, \dots, l\}$.*

Proof. Let $\{q_i\}$ and $\{\tilde{q}_i\}$ two polynomial bases. Then each basis function q_i can be written in terms of the basis function $\tilde{q}_j$, $j = 1, \dots, p$, i.e., $q_i = \sum_{j=1}^{p} t_{i,j}\tilde{q}_j$. Thus, the matrices

Table 3.2: Modification matrices for B-spline bases of order $p = 2, 3$ and coupling orders $l = 1, \ldots, p$ (from left to right) in the case of equidistant inner knots, i.e. $\zeta_i - \zeta_{i-1} = h$ for $i = p+2, \ldots, p+1+l$.

$p = 2$:

$$\boldsymbol{C} = \begin{pmatrix} \frac{3}{2} \\ -\frac{1}{2} \end{pmatrix}, \qquad \boldsymbol{C} = \begin{pmatrix} \frac{5}{2} & 2 \\ -\frac{3}{2} & -1 \end{pmatrix}$$

$p = 3$:

$$\boldsymbol{C} = \begin{pmatrix} \frac{7}{4} \\ -\frac{11}{12} \\ \frac{1}{6} \end{pmatrix}, \qquad \boldsymbol{C} = \begin{pmatrix} \frac{19}{6} & \frac{7}{3} \\ -\frac{10}{3} & -2 \\ \frac{7}{6} & \frac{2}{3} \end{pmatrix}, \qquad \boldsymbol{C} = \begin{pmatrix} \frac{37}{6} & 5 & 3 \\ -\frac{25}{3} & -\frac{19}{3} & -3 \\ \frac{19}{6} & \frac{7}{3} & 1 \end{pmatrix}$$

are related by $\boldsymbol{Q} = \boldsymbol{T}\tilde{\boldsymbol{Q}}$, $\boldsymbol{T} := (t_{i,j})_{i,j}$, from which follows $(\boldsymbol{A}_1, \boldsymbol{A}_2) = \boldsymbol{T}(\tilde{\boldsymbol{A}}_1, \tilde{\boldsymbol{A}}_2)$. The choice of the modification matrix $\boldsymbol{C}$ then gives $\boldsymbol{C} = \tilde{\boldsymbol{A}}_2^{-1}\boldsymbol{T}^{-1}\boldsymbol{T}\tilde{\boldsymbol{A}}_1 = \tilde{\boldsymbol{C}}$. Now without loss of generality we assume that $q_1 = 1$ and due to the fact that $\hat{R}_i$ form a partition of unity, we have $a_{1,j} = 1$, i.e., the first row of $\boldsymbol{A}_1$ and of $\boldsymbol{A}_2$ only contains one as entries. Let $\boldsymbol{e}^p \in \mathbb{R}^p$ and $\boldsymbol{e}^l \in \mathbb{R}^l$ the vectors having ones as entries. Then the second assertion of the lemma is equivalent to $\boldsymbol{C}^{\mathrm{T}}\boldsymbol{e}^p = \boldsymbol{e}^l$. However as the first column of $\boldsymbol{A}_2^{\mathrm{T}}$ is equal to $\boldsymbol{e}^p$, we get $\boldsymbol{A}_2^{-\mathrm{T}}\boldsymbol{e}^p = \boldsymbol{e}_1^p$, where $\boldsymbol{e}_1^p$ is the first unit vector in $\mathbb{R}^p$, i.e. $\boldsymbol{e}_1^p = (\delta_{1,j})_{1 \le j \le p}$. Additionally $\boldsymbol{A}_1^{\mathrm{T}}\boldsymbol{e}_1^p$ results in the first column of $\boldsymbol{A}_1^{\mathrm{T}}$ which is the first row of $\boldsymbol{A}_1$ and thus $\boldsymbol{C}^{\mathrm{T}}\boldsymbol{e}^p = \boldsymbol{A}_1^{\mathrm{T}}\boldsymbol{A}_2^{-\mathrm{T}}\boldsymbol{e}^p = \boldsymbol{A}_1^{\mathrm{T}}\boldsymbol{e}_1^p = \boldsymbol{e}^l$. □

Until now we have described how the number of Lagrange multiplier basis functions which are directly associated with the interface is reduced by l per crosspoint and slave side. However in the case of $l > 1$, a closer look at the coupling conditions listed in Table 3.1 reveals that basis functions associated with the interior of the slave patch also affect the interface coupling constraints. To remove $l(l+1)/2$ basis functions, we have to apply the reduction for each row in the tensor product structure sequentially using the matrices as provided in Table 3.2. Alternatively, we can modify the first l rows of Lagrange multiplier basis functions in the same way, i.e. in total l^2 basis functions are removed and lp are modified per crosspoint and slave side, see Figure 3.3 for a comparison. This is motivated by the fact that only then we preserve the tensor product structure which makes the implementation easier, especially in the three-dimensional case. To distinguish between the two approaches, we will refer to them as reduced and full modification in the following.

Example: We consider the four patch situation shown in Figure 3.1, where we focus on a weak C^1 coupling ($l = 2$) of the two patches $\Omega^{(2)}$ and $\Omega^{(3)}$. For the slave side we choose $\Omega^{(3)}$ and assume a B-spline basis of order $\boldsymbol{p} = (2, 2)$ defined through the two knot vectors $\Theta^1 = \{0, 0, 0, 1/4, 2/4, 3/4, 1, 1, 1\}$, $\Theta^2 = \{0, 0, 0, 1/3, 2/3, 1, 1, 1\}$ to be used to parametrise $\Omega^{(3)}$. The associated B-spline basis consists of 30 functions, where in the case

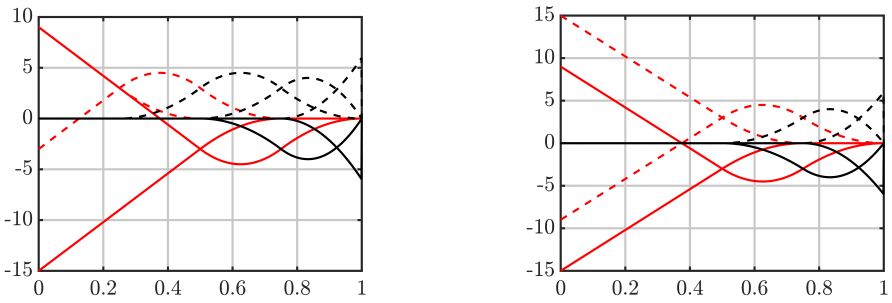

Figure 3.3: First derivatives of modified quadratic B-splines ($\boldsymbol{p} = (2,2)$) in normal direction on the pre-image of the interface associated with a weak C^1 coupling. Left: reduced modification; right: full modification. The dashed curves denote again derivatives associated with the interior of the slave patch.

of a weak C^1 coupling only the twelve functions $\hat{R}_{(i,j)} = \hat{R}_i^1 \hat{R}_j^2$, $i = 1, \dots, 6$, $j = 1, 2$, have to be considered. According to Section 3.2.1, the space of the Lagrange multiplier on the interface is constructed from the functions $\hat{M}_{(i,j)} \colon (0,1) \to \mathbb{R}$, $\hat{M}_{(i,j)}(\xi) = \hat{R}_i^1(\xi)\hat{R}_j^2(0)$, $i = 1, \dots, 6$, $j = 1, 2$, such that we have to modify $\hat{R}_i^1$. Using a reduced modification, we obtain for the first row

$$\hat{M}^m_{(1,1)} = \left(\frac{5}{2}\hat{R}_1^1 + 2\hat{R}_2^1 + \hat{R}_3^1\right)\hat{R}_1^2(0), \quad \hat{M}^m_{(2,1)} = \left(-\frac{3}{2}\hat{R}_1^1 - \hat{R}_2^1 + \hat{R}_4^1\right)\hat{R}_1^2(0),$$

$\hat{M}^m_{(i,1)} = \hat{R}_{i+2}^1 \hat{R}_1^2(0)$, $i = 3, 4$, where we get for the second row

$$\hat{M}^m_{(1,2)} = \left(\frac{3}{2}\hat{R}_1^1 + \hat{R}_2^1\right)\hat{R}_2^2(0), \quad \hat{M}^m_{(2,2)} = \left(-\frac{1}{2}\hat{R}_1^1 + \hat{R}_3^1\right)\hat{R}_2^2(0),$$

$\hat{M}^m_{(i,2)} = \hat{R}_{i+1}^1 \hat{R}_2^2(0)$, $i = 3, 4, 5$. On the other hand, using a full modification, the two rows are modified analogously such that the modified basis is given by

$$\hat{M}^m_{(1,j)} = \left(\frac{5}{2}\hat{R}_1^1 + 2\hat{R}_2^1 + \hat{R}_3^1\right)\hat{R}_j^2(0), \quad \hat{M}^m_{(2,j)} = \left(-\frac{3}{2}\hat{R}_1^1 - \hat{R}_2^1 + \hat{R}_4^1\right)\hat{R}_j^2(0), \quad j = 1, 2,$$

and $\hat{M}^m_{(i,j)} = \hat{R}_{i+2}^1 \hat{R}_j^2(0)$ for $i = 3, 4$ and $j = 1, 2$. Note that in both the reduced and full modification, the basis functions of the second row are identical to zero on $(0,1)$ but not their derivatives, which also appear in the conditions for a weak C^1 coupling. Note also that this example is chosen so that the functions constructed here coincide with those shown in Figure 3.3.

Remark 3.2.1. *Since the modification is performed on the parameter space, it can also be applied to crosspoint situations that occur in weak G^1 couplings. In this case, the basis functions have to be modified as in a weak C^1 coupling.*

3.2.3 Evaluation of mortar integrals

A particular challenge in implementing a mortar method is the evaluation of the interface integrals, due to the product of functions each of which being defined on a different mesh, cf. Table 3.1. Any quadrature rule based on the slave mesh does not respect the mesh lines of the master mesh and vice versa for a quadrature rule based on the master mesh. To overcome this difficulty, it is common to use a quadrature rule based on a merged mesh, i.e. a mesh which respects the reduced smoothness of the master and slave functions at their respective lines leads to an exact evaluation of the integral, see, e.g., [62, 74, 90, 92, 135]. Such a segment-based integration scheme can be carried out for two-dimensional problems with acceptable computational costs but involves a large effort in the implementation and high computational costs in evaluation.

Another method is discussed in [74, 114, 119] for mortar finite elements and in [32, 55] for isogeometric mortar elements. In contrast to the segment-based method, it ignores the reduced smoothness at the mesh lines of one of the two meshes and accepts that the integration error may therefore increase. Nevertheless, the implementation effort and especially the associated computational costs are significantly reduced. This is achieved by an element-wise evaluation of the mortar integrals, which motivates the denomination as element-based integration used in the following. Here we briefly outline the basic features of these two approaches and refer to the literature mentioned above for more details.

Segment-based mortar integration

The segmentation process outlined here is based on the work of Brivadis [30]. It is carried out iteratively over the number of surface elements belonging to the master surface, so that we can focus on a single master element to describe the procedure. Let us consider a parametric master element, where we assume that the element-boundary is tessellated by a certain amount of points, in the following called tessellation points[†]. They ensure the linear interpolation of the boundary which is more or less accurate depending on their number. In a first step, the images of the tessellation points under the corresponding geometric mapping are transferred to the physical slave side of the interface by a ray-tracing operation using the master normal. We point out that if the master and slave boundary differ only a little or the boundaries match, this operation is close to the identity or is the identity. Once the corresponding physical slave points are known, each of them is pulled back into the slave parametric space using the inverse of the geometric mapping corresponding to the slave side. Since the inverse is in general not known, the pull-back is realised by solving a non-linear system of equations for each point. The linear interpolation of the resulting points in the slave parametric space defines the boundary of the counterpart of the current parametric master element. Note that, due to the linear interpolation, the counterpart obtained in this way is an approximation of the exact one, the accuracy of which generally depends on the number of tessellation points, cf.

[†]Often the element corners are chosen as tessellation points.

Figure 3.4(a). In the final step, the parametric slave mesh is now split into polygons according to the counterpart boundary by means of a suitable polygon-clipping process and the resulting polygons are triangularisated, see [127, 148, 152] for details in polygon-clipping and [50, 54, 151] for details in triangolarisation. This gives us a local merged mesh associated with each master element, where the global mesh could be obtained by overlapping the local ones. All of these steps are illustrated in Figure 3.4.

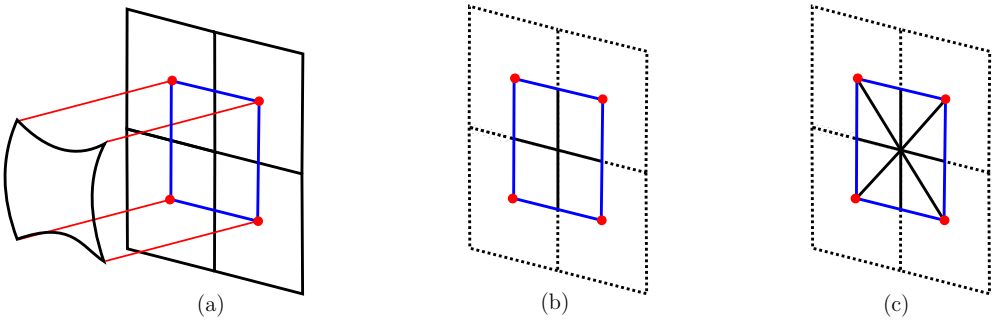

Figure 3.4: Illustration of the different steps to build a local merged mesh. For the sake of simplicity, we assume here that the physical and parametric slave spaces are equal and thus avoid the illustration of the pull-back into the slave parametric space. Moreover, we start the illustration with the physical master element. (a) Ray-tracing operation and linear interpolation. The four edges of the master element are selected as tessellation points and the counterpart boundary obtained by the linear interpolation is marked with blue lines. (b) Polygon clipping operation. The solid lines represent the remaining polygons. (c) Triangolarization. The solid lines represent the local merged mesh.

To evaluate the mortar integrals, suitable quadrature rules for triangles can now be applied to the merged mesh, see, e.g., Cowper [47] for Gaussian quadrature formulas. Therefore, the integration points of the chosen quadrature rule have to be defined on each triangle of the mesh and subsequently transferred to the corresponding parametric master element, again using a ray-tracing operation and a pull-back to the master parametric space. Finally, we note that these two steps, i.e. the projection of the quadrature points from the parametric slave space to the parametric master space may result in the projection of a quadrature point being outside the corresponding parametric master element due to numerical inaccuracies. Therefore it is necessary for the code to measure the occurrences of this issue to intervene if required.

Remark 3.2.2. *In the 2D case, the effort to create a merged mesh is significantly reduced. Since in this case, the interface is simply a curve, only the start and end points of the parametric master element, defined through the corresponding knot vector, have to be transferred into the physical space, projected onto the physical slave side and pulled back into the parametric slave space. The local merged mesh is then defined through the corresponding slave knot vector and the projected master knots.*

Element-based mortar integration

For an element-based mortar integration, one of the two sides of the interface is chosen on which the integration rule is defined. Suppose the slave side is selected. Then for each parametric element, we have a set of points with which we proceed analogously to the tessellation points in the previous section. I.e. the images of the quadrature points under the corresponding geometric mapping are transferred to the physical master side and subsequently pulled back into the master parametric space. The evaluation of the mortar integrals is now performed by means of the integration points on the slave side and the corresponding points on the master side, which generally do not respect the mesh lines of the parametric master mesh.

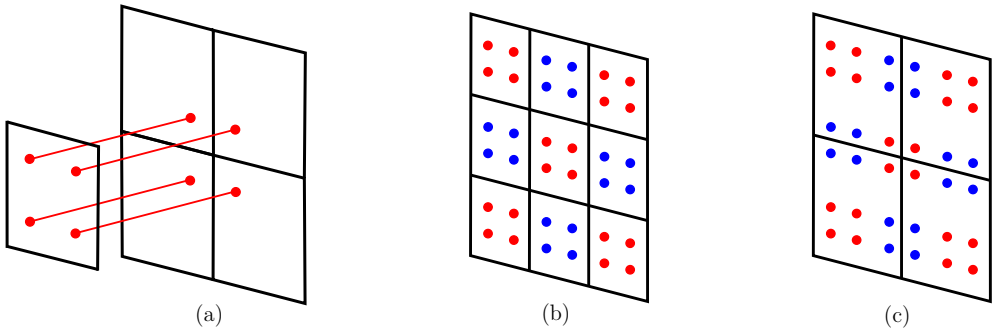

Figure 3.5: Illustration of an application of a quadrature rule based on the mesh of the slave side. For the sake of simplicity, we assume here that the physical and parametric master spaces are equal and start the illustration from the physical slave element. (a) Ray-tracing operation (local). The quadrature points defined on the current slave element are projected to the master side. (b) Global slave mesh consisting of nine elements. The quadrature points of adjacent elements are marked with different colours. (c) Global master mesh consisting of four elements. The quadrature points are the results of the projection of the points from the slave mesh shown in (b).

3.2.4 Construction of constrained spaces

In this section, we deal with the construction of a suitable basis of the discrete constrained spaces introduced in Section 3.2.1, Eq. (3.26) without the presence of crosspoints and wirebaskets, focusing on an element-based integration method. Since the procedure for the two spaces $\mathcal{S}_{\mathrm{h}}^{c}$ and $\mathcal{V}_{\mathrm{h}}^{c}$ is identical, we describe here only the construction of a base of $\mathcal{S}_{\mathrm{h}}^{c}$. The construction is performed separately for each interface and is analogous for weak C^n and weak G^1 coupling conditions. Therefore, we restrict ourselves here to a two-patch situation with one interface under weak C^n coupling conditions. The interested reader will find a detailed discussion of the construction for weak G^1 coupling conditions in the framework of Kirchhoff–Love shells in Schuß et al. [143].

Let us assume that $\Omega^{(1)}$ is chosen as the slave side. We denote the common interface by Γ and assume that, after a possible reordering of the basis $\mathbb{B}_{\mathrm{h}}^{(1)}$ (cf. beginning Section 3.2.1), the space of the Lagrange multiplier is given by $\mathcal{M}_{\mathrm{h}} = \operatorname{span}\{\boldsymbol{N}_j^{(1)}\}_{j=1}^{\mathfrak{l}}$, i.e. the first $\mathfrak{l}$ basis functions on the slave side have an influence on the interface according to the specification in Eq. (3.22). Then, the corresponding coupling matrix has the form $\boldsymbol{\mathcal{A}} = (\boldsymbol{\mathcal{A}}^{\mathfrak{s}}, -\boldsymbol{\mathcal{A}}^{\mathfrak{m}})$, where $\boldsymbol{\mathcal{A}}^{\mathfrak{s}} \in \mathbb{R}^{\mathfrak{l}\times\mathfrak{m}^{(1)}}$, $\boldsymbol{\mathcal{A}}^{\mathfrak{m}} \in \mathbb{R}^{\mathfrak{l}\times\mathfrak{m}^{(2)}}$,

$$[\boldsymbol{\mathcal{A}}^{\mathfrak{s}}]_{\mu,\nu} = \sum_{|\boldsymbol{\alpha}|\leq n} \mathfrak{h}^{|\boldsymbol{\alpha}|}\langle \partial^{\boldsymbol{\alpha}} \boldsymbol{N}_\nu^{(1)}, \partial^{\boldsymbol{\alpha}} \boldsymbol{N}_\mu^{(1)}\rangle_\Gamma, \quad [\boldsymbol{\mathcal{A}}^{\mathfrak{m}}]_{\mu,\nu} = \sum_{|\boldsymbol{\alpha}|\leq n} \mathfrak{h}^{|\boldsymbol{\alpha}|}\langle \partial^{\boldsymbol{\alpha}} \boldsymbol{N}_\nu^{(2)}, \partial^{\boldsymbol{\alpha}} \boldsymbol{N}_\mu^{(1)}\rangle_\Gamma, \tag{3.35}$$

cf. Eqs. (3.24), (3.25) and Table 3.1. We note that due to the local support of the isogeometric basis functions the two matrices $\boldsymbol{\mathcal{A}}^{\mathfrak{s}}$, $\boldsymbol{\mathcal{A}}^{\mathfrak{m}}$ in general contain many zero columns, where, according to the assumed order of $\mathbb{B}_{\mathrm{h}}^{(1)}$, the last $\mathfrak{m}^{(1)} - \mathfrak{l}$ columns of $\boldsymbol{\mathcal{A}}^{\mathfrak{s}}$ are zero. Let us denote by $\boldsymbol{A}^{\mathfrak{s}} \in \mathbb{R}^{\mathfrak{l}\times\mathfrak{l}}$ and $\boldsymbol{A}^{\mathfrak{m}} \in \mathbb{R}^{\mathfrak{l}\times\mathfrak{r}}$ the matrices obtained by deleting these columns and let us assume the basis $\mathbb{B}_{\mathrm{h}}^{(2)}$ to be ordered analogously to $\mathbb{B}_{\mathrm{h}}^{(1)}$ such that $\boldsymbol{A}^{\mathfrak{m}}$ is obtained from $\boldsymbol{\mathcal{A}}^{\mathfrak{m}}$ by deleting the last $\mathfrak{m}^{(2)} - \mathfrak{r}$ columns. Using a suitable quadrature rule based on the slave side to evaluate the L^2 scalar products, the reduced coupling matrices become

$$\begin{aligned}
[\boldsymbol{A}^{\mathfrak{s}}]_{\mu,\nu} &= \sum_{|\boldsymbol{\alpha}|\leq n} \sum_{k=1}^{n_q} w_k \mathfrak{h}^{|\boldsymbol{\alpha}|} \partial^{\boldsymbol{\alpha}} \boldsymbol{N}_\nu^{(1)}(\boldsymbol{z}_k^{(1)}) \cdot \partial^{\boldsymbol{\alpha}} \boldsymbol{N}_\mu^{(1)}(\boldsymbol{z}_k^{(1)}), \\
[\boldsymbol{A}^{\mathfrak{m}}]_{\mu,\nu} &= \sum_{|\boldsymbol{\alpha}|\leq n} \sum_{k=1}^{n_q} w_k \mathfrak{h}^{|\boldsymbol{\alpha}|} \partial^{\boldsymbol{\alpha}} \boldsymbol{N}_\nu^{(2)}(\boldsymbol{z}_k^{(2)}) \cdot \partial^{\boldsymbol{\alpha}} \boldsymbol{N}_\mu^{(1)}(\boldsymbol{z}_k^{(1)}),
\end{aligned} \tag{3.36}$$

where $\boldsymbol{z}_k^{(1)}$ are the quadrature points chosen on the slave side, $\boldsymbol{z}_k^{(2)}$ are the corresponding points on the master side obtained during a possible ray-tracing operation, $w_k > 0$ are the quadrature weights and n_q denotes the number of quadrature points. Let us summarize the contributions of the basis functions in Eq. (3.36) as follows

$$\boldsymbol{B}^{(i)} = \left[\boldsymbol{B}_{k,\mu}^{(i)}\right]_{k,\mu}, \quad \boldsymbol{B}_{k,\mu}^{(i)} = \mathcal{L}^n \boldsymbol{N}_\mu^{(i)}(\boldsymbol{z}_k^{(i)}) \in \mathbb{R}^{sd\times 1}, \tag{3.37}$$

where s denotes the number of multi-indices $\boldsymbol{\alpha} \in \mathbb{N}_0^d$ with $|\boldsymbol{\alpha}| \leq n$ and the linear operator $\mathcal{L}^n$ is introduced to specify an ordering of the partial derivatives to assign them a fixed place in the matrices $\boldsymbol{B}^{(i)}$. For example, for $d = 2$ and $n = 1, 2$ one could define $\mathcal{L}^n$ through

$$\mathcal{L}^1 \boldsymbol{N} = (\boldsymbol{N}^{\mathrm{T}}, \partial_1 \boldsymbol{N}^{\mathrm{T}}, \partial_2 \boldsymbol{N}^{\mathrm{T}})^{\mathrm{T}}, \quad \mathcal{L}^2 \boldsymbol{N} = (\boldsymbol{N}^{\mathrm{T}}, \partial_1 \boldsymbol{N}^{\mathrm{T}}, \partial_2 \boldsymbol{N}^{\mathrm{T}}, \partial_1^2 \boldsymbol{N}^{\mathrm{T}}, \partial_2^2 \boldsymbol{N}^{\mathrm{T}}, \partial_1\partial_2 \boldsymbol{N}^{\mathrm{T}})^{\mathrm{T}}. \tag{3.38}$$

Note that the order determined by the operator can be chosen arbitrarily, but must then be maintained. In the following, we will tacitly assume that the columns of the matrix $\boldsymbol{B}^{(1)}$ are linearly independent, i.e. $\dim(\operatorname{Im}(\boldsymbol{B}^{(1)})) = \mathfrak{l}$. Due to the linear independence of the NURBS approximation functions, this can be achieved by using a sufficient number of quadrature points. In the case of B-splines, the linear independence is guaranteed, if the number of quadrature points per element on the interface slave side is greater or equal to $(p_{\max}^{(1)} + 1)^{(d-1)}$, where $p_{\max}^{(1)}$ denotes the maximum degree in the tensor product structure of the B-spline basis corresponding to $\Omega^{(1)}$.

Let now $\bar{\boldsymbol{v}} = (\bar{\boldsymbol{v}}^{(1)}, \bar{\boldsymbol{v}}^{(2)}) \in \mathbb{R}^{\mathfrak{m}^{(1)}+\mathfrak{m}^{(2)}}$ be the vector containing the dof corresponding to the two patches and let us split the two blocks of $\bar{\boldsymbol{v}}$ as follows $\bar{\boldsymbol{v}}^{(i)} = (\bar{\boldsymbol{v}}_1^{(i)}, \bar{\boldsymbol{v}}_2^{(i)})$, such that $\bar{\boldsymbol{v}}_1^{(1)} \in \mathbb{R}^{\mathfrak{l}}$ and $\bar{\boldsymbol{v}}_1^{(2)} \in \mathbb{R}^{\mathfrak{r}}$ correspond to the columns of $\boldsymbol{A}^{\mathfrak{s}}$ and $\boldsymbol{A}^{\mathfrak{m}}$, respectively. I.e. we divide the dof of the slave and master side into sets where all dof with influence on the coupling are contained in $\bar{\boldsymbol{v}}_1^{(i)}$ and the dof corresponding to the deleted zero columns of $\boldsymbol{\mathcal{A}}^{\mathfrak{s}}$ and $\boldsymbol{\mathcal{A}}^{\mathfrak{m}}$ are contained in $\bar{\boldsymbol{v}}_2^{(1)}$ and $\bar{\boldsymbol{v}}_2^{(2)}$, respectively. Doing so, the coupling condition can be rewritten as follows

$$\underbrace{(\boldsymbol{B}^{(1)})^{\mathrm{T}}\boldsymbol{D}\boldsymbol{B}^{(1)}}_{=\boldsymbol{A}^{\mathfrak{s}}}\bar{\boldsymbol{v}}_1^{(1)} - \underbrace{(\boldsymbol{B}^{(1)})^{\mathrm{T}}\boldsymbol{D}\boldsymbol{B}^{(2)}}_{=\boldsymbol{A}^{\mathfrak{m}}}\bar{\boldsymbol{v}}_1^{(2)} = \boldsymbol{0}, \tag{3.39}$$

where $\boldsymbol{D} \in \mathbb{R}^{n_q sd \times n_q sd}$ is a diagonal matrix containing the products $w_k \mathfrak{h}^{|\boldsymbol{\alpha}|}$ of the quadrature weights and the $|\boldsymbol{\alpha}|$th power of the weighting parameter. Note that the position of $w_k \mathfrak{h}^{|\boldsymbol{\alpha}|}$ in $\boldsymbol{D}$ depends on the definition of $\mathcal{L}^n$ so that the structure of $\boldsymbol{D}$ is not fixed until the operator has been specified. Representing $\boldsymbol{D}$ as product of its square, $\boldsymbol{D} = \sqrt{\boldsymbol{D}}\sqrt{\boldsymbol{D}}$, Eq. (3.39) can be further written as

$$(\boldsymbol{C}^{(1)})^{\mathrm{T}}\boldsymbol{C}^{(1)}\bar{\boldsymbol{v}}_1^{(1)} = (\boldsymbol{C}^{(1)})^{\mathrm{T}}\boldsymbol{C}^{(2)}\bar{\boldsymbol{v}}_1^{(2)}, \tag{3.40}$$

where $\boldsymbol{C}^{(i)} := \sqrt{\boldsymbol{D}}\boldsymbol{B}^{(i)}$. Since the columns of $\boldsymbol{B}^{(1)}$ are assumed to be linearly independent and the entries of $\sqrt{\boldsymbol{D}}$ are positive, the columns of $\boldsymbol{C}^{(i)}$ are also linearly independent. Consequently, the matrix $(\boldsymbol{C}^{(1)})^{\mathrm{T}}\boldsymbol{C}^{(1)}$ is positive definite and we can express the degrees of freedom corresponding to the slave side as a function of the degrees of freedom corresponding to the master side,

$$\bar{\boldsymbol{v}}_1^{(1)} = \bar{\boldsymbol{v}}_1^{(1)}(\bar{\boldsymbol{v}}_1^{(2)}) = \mathfrak{M}\bar{\boldsymbol{v}}_1^{(2)}, \quad \mathfrak{M} := ((\boldsymbol{C}^{(1)})^{\mathrm{T}}\boldsymbol{C}^{(1)})^{-1}(\boldsymbol{C}^{(1)})^{\mathrm{T}}\boldsymbol{C}^{(2)} \in \mathbb{R}^{\mathfrak{l}\times\mathfrak{r}}. \tag{3.41}$$

We note that although the matrix $(\boldsymbol{C}^{(1)})^{\mathrm{T}}\boldsymbol{C}^{(1)}$ is sparse, its inverse is dense and thus the action of $((\boldsymbol{C}^{(1)})^{\mathrm{T}}\boldsymbol{C}^{(1)})^{-1}$ is global with respect to the interface. Outgoing from the representations

$$\boldsymbol{v}_{\mathrm{h}}^{(i)} = \sum_{j=1}^{\mathfrak{m}^{(i)}} \bar{v}_j^{(i)}\boldsymbol{N}_j^{(i)} \iff \boldsymbol{v}_{\mathrm{h}}^{(i)} = \left(\boldsymbol{N}_1^{(i)}, \ldots, \boldsymbol{N}_{\mathfrak{m}^{(i)}}^{(i)}\right)\bar{\boldsymbol{v}}^{(i)}, \quad i = 1, 2, \tag{3.42}$$

of the approximations, we can now substitute $\bar{\boldsymbol{v}}_1^{(1)}$ according to (3.41) and obtain on the slave side

$$\begin{aligned}\boldsymbol{v}_{\mathrm{h}}^{(1)} &= \left(\boldsymbol{N}_1^{(1)}, \ldots, \boldsymbol{N}_{\mathfrak{l}}^{(1)}\right)\bar{\boldsymbol{v}}_1^{(1)} + \left(\boldsymbol{N}_{\mathfrak{l}+1}^{(1)}, \ldots, \boldsymbol{N}_{\mathfrak{m}^{(1)}}^{(1)}\right)\bar{\boldsymbol{v}}_2^{(1)} \\ &= \left(\boldsymbol{N}_1^{(1)}, \ldots, \boldsymbol{N}_{\mathfrak{l}}^{(1)}\right)\mathfrak{M}\bar{\boldsymbol{v}}_1^{(2)} + \left(\boldsymbol{N}_{\mathfrak{l}+1}^{(1)}, \ldots, \boldsymbol{N}_{\mathfrak{m}^{(1)}}^{(1)}\right)\bar{\boldsymbol{v}}_2^{(1)}.\end{aligned} \tag{3.43}$$

Introducing the modified functions $\boldsymbol{M}_j^{(1)} := \mathfrak{M}_{ij}\boldsymbol{N}_i^{(1)}$ (summation over $i = 1, \ldots, \mathfrak{l}$), we finally obtain the following representation of the two approximation functions in terms of the global product basis

$$\begin{pmatrix}\boldsymbol{v}_{\mathrm{h}}^{(1)} \\ \boldsymbol{v}_{\mathrm{h}}^{(2)}\end{pmatrix} = \sum_{i=\mathfrak{l}+1}^{\mathfrak{m}^{(1)}} \bar{v}_i^{(1)}\begin{pmatrix}\boldsymbol{N}_i^{(1)} \\ \boldsymbol{0}\end{pmatrix} + \sum_{i=1}^{\mathfrak{r}} \bar{v}_i^{(2)}\begin{pmatrix}\boldsymbol{M}_i^{(1)} \\ \boldsymbol{N}_i^{(2)}\end{pmatrix} + \sum_{i=\mathfrak{r}+1}^{\mathfrak{m}^{(2)}} \bar{v}_i^{(2)}\begin{pmatrix}\boldsymbol{0} \\ \boldsymbol{N}_i^{(2)}\end{pmatrix}. \tag{3.44}$$

Consequently, a basis $\{\boldsymbol{N}_r^c\}_{r=1}^{\mathfrak{m}^{(1)}+\mathfrak{m}^{(2)}-\mathfrak{l}}$ of the constrained approximation space $\mathcal{S}_{\mathrm{h}}^c$ is given by

$$\left\{ \begin{pmatrix} \boldsymbol{N}_{\mathfrak{l}+1}^{(1)} \\ \boldsymbol{0} \end{pmatrix}, \dots, \begin{pmatrix} \boldsymbol{N}_{\mathfrak{m}^{(1)}}^{(1)} \\ \boldsymbol{0} \end{pmatrix}, \begin{pmatrix} \boldsymbol{M}_1^{(1)} \\ \boldsymbol{N}_1^{(2)} \end{pmatrix}, \dots, \begin{pmatrix} \boldsymbol{M}_{\mathfrak{r}}^{(1)} \\ \boldsymbol{N}_{\mathfrak{r}}^{(2)} \end{pmatrix}, \begin{pmatrix} \boldsymbol{0} \\ \boldsymbol{N}_{\mathfrak{r}+1}^{(2)} \end{pmatrix}, \dots, \begin{pmatrix} \boldsymbol{0} \\ \boldsymbol{N}_{\mathfrak{m}^{(2)}}^{(2)} \end{pmatrix} \right\}, \quad (3.45)$$

where it should be noted that, in contrast to the corresponding saddle point system (3.28), the number of dof of the overall system is reduced by the dimension $\mathfrak{l}$ of the multiplier space.

Remark 3.2.3. *Eq.* (3.41) *determines the solution of the least squares problem: for a given* $\bar{\boldsymbol{v}}_1^{(2)} \in \mathbb{R}^{\mathfrak{r}}$*, find* $\bar{\boldsymbol{v}}_1^{(1)} \in \mathbb{R}^{\mathfrak{l}}$*, such that*

$$\|\boldsymbol{C}^{(1)}\bar{\boldsymbol{v}}_1^{(1)} - \boldsymbol{C}^{(2)}\bar{\boldsymbol{v}}_1^{(2)}\|^2 = \min_{\bar{\boldsymbol{w}}\in\mathbb{R}^{\mathfrak{l}}} \|\boldsymbol{C}^{(1)}\bar{\boldsymbol{w}} - \boldsymbol{C}^{(2)}\bar{\boldsymbol{v}}^{(2)}\|^2. \quad (3.46)$$

Furthermore, due to the structure of the matrices involved, the solution can be interpreted as a solution of a weighted least square problem with weighting matrix $\sqrt{\boldsymbol{D}}$*. In the case of unique weights* $w_k = w \in \mathbb{R}_{>0}$ *and* $\mathfrak{h} = 1$*, the solution further suffices*

$$\|\boldsymbol{B}^{(1)}\bar{\boldsymbol{v}}_1^{(1)} - \boldsymbol{B}^{(2)}\bar{\boldsymbol{v}}_1^{(2)}\|^2 = \min_{\bar{\boldsymbol{w}}\in\mathbb{R}^{\mathfrak{l}}} \|\boldsymbol{B}^{(1)}\bar{\boldsymbol{w}} - \boldsymbol{B}^{(2)}\bar{\boldsymbol{v}}^{(2)}\|^2. \quad (3.47)$$

In this case, it could be interpreted as a pointwise least square optimization of the coupling conditions at the quadrature points.

Example: To illustrate the construction of a constrained basis, we consider a 2-patch situation where the computational domain $\Omega = (0,2)\times(0,1)$ consists of the patches $\Omega^{(1)} = (0,1)^2$ and $\Omega^{(2)} = (1,2)\times(0,1)$ on which a C^1-continuous scalar field is to be approximated. The biquadratic, $\boldsymbol{p}^{(i)} = (2,2)$, $i = 1,2$, B-spline basis functions corresponding to the left and right patch are defined through the knot vectors

$$\Theta^{1,(1)} = (0,0,0,1,1,1), \quad \Theta^{2,(1)} = (0,0,0,0.5,1,1,1), \quad (3.48)$$

$$\Theta^{1,(2)} = (1,1,1,2,2,2), \quad \Theta^{2,(2)} = (0,0,0,1,1,1), \quad (3.49)$$

such that the left patch ($\Omega^{(1)}$, slave) consists of two elements and the right patch ($\Omega^{(2)}$, master) of one element. For the sake of clarity, we deviate here from Assumption 2.1.1 and assume that the parameter spaces and the physical spaces are equal, i.e. the corresponding NURBS parametrisations $\boldsymbol{\mathcal{G}}^{(i)}\colon \hat{\Omega}^{(i)} \to \Omega^{(i)}$, $i = 1,2$, are the identities. For the evaluation of the coupling integrals, we use an element-based integration scheme with a Monte Carlo quadrature rule on the slave side with 20 equidistant distributed quadrature points, such that the coupling conditions correspond to the least square problem (3.47).

Figure 3.6 shows the initial basis functions and the basis functions of the constrained spaces, both plotted over the parameter space. As can be seen in the left image, the values as well as the derivatives of the initial bases do not match at the interface $\Gamma = \{1\}\times(0,1)$. The right image, on the other hand, shows a smooth transition of the basis functions of

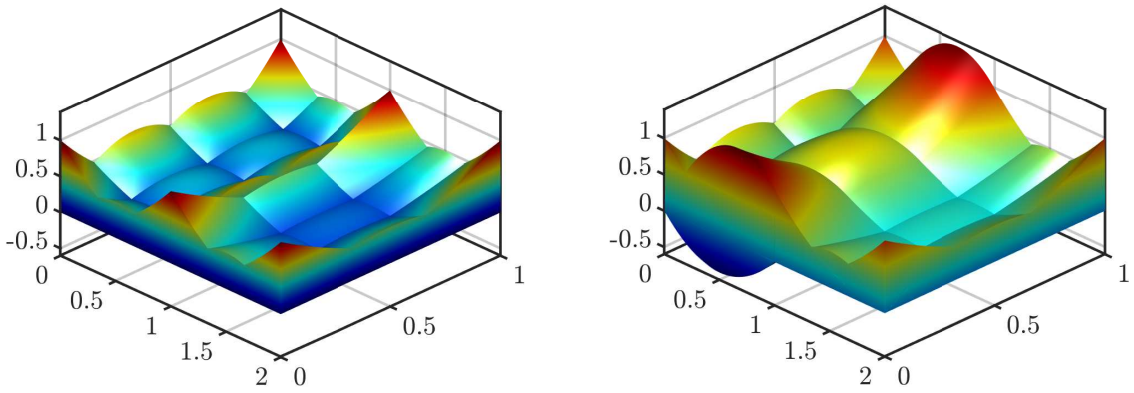

Figure 3.6: Initial basis functions (left) and basis functions of the constrained space (right). Both are plotted over the parameter space.

the corresponding constrained space. Eventually, in Figure 3.7, the six modified functions whose supports are contained in both patches are shown individually.

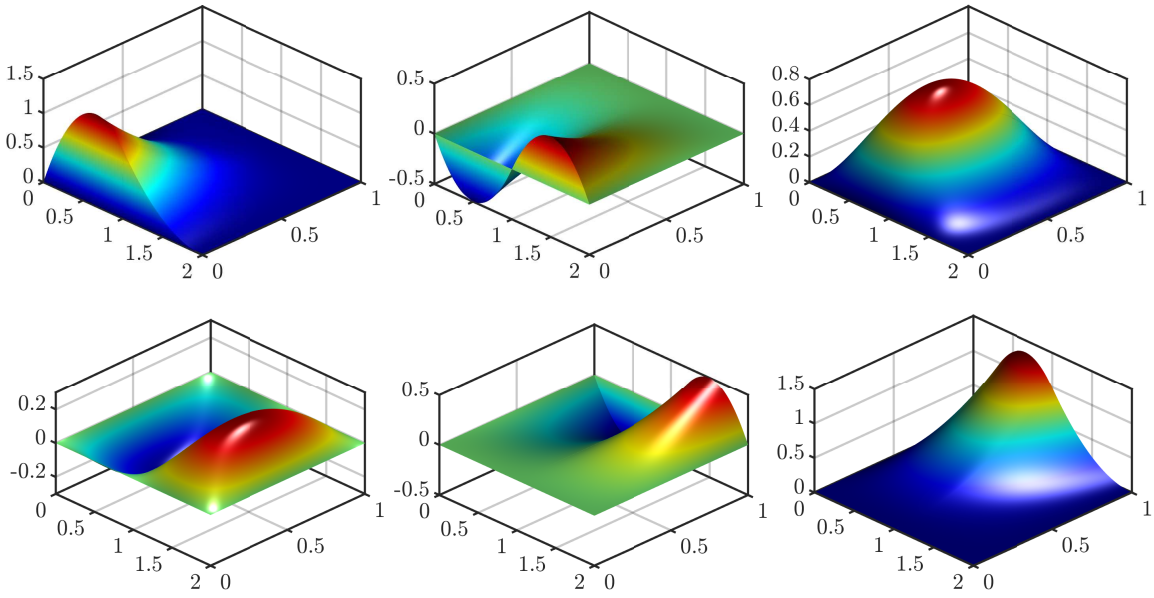

Figure 3.7: Modified basis functions of the constrained space plotted over the parameter space.

3.3 Numerical studies

In this section, we consider two-dimensional settings in order to study the effects of the weighting parameter $\mathfrak{h}$ introduced in Section 3.1.2 and crosspoint modifications as discussed in Section 3.2.2. Therefore we employ polyharmonic equations up to sixth

order, naturally requiring weak C^n couplings up to second order. Here we limit ourselves to the description of the respective problems and refer, e.g., to [104, 105, 113, 160] for more details on this topic. Corresponding convergence studies in case of weak G^1 coupling conditions in the framework of Kirchhoff–Love shells can further be found in Section 4.7.

For $s \in \{1, 2, 3\}$, we consider the following boundary value problems on the domain $\Omega = (0, 2\pi)^2$: for given data $f\colon \Omega \to \mathbb{R}$, find $v\colon \bar{\Omega} \to \mathbb{R}$ such that

$$\Delta^s v = f, \text{ in } \Omega, \quad \left\{ \begin{array}{cc} v = 0, & \text{if } s = 1, \\ v = 0,\ \nabla v \cdot \boldsymbol{n} = 0, & \text{if } s = 2, \\ v = 0,\ \nabla v \cdot \boldsymbol{n} = 0,\ \Delta u = 0, & \text{if } s = 3 \end{array} \right\}, \text{ on } \partial\Omega, \tag{3.50}$$

where $\boldsymbol{n}$ denotes the unique outward normal of Ω and Δ^s the s-times application of the Laplace operator. In all cases, the right-hand side f is manufactured so that the solution is given by

$$v(x, y) = p(x)\cos(x)p(y)\cos(y), \tag{3.51}$$

where $p\colon \bar{\Omega} \to \mathbb{R}$ is a sufficiently smooth piecewise polynomial function defined by

$$p(x) = \begin{cases} x^6 q_1(x), & \text{if } x \in [0, \pi/2), \\ 1, & \text{if } x \in [\pi/2, 3\pi/2), \\ (x - 2\pi)^6 q_2(x), & \text{if } x \in [3\pi/2, 2\pi], \end{cases} \tag{3.52}$$

which ensures that the homogeneous boundary conditions are satisfied, see Figure 3.8 for illustration and Table 3.3 for the specification of q_i.

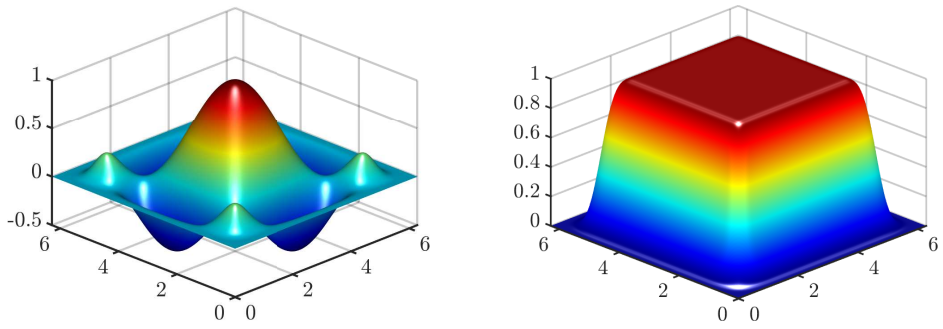

Figure 3.8: Solution v (left) and piecewise polynomial p (right).

To investigate different coupling situations, we assume a decomposition of the domain to be given by $\bar{\Omega} = \bar{\Omega}^{(1)} \cup \bar{\Omega}^{(2)}$ with $\Omega^{(1)} = (0, 2\pi) \times (0, \pi)$, $\Omega^{(2)} = (0, 2\pi) \times (\pi, 2\pi)$, such that we obtain the common interface $\Gamma = (0, 2\pi) \times \{\pi\}$ and two crosspoints $\mathfrak{C} = \{(0, \pi)^{\mathrm{T}}, (2\pi, \pi)^{\mathrm{T}}\}$. Furthermore, we specify $\Omega^{(1)}$ and $\Omega^{(2)}$ as the slave and master side, respectively, and introduce for $s \in \{1, 2, 3\}$ on each patch suitable spaces of trial and test functions $\mathcal{S}_s^{(i)}$, $\mathcal{V}_s^{(i)}$, $i = 1, 2$. Thus, the corresponding (uncoupled) weak problems read:

Table 3.3: Coefficients of the polynomials $q_i(x) = \sum_{j=0}^{6} q_j^i x^j$ introduced in Eq. (3.52).

	q_0^i	q_1^i	q_2^i	q_3^i	q_4^i	q_5^i	q_6^i
$i=1$	$\frac{11195}{182}$	$-\frac{11882}{59}$	$\frac{12901}{46}$	$-\frac{10792}{51}$	$\frac{4001}{44}$	$-\frac{7915}{376}$	$\frac{907}{443}$
$i=2$	$\frac{284017}{15}$	$-\frac{123697}{5}$	$\frac{256110}{19}$	$-\frac{113695}{29}$	$\frac{19261}{30}$	$-\frac{7915}{141}$	$\frac{907}{443}$

find $v = (v^{(1)}, v^{(2)}) \in \mathcal{S}_s = \mathcal{S}_s^{(1)} \times \mathcal{S}_s^{(2)}$ such that for all $\delta v = (\delta v^{(1)}, \delta v^{(2)}) \in \mathcal{V}_s = \mathcal{V}_s^{(1)} \times \mathcal{V}_s^{(2)}$ it holds $\mathrm{V}_s(v, \delta v) = \sum_{i=1}^{2} \mathrm{V}_s^{(i)}(v^{(i)}, \delta v^{(i)}) = 0$, where

$$\mathrm{V}_s^{(i)}(v^{(i)}, \delta v^{(i)}) = \begin{cases} -\langle \nabla v^{(i)}, \nabla \delta v^{(i)} \rangle_{\Omega^{(i)}} - \langle f, \delta v^{(i)} \rangle_{\Omega^{(i)}}, & \text{if } s = 1, \\ \langle \Delta v^{(i)}, \Delta \delta v^{(i)} \rangle_{\Omega^{(i)}} - \langle f, \delta v^{(i)} \rangle_{\Omega^{(i)}}, & \text{if } s = 2, \\ -\langle \nabla \Delta v^{(i)}, \nabla \Delta \delta v^{(i)} \rangle_{\Omega^{(i)}} - \langle f, \delta v^{(i)} \rangle_{\Omega^{(i)}}, & \text{if } s = 3, \end{cases} \tag{3.53}$$

$i = 1, 2$. According to the respective problem, we demand weak C^{s-1} coupling conditions represented by $\mathrm{B}_s \colon \mathcal{S}_s \times \mathcal{M}_s \to \mathbb{R}$, $\mathrm{B}_s(v, \lambda) = \sum_{i=0}^{s-1} \tilde{\mathrm{B}}_i(v, \lambda)$,

$$\begin{aligned} &\tilde{\mathrm{B}}_0(v, \lambda) = \langle v^{(1)} - v^{(2)}, \lambda \rangle_\Gamma, \quad \tilde{\mathrm{B}}_1(v, \lambda) = \mathfrak{h} \sum_{i=1}^{2} (\langle \partial_i (v^{(1)} - v^{(2)}), \partial_i \lambda \rangle_\Gamma, \\ &\tilde{\mathrm{B}}_2(v, \lambda) = \mathfrak{h}^2 \sum_{i=1}^{2} \sum_{j=1}^{i} \langle \partial_i \partial_j (v^{(1)} - v^{(2)}), \partial_i \partial_j \lambda \rangle_\Gamma, \end{aligned} \tag{3.54}$$

where the Lagrange multiplier spaces $\mathcal{M}_s$ are defined, according to Eq. (3.22), as the trace space associated with the slave side and the mortar integrals are evaluated using an element-based integration scheme with a 10-point Gaussian quadrature rule. The respective coupling conditions are enforced using saddle point formulations. In order to investigate the influence of the weighting parameter $\mathfrak{h}$ and the two types of crosspoint modification, we consider the following six settings:

- *fcm*: full modification, $\mathfrak{h} = 1$.
- *fcmh*: full modification, $\mathfrak{h} = h^2$.
- *rcm*: reduced modification, $\mathfrak{h} = 1$.
- *rcmh*: reduced modification, $\mathfrak{h} = h^2$.
- *ncm*: no modification, $\mathfrak{h} = 1$.
- *ncmh*: no modification, $\mathfrak{h} = h^2$.

I.e., in one part of the settings a weighting of the various coupling conditions is omitted, while in the other part the weighting parameter is associated with the mesh size h. Note that in the case of a C^0 coupling, the parameter does not matter and the full crosspoint modification is the same as the reduced one, so that the settings *fcm*, *fcmh*, *rcm*, *rcmh* and *ncm*, *ncmh* match, respectively. In addition, for each setting we consider a corresponding 1-patch situation (1*patch*) for comparison and use B-splines of equal degree in each parametric direction for the approximation. Regarding the meshes, we start in a 1-patch situation with a resolution of 16×16 elements and in a 2-patch situation with a resolution of 17×8 and 16×8 elements on the slave and master sides, respectively, and double the number in each refinement step.

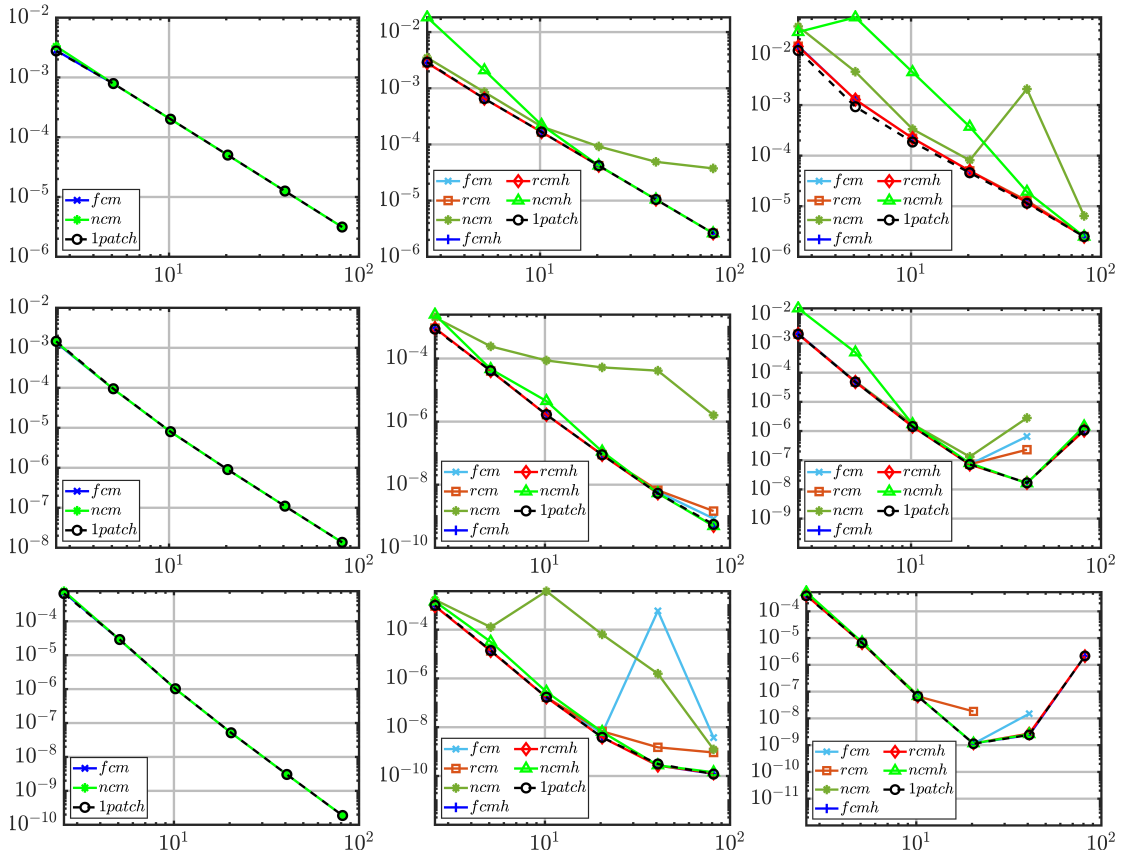

Figure 3.9: Relative L^2 error $\|v - v_\mathrm{h}\|_{L^2(\Omega)}/(2\pi)^2$ as a function of the inverse mesh size h^{-1}. First column: $s = 1$, $p = 1, 2, 3$ (always from top to bottom); second column: $s = 2$, $p = 2, 3, 4$; third column: $s = 3$, $p = 3, 4, 5$.

A numerical error study of the primal solutions of the harmonic ($s = 1$), biharmonic ($s = 2$) and triharmonic ($s = 3$) equation is provided in Figure 3.9 for different spline degrees. In the case of the harmonic problem, the results with modified multiplier as well as the results without crosspoint modification coincide with the 1-patch solution, whereas the situation is different for the bi- and triharmonic problems. Regarding the biharmonic problem, especially *ncm* shows a poor approximation property. Furthermore, an unstable behaviour of fcm with degree $p = 4$ and a decrease of the approximation order of rcm with increasing spline degree can be observed compared to the 1-patch situation at a certain refinement level. In the case of the triharmonic problem, the convergence behaviour of the two settings without crosspoint modifications are significantly different from the 1-patch solution. The triharmonic problem is further characterised by an ill-conditioning of the associated linear systems, which for any setting for $p = 4, 5$ leads to an increase in the errors at a certain refinement level. Moreover, due to the poor conditioning, the systems of fcm, rcm and ncm could be solved at $p = 4$ only up to the fifth refinement level, whereas at $p = 5$ the system of fcm could be solved only up to the fifth level, the system of rcm up to the fourth level and the system of ncm up to the third level. In this context, a solution was considered invalid if the residual in the insertion test exceeded

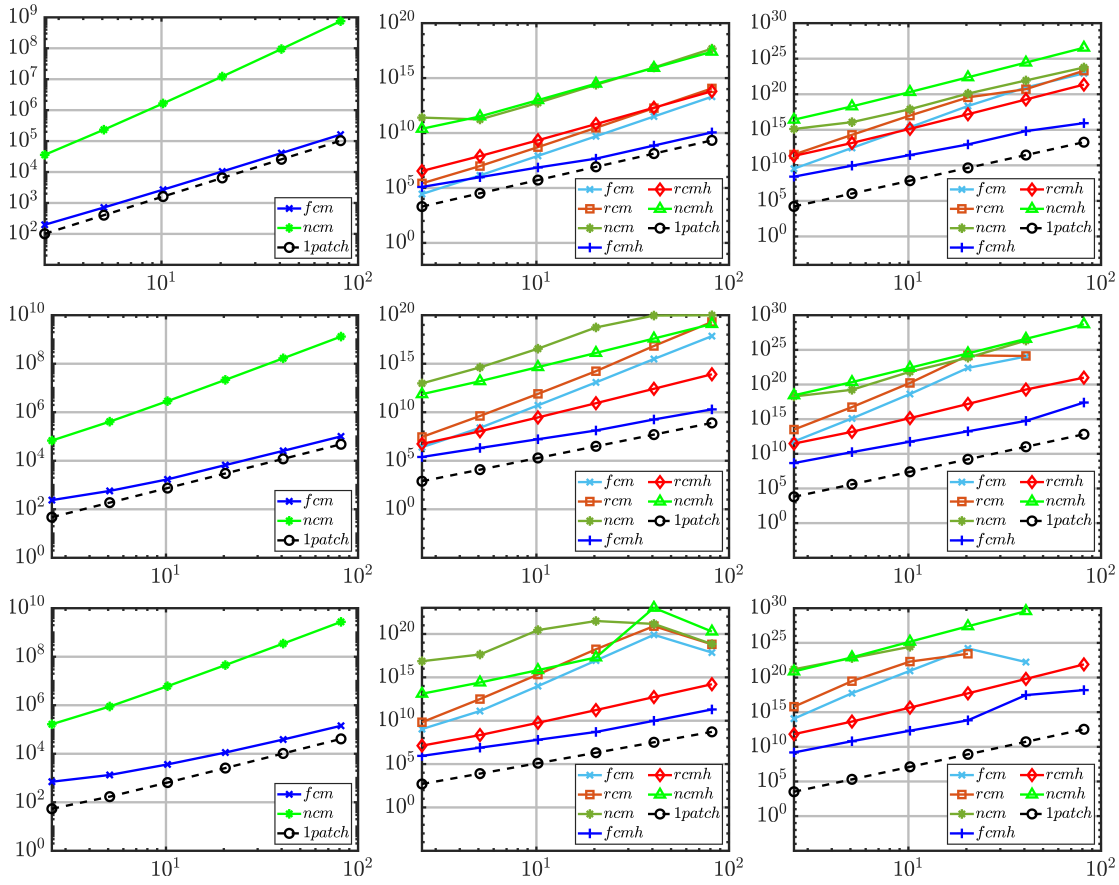

Figure 3.10: Condition number as a function of the inverse mesh size h^{-1}. First column: $s = 1$, $p = 1, 2, 3$ (always from top to bottom); second column: $s = 2$, $p = 2, 3, 4$; third column: $s = 3$, $p = 3, 4, 5$.

0.005. These observations motivated us to have a closer look at the condition numbers of the associated linear systems of each settings.

The evolution of the condition number as a function of the inverse mesh size corresponding to the error plots in Figure 3.9 is shown in Figure 3.10. It can be seen that the condition numbers of the 2-patch systems are greater than those of the 1-patch system in each case, whereby of the 2-patch systems $fcmh$ always has the lowest condition number, followed by $rcmh$. As the refinement level increases, the increase in the condition numbers of $fcmh$ and $rcmh$ is comparable to that of $1patch$, while the increase of the other 2-patch systems is mostly significantly larger. It is noteworthy that in some cases, e.g. $(s, p) = (1, 3)$ or $(s, p) = (2, 3)$, the curve of $1patch$ even shows a greater slope than that of $fcmh$. Moreover, it should be noted that neither the use of a mesh-dependent weighting parameter nor the application of a crosspoint modification alone leads to a lower increase in the condition number, but only the use of both procedures. As for the condition number, we were also interested in the difference between the two methods of implementing the coupling conditions. Here it has been shown that the condition number behaves much better when constrained spaces are used. For example, the condition

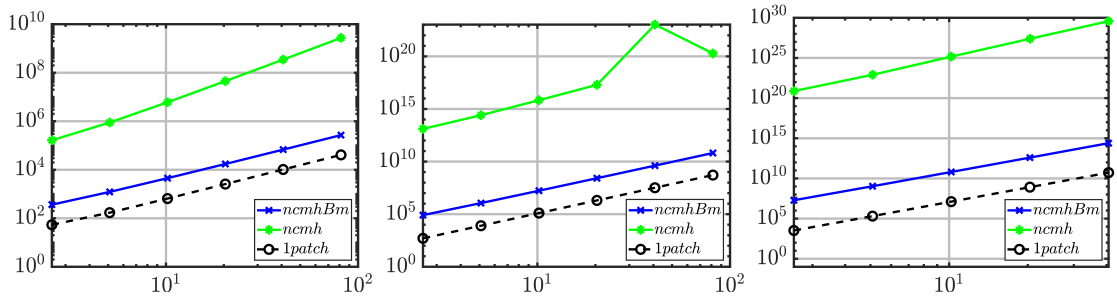

Figure 3.11: Condition number as a function of the inverse mesh size h^{-1} using constrained spaces and a saddle point formulation corresponding to $(s,p) = (1,3),(2,4),(3,5)$ (from left to right).

numbers corresponding to *ncmh* using constrained spaces (called *ncmhBm*) and a saddle point formulation are shown in Figure 3.11.

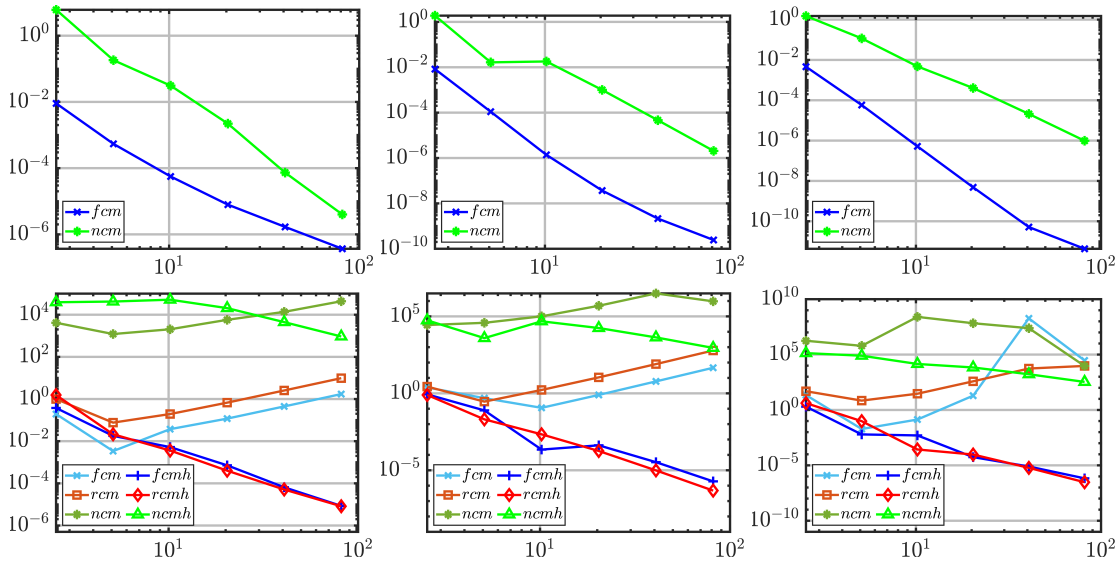

Figure 3.12: Relative L^2 error $\|\lambda - \lambda_h\|_{L^2(\Gamma)}/(2\pi)$ as a function of the inverse mesh size h^{-1}. First row: $s = 1$, $p = 1,2,3$ (always from left to right); second row: $s = 2$, $p = 2,3,4$.

In the case of the harmonic equation, it is well known that the Lagrange multiplier used to enforce the weak C^0 coupling corresponds to the primal fields via $\lambda = \nabla v^{(1)} \cdot \boldsymbol{n}^{(1)} = -\nabla v^{(2)} \cdot \boldsymbol{n}^{(2)}$, which can be immediately justified by a comparison with the boundary integrals representing the natural conditions of the problem. Analogous considerations lead in the case of the bi- and triharmonic problem to the assumption $\lambda = \nabla\Delta v^{(1)} \cdot \boldsymbol{n}^{(1)} = -\nabla\Delta v^{(2)} \cdot \boldsymbol{n}^{(2)}$ and $\lambda = \nabla\Delta^2 v^{(1)} \cdot \boldsymbol{n}^{(1)} = -\nabla\Delta^2 v^{(2)} \cdot \boldsymbol{n}^{(2)}$, respectively, which, however, can be justified by a further comparison of the boundary integrals only under additional conditions. In the case of the biharmonic equation, the solution of the problem must

additionally satisfy the condition

$$\nabla[\nabla\Delta v^{(1)} \cdot \boldsymbol{n}^{(1)}] = -\Delta v^{(1)}\boldsymbol{n}^{(1)} = \Delta v^{(2)}\boldsymbol{n}^{(2)}, \tag{3.55}$$

while in the case of the triharmonic problem even the space of the test functions is subject to certain restrictions, so that the postulated assumption is hardly justified. However, in order to investigate at least the convergence behaviour of the dual field concerning the biharmonic problem, the interface in the example is chosen in such a way that condition (3.55) is fulfilled. A numerical error study of the dual solutions of the harmonic and biharmonic problem is provided in Figure 3.12. In contrast to the primal solution, there are significant differences in the results of the different settings for both problems. In the case of the harmonic equation, the order of convergence of ncm, compared to the order of fcm, decreases with increasing spline degree. Here, convergence can only be observed in the two settings with crosspoint modification and mesh-dependent weighting parameter $\mathfrak{h}$.

Remark 3.3.1. *The simulations here and in the following sections have all been carried out using ESRA. This is a research code for IGA and FEM simulations developed at the Chair of Computational Mechanics at the University of Siegen under the direction of Prof. C. Hesch. The code is largely written in MATLAB, with the use of various C++ routines for performance enhancement at critical points.*

4 Elasticity

As a first example of the application of the extended mortar method, let us consider the problem of elasticity. In this context, we investigate a standard continuum model requiring weak C^0 couplings, as well as a continuum-degenerate model in the framework of the Kirchhoff-Love shell theory requiring weak G^1-continuous couplings. For this purpose, we first summarize the necessary terminology and the basics of continuum mechanics in Sections 4.1-4.5. Thereby, Section 4.1 deals with configurations and motions, Section 4.2 with the use of curvilinear coordinates, Section 4.3 with deformations and strain tensors and Section 4.4 with the notion of hyperelasticity. Eventually, in Section 4.5, the principle of virtual work for a general three-dimensional continuum in terms of material and curvilinear coordinates is formulated and a corresponding multi-patch framework is derived. Based on these fundamentals, we summarize the basics of the Kirchhoff–Love shell theory in Section 4.6 and conclude with some numerical studies in Section 4.7. For additional information on the subject of this chapter, we refer, e.g., to [37, 38, 97, 122, 123]. Regarding the notation, in this chapter we make use of the Einstein summation convention, i.e. whenever an index is repeated in the same term, a summation over the range of this index is implied unless otherwise indicated.

4.1 Configurations and motions of continuum bodies

4.1.1 Configurations.

We consider a continuum body $\mathcal{B}$ which is embedded in the three-dimensional Euclidean space $\mathbb{R}^3$. Therefore, we introduce a right-handed Cartesian coordinate system with fixed origin $\boldsymbol{O}$ and orthonormal basis vectors $\boldsymbol{e}_i$, $i = 1, 2, 3$. As $\mathcal{B}$ moves in space from one point in time to another, it occupies a continuous sequence of (open) geometrical regions $\Omega_t \subset \mathbb{R}^3$, $t \in I = [0, \tau] \subset \mathbb{R}_{\geq 0}$, called configurations of $\mathcal{B}$ at time t. For each configuration, we assume the existence of a suitable regular bijection $\boldsymbol{\kappa}_t \colon \mathcal{B} \to \Omega_t$, $\mathrm{P} \mapsto \boldsymbol{\kappa}_t(\mathrm{P})$, such that the position of a particle $\mathrm{P} \in \mathcal{B}$ at time t is determined by its corresponding position vector $\boldsymbol{x} \in \mathbb{R}^3$, i.e. $\boldsymbol{\kappa}_t(\mathrm{P}) = \boldsymbol{x}$. Following Holzapfel [97], we agree that the initial configuration Ω_0 coincides with the reference configuration* and we make use of upper case letters to mark mathematical objects assigned to Ω_0. In the case $t > 0$, we call Ω_t current configuration at time t (or simply current configuration if confusions are excluded) and make use of lower case letters to mark mathematical objects assigned to Ω_t. For example,

*I.e., at time $t = 0$ the body is supposed to be unloaded, undeformed and unstressed.

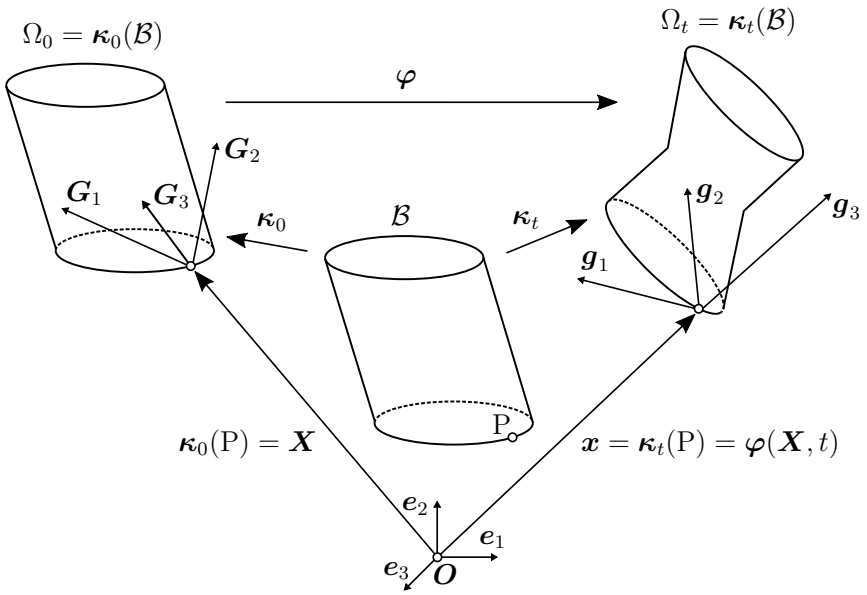

Figure 4.1: Reference and current configuration of a continuum body $\mathcal{B}$.

the position vector $\boldsymbol{X} = \boldsymbol{\kappa}_0(\mathrm{P})$ of a typical point $\mathrm{P} \in \mathcal{B}$ is denoted in terms of coordinates by $\boldsymbol{X} = X_i \boldsymbol{e}_i$, where we refer to X_i as Lagrangian (or material) coordinates. On the other hand, we denote the position vector $\boldsymbol{x} = \boldsymbol{\kappa}_t(\mathrm{P})$ corresponding to the actual configuration by $\boldsymbol{x} = x_i \boldsymbol{e}_i$, where we call x_i Euler (or spatial) coordinates. The geometric quantities introduced here and below are illustrated in Figure 4.1.

4.1.2 Motions.

Starting from a family of configurations $\{\boldsymbol{\kappa}_t\}_{t \in I}$, the motion $\boldsymbol{\varphi} \colon \Omega_0 \times I \to \mathbb{R}^3$ of a body $\mathcal{B}$ is defined as $(\boldsymbol{X}, t) \mapsto \boldsymbol{\varphi}(\boldsymbol{X}, t) = \boldsymbol{\kappa}_t(\boldsymbol{\kappa}_0^{-1}(\boldsymbol{X}))$. For all fixed $t \in I$, $\boldsymbol{\varphi}(\cdot, t) \colon \Omega_0 \to \Omega_t$ is a one-to-one mapping from the reference configuration to the current configuration and its inverse $\boldsymbol{\varphi}^{-1}(\cdot, t) \colon \Omega_t \to \Omega_0$ is given by $\boldsymbol{x} \mapsto \boldsymbol{\varphi}^{-1}(\boldsymbol{x}, t) = \boldsymbol{\kappa}_0(\boldsymbol{\kappa}_t^{-1}(\boldsymbol{x}))$. In the following, we tacitly assume that $\boldsymbol{\varphi}$ is suitable regular, where we make use of the regularity definition stated in Marsden & Hughes [122]†.

Definition 4.1.1. *A motion $\boldsymbol{\varphi} \colon \Omega_0 \times I \to \mathbb{R}^3$ is called C^r regular, if $\boldsymbol{\varphi} \in C^r(\Omega_0 \times I)$ and $\boldsymbol{\varphi}^{-1}(\cdot, t) \in C^r(\Omega_t)$ for all $t \in I$.*

Moreover, we define the material and spatial gradient $\nabla_{\boldsymbol{X}}$ and $\nabla_{\boldsymbol{x}}$ of functions $\boldsymbol{H} \colon \Omega_0 \to \mathbb{R}^3$ and $\boldsymbol{h} \colon \Omega_t \to \mathbb{R}^3$ $(t > 0)$, respectively, through

$$\nabla_{\boldsymbol{X}} \boldsymbol{H} = \frac{\partial \boldsymbol{H}}{\partial X_j} \otimes \boldsymbol{e}_j = \frac{\partial H_i}{\partial X_j} \, \boldsymbol{e}_i \otimes \boldsymbol{e}_j, \quad \nabla_{\boldsymbol{x}} \boldsymbol{h} = \frac{\partial \boldsymbol{h}}{\partial x_j} \otimes \boldsymbol{e}_j = \frac{\partial h_i}{\partial x_j} \, \boldsymbol{e}_i \otimes \boldsymbol{e}_j, \tag{4.1}$$

†Since we a priory assume that the configuration mappings $\boldsymbol{\kappa}_t$ are invertible, our regularity definition slightly differs from the definition stated in [122] .

where H_i, h_i are the Cartesian components of $\boldsymbol{H}$, $\boldsymbol{h}$ and introduce the Jacobian

$$\mathrm{J}(\boldsymbol{X},t) := \det \nabla_{\boldsymbol{X}} \boldsymbol{\varphi}(\boldsymbol{X},t). \tag{4.2}$$

Due to the assumed regularity of $\boldsymbol{\varphi}$, $\nabla_{\boldsymbol{X}}\boldsymbol{\varphi}$ is invertible for all $(\boldsymbol{X},t) \in \Omega_0 \times I$ and it holds $(\nabla_{\boldsymbol{X}}\boldsymbol{\varphi}(\boldsymbol{X},t))^{-1} = \nabla_{\boldsymbol{x}}\boldsymbol{\varphi}^{-1}(\boldsymbol{\varphi}(\boldsymbol{X},t),t)$, [112]. This particularly yields $\mathrm{J}(\boldsymbol{X},t) \neq 0$ for all $(\boldsymbol{X},t) \in \Omega_0 \times I$. In the following we additionally demand $\mathrm{J}(\boldsymbol{X},t) > 0$ for all $(\boldsymbol{X},t) \in \Omega_0 \times I$ to exclude a self-penetration of the body during the deformation process described by $\boldsymbol{\varphi}$.

4.2 Curvilinear coordinates and metric properties

According to the isomorphic relationship between a vector and its coordinates, we can identify them with each other and express the motion of $\mathcal{B}$ and its inverse $\boldsymbol{\varphi}^{-1} = (\bar{\varphi}_1, \bar{\varphi}_2, \bar{\varphi}_3)^{\mathrm{T}}$ at time t in terms of (Lagrangian/Euler) coordinates as follows

$$\begin{aligned} x_i = \varphi_i(X_1, X_2, X_3, t), \quad i = 1,2,3 \quad &\rightarrow \quad \boldsymbol{x} = \boldsymbol{\varphi}(X_1, X_2, X_3, t), \\ X_i = \bar{\varphi}_i(x_1, x_2, x_3, t), \quad i = 1,2,3 \quad &\rightarrow \quad \boldsymbol{X} = \boldsymbol{\varphi}^{-1}(x_1, x_2, x_3, t). \end{aligned} \tag{4.3}$$

When studying special bodies such as shells (cf. Section 4.6), plates and rods, it is often preferable to describe the coordinates X_i as functions of three independent parameters ξ_1, ξ_2, ξ_3 resulting in an, in general, convective curvilinear coordinate system. Therefore we introduce a suitable smooth diffeomorphism $\boldsymbol{\Lambda} = (\Lambda_1, \Lambda_2, \Lambda_3)^{\mathrm{T}} \colon \hat{\Omega} \rightarrow \Omega_0$ defined on an open and bounded subset $\hat{\Omega}$ of $\mathbb{R}^3$, which describes the relation between both coordinate systems as follows

$$\begin{aligned} X_i = \Lambda_i(\xi_1, \xi_2, \xi_3), \quad i = 1,2,3 \quad &\rightarrow \quad \boldsymbol{X} = \boldsymbol{\Lambda}(\xi_1, \xi_2, \xi_3), \\ \xi_i = \bar{\Lambda}_i(X_1, X_2, X_3), \quad i = 1,2,3 \quad &\rightarrow \quad \boldsymbol{\xi} = \boldsymbol{\Lambda}^{-1}(X_1, X_2, X_3), \end{aligned} \tag{4.4}$$

where $\boldsymbol{\Lambda}^{-1} = (\bar{\Lambda}_1, \bar{\Lambda}_2, \bar{\Lambda}_3)^{\mathrm{T}}$. According to (4.3) and (4.4), the position of any particle of the body $\mathcal{B}$ is determined in the undeformed state as well as in the deformed state by the same values of the coordinates ξ_i,

$$\begin{aligned} x_i = \varphi_{c,i}(\xi_1, \xi_2, \xi_3, t), \quad i = 1,2,3 \quad &\rightarrow \quad \boldsymbol{x} = \boldsymbol{\varphi}_c(\xi_1, \xi_2, \xi_3, t), \\ \xi_i = \bar{\varphi}_{c,i}(x_1, x_2, x_3, t), \quad i = 1,2,3 \quad &\rightarrow \quad \boldsymbol{\xi} = \boldsymbol{\varphi}_c^{-1}(x_1, x_2, x_3, t), \end{aligned} \tag{4.5}$$

where $\boldsymbol{\varphi}_c(\xi_1, \xi_2, \xi_3, t) := \boldsymbol{\varphi}(\boldsymbol{\Lambda}(\xi_1, \xi_2, \xi_3), t)$ is the motion of the body expressed in terms of the curvilinear coordinates and $\boldsymbol{\varphi}_c^{-1} := (\bar{\varphi}_{c,1}, \bar{\varphi}_{c,2}, \bar{\varphi}_{c,3})^{\mathrm{T}}$, cf. Figure 4.2.

The corresponding covariant basis vectors in the reference and the current configuration are given by the tangent vectors

$$\boldsymbol{G}_i = \frac{\partial \boldsymbol{\Lambda}}{\partial \xi_i} = \frac{\partial \Lambda_j}{\partial \xi_i}\, \boldsymbol{e}_j, \qquad \boldsymbol{g}_i = \frac{\partial \boldsymbol{\varphi}_c}{\partial \xi_i} = \frac{\partial \boldsymbol{\varphi}_{c,j}}{\partial \xi_i}\, \boldsymbol{e}_j, \quad i = 1,2,3, \tag{4.6}$$

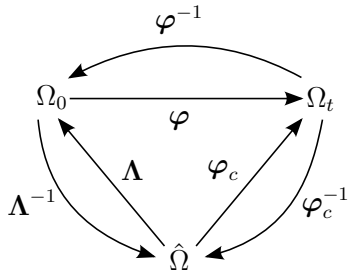

Figure 4.2: Commutative diagram showing the relationships between Ω_0, Ω_t and $\hat{\Omega}$.

and the corresponding contravariant basis vectors $\boldsymbol{G}^i$, $\boldsymbol{g}^i$ are given by

$$\boldsymbol{G}^i = \frac{\partial \bar{\Lambda}_i}{\partial X_j}\,\boldsymbol{e}_j, \qquad \boldsymbol{g}^i = \frac{\partial \bar{\varphi}_{c,i}}{\partial x_j}\,\boldsymbol{e}_j, \quad i = 1,2,3, \tag{4.7}$$

cf. Figure 4.1. Note that the contravariant basis vectors are characterized by the duality relations $\boldsymbol{G}_i \cdot \boldsymbol{G}^j = \delta_{i,j}$ and $\boldsymbol{g}_i \cdot \boldsymbol{g}^j = \delta_{i,j}$, so that the bases $\{\boldsymbol{G}^i\}_{i=1}^3$ and $\{\boldsymbol{g}^i\}_{i=1}^3$ are the dual bases of $\{\boldsymbol{G}_i\}_{i=1}^3$ and $\{\boldsymbol{g}_i\}_{i=1}^3$, respectively. In addition, we introduce the following quantities for further use

$$\begin{aligned} G_{i,j} &:= \boldsymbol{G}_i \cdot \boldsymbol{G}_j, \quad g_{i,j} := \boldsymbol{g}_i \cdot \boldsymbol{g}_j, \\ G^{i,j} &:= \boldsymbol{G}^i \cdot \boldsymbol{G}^j, \quad g^{i,j} := \boldsymbol{g}^i \cdot \boldsymbol{g}^j. \end{aligned} \tag{4.8}$$

The quantities with the same indices represent the squares of the length of the associated basis vectors, where the quantities with different indices represent the product of the length of the associated basis vectors and the cosine of the angle θ between the basis vectors [‡],

$$\|\boldsymbol{G}_i\| = \sqrt{G_{i,i}}, \quad \cos\theta(\boldsymbol{G}_i, \boldsymbol{G}_j) = \frac{G_{i,j}}{\sqrt{G_{i,i}G_{j,j}}}, \quad i,j = 1,2,3 \quad \text{(no summation)}, \tag{4.9}$$

i.e. the quantities determine the geometrical characteristics (the so-called metric) of the associated basis. Furthermore, they link the co- and contravariant basis vectors to each other via the relationships

$$\boldsymbol{G}^i = G^{i,j}\boldsymbol{G}_j, \quad \boldsymbol{G}_i = G_{i,j}\boldsymbol{G}^j, \quad \boldsymbol{g}^i = g^{i,j}\boldsymbol{g}_j, \quad \boldsymbol{g}_i = g_{i,j}\boldsymbol{g}^j, \tag{4.10}$$

from which immediately follows that $[G^{i,j}]_{i,j} = [G_{i,j}]_{i,j}^{-1}$ and $[g^{i,j}]_{i,j} = [g_{i,j}]_{i,j}^{-1}$, respectively. Hence, the quantities (4.8) are customarily referred to as metric coefficients.

Remark 4.2.1. *For simplicity, we will often express the relationships* (4.3)-(4.5) *between the different coordinates in a more compact form, which is common in the mechanics*

[‡]The same holds for the contravariant basis associated with the reference configuration as well as for the covariant and contravariant basis associated with the current configuration.

literature. For example, we indicate the relation (4.3) *between Lagrangian and Euler coordinates simply as follows*

$$x_i = x_i(X_1, X_2, X_3, t), \quad i = 1,2,3 \qquad \rightarrow \quad \boldsymbol{x} = \boldsymbol{x}(X_1, X_2, X_3, t), \tag{4.11a}$$

$$X_i = X_i(x_1, x_2, x_3, t), \quad i = 1,2,3 \qquad \rightarrow \quad \boldsymbol{X} = \boldsymbol{X}(x_1, x_2, x_3, t). \tag{4.11b}$$

Note that in (4.11a) *the symbol x_i appears twice with different meanings. On the right-hand side, x_i represents the function whose arguments are X_i and t, i.e. x_i represents φ_i, while on the left-hand side it represents as usual the ith coordinate of $\boldsymbol{x}$ with respect to the Cartesian coordinate system, i.e. the value of the function $x_i = \varphi_i$. A similar interpretation holds for $\boldsymbol{x}$ in* (4.11a) *and X_i, $\boldsymbol{X}$ in* (4.11b).

4.3 Deformations and strain measures

The deformation gradient $\mathbf{F}$ locally describes the deformation process induced by a motion $\boldsymbol{\varphi}$. Using general convective curvilinear coordinates, $\mathbf{F}$ is defined through the contravariant and covariant basis vectors $\boldsymbol{G}^i$, $\boldsymbol{g}_i$ by

$$\mathbf{F} = \boldsymbol{g}_i \otimes \boldsymbol{G}^i \tag{4.12}$$

and the transposed and inverse of $\mathbf{F}$ are given by

$$\mathbf{F}^{\mathrm{T}} = \boldsymbol{G}^i \otimes \boldsymbol{g}_i, \quad \mathbf{F}^{-1} = \boldsymbol{G}_i \otimes \boldsymbol{g}^i, \quad \mathbf{F}^{-\mathrm{T}} = \boldsymbol{g}^i \otimes \boldsymbol{G}_i, \tag{4.13}$$

cf. Başar & Weichert [12]. Thus, we obtain a relation between the basis vectors corresponding to the reference and the current configuration via $\mathbf{F}$ as follows:

$$\begin{aligned} \boldsymbol{g}_i &= \mathbf{F}\,\boldsymbol{G}_i, & \boldsymbol{G}_i &= \mathbf{F}^{-1}\,\boldsymbol{g}_i, \\ \boldsymbol{g}^i &= \mathbf{F}^{-\mathrm{T}}\,\boldsymbol{G}^i, & \boldsymbol{G}^i &= \mathbf{F}^{\mathrm{T}}\,\boldsymbol{g}^i. \end{aligned} \tag{4.14}$$

So far, we have tacitly assumed that the deformation gradient is invertible. Indeed, according to (4.1), (4.6), (4.7) and (4.12), it holds

$$\mathbf{F} = \frac{\partial x_j}{\partial \xi_i}\frac{\partial \xi_i}{\partial X_k}\,\boldsymbol{e}_j \otimes \boldsymbol{e}_k = \frac{\partial x_j}{\partial X_k}\,\boldsymbol{e}_j \otimes \boldsymbol{e}_k = \frac{\partial \boldsymbol{x}}{\partial \boldsymbol{X}} = \nabla_{\boldsymbol{X}}\boldsymbol{\varphi}, \tag{4.15}$$

ensuring the existence of $\mathbf{F}^{-1}$, cf. Section 4.1. By virtue of (4.15), $\nabla_{\boldsymbol{X}}\boldsymbol{\varphi}$ can alternatively be used to define the deformation gradient if material coordinates X_i are selected for the description of the deformation process. A similar interpretation holds for the spatial gradient $\nabla_{\boldsymbol{x}}\boldsymbol{\varphi}^{-1}$ which characterizes the use of spatial coordinates x_i, since, according to (4.1), (4.6), (4.7) and (4.13),

$$\mathbf{F}^{-1} = \frac{\partial X_j}{\partial \xi_i}\frac{\partial \xi_i}{\partial x_k}\,\boldsymbol{e}_j \otimes \boldsymbol{e}_k = \frac{\partial X_j}{\partial x_k}\,\boldsymbol{e}_j \otimes \boldsymbol{e}_k = \frac{\partial \boldsymbol{X}}{\partial \boldsymbol{x}} = \nabla_{\boldsymbol{x}}\boldsymbol{\varphi}^{-1}. \tag{4.16}$$

The deformation gradient is a generally non-symmetric second order tensor which uniquely describes the deformation of the body. However, it takes into account rigid body motions. Therefore, it can not be used directly as a measure for strains, cf. [25, 150, 168].

Several strain measures are used in continuum mechanics, see, e.g., Ogden [125] for an overview. In this work, we use the right Cauchy–Green strain tensor $\mathbf{C}$ (RCG) and the Green–Lagrange strain strain tensor $\mathbf{E}$ (GL). They are defined through $\mathbf{F}$ and the identity tensor $\mathbf{I}$ by

$$\mathbf{C} = \mathbf{F}^{\mathrm{T}}\,\mathbf{F}, \qquad \mathbf{E} = \frac{1}{2}(\mathbf{F}^{\mathrm{T}}\,\mathbf{F} - \mathbf{I}) = \frac{1}{2}(\mathbf{C} - \mathbf{I}). \tag{4.17}$$

Thus, in consideration of Eqs. (4.8), (4.12), $(4.13)_1$, (4.15), (4.17) and[§]

$$\mathbf{I} = \delta_{i,j}\,\boldsymbol{e}_i \otimes \boldsymbol{e}_j = g_{i,j}\,\boldsymbol{g}^i \otimes \boldsymbol{g}^j = g^{i,j}\,\boldsymbol{g}_i \otimes \boldsymbol{g}_j = G_{i,j}\,\boldsymbol{G}^i \otimes \boldsymbol{G}^j = G^{i,j}\,\boldsymbol{G}_i \otimes \boldsymbol{G}_j, \tag{4.18}$$

the two strain tensors can be expressed in terms of coordinates with respect to the reference configuration as follows

$$\mathbf{C} = \left(\frac{\partial x_k}{\partial X_i}\frac{\partial x_k}{\partial X_j}\right)\boldsymbol{e}_i \otimes \boldsymbol{e}_j = C_{i,j}\,\boldsymbol{G}^i \otimes \boldsymbol{G}^j = C^{i,j}\,\boldsymbol{G}_i \otimes \boldsymbol{G}_j, \tag{4.19}$$

$$\mathbf{E} = \frac{1}{2}\left(\frac{\partial x_k}{\partial X_i}\frac{\partial x_k}{\partial X_j} - \delta_{ij}\right)\boldsymbol{e}_i \otimes \boldsymbol{e}_j = E_{i,j}\boldsymbol{G}^i \otimes \boldsymbol{G}^j = E^{i,j}\,\boldsymbol{G}_i \otimes \boldsymbol{G}_j, \tag{4.20}$$

where the co- and contravariant strain components are given by

$$C_{i,j} = g_{i,j},\ E_{i,j} = \frac{1}{2}(C_{i,j} - G_{i,j}) \quad \text{and} \quad C^{i,j} = G^{i,k}C_{k,l}G^{l,j},\ E^{i,j} = \frac{1}{2}(C^{i,j} - G^{i,j}). \tag{4.21}$$

4.4 Constitutive equations

Constitutive equations describe the relations between strains and stresses via a material law. In this thesis we consider isotropic hyperelastic materials. According to [12, 159], a material is called hyperelastic if there exists an elastic potential function W of the Green–Lagrange strain tensor and the right Cauchy–Green strain tensor, respectively, such that the second Piola–Kirchhoff stress tensor $\mathbf{S}$ (PK2) is determined by

$$\mathbf{S} = \frac{\partial\,\mathrm{W}}{\partial\mathbf{E}} = 2\frac{\partial\,\mathrm{W}}{\partial\mathbf{C}}. \tag{4.22}$$

Note that the second equation in (4.22) holds due to the one to one correspondence $\mathbf{E}(\mathbf{C}) = (\mathbf{C} - \mathbf{I})/2 \;\Leftrightarrow\; \mathbf{C}(\mathbf{E}) = 2\,\mathbf{E} + \mathbf{I}$ and is not part of the definition of hyperelastic materials. In the following, we consider compressible material models and then discuss how such a model can be adapted to describe incompressible materials. Eventually, the elastic potentials used in the numerical investigations in Section 4.7 are summarized.

[§]A proof of (4.18) can be found in Holzapfel [97].

Constitutive laws for compressible isotropic hyperelastic materials. In the case of an isotropic material, the elastic potential can be expressed as a function of the three invariants

$$\mathrm{I}_{\mathbf{C}} = \mathrm{Tr}\,\mathbf{C} = \mathbf{C} : \mathbf{I}, \quad \mathrm{II}_{\mathbf{C}} = \frac{1}{2}\left((\mathrm{Tr}\,\mathbf{C})^2 - \mathrm{Tr}\,\mathbf{C}^2\right), \quad \mathrm{III}_{\mathbf{C}} = \det\mathbf{C} = \mathrm{J}^2 \tag{4.23}$$

of the RCG strain tensor $\mathbf{C}$, Ciarlet [37], and the general constitutive law (4.22) can be rewritten as follows

$$\mathbf{S} = 2\left[(a_{\mathrm{I}} + a_{\mathrm{II}}\mathrm{I}_{\mathbf{C}})\,\mathbf{I} - a_{\mathrm{II}}\,\mathbf{C} + a_{\mathrm{III}}\mathrm{III}_{\mathbf{C}}\,\mathbf{C}^{-1}\right], \tag{4.24}$$

where a_{I}, a_{II} and a_{III} are functions of the invariants of $\mathbf{C}$,

$$a_{\mathrm{I}} = \frac{\partial\,\mathrm{W}}{\partial\mathrm{I}_{\mathbf{C}}}, \qquad a_{\mathrm{II}} = \frac{\partial\,\mathrm{W}}{\partial\mathrm{II}_{\mathbf{C}}}, \qquad a_{\mathrm{III}} = \frac{\partial\,\mathrm{W}}{\partial\mathrm{III}_{\mathbf{C}}}, \tag{4.25}$$

cf. Başar & Weichert [12]. Bearing in mind Eqs. (4.10), (4.18), (4.19) and (4.21), the contravariant stress components with respect to the reference configuration are consequently given by

$$S^{i,j} = 2\left[(a_{\mathrm{I}} + a_{\mathrm{II}}\mathrm{I}_{\mathbf{C}})G^{i,j} - a_{\mathrm{II}}C^{i,j} + a_{\mathrm{III}}\mathrm{III}_{\mathbf{C}}\bar{C}^{i,j}\right], \tag{4.26}$$

where $\bar{C}^{i,j}$ denote the contravariant components of $\mathbf{C}^{-1}$ with respect to the reference configuration. Note that due to $[g^{i,j}]_{i,j} = [g_{i,j}]^{-1}_{i,j}$ and $C_{i,j} = g_{i,j}$ it holds $\bar{C}^{i,j} = g^{i,j}$.

Constitutive laws for incompressible isotropic hyperelastic materials. With slight modifications, the equations in the previous section can be applied to incompressible isotropic hyperelastic materials. According to (4.2) and (4.15) incompressible deformations, also called isochoric (volume preserving), are described by one of the following conditions:

$$\mathrm{J} = \det\mathbf{F} = 1, \quad \mathrm{III}_{\mathbf{C}} = 1. \tag{4.27}$$

Consequently, in this case, the elastic potential W is only expressible in terms of the first two invariants $\mathrm{I}_{\mathbf{C}}$ and $\mathrm{II}_{\mathbf{C}}$, i.e. $\mathrm{W} = \mathrm{W}(\mathrm{I}_{\mathbf{C}}, \mathrm{II}_{\mathbf{C}})$, and the constitutive equation (4.24) reduces to

$$\mathbf{S} = 2\left[(a_{\mathrm{I}} + a_{\mathrm{II}}\mathrm{I}_{\mathbf{C}})\,\mathbf{I} - a_{\mathrm{II}}\,\mathbf{C} + a_{\mathrm{III}}\,\mathbf{C}^{-1}\right], \tag{4.28}$$

where the functions a_{I} and a_{II} are given according to Eq. (4.25). However, the function a_{III} cannot be determined from Eq. (4.25), since the value of the derivative $\partial\,\mathrm{W}/\partial\mathrm{III}_{\mathbf{C}}$ at $\mathrm{III}_{\mathbf{C}} = 1$ is unknown. Consequently, the incompressibility condition (4.27) renders $a_{\mathrm{III}} =: \mathrm{p}$ an unknown variable which corresponds to the hydrostatic pressure. Its determination can be carried out through equilibrium and boundary conditions, see, e.g., Holzapfel [97], Green & Zerna [84], Başar & Ding [10] and Başar & Itskov [11] for more information on this topic. Note that, by setting $\mathrm{J} = 1$ and $\mathrm{III}_{\mathbf{C}} = 1$, the component relation (4.26) still holds in the present case.

Special constitutive models for isotropic hyperelasticity. In this thesis, we make use of Neo-Hookean and Mooney-Rivlin material models given by the elastic potentials

$$\mathrm{W}_1 = \frac{\mu}{2}(\mathrm{I}_{\mathbf{C}} - 3) - \mu \ln(\sqrt{\mathrm{III}_{\mathbf{C}}}) + \frac{\lambda}{2} \ln(\sqrt{\mathrm{III}_{\mathbf{C}}})^2, \tag{4.29}$$

$$\mathrm{W}_2 = \frac{\mu}{2}(\mathrm{I}_{\mathbf{C}} - 3) - p(\sqrt{\mathrm{III}_{\mathbf{C}}} - 1), \tag{4.30}$$

$$\mathrm{W}_3 = \frac{\mu_1}{2}\left(\mathrm{III}_{\mathbf{C}}^{-\frac{1}{3}}\mathrm{I}_{\mathbf{C}} - 3\right) + \frac{\mu_2}{4}\left(\mathrm{III}_{\mathbf{C}} - 1 - 2\ln(\sqrt{\mathrm{III}_{\mathbf{C}}})\right), \tag{4.31}$$

$$\mathrm{W}_4 = \frac{\mu_1}{2}(\mathrm{I}_{\mathbf{C}} - 3) + \frac{\mu_2}{2}(\mathrm{II}_{\mathbf{C}} - 3) - (\mu_1 + 2\mu_2)\ln(\sqrt{\mathrm{III}_{\mathbf{C}}}) + \frac{\lambda}{2}\ln(\sqrt{\mathrm{III}_{\mathbf{C}}})^2, \tag{4.32}$$

where μ, μ_1, μ_2 and λ are material parameters. Thereby, the first three functions describe Neo-Hookean materials and the last one describes a Mooney-Rivlin material. Thus, the functions (4.25) of the different material models are given by:

$$a_{\mathrm{I}}^1 = \frac{\mu}{2}, \qquad a_{\mathrm{II}}^1 = 0, \qquad a_{\mathrm{III}}^1 = \frac{1}{2\mathrm{III}_{\mathbf{C}}}\left(\lambda\ln(\sqrt{\mathrm{III}_{\mathbf{C}}}) - \mu\right), \tag{4.33}$$

$$a_{\mathrm{I}}^2 = \frac{\mu}{2}, \qquad a_{\mathrm{II}}^2 = 0, \qquad a_{\mathrm{III}}^2 = -\frac{p}{2\sqrt{\mathrm{III}_{\mathbf{C}}}}, \tag{4.34}$$

$$a_{\mathrm{I}}^3 = \frac{\mu_1}{2}\mathrm{III}_{\mathbf{C}}^{-\frac{1}{3}} \qquad a_{\mathrm{II}}^3 = 0, \qquad a_{\mathrm{III}}^3 = -\frac{\mu_1}{6}\mathrm{III}_{\mathbf{C}}^{-\frac{4}{3}}\mathrm{I}_{\mathbf{C}} + \frac{\mu_2}{4}\left(1 - \mathrm{III}_{\mathbf{C}}^{-1}\right), \tag{4.35}$$

$$a_{\mathrm{I}}^4 = \frac{\mu_1}{2}, \qquad a_{\mathrm{II}}^4 = \frac{\mu_2}{2}, \qquad a_{\mathrm{III}}^4 = \frac{1}{2\mathrm{III}_{\mathbf{C}}}\left(\lambda\ln(\sqrt{\mathrm{III}_{\mathbf{C}}}) - (\mu_1 + 2\mu_2)\right). \tag{4.36}$$

Furthermore, the elastic potential (4.30) describes an incompressible material, where the incompressibility condition $(\sqrt{\mathrm{III}_{\mathbf{C}}} - 1) = 0$ is enforced via a Lagrange multiplier p, which can be considered as the hydrostatic pressure, [97].

4.5 Equation of motion and multi-patch framework

In this section, we introduce Cauchy's equation of motion and derive a corresponding uncoupled multi-patch framework of the form (3.3), which can be treated with the methods from Chapters 2-3. In the reference configuration, the equation reads

$$\rho_0(\boldsymbol{X})\ddot{\boldsymbol{\varphi}}(\boldsymbol{X},t) = \nabla_{\boldsymbol{X}} \cdot \mathbf{P}(\boldsymbol{X},t) + \boldsymbol{B}(\boldsymbol{X},t) \quad \forall (\boldsymbol{X},t) \in \Omega_0 \times I, \tag{4.37}$$

where $I = [0,\tau]$, ρ_0 denotes the mass density of the reference configuration, $\mathbf{P} := \mathbf{FS}$ the first Piola–Kirchhoff stress tensor (PK1), $\boldsymbol{B}$ a prescribed body force per unit volume and the term $\rho_0\ddot{\boldsymbol{\varphi}}$ describes the inertia force per unit volume. To obtain a complete characterisation of the motion of the body, (4.37) has to be supplemented by appropriate initial and boundary conditions. We specify initial conditions as

$$\boldsymbol{\varphi} = \mathrm{id}_{\Omega_0}, \qquad \dot{\boldsymbol{\varphi}} = \boldsymbol{v} \quad \text{in } \Omega_0 \times \{0\}, \tag{4.38}$$

where id_{Ω_0} is the identity map on Ω_0 and the vector field $\boldsymbol{v}\colon \Omega_0 \to \mathbb{R}^3$ a prescribed initial velocity. With regard to the boundary, we assume essential and natural conditions to be given by

$$\boldsymbol{\varphi} = \bar{\boldsymbol{\varphi}} \quad \text{on } \Gamma_\mathrm{e} \times I \qquad \text{and} \qquad \mathbf{P}\boldsymbol{N} = \boldsymbol{T} \quad \text{on } \Gamma_\mathrm{n} \times I, \tag{4.39}$$

where $\bar{\boldsymbol{\varphi}}$ is a prescribed motion, $\boldsymbol{N}$ the outer normal vector on Γ_n, $\boldsymbol{T}$ a prescribed surface traction and Γ_e, Γ_n are open subsets of $\partial\Omega_0$ such that $\bar{\Gamma}_\mathrm{e} \cup \bar{\Gamma}_\mathrm{n} = \partial\Omega_0$ and $\Gamma_\mathrm{e} \cap \Gamma_\mathrm{n} = \emptyset$.

Given a multi-patch geometry consisting of patches $\Omega_0^{(1)}, \dots, \Omega_0^{(N)}$, Eqs. (4.38)-(4.39) characterise the motion $\boldsymbol{\varphi}^{(i)}\colon \Omega_0^{(i)} \to \mathbb{R}^3$ of each patch by replacing Ω_0 with $\Omega_0^{(i)}$ and considering the restriction of the functions to $\Omega_0^{(i)}$, i.e.

$$\left\{ \begin{aligned} \rho_0^{(i)} \ddot{\boldsymbol{\varphi}}^{(i)} &= \nabla_{\boldsymbol{X}} \cdot \mathbf{P}^{(i)} + \boldsymbol{B}^{(i)}, && \text{in } \Omega_0^{(i)} \times I, \\ \boldsymbol{\varphi}^{(i)} &= \mathrm{id}_{\Omega_0^{(i)}},\ \dot{\boldsymbol{\varphi}}^{(i)} = \boldsymbol{v}^{(i)}, && \text{in } \Omega_0^{(i)} \times \{0\}, \\ \boldsymbol{\varphi}^{(i)} &= \bar{\boldsymbol{\varphi}}^{(i)} \text{ on } \Gamma_\mathrm{e}^{(i)} \times I, && \mathbf{P}^{(i)}\boldsymbol{N}^{(i)} = \boldsymbol{T}^{(i)} \text{ on } \Gamma_\mathrm{n}^{(i)} \times I, \end{aligned} \right\} \tag{4.40}$$

where $\Gamma_\mathrm{e}^{(i)} := \Gamma_\mathrm{e} \cap \partial\Omega_0^{(i)}$ and $\Gamma_\mathrm{n}^{(i)} := \Gamma_\mathrm{n} \cap \partial\Omega_0^{(i)}$. To derive a variational problem, (4.40) could now be treated within an isogeometric space-time framework by interpreting the initial boundary value problems as pure boundary value problems on a space-time cylinder, cf. Schuß et al. [144]. In this work, however, we use a semi-discretisation scheme in which space and time are treated separately. Therefore, in the first step, we introduce a time grid $0 = t_0 < t_1 < \ldots < t_M = \tau$ and express the problems (4.40) as a sequence of boundary value problems according to Appendix A: for $\nu = 1, \dots, M$ find $\boldsymbol{\varphi}_\nu^{(i)}\colon \bar{\Omega}_0^{(i)} \to \mathbb{R}^3$ such that

$$\left\{ \begin{aligned} \rho_0^{(i)} \mathcal{H}_\nu(\boldsymbol{\varphi}_\nu^{(i)}, \boldsymbol{\varphi}_{\nu-1}^{(i)}, \tilde{\boldsymbol{\varphi}}_{\nu-1}^{(i)}) - [\nabla_{\boldsymbol{X}} \cdot \mathbf{P}^{(i)} + \boldsymbol{B}^{(i)}]_{\nu-1/2} &= \mathbf{0}, \text{ in } \Omega_0^{(i)}, \\ \boldsymbol{\varphi}_\nu^{(i)} = \bar{\boldsymbol{\varphi}}_\nu^{(i)} \text{ on } \Gamma_\mathrm{e}^{(i)}, \quad [\mathbf{P}^{(i)}\boldsymbol{N}^{(i)}]_{\nu-1/2} &= \boldsymbol{T}_{\nu-1/2}^{(i)} \text{ on } \Gamma_\mathrm{n}^{(i)}, \end{aligned} \right\} \tag{4.41}$$

where the step-size is denoted by $h_\nu := t_\nu - t_{\nu-1}$ and the subscripts $[\bullet]_\nu$, $[\bullet]_{\nu-1}$, $[\bullet]_{\nu-1/2}$ indicate the evaluation at the grid points t_ν, $t_{\nu-1}$ and $t_{\nu-1/2} := t_{\nu-1} + h_\nu/2$. Within this notation, $\boldsymbol{\varphi}_\nu^{(i)}$ denotes the function $\boldsymbol{\varphi}_\nu^{(i)}\colon \Omega_0^{(i)} \to \mathbb{R}^3$ defined by $\boldsymbol{\varphi}_\nu^{(i)}(\boldsymbol{X}) = \boldsymbol{\varphi}^{(i)}(\boldsymbol{X}, t_\nu)$ and sums or products of functions inside brackets are to be treated separately, e.g. $[\nabla_{\boldsymbol{X}} \cdot \mathbf{P}^{(i)} + \boldsymbol{B}^{(i)}]_{\nu-1/2} = \nabla_{\boldsymbol{X}} \cdot \mathbf{P}_{\nu-1/2}^{(i)} + \boldsymbol{B}_{\nu-1/2}^{(i)}$. The start functions of the sequence result from the initial conditions, i.e. $\boldsymbol{\varphi}_0^{(i)} = \mathrm{id}_{\Omega_0^{(i)}}$, $\tilde{\boldsymbol{\varphi}}_0^{(i)} = \boldsymbol{v}^{(i)}$, and the approximation of the acceleration is captured by the operator

$$\mathcal{H}_\nu(\boldsymbol{\varphi}_\nu^{(i)}, \boldsymbol{\varphi}_{\nu-1}^{(i)}, \tilde{\boldsymbol{\varphi}}_{\nu-1}^{(i)}) := 2h_\nu^{-1}[h_\nu^{-1}(\boldsymbol{\varphi}_\nu^{(i)} - \boldsymbol{\varphi}_{\nu-1}^{(i)}) - \tilde{\boldsymbol{\varphi}}_{\nu-1}^{(i)}], \tag{4.42}$$

where $\tilde{\boldsymbol{\varphi}}_{\nu-1}^{(i)}$ can be understood as an approximation of the velocity $\dot{\boldsymbol{\varphi}}_{\nu-1}^{(i)}$ and is given in the further course by $\tilde{\boldsymbol{\varphi}}_{\nu-1}^{(i)} := 2h_{\nu-1}^{-1}(\boldsymbol{\varphi}_{\nu-1}^{(i)} - \boldsymbol{\varphi}_{\nu-2}^{(i)}) - \tilde{\boldsymbol{\varphi}}_{\nu-2}^{(i)}$, $\nu = 2, \dots, M$. In order to derive corresponding weak formulations, we now introduce for each time step and patch suitable spaces of admissible solutions $\mathcal{S}_\nu^{(i)}$ and test functions $\mathcal{V}^{(i)}$, such that

$$\mathcal{S}_\nu^{(i)} \subset \left\{ \boldsymbol{\varphi} \in H^1(\Omega_0^{(i)})^3 \,|\, \boldsymbol{\varphi} = \bar{\boldsymbol{\varphi}}^{(i)}(\bullet, t_\nu) \text{ on } \Gamma_\mathrm{e}^{(i)} \right\}, \tag{4.43a}$$

$$\mathcal{V}^{(i)} \subset \left\{ \delta\boldsymbol{\varphi} \in H^1(\Omega_0^{(i)})^3 \,|\, \boldsymbol{\varphi} = \mathbf{0} \text{ on } \Gamma_\mathrm{e}^{(i)} \right\}. \tag{4.43b}$$

The inclusions ensure that the essential boundary conditions are fulfilled, the deformation gradient exists and the integral expressions in the following variational problems exist. How the spaces have to be further specified to ensure the unique solubility of the problems still depends on the properties of the elastic potential defining the material model. Details on this topic can be found in Court & Kunisch [46]. Scalar multiplication of the partial differential equation in (4.41) by an arbitrary test function and subsequent integration yields, after some standard calculations, the following sequence of variational problems: for $\nu = 1, \dots, M$ find $\boldsymbol{\varphi}_\nu^{(i)} \in \mathcal{S}_\nu^{(i)}$, where

$$\begin{aligned} \mathrm{V}_\nu^{(i)}(\boldsymbol{\varphi}_\nu^{(i)}, \delta\boldsymbol{\varphi}^{(i)}) := \langle \rho_0^{(i)} \mathcal{H}_\nu(\boldsymbol{\varphi}_\nu^{(i)}, \boldsymbol{\varphi}_{\nu-1}^{(i)}, \tilde{\boldsymbol{\varphi}}_{\nu-1}^{(i)}) - \boldsymbol{B}_{\nu-\frac{1}{2}}^{(i)}, \delta\boldsymbol{\varphi}^{(i)} \rangle_{\Omega_0^{(i)}} \\ + \langle \mathbf{P}_{\nu-\frac{1}{2}}^{(i)}, \nabla_{\boldsymbol{X}} \delta\boldsymbol{\varphi}^{(i)} \rangle_{\Omega_0^{(i)}} - \langle \boldsymbol{T}_{\nu-\frac{1}{2}}^{(i)}, \delta\boldsymbol{\varphi}^{(i)} \rangle_{\Gamma_{\mathrm{n}}^{(i)}} = 0 \end{aligned} \tag{4.44}$$

for all $\delta\boldsymbol{\varphi}^{(i)} \in \mathcal{V}^{(i)}$, which can be merged into a sequence of global, uncoupled problems by introducing the product spaces $\mathcal{S}_\nu = \prod_{i=1}^N \mathcal{S}_\nu^{(i)}$, $\mathcal{V} = \prod_{i=1}^N \mathcal{V}^{(i)}$ and the functional $\mathrm{V}_\nu \colon \mathcal{S}_\nu \times \mathcal{V} \to \mathbb{R}$, $\mathrm{V}_\nu(\boldsymbol{\varphi}_\nu, \delta\boldsymbol{\varphi}) = \sum_{i=1}^N \mathrm{V}_\nu^{(i)}(\boldsymbol{\varphi}_\nu^{(i)}, \delta\boldsymbol{\varphi}^{(i)})$, according to Section 3.1.1. It should be noted that (4.44) is a semi-discretized version of the principle of virtual work expressed in Lagrangian coordinates. Using arbitrary curvilinear coordinates given by a diffeomorphism $\boldsymbol{\Lambda}^{(i)} \colon \hat{\Omega}^{(i)} \to \Omega_0^{(i)}$, cf. Section 4.2, (4.44) yields a corresponding sequence of variational problems as follows: for $\nu = 1, \dots, M$ find $\boldsymbol{\varphi}_{c,\nu}^{(i)} \in \hat{\mathcal{S}}_\nu^{(i)}$ such that

$$\begin{aligned} \hat{\mathrm{V}}_\nu^{(i)}(\boldsymbol{\varphi}_{c,\nu}^{(i)}, \delta\boldsymbol{\varphi}_c^{(i)}) := \langle \hat{\rho}_0^{(i)} \mathcal{H}_\nu(\boldsymbol{\varphi}_{c,\nu}^{(i)}, \boldsymbol{\varphi}_{c,\nu-1}^{(i)}, \tilde{\boldsymbol{\varphi}}_{c,\nu-1}^{(i)}) - \hat{\boldsymbol{B}}_{\nu-\frac{1}{2}}^{(i)}, \delta\boldsymbol{\varphi}_c^{(i)} \sqrt{G} \rangle_{\hat{\Omega}^{(i)}} \\ + \langle \hat{\mathbf{P}}_{\nu-\frac{1}{2}}^{(i)}, \nabla_{\boldsymbol{\xi}} \delta\boldsymbol{\varphi}_c^{(i)} \sqrt{G} \rangle_{\hat{\Omega}^{(i)}} - \langle \hat{\boldsymbol{T}}_{\nu-\frac{1}{2}}^{(i)}, \delta\boldsymbol{\varphi}_c^{(i)} \sqrt{GQ} \rangle_{\hat{\Gamma}_{\mathrm{n}}^{(i)}} = 0 \end{aligned} \tag{4.45}$$

for all $\delta\boldsymbol{\varphi}_c^{(i)} \in \hat{\mathcal{V}}^{(i)}$, where the spaces of admissible solutions and test functions result from the underlying diffeomorphism and the spaces (4.43) as follows

$$\hat{\mathcal{S}}_\nu^{(i)} = \left\{ \boldsymbol{\varphi}_\nu^{(i)} \circ \boldsymbol{\Lambda}^{(i)} \,|\, \boldsymbol{\varphi}_\nu^{(i)} \in \mathcal{S}_\nu^{(i)} \right\}, \quad \hat{\mathcal{V}}^{(i)} = \left\{ \delta\boldsymbol{\varphi}^{(i)} \circ \boldsymbol{\Lambda}^{(i)} \,|\, \delta\boldsymbol{\varphi}^{(i)} \in \mathcal{V}^{(i)} \right\}. \tag{4.46}$$

Moreover, $\hat{\Gamma}_n \subset \partial\hat{\Omega}$ is defined by $\hat{\Gamma}_n = \boldsymbol{\Lambda}^{-1}(\Gamma_{\mathrm{n}})$, $\nabla_{\boldsymbol{\xi}}(\bullet) := (\partial(\bullet)/\partial\xi_i) \otimes \boldsymbol{G}^i$ is the gradient w.r.t. the curvilinear coordinates, $G := \det[G_{i,j}]_{i,j}$, $Q := \hat{\boldsymbol{N}}^{\mathrm{T}} [G^{i,j}]_{i,j} \hat{\boldsymbol{N}}$ and the symbol $\hat{(\bullet)}$ indicates the change of variables, e.g.

$$\hat{\boldsymbol{N}} = \hat{\boldsymbol{N}}(\boldsymbol{\xi}) := \boldsymbol{N}(\boldsymbol{\Lambda}(\boldsymbol{\xi})), \quad \hat{\boldsymbol{B}}_{\nu-\frac{1}{2}}^{(i)} = \hat{\boldsymbol{B}}_{\nu-\frac{1}{2}}^{(i)}(\boldsymbol{\xi}) := \boldsymbol{B}_{\nu-\frac{1}{2}}^{(i)}(\boldsymbol{\Lambda}(\boldsymbol{\xi})), \tag{4.47}$$

etcetera. More details concerning the derivation of the principle of virtual work in terms of curvilinear coordinates can be found in the textbooks of Ciarlet [38, 39] and Washizu [166].

Remark 4.5.1. *We have considered here the general case of time-dependent quantities. However, the previous considerations also apply to the static case, whereby the representation is considerably simplified. In particular, the application of a time-stepping method*

is omitted. For the static case, we obtain in Lagrangian coordinates for each patch the problem: find $\boldsymbol{\varphi}^{(i)} \in \mathcal{S}^{(i)}$*, such that*

$$\langle \boldsymbol{P}^{(i)}, \nabla_{\boldsymbol{X}} \delta\boldsymbol{\varphi}^{(i)} \rangle_{\Omega_0^{(i)}} - \langle \boldsymbol{B}^{(i)}, \delta\boldsymbol{\varphi}^{(i)} \rangle_{\Omega_0^{(i)}} - \langle \boldsymbol{T}^{(i)}, \delta\boldsymbol{\varphi}^{(i)} \rangle_{\Gamma_{\mathrm{n}}^{(i)}} = 0 \tag{4.48}$$

for all $\delta\boldsymbol{\varphi}^{(i)} \in \mathcal{V}^{(i)}$*, where the space of admissible solutions* $\mathcal{S}^{(i)}$ *coincides with the spaces* $\mathcal{S}_\nu^{(i)}$*. Thereby, it should be noted that the sequence* $\mathcal{S}_\nu^{(i)}$ *is constant in the static case. Accordingly, in curvilinear coordinates the variational problems arise: find* $\boldsymbol{\varphi}_c^{(i)} \in \hat{\mathcal{S}}^{(i)}$ *such that for all* $\delta\boldsymbol{\varphi}_c^{(i)} \in \hat{\mathcal{V}}^{(i)}$ *holds*

$$\langle \hat{\boldsymbol{P}}^{(i)}, \nabla_{\boldsymbol{\xi}} \delta\boldsymbol{\varphi}_c^{(i)} \sqrt{G} \rangle_{\hat{\Omega}^{(i)}} - \langle \hat{\boldsymbol{B}}^{(i)}, \delta\boldsymbol{\varphi}_c^{(i)} \sqrt{G} \rangle_{\hat{\Omega}^{(i)}} - \langle \hat{\boldsymbol{T}}^{(i)}, \delta\boldsymbol{\varphi}_c^{(i)} \sqrt{GQ} \rangle_{\hat{\Gamma}_{\mathrm{n}}^{(i)}} = 0. \tag{4.49}$$

4.6 Kirchhoff–Love shell theory

The Kirchhoff–Love shell theory is a direct approach, i.e. the shell is considered ab initio as a two-dimensional surface and appropriate kinematic assumptions are postulated to represent the three-dimensional behaviour. A comprehensive review of different approaches to shell formulations can be found e.g. in Naghdi [123], Palazotto & Dennis [126] or Ciarlet [38]. The Kirchhoff–Love theory is based on the following hypotheses: (1) the shell is thin, (2) the cross-sections of the shell continuum normal to the middle surface in the reference configuration remain normal to the middle surface in the deformed configuration, (3) the model satisfies the plane stress condition[¶]. The second hypothesis implies that the strain is linear through the thickness and the transverse shear strains are zero, which is a reasonable assumption for thin structures. For shell theories based on the direct approach, normal strains and stresses in through-the-thickness direction are usually not regarded. However, in the case of large strains, the transverse normal strain can not be neglected. Therefore, we use in this work an extended shell formulation for general hyperelastic materials introduced by Kiendl et al. [109]. In the following, the above-stated assumptions are applied to the kinematic, constitutive, and equilibrium equations introduced in the previous sections.

Regarding the notation, throughout this section, Latin indices always take on values from $\{1, 2, 3\}$, while Greek indices only take on values from $\{1, 2\}$. Following this convention, we write, for example, $[g_{\alpha,\beta}]_{\alpha,\beta}$ to address the matrix $[g_{\alpha,\beta}]_{1\leq\alpha,\beta\leq 2}$, while $[g_{i,j}]_{i,j}$ refers to the matrix $[g_{i,j}]_{1\leq i,j\leq 3}$. In addition, it should be noted that according to Einstein's summation convention, sums indexed with Latin indices run from 1 to 3 and sums indexed with Greek letters run from 1 to 2.

4.6.1 Shell-kinematics

Let us assume that the motion of the shell's middle surface is determined via a parametrisation $\boldsymbol{s}\colon [0,1]^2 \times I \to \mathbb{R}^3$, cf. Section 2.1.2. Then, the tangent base vectors $\boldsymbol{a}_\alpha$, $\alpha = 1, 2$,

[¶]In this work we adopt the commonly accepted, although incorrect, use of the term "plane stress" for referring to the state of zero transverse normal stress $S^{33} = 0$.

and the unit normal vector $\boldsymbol{a}_3$ of the surface are obtained by[‖]

$$\boldsymbol{a}_\alpha = \partial_{\xi_\alpha}\boldsymbol{s},\ \alpha = 1,2, \quad \boldsymbol{a}_3 = \frac{\boldsymbol{a}_1 \times \boldsymbol{a}_2}{\|\boldsymbol{a}_1 \times \boldsymbol{a}_2\|}. \tag{4.50}$$

Based on the Kirchhoff hypotheses, the position of a material point in the shell continuum at time t is determined by the motion

$$\boldsymbol{\varphi}_c(\xi_1,\xi_2,\xi_3,t) = \boldsymbol{s}(\xi_1,\xi_2,t) + \xi_3\boldsymbol{a}_3(\xi_1,\xi_2,t), \quad (\xi_1,\xi_2,\xi_3,t) \in [0,1]^2 \times J \times I, \tag{4.51}$$

expressed in curvilinear coordinates defined through $\boldsymbol{\Lambda}\colon \hat{\Omega} := [0,1]^2 \times J \to \Omega_0$,

$$\boldsymbol{\Lambda}(\xi_1,\xi_2,\xi_3) = \boldsymbol{S}(\xi_1,\xi_2) + \xi_3\boldsymbol{A}_3(\xi_1,\xi_2) = \boldsymbol{X}, \tag{4.52}$$

where $J = [-h/2, h/2]$ and h is the shell thickness. According to Section 4.2, the base vectors at an arbitrary point in the actual configuration of the shell continuum are given by

$$\boldsymbol{g}_\alpha = \boldsymbol{a}_\alpha + \xi_3[\partial_{\xi_\alpha}\boldsymbol{a}_3],\ \alpha = 1,2, \quad \boldsymbol{g}_3 = \boldsymbol{a}_3 \tag{4.53}$$

and the corresponding covariant metric coefficients result in

$$g_{\alpha,\beta} = a_{\alpha,\beta} - 2\xi_3 b_{\alpha,\beta} + \xi_3^2[\partial_{\xi_\alpha}\boldsymbol{a}_3]\cdot[\partial_{\xi_\beta}\boldsymbol{a}_3], \quad \alpha,\beta = 1,2, \tag{4.54a}$$

$$g_{\alpha,3} = g_{3,\alpha} = \boldsymbol{a}_\alpha\cdot\boldsymbol{a}_3 + \xi_3[\partial_{\xi_\alpha}\boldsymbol{a}_3]\cdot\boldsymbol{a}_3 = 0, \quad \alpha = 1,2, \tag{4.54b}$$

$$g_{3,3} = a_{3,3} = 1, \tag{4.54c}$$

where $a_{\alpha,\beta}$ and $b_{\alpha,\beta}$ are the covariant metric coefficients and the curvature coefficients of the middle surface, respectively, i.e.

$$a_{\alpha,\beta} = \boldsymbol{a}_\alpha\cdot\boldsymbol{a}_\beta, \quad b_{\alpha,\beta} = -\boldsymbol{a}_\alpha\cdot[\partial_{\xi_\beta}\boldsymbol{a}_3] = -\boldsymbol{a}_\beta\cdot[\partial_{\xi_\alpha}\boldsymbol{a}_3] = [\partial_{\xi_\beta}\boldsymbol{a}_\alpha]\cdot\boldsymbol{a}_3. \tag{4.55}$$

As already mentioned, for thin and moderately thick shells the classical assumption is a linear strain distribution through the thickness, such that the quadratic term with respect to ξ_3 in Eq. (4.54a) can be neglected,

$$g_{\alpha,\beta} = a_{\alpha,\beta} - 2\xi_3 b_{\alpha,\beta}. \tag{4.56}$$

According to Eqs. (4.19) and (4.21), which are valid for a general 3D continuum, the covariant coefficients of the RCG strain tensor are identical to the metric coefficients. Due to the application of the Kirchhoff hypothesis, we have $g_{3,3} \equiv 1$, while $C_{3,3}$ needs to describe the actual thickness deformation. Following Kiendl et al. [109], we therefore represent the RCG strain tensor $\mathbf{C} = C_{i,j}\boldsymbol{G}^i\otimes\boldsymbol{G}^j$ and its inverse $\mathbf{C}^{-1} = \bar{C}^{i,j}\boldsymbol{G}_i\otimes\boldsymbol{G}_j$ with respect to the reference configuration as follows

$$[C_{i,j}]_{i,j} = \begin{pmatrix} g_{1,1} & g_{1,2} & 0 \\ g_{2,1} & g_{2,2} & 0 \\ 0 & 0 & C_{3,3} \end{pmatrix}, \quad [\bar{C}^{i,j}]_{i,j} = [C_{i,j}]^{-1}_{i,j} = \begin{pmatrix} g^{1,1} & g^{1,2} & 0 \\ g^{2,1} & g^{2,2} & 0 \\ 0 & 0 & C^{-1}_{3,3} \end{pmatrix}, \tag{4.57}$$

[‖]Note that the following equations hold analogously for the reference configuration and we make further on use of capital letters to mark objects assigned to it.

where $C_{3,3}$ can be computed from the in-plane metric coefficients in the case of an incompressible material or is determined by the plane stress condition in the case of a compressible material as outlined in the following section. Consequently, the transverse shear strains of the GL strain tensor vanish, i.e. $E_{\alpha,3} = E_{3,\alpha} = 0$, and we obtain the relation $E_{3,3} = (C_{3,3} - 1)/2$, cf. Eqs. $(4.17)_2$, (4.20), (4.54). Accordingly, only the in-plane components $E_{\alpha,\beta}$ are considered for the shell kinematics. Bearing in mind Eq. (4.56), these components can be separated into a constant part due to the membrane strains and a linear part due to bending,

$$E_{\alpha,\beta} = \varepsilon_{\alpha,\beta} + \xi_3 \kappa_{\alpha,\beta}, \tag{4.58}$$

where

$$\varepsilon_{\alpha,\beta} = \frac{1}{2}(a_{\alpha,\beta} - A_{\alpha,\beta}) \quad \text{and} \quad \kappa_{\alpha,\beta} = (b_{\alpha,\beta} - B_{\alpha,\beta}) \tag{4.59}$$

are the membrane strains and the changes in curvature obtained from bending, respectively.

4.6.2 Constitutive equations

We consider an arbitrary isotropic hyperelastic model, described by an elastic potential function W as introduced in Section 4.4. If $C_{3,3} = g_{3,3} \equiv 1$ is used for the shell model, the plane stress condition is, in general, violated, since in this case, it holds according to Eq. (4.26)

$$S^{3,3} = 2\left[(a_{\mathrm{I}} + a_{\mathrm{II}}\mathrm{I}_{\mathbf{C}}) - a_{\mathrm{II}} + a_{\mathrm{III}}\mathrm{III}_{\mathbf{C}}\right], \tag{4.60}$$

where it should be noted that due to $G^{3,\alpha} = G^{\alpha,3} = 0$ and $G^{3,3} = 1$ we have $C^{3,3} = C_{3,3}$, cf. Eq. $(4.21)_3$. Accordingly, the transverse normal deformation $C_{3,3}$ needs to be determined such that $S^{3,3} = 0$. This can be done numerically for compressible materials or analytically for incompressible materials. In this section we briefly outline the main ideas of these procedures and present the results. A detailed derivation from the 3D continuum to the shell model can be found in Kiendl et al. [109].

For compressible materials, we enforce the plane stress condition in the form of a constraint at runtime. Since the components $C_{i,j}$ are determined for $(i,j) \neq (3,3)$ by the metric coefficients of the shell continuum, the corresponding problem reads: find $C_{3,3}$ such that $S^{3,3} = S^{3,3}(C_{3,3}) = 0$. The latter is a root-finding problem which can be solved numerically, for example, with a Newton-Raphson scheme.

For incompressible materials, we make use of the incomprehensibility condition $(4.27)_2$ such that the transverse normal deformation is determined by $\mathrm{III}_{\mathbf{C}} = 1 \Leftrightarrow C_{3,3} = \mathrm{J}_0^{-2}$**, where $\mathrm{J}_0 := \sqrt{\det([g_{\alpha,\beta}]_{\alpha,\beta})/\det([G_{\alpha,\beta}]_{\alpha,\beta})}$ is the in-plane Jacobian, related to the Jacobian by $\mathrm{J} = \mathrm{J}_0\sqrt{C_{3,3}}$. The plane stress condition is satisfied by solving

$$S^{3,3} = 2\left[(a_{\mathrm{I}} + a_{\mathrm{II}}\mathrm{I}_{\mathbf{C}}) - a_{\mathrm{II}}\,\mathrm{J}_0^{-2} + \mathrm{p}\,\mathrm{J}_0^2\right] = 0, \tag{4.61}$$

**Here it should be noted, that for a tensor expressed in the contravariant basis of the undeformed configuration, $\boldsymbol{A} = A_{i,j}\boldsymbol{G}^i \otimes \boldsymbol{G}^j$, the determinant is obtained by $\det(\boldsymbol{A}) = \det([A_{i,j}]_{i,j})/\det([G_{i,j}]_{i,j}) = \det([A_{i,j}]_{i,j})/\det([G_{\alpha,\beta}]_{\alpha,\beta})$, where the latter equation holds due to $G_{3,\alpha} = G_{\alpha,3} = 0$ and $G_{3,3} = 1$. The equivalence then follows directly from $\det([C_{i,j}]_{i,j}) = C_{3,3}\det([g_{\alpha,\beta}]_{\alpha,\beta})$, cf. Eq. $(4.57)_1$.

cf. Eqs. (4.26), (4.28), for the hydrostatic pressure,

$$S^{3,3} = 0 \iff \mathrm{p} = -\,\mathrm{J}_0^{-2}\left[(a_\mathrm{I} + a_\mathrm{II}\mathrm{I}_\mathbf{C}) - a_\mathrm{II}\,\mathrm{J}_0^{-2}\right], \tag{4.62}$$

and substituting Eq. (4.62) into Eq. (4.26). Thus, the components of the PK2 stress tensor are obtained as follows:

$$S^{i,j} = 2\left[(a_\mathrm{I} + a_\mathrm{II}\mathrm{I}_\mathbf{C})(G^{i,j} - \mathrm{J}_0^{-2}\,\bar{C}^{i,j}) - a_\mathrm{II}(C^{i,j} - \mathrm{J}_0^{-4}\,\bar{C}^{i,j})\right]. \tag{4.63}$$

Finally, we remark, that the plane stress condition has also to be considered during a linearisation procedure, since $S^{3,3} \equiv 0 \;\Rightarrow\; \mathrm{d}S^{3,3} \equiv 0$, where $\mathrm{d}S^{3,3}$ denotes the total differential of $S^{3,3}$. Therefore, the elasticity tensor $\mathbb{C} = \partial\mathbf{S}\,/\partial\mathbf{E} = \mathbb{C}^{i,j,k,l}\boldsymbol{G}_i\otimes\boldsymbol{G}_j\otimes\boldsymbol{G}_k\otimes\boldsymbol{G}_l$ must also be adjusted for the shell model. Once the plane stress condition is enforced, the contravariant components of the adjusted tensor $\hat{\mathbb{C}}$ with respect to the reference configuration are given by

$$\hat{\mathbb{C}}^{i,j,k,l} = \mathbb{C}^{i,j,k,l} - \frac{\mathbb{C}^{i,j,3,3}\mathbb{C}^{3,3,k,l}}{\mathbb{C}^{3,3,3,3}}. \tag{4.64}$$

4.6.3 Multi-patch framework

Finally, we derive a multi-patch framework in the context of the Kirchhoff-Love theory. The starting point is the sequence of variational problems (4.45) expressed in curvilinear coordinates, which we will reformulate according to the Kirchhoff hypotheses. More specifically, under reasonable assumptions, we will approximate the volume integrals in (4.45) by surface integrals and thus obtain a semi-discrete version of the principle of virtual work for shells. To this end, we introduce the stress and bending tensors $\boldsymbol{\varepsilon} := \varepsilon_{\alpha,\beta}\boldsymbol{G}^\alpha\otimes\boldsymbol{G}^\beta$, $\boldsymbol{\kappa} := \kappa_{\alpha,\beta}\boldsymbol{G}^\alpha\otimes\boldsymbol{G}^\beta$ and find that according to Eq. (4.59), the GL strain tensor has the representation $\mathbf{E} = \boldsymbol{\varepsilon} + \xi_3\boldsymbol{\kappa}$. Using the identity $\mathbf{P} : \nabla_{\boldsymbol{X}}\delta\boldsymbol{\varphi} = \mathbf{S} : \delta\mathbf{E}$, see Holzapfel [97] for a proof, the functionals in Eq. (4.45) become:

$$\begin{aligned}\mathrm{V}_\nu^{(i)}(\boldsymbol{\varphi}_\nu^{(i)}, \delta\boldsymbol{\varphi}^{(i)}) = {}& \langle\rho_0^{(i)}\mathcal{H}_\nu(\boldsymbol{\varphi}_\nu^{(i)}, \boldsymbol{\varphi}_{\nu-1}^{(i)}, \tilde{\boldsymbol{\varphi}}_{\nu-1}^{(i)}) - \boldsymbol{B}_{\nu-\frac{1}{2}}^{(i)}, \delta\boldsymbol{\varphi}^{(i)}\sqrt{G}\rangle_{\hat{\Omega}^{(i)}} \\ & + \langle\mathbf{S}_{\nu-\frac{1}{2}}^{(i)}, [\delta\boldsymbol{\varepsilon}^{(i)} + \xi_3\delta\boldsymbol{\kappa}^{(i)}]\sqrt{G}\rangle_{\hat{\Omega}^{(i)}} - \langle\boldsymbol{T}_{\nu-\frac{1}{2}}^{(i)}, \delta\boldsymbol{\varphi}^{(i)}\sqrt{GQ}\rangle_{\hat{\Gamma}_\mathrm{n}^{(i)}} = 0,\end{aligned} \tag{4.65}$$

whereby we omit the marker $\hat{(\bullet)}$ and the subscript c here, as it is clear that we are working with curvilinear coordinates. For thin shells, it is reasonable to assume that the mass density, the body force and the surface traction are constant through the thickness of the shell. Moreover, according to Başar & Itskov [11], it is also reasonable to assume that the shifter $Z := \sqrt{G/A}$, where $A := \det[A_{\alpha,\beta}]_{\alpha,\beta} = \|\partial_{\xi_1}\boldsymbol{S}\times\partial_{\xi_2}\boldsymbol{S}\|^2$, can be approximated by unity, i.e. $Z \approx 1$. On the basis of these assumptions, neglecting terms containing a factor h^s with $s \geq 2$, and bearing in mind the representations $\boldsymbol{\varphi}^{(i)} = \boldsymbol{s}^{(i)} + \xi_3\boldsymbol{a}_3^{(i)}$, $\delta\boldsymbol{\varphi}^{(i)} = \delta\boldsymbol{s}^{(i)} + \xi_3\delta\boldsymbol{a}_3^{(i)}$, the volume integrals in Eq. (4.65) can be approximated by surface integrals as follows

$$\langle\rho_0^{(i)}\mathcal{H}_\nu(\boldsymbol{\varphi}_\nu^{(i)}, \boldsymbol{\varphi}_{\nu-1}^{(i)}, \tilde{\boldsymbol{\varphi}}_{\nu-1}^{(i)}), \delta\boldsymbol{\varphi}^{(i)}\sqrt{G}\rangle_{\hat{\Omega}^{(i)}} \approx h\langle\rho_0^{(i)}\mathcal{H}_\nu(\boldsymbol{s}_\nu^{(i)}, \boldsymbol{s}_{\nu-1}^{(i)}, \tilde{\boldsymbol{s}}_{\nu-1}^{(i)}), \delta\boldsymbol{s}^{(i)}\sqrt{A}\rangle_{[0,1]^2}, \tag{4.66}$$

$$\langle \mathbf{S}^{(i)}_{\nu-\frac{1}{2}}, [\delta\boldsymbol{\varepsilon}^{(i)} + \xi_3 \delta\boldsymbol{\kappa}^{(i)}]\sqrt{G}\rangle_{\hat{\Omega}^{(i)}} \approx \langle \boldsymbol{n}^{(i)}_{\nu-\frac{1}{2}}, \delta\boldsymbol{\varepsilon}^{(i)}\sqrt{A}\rangle_{[0,1]^2} + \langle \boldsymbol{m}^{(i)}_{\nu-\frac{1}{2}}, \delta\boldsymbol{\kappa}^{(i)}\sqrt{A}\rangle_{[0,1]^2}, \tag{4.67}$$

$$\langle \boldsymbol{B}^{(i)}_{\nu-\frac{1}{2}}, \delta\boldsymbol{\varphi}^{(i)}\sqrt{G}\rangle_{\hat{\Omega}} \approx h\langle \boldsymbol{B}^{(i)}_{\nu-\frac{1}{2}}, \delta\boldsymbol{s}^{(i)}\sqrt{A}\rangle_{[0,1]^2}, \tag{4.68}$$

where $\boldsymbol{n} = n^{\alpha,\beta}\boldsymbol{G}_\alpha \otimes \boldsymbol{G}_\beta$ and $\boldsymbol{m} = m^{\alpha,\beta}\boldsymbol{G}_\alpha \otimes \boldsymbol{G}_\beta$ are resultant normal forces and bending moments given by

$$n^{\alpha,\beta} = \int_{-h/2}^{h/2} S^{\alpha,\beta}\, \mathrm{d}\xi_3, \qquad m^{\alpha,\beta} = \int_{-h/2}^{h/2} \xi_3 S^{\alpha,\beta}\, \mathrm{d}\xi_3. \tag{4.69}$$

The last two approximations (4.67), (4.68) are easily obtained by using the assumptions, considering of $\sqrt{G} = \sqrt{A}Z \approx \sqrt{A}$ and pre-integration in thickness direction. The first approximation (4.66), however, is not immediately obvious due to the operator $\mathcal{H}_\nu$ and requires further consideration, which we postpone to the end of this section. With regard to the surface integral in Eq. (4.65), representing the natural boundary condition, different cases are to be distinguished, depending on how $\hat{\Gamma}^{(i)}_{\mathrm{n}}$ is specified with regard to the shell continuum. E.g. in the continuum a load can act on the surface with $\xi_3 = h/2$, which corresponds to a load on the entire middle surface after omission of the thickness direction. On the other hand, a load on the surface portion with $\xi_1 = 0$ would correspond to a line load. In order to take all cases into account, the traction $\boldsymbol{T}$ is reformulated accordingly and integrated over the entire middle surface. For more details see Başar & Itskov [11]. Altogether, we finally obtain a sequence of variational problems for each patch as follows: for $\nu = 1, \ldots, M$ find $\boldsymbol{s}^{(i)}_\nu \in \mathcal{S}^{(i)}_\nu$ such that

$$\begin{aligned} \mathrm{V}^{(i)}_\nu(\boldsymbol{s}^{(i)}_\nu, \delta\boldsymbol{s}^{(i)}) &= h\langle \rho^{(i)}_0 \mathcal{H}_\nu(\boldsymbol{s}^{(i)}_\nu, \boldsymbol{s}^{(i)}_{\nu-1}, \tilde{\boldsymbol{s}}^{(i)}_{\nu-1}) - \boldsymbol{B}^{(i)}_{\nu-\frac{1}{2}}, \delta\boldsymbol{s}^{(i)}\sqrt{A}\rangle_{[0,1]^2} \\ &\quad + \langle \boldsymbol{n}^{(i)}_{\nu-\frac{1}{2}}, \delta\boldsymbol{\varepsilon}^{(i)}\sqrt{A}\rangle_{[0,1]^2} + \langle \boldsymbol{m}^{(i)}_{\nu-\frac{1}{2}}, \delta\boldsymbol{\kappa}^{(i)}\sqrt{A}\rangle_{[0,1]^2} - \langle \boldsymbol{T}^{(i)}_{\nu-\frac{1}{2}}, \delta\boldsymbol{s}^{(i)}\sqrt{A}\rangle_{[0,1]^2} = 0, \end{aligned} \tag{4.70}$$

for all $\delta\boldsymbol{s}^{(i)} \in \mathcal{V}^{(i)}$, where $\mathcal{S}^{(i)}_\nu$ and $\mathcal{V}^{(i)}$, are suitable spaces of trial and test functions. Note that here, in contrast to Section 4.5, the space of trial solutions as well as the space of test functions must be contained in $H^2([0,1]^2)^3$ due to the curvature terms introduced in Eq. (4.55). Concerning the existence and uniqueness of weak solutions, we refer to Healey [88].

Remark 4.6.1. *As in Section 4.5, the problems* (4.70) *simplify considerably in the static case: find* $\boldsymbol{s}^{(i)} \in \mathcal{S}^{(i)}$ *such that for all* $\delta\boldsymbol{s}^{(i)} \in \mathcal{V}^{(i)}$ *holds*

$$\begin{aligned} &\langle \boldsymbol{n}^{(i)}, \delta\boldsymbol{\varepsilon}^{(i)}\sqrt{A}\rangle_{[0,1]^2} + \langle \boldsymbol{m}^{(i)}, \delta\boldsymbol{\kappa}^{(i)}\sqrt{A}\rangle_{[0,1]^2} \\ &\qquad - h\langle \boldsymbol{B}^{(i)}, \delta\boldsymbol{s}^{(i)}\sqrt{A}\rangle_{[0,1]^2} - \langle \boldsymbol{T}^{(i)}, \delta\boldsymbol{s}^{(i)}\sqrt{A}\rangle_{[0,1]^2} = 0, \end{aligned} \tag{4.71}$$

Finally, we look at Approximation (4.66) in more detail. To this end, we first need a closed form for the iterated $\tilde{\boldsymbol{\varphi}}^{(i)}_\nu$. Considering the initial value and the inductive definition, it can be easily shown by induction on ν that $\tilde{\boldsymbol{\varphi}}^{(i)}_\nu = 2\sum_{k=1}^{\nu}(-1)^{\nu+k} h_k^{-1}(\boldsymbol{\varphi}^{(i)}_k - \boldsymbol{\varphi}^{(i)}_{k-1}) + (-1)^\nu \boldsymbol{v}$ for all $\nu \in \mathbb{N}_0$, where $\boldsymbol{v}$ is the initial data introduced in Eq. (4.38). Due to the structure

of the motion of the shell continuum, the prescribed velocity has in the context of the Kirchhoff–Love theory the form $\boldsymbol{v} = \boldsymbol{v}_s + \xi_3 \boldsymbol{v}_{\boldsymbol{a_3}}$ for reasons of consistency, where $\boldsymbol{v}_s$ is the velocity of the mid-surface and $\boldsymbol{v}_{a_3}$ is the velocity of the normal field. We first note that due to $\sqrt{G} = Z\sqrt{A} \approx \sqrt{A}$, we get an approximation for the first term in Eq. (4.65) as follows

$$\begin{aligned}&\langle \rho_0^{(i)} \mathcal{H}_\nu(\boldsymbol{\varphi}_\nu^{(i)}, \boldsymbol{\varphi}_{\nu-1}^{(i)}, \tilde{\boldsymbol{\varphi}}_{\nu-1}^{(i)}), \delta\boldsymbol{\varphi}^{(i)} \sqrt{G} \rangle_{\hat{\Omega}^{(i)}} \approx \\ &\int\limits_{[0,1]^2} C_1^{(i)} \int\limits_{-h/2}^{h/2} (\boldsymbol{\varphi}_\nu^{(i)} - \boldsymbol{\varphi}_{\nu-1}^{(i)}) \cdot \delta\boldsymbol{\varphi}^{(i)} \, \mathrm{d}\xi_3 - C_2^{(i)} \int\limits_{-h/2}^{h/2} \tilde{\boldsymbol{\varphi}}_{\nu-1}^{(i)} \cdot \delta\boldsymbol{\varphi}^{(i)} \, \mathrm{d}\xi_3 \, \mathrm{d}(\xi_1, \xi_2),\end{aligned} \tag{4.72}$$

where we have further used the definition of the operator $\mathcal{H}_\nu$, cf. Eq. (4.42), and summarised in $C_1^{(i)}$ and $C_2^{(i)}$ all quantities that are constant in the thickness direction, i.e. $C_1^{(i)} := 2\rho_0^{(i)}\sqrt{A}h_\nu^{-2}$, $C_2^{(i)} := 2\rho_0^{(i)}\sqrt{A}h_\nu^{-1}$. Note that the letter h is used here with different meanings. While quantities with subscript (e.g. h_ν) denote the step-size of the time-stepping scheme, h refers to the shell thickness. Taking into account $\boldsymbol{\varphi}_k^{(i)} \cdot \delta\boldsymbol{\varphi}^{(i)} = \boldsymbol{s}_k^{(i)} \cdot \delta\boldsymbol{s}^{(i)} + \xi_3(\boldsymbol{s}_k^{(i)} \cdot \delta\boldsymbol{a}_3^{(i)} + \boldsymbol{a}_{3,k}^{(i)} \cdot \delta\boldsymbol{s}^{(i)}) + \xi_3^2 \boldsymbol{a}_{3,k}^{(i)} \cdot \delta\boldsymbol{a}_3^{(i)}$, we obtain

$$\int\limits_{-h/2}^{h/2} \boldsymbol{\varphi}_k^{(i)} \cdot \delta\boldsymbol{\varphi}^{(i)} \, \mathrm{d}\xi_3 = h\boldsymbol{s}_k^{(i)} \cdot \delta\boldsymbol{s}^{(i)} + 12^{-1}h^3(\boldsymbol{a}_{3,k}^{(i)} \cdot \delta\boldsymbol{a}_3^{(i)}) \approx h\boldsymbol{s}_k^{(i)} \cdot \delta\boldsymbol{s}^{(i)}, \tag{4.73}$$

where, as agreed above, we have omitted the term with cubic thickness h. According to Eq. (4.73), we obtain in Eq. (4.72) an approximation for the first integral with respect to the thickness direction. For the second integral, using the closed representation for $\tilde{\boldsymbol{\varphi}}_{\nu-1}^{(i)}$ and bearing in mind the shape of $\boldsymbol{v}$ we further obtain with Eq. (4.73)

$$\begin{aligned}\int\limits_{-h/2}^{h/2} \tilde{\boldsymbol{\varphi}}_{\nu-1}^{(i)} \cdot \delta\boldsymbol{\varphi}^{(i)} \, \mathrm{d}\xi_3 &= 2\sum_{k=1}^{\nu-1}(-1)^{\nu-1+k} h_k^{-1} \int\limits_{-h/2}^{h/2} (\boldsymbol{\varphi}_k^{(i)} - \boldsymbol{\varphi}_{k-1}^{(i)}) \cdot \delta\boldsymbol{\varphi}^{(i)} \, \mathrm{d}\xi_3 \\ &+ (-1)^{\nu-1} \int\limits_{-h/2}^{h/2} \boldsymbol{v}^{(i)} \cdot \delta\boldsymbol{\varphi}^{(i)} \, \mathrm{d}\xi_3 \approx 2h\sum_{k=1}^{\nu-1}(-1)^{\nu-1+k} h_k^{-1}(\boldsymbol{s}_k^{(i)} - \boldsymbol{s}_{k-1}^{(i)}) \cdot \delta\boldsymbol{s}^{(i)} \\ &+ h(-1)^{\nu-1}\boldsymbol{v}_s^{(i)} \cdot \delta\boldsymbol{s}^{(i)} = h\tilde{\boldsymbol{s}}_{\nu-1}^{(i)} \cdot \delta\boldsymbol{s}^{(i)},\end{aligned} \tag{4.74}$$

where $\tilde{\boldsymbol{s}}_\nu^{(i)} := 2\sum_{k=1}^{\nu}(-1)^{\nu+k} h_k^{-1}(\boldsymbol{s}_k^{(i)} - \boldsymbol{s}_{k-1}^{(i)}) + (-1)^\nu \boldsymbol{v}_s$, i.e. like $\tilde{\boldsymbol{\varphi}}_\nu^{(i)}$, $\tilde{\boldsymbol{s}}_\nu^{(i)}$ is inductively given by $\tilde{\boldsymbol{s}}_0^{(i)} = \boldsymbol{v}_s^{(i)}$ and $\tilde{\boldsymbol{s}}_\nu^{(i)} = 2h_\nu^{-1}(\boldsymbol{s}_\nu^{(i)} - \boldsymbol{s}_{\nu-1}^{(i)}) - \tilde{\boldsymbol{s}}_{\nu-1}^{(i)}$, $\nu \in \mathbb{N}$. With these considerations, we now obtain from Eq. (4.72) the relationship

$$\begin{aligned}&\langle \rho_0^{(i)} \mathcal{H}_\nu(\boldsymbol{\varphi}_\nu^{(i)}, \boldsymbol{\varphi}_{\nu-1}^{(i)}, \tilde{\boldsymbol{\varphi}}_{\nu-1}^{(i)}), \delta\boldsymbol{\varphi}^{(i)} \sqrt{G} \rangle_{\hat{\Omega}^{(i)}} \approx \\ &\qquad h \int\limits_{[0,1]^2} [C_1^{(i)}(\boldsymbol{s}_\nu^{(i)} - \boldsymbol{s}_{\nu-1}^{(i)}) - C_2^{(i)} \tilde{\boldsymbol{s}}_{\nu-1}^{(i)}] \cdot \delta\boldsymbol{s}^{(i)} \, \mathrm{d}(\xi_1, \xi_2),\end{aligned} \tag{4.75}$$

which corresponds to (4.66). Finally, note that the Approximations (4.67) and (4.68) also follow from the above considerations, especially from Eq. (4.73).

4.7 Numerical studies

In the following section, we consider a number of numerical investigations within the multi-patch framework. The first two sections deal with solids, where we first investigate the influence of different quadrature formulas in an element-based integration scheme. To this end, we compare Gaussian quadrature with a simpler midpoint rule on a sub-mesh, where we consider coupling orders up to a weak C^2 coupling. The second example on solids deals with the question of the optimal choice of multiplier spaces. In addition to the multiplier space introduced in Section 3.2, an extended space is considered that results from the use of basis functions from both the slave and the master side. The remaining sections then deal with the application of the extended mortar method in the Kirchhoff–Love theory. In the third example, we investigate the influence of a G^1 coupling on the approximation quality of the IGA framework by comparing the approximation errors in a 1-patch system with those of a 2-patch system. In the following section, we consider a 4-patch system with crosspoints. Here we study the coupling of shape functions of different order and the influence of the choice of master and slave with regard to the number of elements. Finally, the last example deals with different coupling conditions and compares a C^1 with a (real) G^1 coupling. In all of the following examples the spatial dimensions are given in units of [m] and the time in units of [s].

4.7.1 Solid: Patch test

In this section, we investigate the influence of quadrature errors in an element-based mortar integration using a static patch test, where we compare Gaussian quadrature and a simple midpoint quadrature formula on a sub-mesh of the parametric domain. Moreover, we consider a flat as well as a curved interface and coupling conditions up to C^2-continuity. In the example, a block given by $\Omega_0 = (-0.5, 0.5) \times (-0.5, 0.5) \times (-1.5, 0.5)$ is represented through two patches, each parametrized by tricubic shape functions, so that the lower patch ($\Omega_0^{(1)}$; slave side) consists of $5 \times 5 \times 5$ elements and the upper patch ($\Omega_0^{(2)}$; master side) consists of $4 \times 4 \times 4$ elements, see Figure 4.3 and Figure 4.5 for illustration.

Concerning the material, we use a Neo-Hook model described by the elastic potential function

$$\mathrm{W}(\mathrm{I}_{\mathbf{C}}, \mathrm{II}_{\mathbf{C}}, \mathrm{III}_{\mathbf{C}}) = \frac{\mu}{2}(\mathrm{I}_{\mathbf{C}} - 3) - \mu \ln(\sqrt{\mathrm{III}_{\mathbf{C}}}) + \frac{\lambda}{2} \ln(\sqrt{\mathrm{III}_{\mathbf{C}}})^2, \tag{4.76}$$

with Lamé parameters $\mu = 11250/13$ Pa and $\lambda = 12081/10$ Pa. Furthermore, on the upper surface of $\Omega_0^{(2)}$ a surface load $\boldsymbol{T} = (0, 0, -750)^{\mathrm{T}}$ N/m^2 is applied, where the lower surface of $\Omega_0^{(1)}$ is clamped in such a way that the body is able to expand in horizontal direction, resulting in a homogeneous stress distribution such that the Cauchy stress tensor $\boldsymbol{\sigma} = \mathrm{J}^{-1}\,\mathbf{P}\,\mathbf{F}^{\mathrm{T}}$ is given by $[\boldsymbol{\sigma}]_{i,j} = -750\,\mathrm{N/m}^2$ if $i = j = 3$ and $[\boldsymbol{\sigma}]_{i,j} = 0\,\mathrm{N/m}^2$ otherwise.

The influence of quadrature errors on isogeometric mortar elements using element-based mortar integration is discussed in Brivadis et al. [32] by means of a second order elliptic

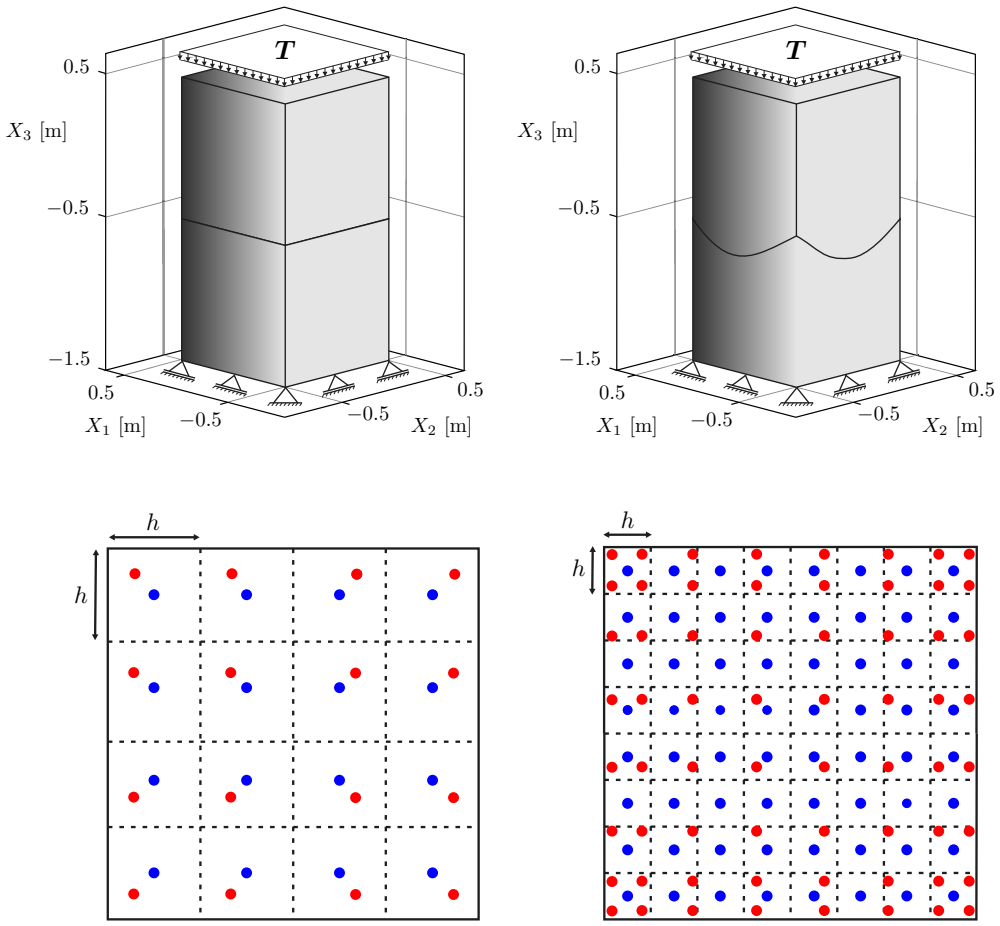

Figure 4.3: *Patch test.* Upper row: boundary conditions and reference configuration with flat (left) and curved (right) interface. Lower row: Gauss points (red) and sample points (blue) on a square element, employing four quadrature points per direction (left) and eight quadrature points per direction (right). The dashed lines indicate the sub-mesh of size h corresponding to the midpoint rule.

boundary value problem. The numerical examples there have shown, that if the quadrature formula is high enough then the error for the primal variable is quantitatively and qualitatively the same for meshes of practical interest, where for the evaluation of the mortar integrals Gaussian quadrature rules were employed. In this case, an increase of the number of quadrature points does enlarge the order but not necessarily the accuracy. We recall that the IGA basis functions of the master side restricted to an element on the slave side are in general of at most C^{p-1} regularity, where p depends on the order of the NURBS basis function. Thus higher order Gauss quadrature formula may not be the best choice. Alternatively, a low-order quadrature formula on a sub-mesh may lead to a more accurate result if one increases the number of quadrature points. Therefore, we consider here additionally to Gaussian quadrature a midpoint quadrature formula on a sub-mesh of the parametric domain with constant quadrature weights $w_k = 1$. To this

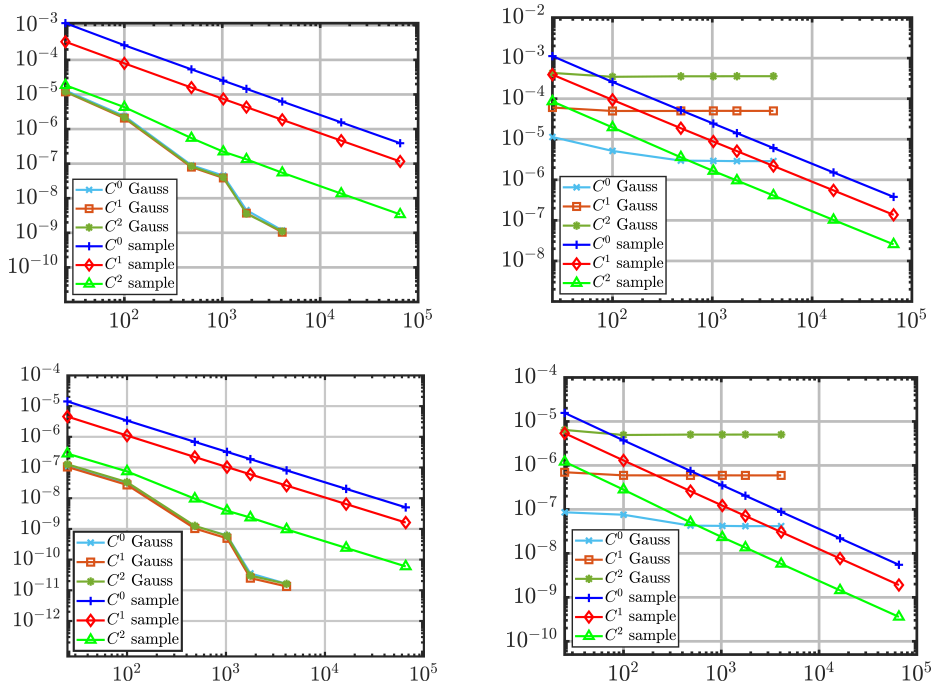

Figure 4.4: *Patch test.* Upper row: Cauchy stress error err_σ as a function of the number of quadrature points in the case of a flat (left) and curved (right) interface. Lower row: relative displacement error err_d as a function of the number of quadrature points in the case of a flat (left) and curved (right) interface.

end, we distribute equidistantly spaced sample points $\boldsymbol{\xi}_1^{(1)}, \dots, \boldsymbol{\xi}_{n_q}^{(1)}$ on the pre-image $\hat{\Gamma}_2^1$ and approximate the weak C^n coupling conditions (3.11) via

$$\mathrm{B}(\boldsymbol{\varphi}_\mathrm{h}, \delta\boldsymbol{\lambda}_\mathrm{h}) \approx \sum_{|\boldsymbol{\alpha}|\leq n} \mathfrak{h}^{|\boldsymbol{\alpha}|} \sum_{k=1}^{n_q} \partial^{\boldsymbol{\alpha}}[\boldsymbol{\varphi}_\mathrm{h}^{(1)}(\boldsymbol{X}_k) - \boldsymbol{\varphi}_\mathrm{h}^{(2)}(\boldsymbol{X}_k)] \cdot \partial^{\boldsymbol{\alpha}} \delta\boldsymbol{\lambda}_\mathrm{h}(\boldsymbol{X}_k), \tag{4.77}$$

where $\mathfrak{h} = h^2$, $\boldsymbol{X}_k = \boldsymbol{\mathcal{G}}^{(1)}(\boldsymbol{\xi}_k^{(1)})$ and $\boldsymbol{\mathcal{G}}^{(1)}$ is the parametrisation of $\Omega_0^{(1)}$, see Figure 4.3 for a comparison of the two types of quadrature rules.

A numerical error study of the Cauchy stress and the displacements at the interface is provided in Figure 4.4 for the two quadrature schemes where we consider the two relative errors

$$err_\sigma = \|\boldsymbol{\sigma}\|_{L^2(\Gamma)}^{-1} \|\boldsymbol{\sigma} - \boldsymbol{\sigma}_\mathrm{h}\|_{L^2(\Gamma)}, \quad err_d = n_q^{-1} \sum_{i=1}^{n_q} \|\boldsymbol{\varphi}^{(1)}(\boldsymbol{X}_i) - \boldsymbol{\varphi}^{(2)}(\boldsymbol{X}_i)\| \tag{4.78}$$

as functions of the number of quadrature points on a constant mesh. As expected, the qualitative behaviour of the stress error err_σ and the displacement error err_d is the same. In the case of a flat interface, the error decreases with increasing number of quadrature points for both quadrature formulas, although in part a better error behaviour can be seen for the Gauss quadrature compared to the midpoint rule. It is noteworthy here

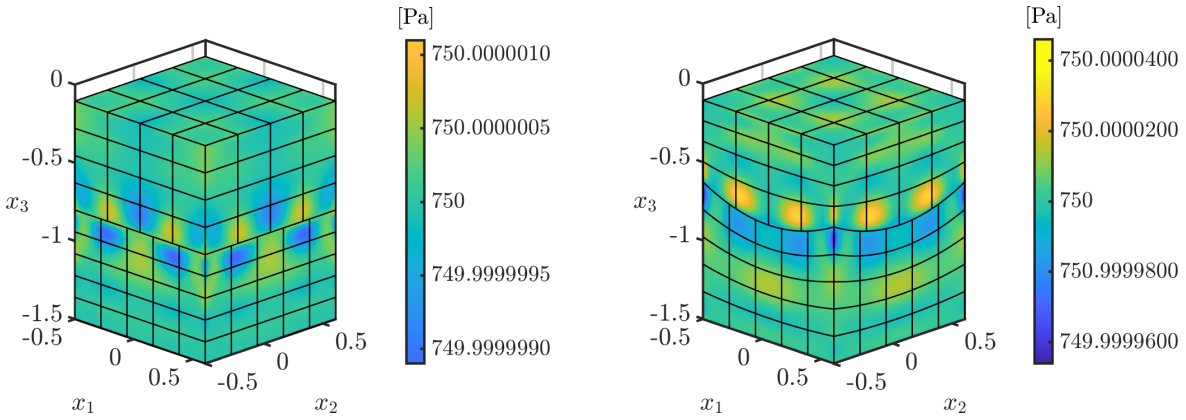

Figure 4.5: *Patch test.* Von Mises stress distribution. Left: flat interface, weak C^1-continuous coupling, 64×64-point Gauss integration; right: curved interface, weak C^2-continuous coupling, 256×256-point midpoint integration.

that the error of the Gauss quadrature does not change significantly with respect to the coupling order, whereas the error of the midpoint rule decreases with increasing coupling order. The situation is quite different for a curved interface. While the error behaviour of the midpoint rule hardly changes compared to a flat interface, the error of the Gaussian quadrature cannot be improved by increasing the number of quadrature points. Furthermore, it can be seen that the error of the Gauss quadrature increases with increasing coupling order, while the behaviour of the midpoint rule does not change compared to the flat interface. Eventually, an illustration of the stress distribution with the best results in terms of errors can be seen in Figure 4.5.

4.7.2 Solid: Twisted block

In domain coupling, the total error at the interface is a combination of the approximation error and the consistency error (coupling error). To achieve an optimal result, it is therefore desirable that the ratio of the two errors is close to one, such that the total error is evenly distributed between them. In Section 3.2.1 we introduced the space $\mathcal{M}_\mathrm{h}$ of the discrete Lagrangian multipliers as the trace-space of the basis functions defined on the slave side, cf. Eqs. (3.22), (3.23). Through this choice, the consistency error depends immediately on the mesh of the slave side, whereas the approximation error is linked to the master side. However, under certain conditions, it is possible to increase the dimension of $\mathcal{M}_\mathrm{h}$ by adding shape functions from the master side or by choosing a combination of basis functions from both sides. Thereby it can be expected that the consistency error is reduced at the price of increasing the approximation error. In this section, a static example is used to examine this relationship in more detail.

We consider a cuboid given by $\Omega_0 = (-0.5, 0.5)^2 \times (-2.75, 1.75)$ subdivided into two patches $\Omega_0^{(1)} = (-0.5, 0.5)^2 \times (-2.75, -0.5)$ (slave side), $\Omega_0^{(2)} = (-0.5, 0.5)^2 \times (-0.5, 1.75)$ (master side), where the material is determined through the elastic potential (4.32) with

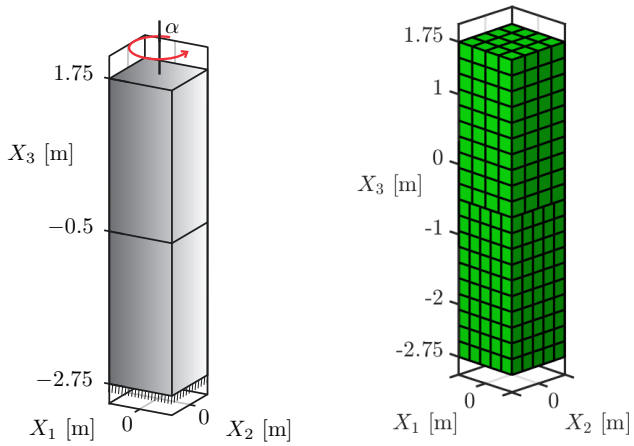

Figure 4.6: *Twisted block.* Reference configuration and boundary conditions (left) and computational mesh (right).

the material parameters $\mu_1 = 6750/13$ Pa, $\mu_2 = 4500/13$ Pa and $\lambda = 12081/10$ Pa. For the parametrisation of the two patches, we use triquadratic as well as tricubic shape functions, such that in both cases the lower patch consists of $5 \times 5 \times 10$ elements and the upper one of $4 \times 4 \times 10$ elements. The lower surface of the cuboid is fixed in space, whereas the upper one is rotated by an angle of $\alpha = 720°$, see Figure 4.6 for illustration. Furthermore, weak C^0 coupling conditions are imposed on the common surface of the two patches, for which we resort to an element-based integration scheme with Gauss quadrature for implementation. On the master and slave side together, a total of 255 degrees of freedom in the triquadratic case and 339 degrees of freedom in the tricubic case thus influence the coupling. In one of the two settings considered herein, the space $\mathcal{M}_\mathrm{h}$ is spanned by the basis functions of the slave side, so that we obtain $\dim(\mathcal{M}_\mathrm{h}) = 147$ in the triquadratic case and $\dim(\mathcal{M}_\mathrm{h}) = 192$ in the tricubic case. For the second setting, we use as basis of the multiplier space a combination of functions from the trace-spaces of the slave and master side so that $\dim(\mathcal{M}_\mathrm{h}) = 228$ holds in the triquadratic case and $\dim(\mathcal{M}_\mathrm{h}) = 291$ in the tricubic case[††]. In the following, we will refer to *set*1 and *set*2 for short in order to distinguish between the two settings. To verify the approximation error due to the coupling conditions, we also include a numerical reference solution $\boldsymbol{\varphi}_\mathrm{h}^\mathrm{r}$ on a 1-patch geometry, where the cuboid is appropriately parametrised with triquadratic and tricubic functions, respectively, such that Ω_0 is subdivided into $4 \times 4 \times 20$ elements. Based on this, we use the two distances

$$d_a(\boldsymbol{z}) = \|\boldsymbol{\varphi}_\mathrm{h}^{(2)}(\boldsymbol{X}) - \boldsymbol{\varphi}_\mathrm{h}^\mathrm{r}(\boldsymbol{X})\| \quad \text{and} \quad d_c(\boldsymbol{z}) = \|\boldsymbol{\varphi}_\mathrm{h}^{(2)}(\boldsymbol{X}) - \boldsymbol{\varphi}_\mathrm{h}^{(1)}(\boldsymbol{X})\| \tag{4.79}$$

as a measure for the approximation and consistency error, respectively, and quantify the total approximation and consistency error through

$$tot_a = \frac{1}{6000}\sum_{i=1}^{6000} d_a(\boldsymbol{X}_i) \quad \text{and} \quad tot_c = \frac{1}{6000}\sum_{i=1}^{6000} d_c(\boldsymbol{X}_i), \tag{4.80}$$

[††]For reasons of clarity, details regarding the construction of a mixed base are omitted here. The interested reader can find a comprehensive description in Dittmann et al. [64].

Table 4.1: *Twisted block.* Total approximation and consistency error of $set1$ and $set2$.

order	$set1$		$set2$	
	tot_a	tot_c	tot_a	tot_c
$(2,2,2)$	$8.41 \cdot 10^{-3}$	$6.55 \cdot 10^{-4}$	$1.82 \cdot 10^{-2}$	$5.23 \cdot 10^{-13}$
$(3,3,3)$	$5.11 \cdot 10^{-3}$	$3.04 \cdot 10^{-4}$	$5.63 \cdot 10^{-3}$	$6.78 \cdot 10^{-4}$

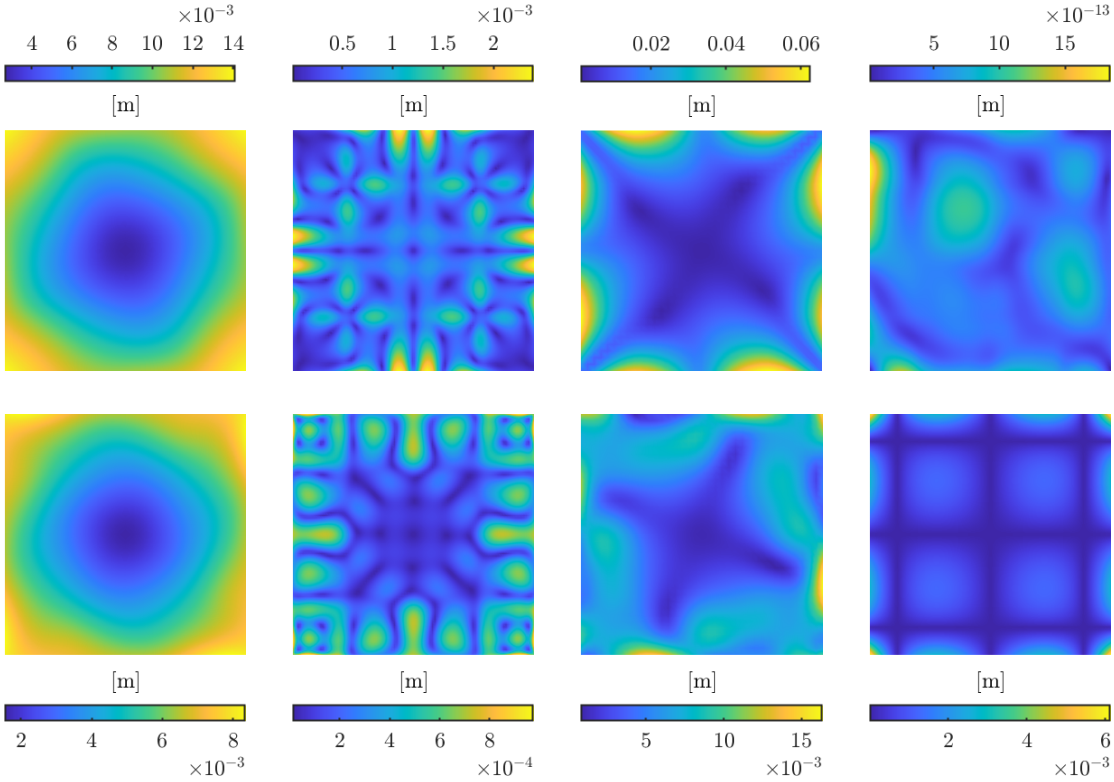

Figure 4.7: *Twisted block.* Approximation and consistency error of $set1$ (columns $1-2$) and $set2$ (columns $3-4$) for $\boldsymbol{p} = (2,2,2)$ (first row) and $\boldsymbol{p} = (3,3,3)$ (second row). Columns 1 and 3: distance d_a plotted over the undeformed interface Γ, cf. Eq. $(4.79)_1$; columns 2 and 4: distance d_c plotted over the undeformed interface Γ, cf. Eq. $(4.79)_2$.

respectively, where the points $\boldsymbol{X}_i$ are uniformly distributed on the reference configuration of the interface.

A comparison of the results for the displacement on the interface is presented in Table 4.1 and Figure 4.7 for the different dimensions of the Lagrange multiplier space. In Figure 4.7, the top row shows the results of the triquadratic approach and the bottom row the results of the tricubic approximation, where the first two columns correspond to $set1$ and the last two columns to $set2$. Furthermore, columns 1 and 3 show the distance d_a and columns 2 and 4 show d_c, both plotted over the undeformed reference configuration of

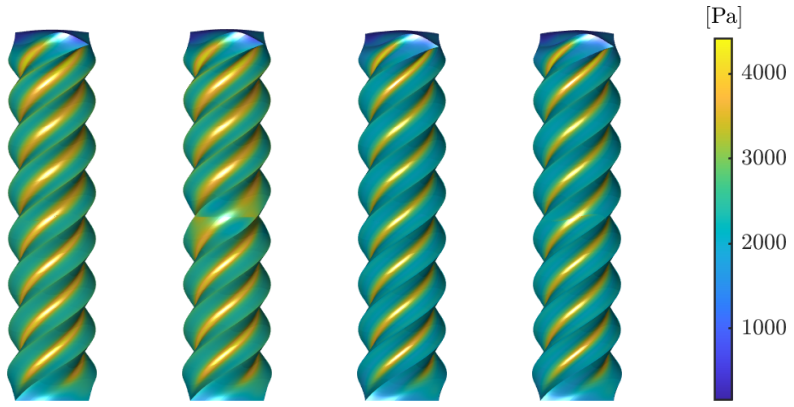

Figure 4.8: *Twisted block.* Von Mises stress distribution of *set*1 (pic. 1 and 3) and *set*2 (pic. 2 and 4) with $\boldsymbol{p} = (2,2,2)$ (pic. 1, 2) and $\boldsymbol{p} = (3,3,3)$ (pic. 3, 4).

the interface. In the triquadratic case as well as in the tricubic case, the approximation and consistency error of *set*1 are nearly of the same order of magnitude, such that with a ratio of $tot_a/tot_c \approx 12.834$ for $\boldsymbol{p} = (2,2,2)$ and $tot_a/tot_c \approx 16.809$ for $\boldsymbol{p} = (3,3,3)$ a reasonable distribution of the total error is archived in the sense that neither error dominates the overall error performance. A different behaviour is shown by *set*2. With increasing dimension of $\mathcal{M}_{\mathrm{h}}$, the consistency error reduces in the triquadratic case at the price of the approximation error up to machine precision, which with a ratio of $tot_a/tot_c \approx 3.48 \cdot 10^{10}$ leads to a highly unbalanced distribution of the total error. The effect on the approximation quality in the region of the interface becomes even more evident considering the stress distribution in Figure 4.8, where a locking effect is quite visible. On the other hand, the cubic approach shows a totally different behaviour as the dimension of the multiplier space is increased. While the consistency error decreases in the quadratic approach, both the approximation error and the consistency error remain almost unchanged and the ratio becomes $tot_a/tot_c \approx 8.30$.

4.7.3 Shell: Bended plate

In our first example concerning the Kirchhoff-Love shell theory, we investigate the influence of a G^1 coupling on the approximation quality by comparing the performance of a 2-patch system with that of a 1-patch system. For this purpose, we apply a static setting where we consider a thin plate, the left end of which is fixed, while the right end is subjected to an external moment. The reference configuration of the plate is given by $\Omega_0 = (0,1) \times (0,0.1) \times \{0\}$, where in the 2-patch case it is described as the union of the two parts $\Omega_0^{(1)} = (0,0.5) \times (0,0.1) \times \{0\}$ (slave side), $\Omega^{(2)} = (0.5,1) \times (0,0.1) \times \{0\}$ (master side) so that the interface is given by $\Gamma = \{0.5\} \times (0,0.1) \times \{0\}$. We also assume a thickness of $h = 0.002\,\mathrm{m}$ and a compressible material described by the elastic potential

$$\mathrm{W}(\mathrm{I}_{\mathbf{C}}, \mathrm{II}_{\mathbf{C}}, \mathrm{III}_{\mathbf{C}}) = \frac{\mu_1}{2}\left(\mathrm{III}_{\mathbf{C}}^{-\frac{1}{3}}\mathrm{I}_{\mathbf{C}} - 3\right) + \frac{\mu_2}{4}\left(\mathrm{III}_{\mathbf{C}} - 1 - 2\ln(\sqrt{\mathrm{III}_{\mathbf{C}}})\right), \tag{4.81}$$

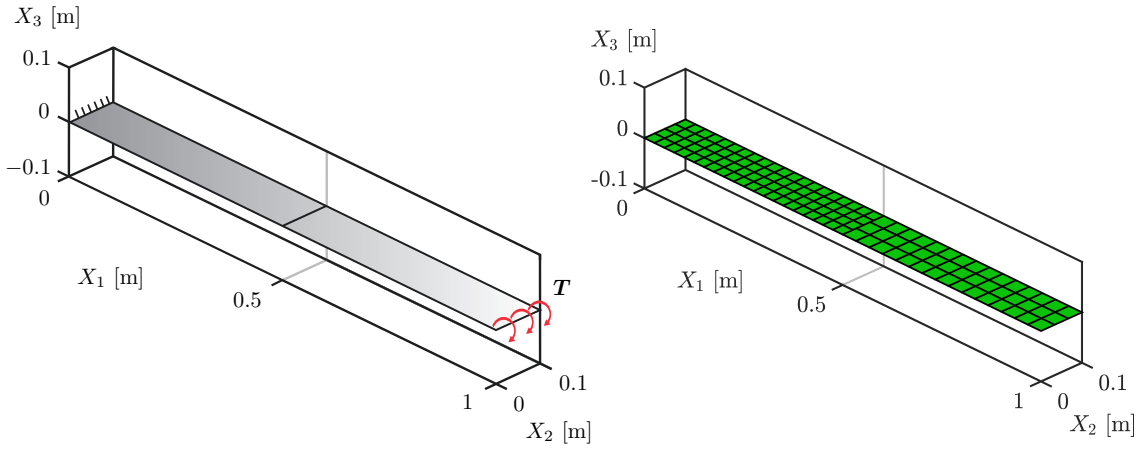

Figure 4.9: *Bended plate.* Reference configuration and boundary conditions (left), computational mesh in the first refinement level (right).

with the material parameters $\mu_1 = 5/3\,\mathrm{MPa}$, $\mu_2 = 10/9\,\mathrm{MPa}$, see Figure 4.9 for illustration. The external moment is chosen so that a tip rotation of 360° is expected, bending the straight plate into a circle. With Young's modulus E, moment of inertia I and the plate length l, the corresponding bending moment is thus given by $M = 2\pi EI/l$. To illustrate the scenario, Figure 4.10 shows the simulation results of a 2-patch system with bi-quartic ($\boldsymbol{p} = (4, 4)$) shape functions during different load steps. It can be observed that due to

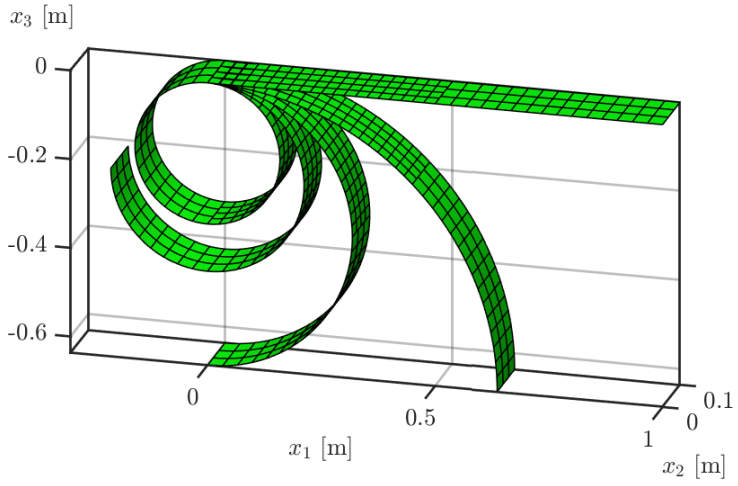

Figure 4.10: *Bended plate.* Deformation of a bi-quartic 2-patch plate during different load steps.

the high approximation quality of the bi-quartic shape functions, acceptable results can be achieved even with a small number of elements. In each of the steps shown, the plate is deformed by an incremental rotation of 90°, resulting in a quarter, half, three-quarter and full circle each with a perimeter of $l = 1$.

For the convergence studies, we consider a total of six refinement levels, whereby in the

kth level the 1-patch system (P1) is resolved with respect to the geometric dimensions of the plate by $(2^{k+1} \cdot 10) \times 2^{k+1}$ elements and the 2-patch system (P2) is resolved by $(2^{k+1} \cdot 5) \times 2^{k+1}$ (slave side $\Omega_0^{(1)}$) and $((2^{k+1}-1) \cdot 5) \times (2^{k+1}-1)$ (master side $\Omega_0^{(2)}$) elements. Notice that in Figure 4.10 a resolution according to the first refinement level is shown. Note also that with these resolutions the master side always takes one element less in the ξ_2-direction than the slave side, resulting in each level in non-conforming meshes. In particular, the element boundaries do not generally coincide. Therefore we use here and in the following examples concerning shell elements a segment-based integration scheme for the evaluation of the corresponding mortar integrals, cf. Section 3.2.3.

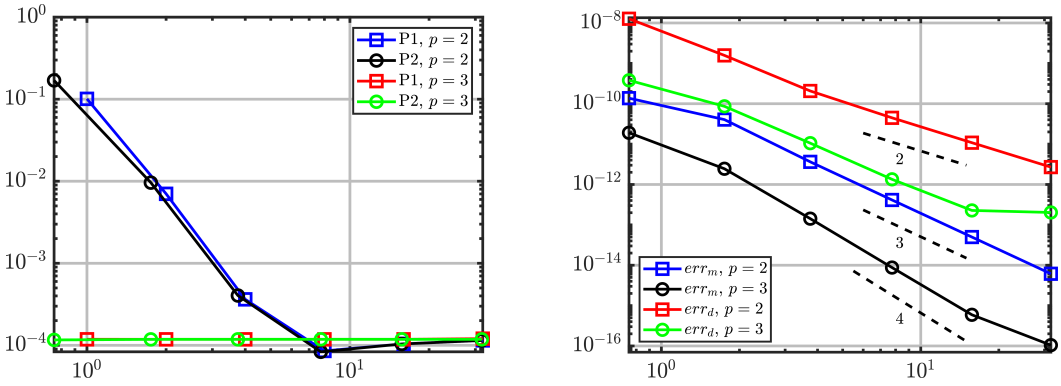

Figure 4.11: *Bended plate.* Mean value $err_d = (d_1 + d_2)/2$ of the two distances d_1, d_2 introduced in Eq. (4.82) as a function of the inverse mesh size h^{-1} (left), interface errors err_m, err_d introduced in Eq. (4.83) as functions of the inverse mesh size h^{-1} (right)

A numerical error study of the motion of the two systems is provided in the left picture in Figure 4.11 for different spline degrees. Since the current configuration is supposed to describe a circle, we use the mean value $err_d = (d_1 + d_2)/2$ of the two distances,

$$d_1 = \|\boldsymbol{s}_\mathrm{h}(1,0)\|, \quad d_2 = \|\boldsymbol{s}_\mathrm{h}(1,1) - (0,0.1)^\mathrm{T}\|, \tag{4.82}$$

as error measure, where $\boldsymbol{s}_\mathrm{h}(1,0)$ is the lower right and $\boldsymbol{s}_\mathrm{h}(1,1)$ the upper right corner of the plate in the actual configuration[‡‡] according to Assumption 2.1.1. Roughly speaking, we measure how tightly the circle has been closed. For both the biquadratic and bicubic approximation functions, P1 and P2 show the same convergence behaviour, which indicates that the additional coupling conditions in P2 have no influence on the approximation quality of the system. In addition, it can be observed that in all the cases above a magnitude of 10^{-4}, the error does not decrease any further. Due to the high approximation quality, the error in the tricubic approach is already of this order of magnitude in the first refinement level, so that no convergence behaviour can be observed. It should be noted, however, that in the context of IGA, the degrees of freedom consist of the control

[‡‡]Note that in the case of the 2-patch system, for the definition of the distances in equation (4.82), $\boldsymbol{s}_\mathrm{h}$ must be replaced by $\boldsymbol{s}_\mathrm{h}^{(2)}$.

points, while the NURBS weights remain unchanged. As we have used different weights to describe the straight plate in the reference configuration than are needed to represent a circle, the results in this example cannot describe an exact circle.

Additional, the right image in Figure 4.11 shows the error behaviour regarding the G^1 coupling of the 2-patch system as a function of the inverse mesh size, whereby the position and derivative conditions are considered separately. The following are used here as error measure

$$err_m = \|\boldsymbol{s}_{\mathrm{h}}^{(1)} - \boldsymbol{s}_{\mathrm{h}}^{(2)} \circ \mathrm{P}_2^1 \|_{L^2(\hat{\Gamma}_2^1)}, \quad err_d = \frac{1}{2}\sum_{i=1}^{2} \|\partial_i \boldsymbol{s}_{\mathrm{h}}^{(1)} - \sum_{j=1}^{2} (\gamma_j^i \partial_j \boldsymbol{s}_{\mathrm{h}}^{(2)}) \circ \mathrm{P}_2^1 \|_{L^2(\hat{\Gamma}_2^1)}, \quad (4.83)$$

where $\hat{\Gamma}_2^1$ is the pre-image of Γ under the geometric map corresponding to the reference configuration of the slave side and $\mathrm{P}_2^1 \colon \hat{\Gamma}_2^1 \to \hat{\Gamma}_1^2$ the corresponding parametric map as introduced in Section 2.1.4. In the first refinement level, the errors are in the order of $1.2 \cdot 10^{-8}$ to $1.9 \cdot 10^{-11}$, such that the coupling conditions are already well fulfilled. In the further course, the derivative error err_d in the biquadratic system reduces according to a convergence order of 2, the errors err_m and err_d in the biquadratic and bicubic system, respectively, according to an order of 3 and err_m in the bicubic system according to an order of 4. Furthermore, it can be seen that err_d in the bicubic system does not decrease further in the last refinement step, whereby an order of magnitude of $2 \cdot 10^{-13}$ is already reached there. Eventually, machine precision is reached by err_m in the bicubic case, leading to a flattening of the error curve.

4.7.4 Shell: Inner pressure

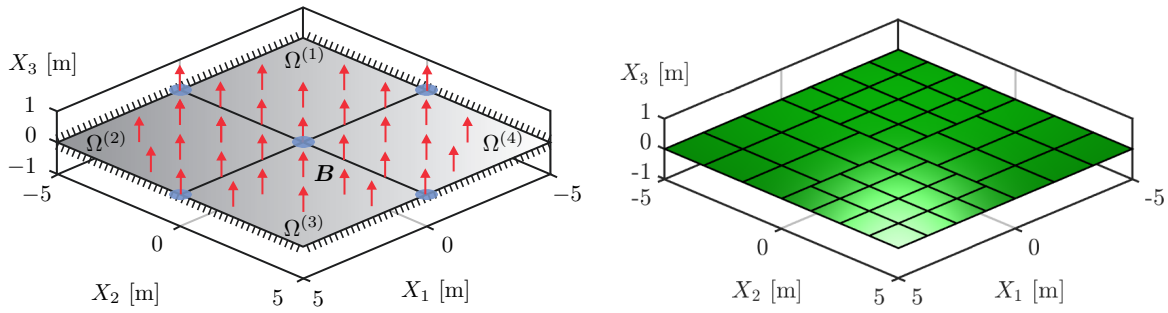

Figure 4.12: *Inner pressure.* Reference configuration and boundary conditions at $t = 0\,\mathrm{s}$ (left), computational mesh in the first refinement level (right). The five crosspoints are marked with blue bullets.

In this section, we study the error behaviour of a G^1 coupling in a dynamic 4-patch system with crosspoints. In this context, we also investigate the influence of the choice of the master and slave side in terms of the number of elements and consider couplings with different orders of the underlying shape functions. For this purpose, we consider

Table 4.2: *Inner pressure.* Numbering of the non-empty interfaces $\Gamma_{i,j} \leftrightarrow \Gamma_k$ (left) and assignment of the master- and slave-side at each interface Γ_k (right).

(i,j)	$(1,2)$	$(2,3)$	$(3,4)$	$(1,4)$
k	1	2	3	4

k	1	2	3	4
$(s(k), m(k))$	$(1,2)$	$(2,3)$	$(3,4)$	$(4,1)$

in the time period $I = [0, 10]$ a square plate with a reference configuration of the form $\bar{\Omega}_0 = \bigcup_{i=1}^{4} \bar{\Omega}_0^{(i)}$, where the four patches are given by

$$\Omega_0^{(1)} = (-5, 0) \times (-5, 0) \times \{0\}, \qquad \Omega_0^{(2)} = (0, 5) \times (-5, 0) \times \{0\}, \tag{4.84}$$

$$\Omega_0^{(3)} = (0, 5) \times (0, 5) \times \{0\}, \qquad \Omega_0^{(4)} = (-5, 0) \times (0, 5) \times \{0\}. \tag{4.85}$$

The plate has a thickness of $h = 0.1\,\mathrm{m}$, a mass density of $\rho_0 = 100\,\mathrm{kg/m^3}$ and consists of an incompressible material described by the elastic potential

$$\mathrm{W}(\mathrm{I}_{\mathbf{C}}, \mathrm{II}_{\mathbf{C}}, \mathrm{III}_{\mathbf{C}}) = \frac{\mu}{2}(\mathrm{I}_{\mathbf{C}} - 3) - p(\sqrt{\mathrm{III}_{\mathbf{C}}} - 1), \tag{4.86}$$

where $\mu = 1\,\mathrm{kPa}$ and the incompressibility condition $(\sqrt{\mathrm{III}_{\mathbf{C}}} - 1) = 0$ is enforced via a Lagrange multiplier p. It is further assumed that the four patches are subjected to internal pressure, which for $i = 1, \ldots, 4$, is modelled by the body forces $\boldsymbol{B}^{(i)} \colon \hat{\Omega} \times I \to \Omega_0^{(i)}$

$$\boldsymbol{B}^{(i)}(\xi_1, \xi_2, t) = \begin{cases} 10t\boldsymbol{a}_3(\xi_1, \xi_2, t), & \text{if } \|\boldsymbol{S}^{(i)}(\xi_1, \xi_2)\| \leq 5, \\ \mathbf{0}, & \text{otherwise,} \end{cases} \tag{4.87}$$

where $\boldsymbol{S}^{(i)}$ is the parametrisation of $\Omega_0^{(i)}$ and $\boldsymbol{a}_3$ denotes the corresponding normal as introduced in Section 4.6.1, see also Figure 4.12 and Figure 4.13 for the illustration of the setting. In addition, Table 4.2 provides an overview of the numbering of the interfaces and the assignment of the master- and slave-side at each interface. As initial condition, we assume for each patch a zero velocity $\dot{\boldsymbol{s}}^{(i)}(\xi_1, \xi_2, 0) = \mathbf{0}$, $(\xi_1, \xi_2) \in \hat{\Omega}$, and with regard to the boundary condition we assume that the outer edges of the four patches are fixed. Thus, in addition to the apparent crosspoint in the centre of Ω_0, four further crosspoints result from the coincidence of the boundaries of the interfaces with the boundary parts $\Gamma_{\mathrm{e}}^{(i)}$. The set of points at which a corresponding modification of the multiplier space is required is therefore given by

$$\mathfrak{C} = \left\{ \begin{pmatrix} 0 \\ 0 \\ 0 \end{pmatrix}, \begin{pmatrix} 0 \\ -5 \\ 0 \end{pmatrix}, \begin{pmatrix} 5 \\ 0 \\ 0 \end{pmatrix}, \begin{pmatrix} 0 \\ 5 \\ 0 \end{pmatrix}, \begin{pmatrix} -5 \\ 0 \\ 0 \end{pmatrix} \right\}, \tag{4.88}$$

whereby we use a reduced modification in this example, cf. Section 3.2.2. In the temporal discretisation, we perform 10 time steps of length 1 and for the convergence studies we again consider a total of six refinement levels in the spatial discretisation, where in the kth level the ith patch is resolved by $2^{k+1} \times 2^{k+1}$ elements if i is odd and by $(2^{k+1}-1) \times (2^{k+1}-1)$

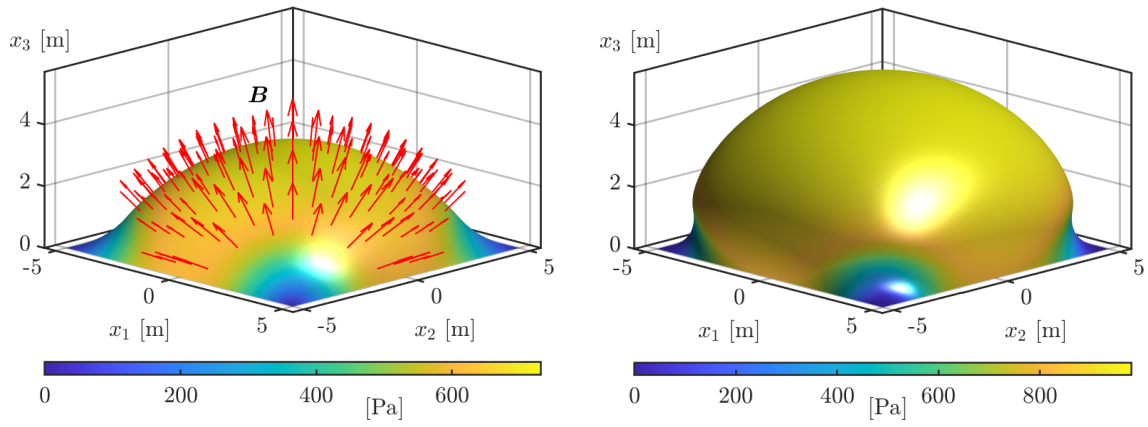

Figure 4.13: *Inner pressure.* Deformation of a bi-quartic 4-patch plate (setting $cp(4,4)$, 6th refinement level) subjected to the body-force $\boldsymbol{B}$. Left: von Mises stress distribution and body-force at $t = 3\,\mathrm{s}$; right: von Mises stress distribution at $t = 10\,\mathrm{s}$.

elements if i is even, see Figure 4.12 for illustration of the first refinement level. Note that here the resolutions and slave sides are chosen so that the number of elements on the two sides of each interface differs by one. Thereby, in the sub-skeleton $\Gamma_1 \cup \Gamma_3$, there are more elements on the slave sides, whereas in the part $\Gamma_2 \cup \Gamma_4$, there are more elements on the master sides. In order to take this into account and to examine the effect on the couplings, we consider the two skeleton parts separately. Furthermore, as in the previous example, the position and derivative errors corresponding to the G^1 couplings are also considered separately. Therefore we utilise the three functions

$$\begin{aligned} E^{[0]}(\boldsymbol{s}_{\mathrm{h}}^{(\mu)}, \boldsymbol{s}_{\mathrm{h}}^{(\nu)}) &= \| \boldsymbol{s}_{\mathrm{h}}^{(\mu)} - \boldsymbol{s}_{\mathrm{h}}^{(\nu)} \circ \mathrm{P}_{\nu}^{\mu} \|_{L^2(\hat{\Gamma}_{\nu}^{\mu})}, \\ E^{[k]}(\boldsymbol{s}_{\mathrm{h}}^{(\mu)}, \boldsymbol{s}_{\mathrm{h}}^{(\nu)}) &= \| \partial_k \boldsymbol{s}_{\mathrm{h}}^{(\mu)} - \sum_{j=1}^{2} (\gamma_j^i \partial_j \boldsymbol{s}_{\mathrm{h}}^{(\nu)}) \circ \mathrm{P}_{\nu}^{\mu} \|_{L^2(\hat{\Gamma}_{\nu}^{\mu})}, \quad k = 1, 2, \end{aligned} \tag{4.89}$$

where $\boldsymbol{s}_{\mathrm{h}}^{(i)}$ denotes the approximation on $\Omega^{(i)}$ at time $t = 10$, $E^{[0]}(\boldsymbol{s}_{\mathrm{h}}^{(\mu)}, \boldsymbol{s}_{\mathrm{h}}^{(\nu)})$ quantifies the position error and $E^{[k]}(\boldsymbol{s}_{\mathrm{h}}^{(\mu)}, \boldsymbol{s}_{\mathrm{h}}^{(\nu)})$, $k \in \{1, 2\}$, the derivative error with respect to ξ_k on the interface $\Gamma_{\mu,\nu}$. Using these functions, we eventually define on $\Gamma_1 \cup \Gamma_3$ the relative L^2 errors

$$err_{1,3}^{[k]} = \frac{1}{2} \sqrt{\left[E^{[k]}(\boldsymbol{s}_{\mathrm{h}}^{(1)}, \boldsymbol{s}_{\mathrm{h}}^{(2)}) \right]^2 + \left[E^{[k]}(\boldsymbol{s}_{\mathrm{h}}^{(3)}, \boldsymbol{s}_{\mathrm{h}}^{(4)}) \right]^2}, \quad k = 0, 1, 2, \tag{4.90}$$

and similarly on $\Gamma_2 \cup \Gamma_4$ the error measures

$$err_{2,4}^{[k]} = \frac{1}{2} \sqrt{\left[E^{[k]}(\boldsymbol{s}_{\mathrm{h}}^{(2)}, \boldsymbol{s}_{\mathrm{h}}^{(3)}) \right]^2 + \left[E^{[k]}(\boldsymbol{s}_{\mathrm{h}}^{(4)}, \boldsymbol{s}_{\mathrm{h}}^{(1)}) \right]^2}, \quad k = 0, 1, 2, \tag{4.91}$$

at $t = 10$. In addition to the L^2 errors, the influence of the spline degree on the G^1 coupling is also considered in the following. For this purpose, we specify five different settings as follows

- $cp(p,p)$: $\boldsymbol{p}^{(i)} = (p,p)$, $i = 1,\dots,4$, with $p \in \{2,3,4\}$,
- $cp(p,q)$: $\boldsymbol{p}^{(i)} = (p,p)$, $i = 1,3$, $\boldsymbol{p}^{(i)} = (q,q)$, $i = 2,4$, with $q = p-1$ and $p \in \{3,4\}$,

where $\boldsymbol{p}^{(i)}$ denotes the order of the shape functions corresponding to the ith patch. Note that in the first three settings, the order on the slave and master sides is the same, whereas in the last two settings, there is a coupling of different orders, i.e. the spline order on the master and slave sides of each interface differs by one.

A numerical error study concerning the G^1 conditions is provided in Figure 4.14. The first row shows $err_{1,3}^{[k]}$ and the second row $err_{2,4}^{[k]}$ for $k = 0,1,2$, both as functions of the inverse mesh size h^{-1}, where the errors are arranged from left to right with increasing k. Independent of the spline degree, almost all settings show qualitatively the same

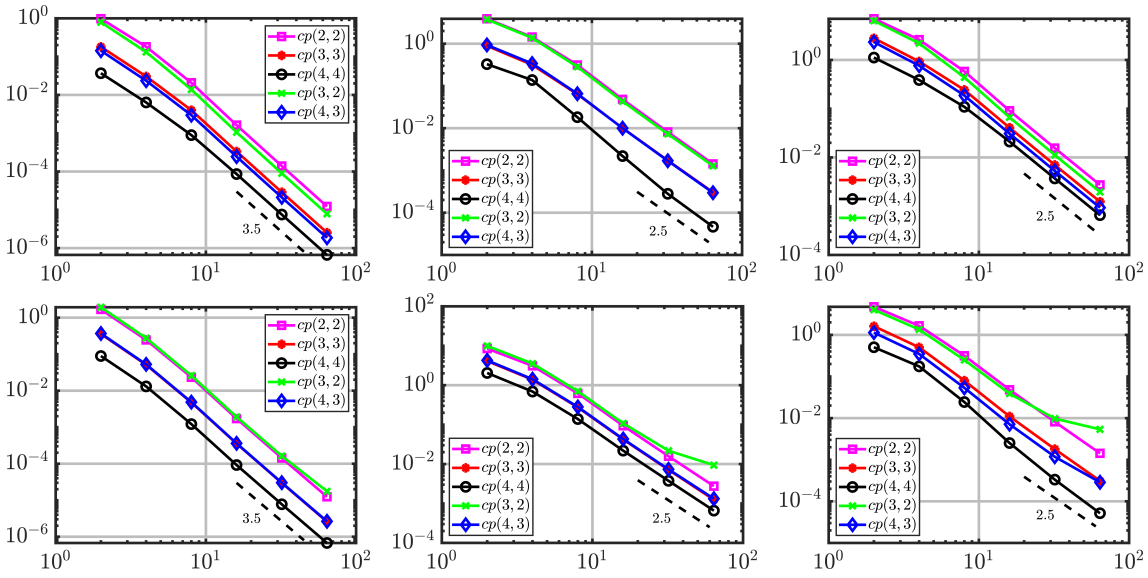

Figure 4.14: *Inner pressure.* First row: $err_{1,3}^{[k]}$ for $k = 0,1,2$ (from left to right) as functions of the inverse mesh size h^{-1}; second row: $err_{2,4}^{[k]}$ for $k = 0,1,2$ (from left to right) as functions of the inverse mesh size h^{-1}.

convergence behaviour. In the case $k = 0$, the errors reduce according to a convergence order of 3.5, whereas in the cases $k = 1,2$ the errors reduce according to an order of 2.5. The choice of the slave side also seems to have a minor influence, so that the errors $err_{1,3}^{[k]}$ (more elements on the slave side) and $err_{2,4}^{[k]}$ (more elements on the master side) also behave qualitatively the same for each k, except the derivative errors of the different order couples $cp(3,2)$ and $cp(4,3)$. In $cp(3,2)$, a flattening of the error curve corresponding to $err_{2,4}^{[1]}$ and $err_{2,4}^{[2]}$ can be observed in the last refinement step, where a similar behaviour is shown by $err_{2,4}^{[2]}$ of $cp(4,3)$. However, it should be noted that in these constellations there are both, fewer elements and a reduced spline order on the slave side, so that the approximation quality of the shape functions on the master side is significantly higher. Finally, it should be noted that the coupling errors do not behave completely independently of the choice

of the spline orders and slave sides. Quantitatively, it can be seen that in all cases the errors decrease with increasing spline order. In addition, the errors increase when a side with fewer elements is chosen as the slave side.

4.7.5 Shell: Pinched cylinder

In many practical applications of multi-patch isogeometric Kirchhoff-Love shell elements, the geometries and computational meshes are such that the patches meet C^1-continuously. For example, this has been the case in the two previous examples. In this section, we compare the general G^1 case with the special case of a C^1 coupling, examining the error behaviour at the interfaces in both cases. In addition, the necessity of working with G^1 couplings in the Kirchhoff-Love theory is demonstrated by considering a C^0 coupling.

We consider a static system consisting of a cylinder given in its reference configuration by $\bar{\Omega}_0 = \bar{\Omega}_0^{(1)} \cup \bar{\Omega}_0^{(2)}$, where the two patches are defined through

$$\begin{aligned} \Omega_0^{(1)} &= \left\{ \boldsymbol{X} \in \mathbb{R}^3 \,|\, X_1^2 + X_3^2 = 1,\, X_3 < 0,\, X_2 \in (-1.5, 1.5) \right\}, \\ \Omega_0^{(2)} &= \left\{ \boldsymbol{X} \in \mathbb{R}^3 \,|\, X_1^2 + X_3^2 = 1,\, X_3 > 0,\, X_2 \in (-1.5, 1.5) \right\}, \end{aligned} \tag{4.92}$$

so that the entire cylinder has a radius of 1 m, a height of 3 m and the interface is located in the $X_1 - X_2$ plane, i.e. $\Gamma = \{\boldsymbol{X} \in \mathbb{R}^3 \,|\, |X_1| = 1,\, X_2 \in (-1.5, 1.5)\}$. Note that, according to the notation introduced in Section 2.1.4, there is only one interface, consisting of two unconnected parts. The lower part of the cylinder is assumed to be fixed along the line $\Gamma_{\mathrm{e}} = \{\boldsymbol{X} \in \mathbb{R}^3 \,|\, X_1 = 0,\, X_3 = -1,\, X_2 \in (-1.5, 1.5)\}$, whereby a line load

$$\boldsymbol{T}_k \colon \mathbb{R}^3 \to \mathbb{R}^3, \quad \boldsymbol{T}_k(\boldsymbol{X}) = \begin{cases} (0, 0, -1)^{\mathrm{T}} l_k & \text{if } \boldsymbol{X} \in \Gamma_{\mathrm{n}}, \\ \boldsymbol{0} & \text{otherwise}, \end{cases} \tag{4.93}$$

is acting on the upper line $\Gamma_{\mathrm{n}} = \{\boldsymbol{X} \in \mathbb{R}^3 \,|\, X_1 = 0,\, X_3 = 1,\, X_2 \in (-1.5, 1.5)\}$, see Figure 4.15 for illustration. In the simulations, the total load is applied stepwise through seven load steps, so that the intensity within the kth step is given by $l_k = (5k/2)\,\mathrm{N/m}$ in the case of a G^1 coupling, where a lower intensity of $l_k = (5k/4)\,\mathrm{N/m}$ is applied in the C^0 case. Eventually, we assume that the walls of the cylinder are 0.02 m thick and consist of an incompressible material specified by the elastic potential (4.86) and the material parameter $\mu = 1\,\mathrm{MPa}$.

For the parametrisation of the two patches, we use bicubic shape functions, such that the lower patch consists of 20×20 elements and the upper one of 18×18. Thereby, the NURBS weights are chosen such that respective parametrisations represent two perfect half-cylinders. Further, we consider two different settings in which we implemented G^1-continuous coupling conditions and a third one with a C^0 coupling. In the first G^1-setting ($set1$), the control points of the parametrisations are distributed in such a way that the mesh of the two patches consists of curved, rectangular elements, leading to a C^1-continuous transition at the interface as shown in the upper right and lower left picture in Figure 4.15. In the second G^1-setting ($set2$), the control points at the interface are shifted

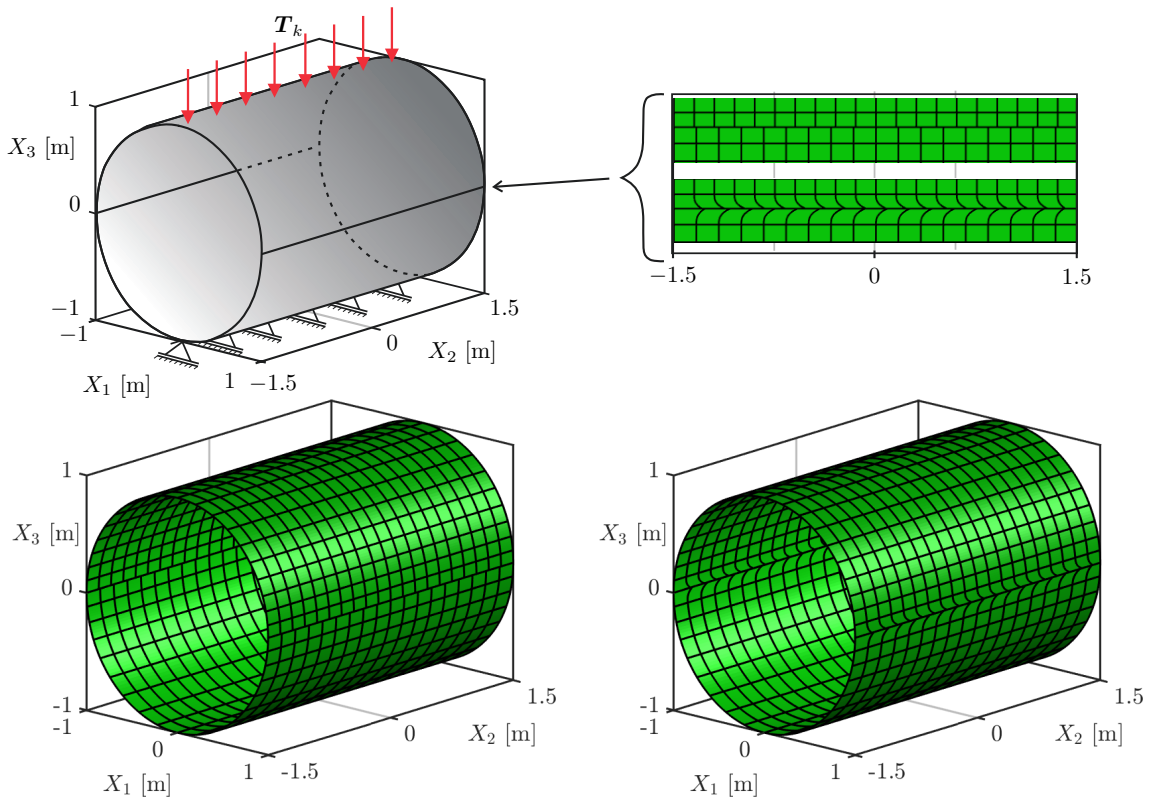

Figure 4.15: *Pinched cylinder*. Upper left: Reference configuration and boundary conditions. Upper right: Detailed view of the computational meshes at the interface, where the upper picture shows the mesh of *set*1 and *set*3 and the lower one the mesh of *set*2. Lower left: computational mesh of *set*1 and *set*3. Lower right: computational mesh of *set*2.

along the X_2-direction such that the elements are heavily distorted in this area, resulting in a more general G^1 situation, cf. the upper and lower right picture in Figure 4.15. To be more specific. In *set*1 the G^1 parameter functions γ_i^j, cf. Section 2.1.5, are constant and given by $(\gamma_1^1, \gamma_2^1, \gamma_1^2, \gamma_2^2) = (1, 0, 0, 1)$, such that the patch-parametrisations satisfy Eq. (2.24) on Γ. In *set*2, however, the functions γ_j^i take on different values depending on the location, such that only the more general condition (2.25) is satisfied on Γ. Eventually, in the C^0-setting (*set*3) the same mesh as in *set*1 is used. For further illustration, the simulation results corresponding to *set*2 and *set*3 are shown in Figure 4.16, where the displacement lengths

$$d_l^{(i)}(\boldsymbol{\xi}) := \|\boldsymbol{s}_{\mathrm{h}}^{(i)}(\boldsymbol{\xi}) - \boldsymbol{S}_{\mathrm{h}}(\boldsymbol{\xi})\|, \quad i = 1, 2, \quad \xi \in \hat{\Omega}, \tag{4.94}$$

are plotted over the deformed configuration. Thereby, we have refrained from presenting the results of *set*1, as they are almost identical to those of *set*2. Figure 4.16 shows that a C^0 coupling does not allow for a transfer of bending moments across the interface. Here, even for a reduced load, the simulation yields large deformations with almost self-contact. The situation is quite different in the case of the G^1 coupling. Even for the highly distorted meshes at the interface the coupling conditions can counterbalance the

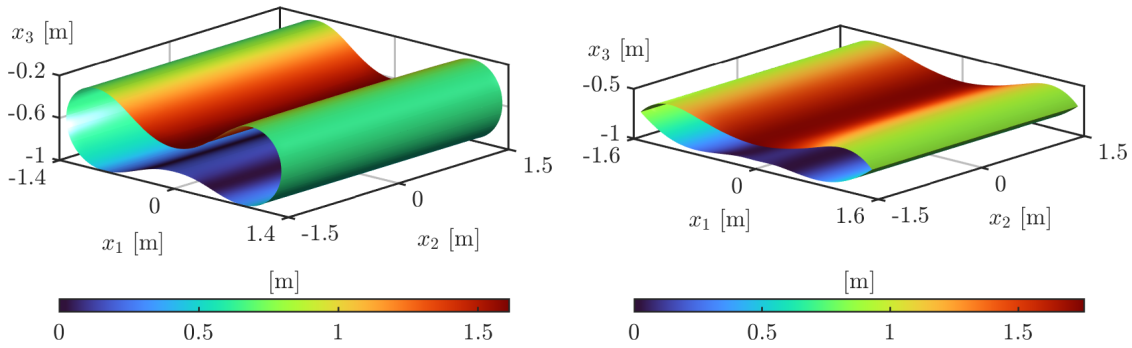

Figure 4.16: *Pinched cylinder.* Contour plots of the displacement lengths $d_l^{(i)}$, $i = 1, 2$, from Eq. (4.94) on the deformed configurations corresponding to *set*2 (left) and *set*3 (right).

non-matching meshes and result in an acceptable approximation.

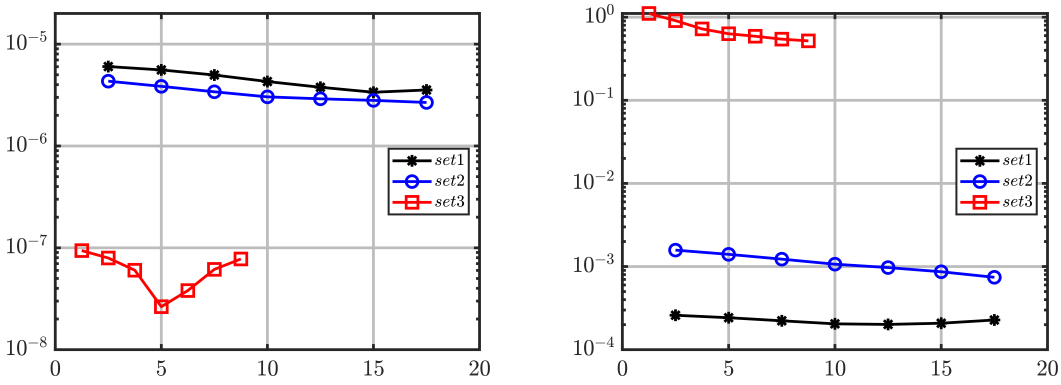

Figure 4.17: *Pinched cylinder.* Relative displacement error $err^{[0]}$ (left) and relative derivative error $err^{[1]}$ (right). Both are shown as a function of the load intensity l_k, cf. Eq. (4.93).

A numerical error study concerning the coupling conditions on the interface is provided in Figure 4.17, where we consider the two relative errors defined through

$$err^{[0]} = \frac{1}{2m_d} E^{[0]}(\boldsymbol{s}_{\mathrm{h}}^{(1)}, \boldsymbol{s}_{\mathrm{h}}^{(2)}), \quad err^{[1]} = \frac{1}{4m_d} \sum_{i=1}^{2} E^{[i]}(\boldsymbol{s}_{\mathrm{h}}^{(1)}, \boldsymbol{s}_{\mathrm{h}}^{(2)}), \tag{4.95}$$

with the quantities $E^{[i]}$ introduced in Eq. (4.89) and the maximal displacement length $m_d = \max\{\max_{\boldsymbol{\xi}\in\hat{\Omega}} d_l^{(1)}(\boldsymbol{\xi}), \max_{\boldsymbol{\xi}\in\hat{\Omega}} d_l^{(2)}(\boldsymbol{\xi})\}$. The picture on the left shows $err^{[0]}$ as a function of the load intensity l_k, cf. Eq.(4.93), so that the curves represent the course of the displacement error during the load pick-up. It can be observed that the errors of *set*1 and *set*2 are of the same order of magnitude, with both errors remaining almost constant as the load increases. Over the entire course, the error of *set*2 lies in $(3.3 \cdot 10^{-6}, 6.1 \cdot 10^{-6})$ and is even slightly smaller than the error of *set*1, which lies in $(2.6 \cdot 10^{-6}, 4.4 \cdot 10^{-6})$. Furthermore,

the error of *set*3 ranges between $2.6 \cdot 10^{-8}$ and $9.4 \cdot 10^{-8}$ and is thus significantly smaller than the errors corresponding to the G^1 couplings, which was, however, to be expected. According to Section 3.1.2, in a C^0 coupling the underlying minimisation problem is specified by a functional $\mathrm{M}_0 \colon \mathcal{S}^{(1)} \times \mathcal{S}^{(2)} \to \mathbb{R}$ of the form (3.4) with $n = 0$, whereas in a G^1 coupling the corresponding functional $\mathrm{M}_1 \colon \mathcal{S}^{(1)} \times \mathcal{S}^{(2)} \to \mathbb{R}$ is given by (3.5). This immediately gives rise to the relation

$$\inf_{\boldsymbol{w} \in \mathcal{S}^{(1)}} \mathrm{M}_0(\boldsymbol{w}, \boldsymbol{s}^{(2)}) \leq \inf_{\boldsymbol{w} \in \mathcal{S}^{(1)}} \mathrm{M}_1(\boldsymbol{w}, \boldsymbol{s}^{(2)}), \tag{4.96}$$

for all admissible solutions $\boldsymbol{s}^{(2)} \in \mathcal{S}^{(2)}$, which is reflected here by the results. Moreover, the right picture in Figure 4.17 shows the derivative error $err^{[1]}$ as a function of the load intensity l_k. Here, the error of *set*2 lies in $(7.3 \cdot 10^{-4}, 1.6 \cdot 10^{-3})$ and is thus slightly larger than the error of *set*1, which ranges between $2 \cdot 10^{-4}$ and $2.6 \cdot 10^{-4}$. Eventually, the error of *set*3 lies in $(0.5, 1.5)$ reflecting the kink in the transition area shown in the right picture in Figure 4.16.

5 Thermal conduction and diffusion

In this chapter, we investigate the application of the extended mortar method to heat conduction and mass diffusion problems. To this end, we discuss the theoretical foundations in the first two sections, where we introduce the two classical balance principles of conservation of mass and conservation of energy in Section 5.1. Based on these principles, in Section 5.2 we formulate evolution equations for the distribution of the absolute temperature in a body and the mass distribution in a binary alloy and derive corresponding multi-patch frameworks. The first equation is the well-known heat equation, whose variational statement naturally contains derivatives up to the 1st order and can be treated in the context of a multi-patch isogeometric analysis with a C^0-continuous basis and corresponding C^0-continuous couplings. The second equation is known as the Cahn-Hilliard equation and contains derivatives up to order 4. Accordingly, the corresponding variational statement involves derivatives up to 2nd order, requiring a C^1-continuous IGA basis and, in the multi-patch case, C^1-continuous couplings. These relationships are examined, among others, in more detail in Section 5.3 by means of various examples.

5.1 Conservation laws

5.1.1 Conservation of mass in a multicomponent system

The presentation in this section is based on de Groot & Mazur [53], whereby we express the relationships in terms of the molar density instead of the mass density. To be specific, we consider a multi-component system consisting of m components in which no chemical reactions take place. Let $\Omega_0 \subset \mathbb{R}^3$ be an open, bounded domain with a sufficiently smooth boundary, in which the system is assumed to be embedded. Then, the rate of change in the mass of component k within an arbitrary open subdomain $\Omega \subset \Omega_0$ can be described by

$$\frac{\mathrm{d}}{\mathrm{d}t} \int_\Omega N_k \, \mathrm{d}V = \int_\Omega \dot{N}_k \, \mathrm{d}V, \quad t \in I, \tag{5.1}$$

where $N_k = n_k/V \colon \bar{\Omega}_0 \times I \to \mathbb{R}_{>0}$ is the molar density of k, $n_k \colon \bar{\Omega}_0 \times I \to \mathbb{R}_{>0}$ the amount of k (expressed in moles), V the volume of Ω and $I = [0, \tau]$, $\tau > 0$, is a real interval representing the timespan under consideration*. Since we have excluded chemical

*We point out, that the molar density N_k is related to the mass density ρ_k of component k by means of $\rho_k = M_k N_k$, where M_k is the molar mass of k. Since M_k is constant, the considerations in this section can alternatively be expressed in terms of the mass density.

reactions, the amount of a substance in Ω can only change if the substance leaves or is added to the domain. In other words, the rate of change (5.1) is equal to the material flow into or out of the domain Ω through its surface, i.e.

$$\int_\Omega \dot{N}_k \, \mathrm{d}V = -\int_{\partial\Omega} N_k \boldsymbol{v}_k \cdot \boldsymbol{N} \, \mathrm{d}\sigma = -\int_\Omega \nabla_{\boldsymbol{X}} \cdot (N_k \boldsymbol{v}_k) \, \mathrm{d}V, \quad t \in I, \tag{5.2}$$

where $\boldsymbol{v}_k \colon \bar{\Omega}_0 \times I \to \mathbb{R}^3$ is the velocity of component k and $\boldsymbol{N}$ the unit outward normal on $\partial\Omega$. Note that the second equation in (5.2) holds due to the Gauss's theorem. Since the subset Ω can be chosen arbitrarily, it follows that the integrands must coincide on the whole domain Ω_0 and we obtain the local version of (5.2) as follows

$$\dot{N}_k = -\nabla_{\boldsymbol{X}} \cdot (N_k \boldsymbol{v}_k), \quad \text{in } \Omega_0 \times I. \tag{5.3}$$

These equations have the form of a so-called balance equation: the local change of the left side is equal to the negative divergence of the flux of k. Summing Eqs. (5.3) over all components k gives rise to the continuity mass equation

$$\dot{N} = -\nabla_{\boldsymbol{X}} \cdot (N \boldsymbol{v}), \quad \text{in } \Omega_0 \times I, \tag{5.4}$$

where $N = N_1 + \cdots + N_m$ is the total molar density, $\boldsymbol{v}$ is the mean molar velocity given by

$$\boldsymbol{v} = \sum_{k=1}^{m} \frac{N_k}{N} \boldsymbol{v}_k = \sum_{k=1}^{m} c_k \boldsymbol{v}_k \tag{5.5}$$

and $c_k := N_k/N$ are the molar fractions of the components. Eq. (5.4) expresses the fact, that the total mass is conserved, i.e. the total mass of any system in which no chemical reactions are taking place, can only change if matter flows into or out of the system.

Finally, we derive an alternative expression of mass conservation in terms of molar fractions and diffusion flows, which we will need for the investigation of diffusion phenomena in Section 5.2. Introducing the substantial time derivative

$$\mathrm{d}_t(\bullet) := \partial_t(\bullet) + \boldsymbol{v} \cdot \nabla_{\boldsymbol{X}}(\bullet) \tag{5.6}$$

and the diffusion flows $\boldsymbol{J}_k := N_k(\boldsymbol{v}_k - \boldsymbol{v})$ defined with respect to the mean molar velocity, Eqs. (5.3), (5.4) can be rewritten as follows

$$\mathrm{d}_t N_k = -N_k \nabla_{\boldsymbol{X}} \cdot \boldsymbol{v} - \nabla_{\boldsymbol{X}} \cdot \boldsymbol{J}_k, \quad \text{in } \Omega_0 \times I, \tag{5.7}$$

$$\mathrm{d}_t N = -N \nabla_{\boldsymbol{X}} \cdot \boldsymbol{v}, \quad \text{in } \Omega_0 \times I. \tag{5.8}$$

Taking into account Eq. (5.8), we now obtain from Eq. (5.7) a balance equation for the molar fractions as follows

$$\mathrm{d}_t c_k = -V_m \nabla_{\boldsymbol{X}} \cdot \boldsymbol{J}_k, \tag{5.9}$$

where V_m denotes the molar volume of the multi-component system. Here it should be noted that the usual differentiation rules apply to the substantial time derivative and that the total molar density and the molar volume are related via $N = V_m^{-1}$.

5.1.2 Conservation of energy

Let us now consider a system assumed to be embedded in an open, bounded domain $\Omega_0 \subset \mathbb{R}^3$ subjected to a motion $\boldsymbol{\varphi}\colon \Omega_0 \times I \to \mathbb{R}^3$, cf. Section 4.1. The first law of thermodynamics states that the energy of the system remains preserved during an entire thermodynamic process. The energy can be transformed from one form into another but it can neither be created nor destroyed. In material description the global form of the energy balance law reads

$$\frac{\mathrm{d}}{\mathrm{d}t}\int\limits_{\Omega_0} \frac{1}{2}\,\rho_0 \dot{\boldsymbol{\varphi}}\cdot\dot{\boldsymbol{\varphi}} + \rho_0 e \;\mathrm{d}V = \int\limits_{\partial\Omega_0} \boldsymbol{T}\cdot\dot{\boldsymbol{\varphi}} + Q_N \;\mathrm{d}\sigma + \int\limits_{\Omega_0} \boldsymbol{B}\cdot\dot{\boldsymbol{\varphi}} + R \;\mathrm{d}V, \quad t \in I, \tag{5.10}$$

where ρ_0 and e are the mass density and the internal energy per unit mass. In addition, $\boldsymbol{T}$ denotes a surface traction, $\boldsymbol{B}$ a body force, Q_N a normal heat flux and R a heat source per unit time and per unit reference volume. According to Cauchy's stress theorem and Stokes' heat flux theorem it holds $\boldsymbol{T} = \mathbf{P}\,\boldsymbol{N}$ and $Q_N = -\boldsymbol{Q}\cdot\boldsymbol{N}$, respectively, where $\mathbf{P}$ and $\boldsymbol{Q}$ are the first Piola-Kirchhoff stress tensor and the Piola-Kirchhoff heat flux vector and $\boldsymbol{N}$ denotes the unit outward normal on $\partial\Omega_0$. Using these relations, we obtain from (5.10) after some standard calculations and under consideration of Eq. (4.37)

$$\int\limits_{\Omega_0} \rho_0 \dot{e} \;\mathrm{d}V = \int\limits_{\Omega_0} \mathbf{P} : \dot{\mathbf{F}} - \nabla_{\boldsymbol{X}}\cdot\boldsymbol{Q} + R \;\mathrm{d}V, \quad t \in I. \tag{5.11}$$

Since Eq. (5.11) holds for an arbitrary subdomain of Ω_0, we can further deduce the local form of the energy balance which reads

$$\rho_0 \dot{e} = \mathbf{P} : \dot{\mathbf{F}} - \nabla_{\boldsymbol{X}}\cdot\boldsymbol{Q} + R, \quad \text{in } \Omega_0 \times I. \tag{5.12}$$

For a rigid motion, i.e. a motion in which no deformation occurs, Eq. (5.12) results in a special case that describes the distribution of the absolute temperature in the underlying body. To be more specific, a motion $\boldsymbol{\varphi}$ is called rigid if $\mathbf{C} = \mathbf{I}$, where $\mathbf{C}$ is the right Cauchy-Green strain tensor and $\mathbf{I}$ the identity tensor. According to Eq. $(4.17)_2$, the Green-Lagrange strain tensor vanishes in this case, i.e. $\mathbf{E} = \mathbf{0}$, and it follows $\mathbf{P} : \dot{\mathbf{F}} = \mathbf{S} : \dot{\mathbf{E}} = 0$, where $\mathbf{S}$ is the second Piola-Kirchhoff stress tensor and we have exploited the identity $\mathbf{P} : \dot{\mathbf{F}} = \mathbf{S} : \dot{\mathbf{E}}$, see Holzapfel [97] for a proof. Consequently, the internal energy of the body depends only on the absolute temperature T and Eq. (5.12) becomes

$$\rho_0 c_{\mathrm{p}} \dot{T} = -\nabla_{\boldsymbol{X}}\cdot\boldsymbol{Q} + R, \quad \text{in } \Omega_0 \times I, \tag{5.13}$$

where $c_{\mathrm{p}} := \partial e/\partial T$ is the specific heat capacity of the system.

5.2 Phenomenological formulations and the differential equations

The conservation equations for mass (5.9) and energy (5.13) have essentially the same structure. They state that the temporal change of the respective quantities corresponds to

the divergence of a flow, whereby sources and sinks in the system under consideration must be taken into account if necessary. In order to fully characterise the temperature or the mole fractions with these equations, the actual task is to provide a suitable model for the corresponding flow. It is known empirically that for a large class of irreversible phenomena and under a wide range of experimental conditions, flows are linear functions of the thermodynamic forces. For a multi-component system with m components subjected to a temperature gradient it is therefore appropriate to describe the diffusion flows $\boldsymbol{J}_k$ and the heat flow $\boldsymbol{Q}$ quite generally by linear relations of the form

$$\boldsymbol{J}_k = \sum_{i=1}^{m} L_{k,i} \left(\boldsymbol{F}_i - (\nabla_{\boldsymbol{X}} \mu_i)_T \right) - L_{k,q} \frac{\nabla_{\boldsymbol{X}} T}{T}, \quad k = 1, ..., m, \tag{5.14}$$

$$\boldsymbol{Q} = \sum_{i=1}^{m} L_{q,i} \left(\boldsymbol{F}_i - (\nabla_{\boldsymbol{X}} \mu_i)_T \right) - L_{q,q} \frac{\nabla_{\boldsymbol{X}} T}{T}, \tag{5.15}$$

where μ_i is the chemical potential of component i, $\boldsymbol{F}_i$ is the external force per atom of i, the quantities $L_{i,j}$ are called phenomenological coefficients and the index T in the expression $(\nabla_{\boldsymbol{X}} \mu_i)_T$ indicates that the gradient has to be taken at constant temperature, c.f. de Groot & Mazur [53], Howard & Lidiard [99]. According to Howard & Lidiard [99], for heat conduction and diffusion phenomena, it is also reasonable to assume that the system under consideration is in mechanical equilibrium, i.e. $\boldsymbol{F}_i = \boldsymbol{0}$, since the adjustments to unbalanced mechanical forces are rapid compared with the adjustments caused by the gradient of the chemical potential or temperature gradient. Furthermore, we consider isotropic systems for which the phenomenological coefficients are scalars in contrast to anisotropic systems where they are tensor-valued quantities and neglect cross effects indicated by the coupling coefficients $L_{q,i}$, $L_{k,i}$. To be more precise, with assumption $L_{k,q} = 0$ we neglect the phenomenon of thermal diffusion, a mass flow caused by a temperature gradient, and with assumption $L_{q,i} = 0$ we neglect the Dufour effect, which conversely is a heat flow caused by a gradient of the chemical potential. For a detailed discussion of models including these effects we refer to Schuß at al. [142]. Eventually, under these assumptions, the flows have the general form

$$\boldsymbol{J}_k = -\sum_{i=1}^{m} L_{k,i} (\nabla_{\boldsymbol{X}} \mu_i)_T, \quad k = 1, ..., m, \quad \boldsymbol{Q} = -L_{q,q} \frac{\nabla_{\boldsymbol{X}} T}{T}. \tag{5.16}$$

In the next two sections, we will use these representations, together with the results from Section 5.1, to establish evolution equations and corresponding multi-patch problems for the absolute temperature and the mole fractions in a binary alloy.

5.2.1 The heat equation and multi-patch framework

According to Fourier's law, $\boldsymbol{Q} = -\lambda \nabla_{\boldsymbol{X}} T$, the thermal conductivity λ is related to the phenomenological coefficient $L_{q,q}$ in Eq. (5.16) by the relationship $\lambda = L_{q,q}/T$. Together with the equation of energy conservation (5.13), this gives the evolution equation

$$\rho_0 c_{\mathrm{p}} \dot{T} = \nabla_{\boldsymbol{X}} \cdot (\lambda \nabla_{\boldsymbol{X}} T) + R, \quad \text{in } \Omega_0 \times I, \tag{5.17}$$

for the absolute temperature, known as the heat equation. Eq. (5.17) characterises for each time point in $I = [0, \tau] \subset \mathbb{R}_{\geq 0}$ the temperature distribution in the domain Ω_0, where the underlying material is defined by the mass density, the specific heat capacity and the conductivity. For a complete characterisation, we further assume that initial and boundary data are given and supplement Eq. (5.17) by the conditions

$$T = T_0, \quad \text{in } \Omega_0 \times \{0\}, \quad T = \bar{T}, \quad \text{on } \Gamma_\mathrm{e} \times I, \quad -\boldsymbol{Q} \cdot \boldsymbol{N} = Q, \quad \text{on } \Gamma_\mathrm{n} \times I, \tag{5.18}$$

where Γ_e, Γ_n are parts of the boundary $\partial\Omega_0$ such that $\bar{\Gamma}_\mathrm{e} \cup \bar{\Gamma}_\mathrm{n} = \partial\Omega_0$ and $\Gamma_\mathrm{e} \cap \Gamma_\mathrm{n} = \emptyset$. In addition, $T_0 \colon \Omega_0 \to \mathbb{R}$ and $\bar{T} \colon \Gamma_\mathrm{e} \times I \to \mathbb{R}$ are prescribed initial and boundary temperature distributions, respectively, $\boldsymbol{N}$ denotes the unit outward normal on Γ_n and Q represents the normal heat flux in or out of Ω_0 through Γ_n.

To derive a corresponding multi-patch framework, we proceed analogously to Section 4.5. Assuming a multi-patch geometry consisting of N patches $\Omega_0^{(1)}, \dots, \Omega_0^{(N)}$, we first note that Eqs. (5.17), (5.18) characterise the temperature distribution on each patch through the N initial boundary value problems

$$\left\{ \begin{array}{c} \rho_0^{(i)} c_\mathrm{p}^{(i)} \dot{T}^{(i)} = \nabla_{\boldsymbol{X}} \cdot (\lambda^{(i)} \nabla_{\boldsymbol{X}} T^{(i)}) + R^{(i)}, \quad \text{in } \Omega_0^{(i)} \times I, \\ T^{(i)} = T_0^{(i)}, \quad \text{in } \Omega_0^{(i)} \times \{0\}, \\ T^{(i)} = \bar{T}^{(i)}, \text{ on } \Gamma_\mathrm{e}^{(i)} \times I, \quad -\boldsymbol{Q}^{(i)} \cdot \boldsymbol{N}^{(i)} = Q^{(i)}, \text{ on } \Gamma_\mathrm{n}^{(i)} \times I, \end{array} \right\} \tag{5.19}$$

where $\Gamma_\mathrm{e}^{(i)} := \Gamma_\mathrm{e} \cap \partial\Omega_0^{(i)}$ and $\Gamma_\mathrm{n}^{(i)} := \Gamma_\mathrm{n} \cap \partial\Omega_0^{(i)}$. By introducing a time grid $0 = t_0 < t_1 < \ldots < t_M = \tau$, we further obtain, according to Appendix A, for each patch a sequence of boundary value problems of the form: for $\nu = 1, \dots, M$ find $T_\nu^{(i)} \colon \bar{\Omega}_0^{(i)} \to \mathbb{R}$ such that

$$\left\{ \begin{array}{c} h_\nu^{-1} \rho_0^{(i)} c_{\mathrm{p},\nu-\frac{1}{2}}^{(i)} (T_\nu^{(i)} - T_{\nu-1}^{(i)}) = \nabla_{\boldsymbol{X}} \cdot [\lambda^{(i)} \nabla_{\boldsymbol{X}} T^{(i)}]_{\nu-\frac{1}{2}} + R_{\nu-\frac{1}{2}}^{(i)}, \quad \text{in } \Omega_0^{(i)}, \\ T_\nu^{(i)} = \bar{T}_\nu^{(i)}, \text{ on } \Gamma_\mathrm{e}^{(i)}, \quad -[\boldsymbol{Q}^{(i)} \cdot \boldsymbol{N}^{(i)}]_{\nu-\frac{1}{2}} = Q_{\nu-\frac{1}{2}}^{(i)}, \text{ on } \Gamma_\mathrm{n}^{(i)}, \end{array} \right\} \tag{5.20}$$

where the start functions are given through the initial condition, $h_\nu := t_\nu - t_{\nu-1}$ is the step-size and the subscripts $[\bullet]_\nu$, $[\bullet]_{\nu-1}$, $[\bullet]_{\nu-1/2}$ indicate the evaluation at t_ν, $t_{\nu-1}$ and $t_{\nu-1/2} := t_{\nu-1} + h_\nu/2$. Introducing the spaces

$$\mathcal{S}_\nu^{(i)} = \left\{ T \in H^1(\Omega_0^{(i)}) \,|\, T = \bar{T}^{(i)}(\bullet, t_\nu) \text{ on } \Gamma_\mathrm{e}^{(i)} \right\}, \tag{5.21}$$

$$\mathcal{V}^{(i)} = \left\{ \delta T \in H^1(\Omega_0^{(i)}) \,|\, T = 0 \text{ on } \Gamma_\mathrm{e}^{(i)} \right\} \tag{5.22}$$

of trial solutions and test functions, multiplication of the differential equation in (5.20) with an arbitrary $\delta T^{(i)} \in \mathcal{V}^{(i)}$ and integration over the respective patch yields, after some standard calculations, a corresponding sequence of weak problems: for $\nu = 1, \dots, M$ find $T_\nu^{(i)} \in \mathcal{S}_\nu^{(i)}$

$$\begin{aligned} \mathrm{V}_\nu^{(i)}(T_\nu^{(i)}, \delta T^{(i)}) := \langle h_\nu^{-1} \rho_0^{(i)} c_{\mathrm{p},\nu-\frac{1}{2}}^{(i)} (T_\nu^{(i)} - T_{\nu-1}^{(i)}) - R_{\nu-\frac{1}{2}}^{(i)}, \delta T^{(i)} \rangle_{\Omega_0^{(i)}} \\ + \langle [\lambda^{(i)} \nabla_{\boldsymbol{X}} T^{(i)}]_{\nu-\frac{1}{2}}, \nabla_{\boldsymbol{X}} \delta T^{(i)} \rangle_{\Omega_0^{(i)}} + \langle Q_{\nu-\frac{1}{2}}^{(i)}, \delta T^{(i)} \rangle_{\Gamma_\mathrm{n}^{(i)}} = 0 \end{aligned} \tag{5.23}$$

for all $\delta T^{(i)} \in \mathcal{V}^{(i)}$. According to Section 3.1.1, we finally obtain a sequence of global, uncoupled problems by introducing the corresponding product spaces and summation of the sub-problems (5.23).

5.2.2 The Cahn–Hilliard equation and multi-patch framework

In the following, we provide an evolution equation for the molar fractions of a binary alloy based on the conservation of mass equation (5.9) and the representation (5.16) of the atomic fluxes. To this end, we will briefly outline the main ideas and indicate the most important relationships. For a rigorous derivation, starting from the general representations (5.14), (5.15) and further information on this topic, we refer to Schuß et al. [142]. Based on the evolution equation, we eventually derive a corresponding multi-patch framework.

According to Howard & Lidiard [99], the complete thermodynamic description in the case of a solid system in which a vacancy mechanism operates can be obtained by explicitly including vacancies as an additional component of the system. Through reasonable assumptions, the vacancies can subsequently be condensed into the material properties of the alloy components, resulting in a system with the initial number of species in which vacancies are implicitly included. Assuming that only a vacancy mechanism operates, the atomic fluxes within a binary alloy consisting of a and b in an isothermal environment is then given by

$$\boldsymbol{J} = -c(1-c)(cM_a + (1-c)M_b)\nabla_{\boldsymbol{X}}\mu_b^{\text{eff}}, \quad \boldsymbol{J}_a = -\boldsymbol{J}, \tag{5.24}$$

where $\boldsymbol{J}_a$ is the flow of a, $\boldsymbol{J}$ the flow of b and c denotes the mole fraction of b. In addition, the corresponding effective chemical potentials are defined by $\mu_a^{\text{eff}} = -\mu_b^{\text{eff}} = \mu_a - \mu_b$ and M_a, M_b are the atomic mobilities of the two components related to the phenomenological coefficients $L_{i,j}$ in Eq. (5.16) via

$$M_a = \frac{[cL_{a,a} - (1-c)L_{a,b}]V_m}{c(1-c)}, \quad M_b = \frac{[(1-c)L_{b,b} - cL_{b,a}]V_m}{c(1-c)}. \tag{5.25}$$

Let Ω_0 be the region occupied by the alloy and the Helmholtz free energy be given through a functional relationship of the form

$$\mathcal{F}(c,T) = \int_{\Omega_0} \Psi^{\text{con}}(c,T) + \Psi^{\text{int}}(c,T)\ \mathrm{d}V, \tag{5.26}$$

where Ψ^{con} denotes the configurational free energy density and Ψ^{int} is the internal interface energy. We further assume that the internal interface energy is given by $\Psi^{\text{int}}(c,T) = \kappa(T)\|\nabla_{\boldsymbol{X}}c\|^2/2$, where the term $\|\nabla_{\boldsymbol{X}}c\|^2$ reflects molecular iterations and can be seen as penalising the formation of interfaces between the phases. In addition, the gradient energy coefficient κ is related to the surface energy density and the length of the transition regions between each phase. According to Cahn [33] and Cahn & Hilliard [34], the effective chemical potential μ_b^{eff} of b can be determined by the variation of the Helmholtz free energy functional with respect to c, such that we obtain

$$\mu_b^{\text{eff}} = \frac{\delta\mathcal{F}}{\delta c} = (\partial_c\Psi^{\text{con}} - \kappa\Delta_{\boldsymbol{X}}c) \tag{5.27}$$

and consequently $\boldsymbol{J} = -M\nabla_{\boldsymbol{X}}(\partial_c \Psi^{\mathrm{con}} - \kappa\Delta_{\boldsymbol{X}} c)$, where $M := c(1-c)(cM_a + (1-c)M_b)$ is the mobility of the alloy. According to these considerations, the atomic fluxes in a binary alloy can be modelled through the atomic mobilities, the configurational free energy density and the gradient energy coefficient. As an example, the corresponding material parameters for a tin-lead alloy are given in Appendix B. If we now assume a constant molar volume, the mean molar velocity (5.5) vanishes, cf. de Groot & Mazur [53], and from the conservation of mass (5.9) we obtain the evolution equation

$$\dot{c} = -V_m \nabla_{\boldsymbol{X}} \cdot \boldsymbol{J} = V_m \nabla_{\boldsymbol{X}} \cdot (M \nabla_{\boldsymbol{X}} [\partial_c \Psi^{\mathrm{con}} - \kappa \Delta_{\boldsymbol{X}} c]), \quad \text{in } \Omega_0 \times I, \tag{5.28}$$

characterising the molar fractions in a binary alloy. It should be noted that due to $c_a = 1 - c$, the entire mass distribution of the alloy is determined by the equation. Eventually, to obtain a complete description of the time course of the alloy, we assume an initial mole fraction $\bar{c}\colon \Omega_0 \to [0,1]$ to be given and supplement Eq. (5.28) with the following conditions

$$c = \bar{c}, \quad \text{in } \Omega_0 \times \{0\}, \quad \boldsymbol{J} \cdot \boldsymbol{N} = 0 \quad \text{and} \quad \nabla_{\boldsymbol{X}} c \cdot \boldsymbol{N} = 0, \quad \text{on } \partial\Omega^{(i)} \times I. \tag{5.29}$$

While the first condition specifies the mass distribution at time 0, the second equation ensures a closed system in which no mass can be added or removed and the third equation excludes further effects at the external surface with the environment of the system. It should be noted that the first boundary condition is natural while the second one is essential and must be treated accordingly in the associated variational formulation.

The derivation of a multi-patch framework is now analogous to Section 5.2.1. With the evolution equation (5.28) and the initial and boundary conditions (5.29), one obtains an initial boundary value problem for the molar fractions of the individual patches. These are discretised in time according to Appendix A and the semi-discrete problems are subsequently converted into a weak form with the usual methods. For the latter, it should be noted that in Eq. (5.28), derivatives up to the 4th order occur, so that partial integration must be performed twice. Finally, we obtain a sequence of variational problems: given $c_0^{(i)} = \bar{c}^{(i)}$, for $\nu = 1, \ldots, M$ find $c_\nu^{(i)} \in \mathcal{S}^{(i)}$ such that

$$\begin{aligned} \mathrm{V}_\nu^{(i)}(c_\nu^{(i)}, \delta c^{(i)}) := V_m^{-1} \langle h_\nu^{-1}(c_\nu^{(i)} - c_{\nu-1}^{(i)}), \delta c^{(i)} \rangle_{\Omega_0^{(i)}} + \langle [M^{(i)} \nabla_{\boldsymbol{X}} \partial_c \Psi^{\mathrm{con},(i)}]_{\nu-\frac{1}{2}}, \nabla_{\boldsymbol{X}} \delta c^{(i)} \rangle_{\Omega_0^{(i)}} \\ + \langle [\kappa^{(i)} M^{(i)} \Delta_{\boldsymbol{X}} c^{(i)}]_{\nu-\frac{1}{2}}, \Delta_{\boldsymbol{X}} \delta c^{(i)} \rangle_{\Omega_0^{(i)}} + \langle [\kappa^{(i)} \Delta_{\boldsymbol{X}} c^{(i)}]_{\nu-\frac{1}{2}}, \nabla_{\boldsymbol{X}} M^{(i)}_{\nu-\frac{1}{2}} \cdot \nabla_{\boldsymbol{X}} \delta c^{(i)} \rangle_{\Omega_0^{(i)}} = 0 \end{aligned} \tag{5.30}$$

for all $\delta c^{(i)} \in \mathcal{V}^{(i)}$, which can further be treated with the methods from Chapter 3. It should be noted that derivatives up to the 2nd order occur in the weak formulation, which must be taken into account when choosing suitable spaces of admissible solution and test functions. I.e. in order to guarantee the existence of the integrals and the compliance with the essential boundary conditions, the spaces must fulfil

$$\mathcal{S}^{(i)} = \mathcal{V}^{(i)} \subset \left\{ c \in H^2(\Omega_0^{(i)}) \,|\, \nabla_{\boldsymbol{X}} c \cdot \boldsymbol{N} = 0 \text{ on } \Gamma_{\mathrm{e}}^{(i)} \right\}, \tag{5.31}$$

where the time dependence of $\mathcal{S}^{(i)}$ is omitted here, since the essential conditions are not time-dependent and the two spaces coincide because the conditions are homogeneous. In

addition, $\Gamma_{\mathrm{e}}^{(i)}$ results from the intersection of the outer boundaries of the patches and the main domain, i.e. $\Gamma_{\mathrm{e}}^{(i)} := \partial\Omega_0^{(i)} \cap \partial\Omega_0$. How the spaces must be further specified to ensure unique solubility also depends on the choice of the material model, i.e. on the properties of configurational free energy density, the mobility and the gradient energy coefficient. Further considerations on this can be found in [27, 28, 68, 140, 165].

5.3 Numerical studies

Finally, we present various numerical investigations of thermal conduction and diffusion problems in the context of an isogeometric multi-patch analysis using the extended mortar method. In Section 5.3.1, we consider a two-dimensional heat conduction problem and address the question of whether the approximation quality of the IGA framework changes by applying the extended mortar method and investigate the influence of the different coupling conditions on each other. Subsequently, in Section 5.3.2 we consider a two-dimensional example on diffusion in a tin-lead alloy, formulated as a 4-patch system. Instead of the boundary conditions given in Eq. (5.29), periodic boundaries are used there. In the Cahn-Hilliard context, this corresponds to a C^1 coupling with spatially separated interfaces and is treated with generalised coupling conditions according to Section 3.1.3. The last example in Section 5.3.3 is motivated by a widely used mounting technique in the chip industry and serves as proof of concept. Therein, we investigate segregation phenomena in a three-dimensional model of a tin-lead solder bump described by two patches with a curved interface.

5.3.1 Thermal conduction 2D

In the following, we consider a two-dimensional heat conduction problem and investigate the influence of C^n couplings up to the 2nd order on the approximation quality of the IGA framework. For this purpose, we formulate a problem whose analytical solution is known and compare the global L^2 errors of a 1-patch system with the corresponding errors of three 4-patch systems in which we implement C^0-, C^1- and C^2-continuous couplings, respectively. Since derivatives up to the first order occur in the variational formulation (5.23), a C^0-continuous IGA basis is required for the approximation and consequently, in the multi-patch case, C^0-continuous couplings are inevitable. I.e. at least it must be ensured that the temperatures of the patches at the interfaces match. In the case of higher order couplings, the question arises as to whether and to what extent the realisation of the temperature coupling is affected by additional coupling conditions. To investigate this question, the realisation of the temperature couplings in C^1- and C^2-continuous implementations is compared with that in a C^0-continuous coupling, in addition to the investigations on the approximation quality.

In the period $I = [0,1]$ we consider a square plate $\Omega_0 = (0,1)^2$, which, in the case of multiple patches, is divided into the four parts

$$\Omega_0^{(1)} = (0,0.5) \times (0,0.5), \qquad \Omega_0^{(2)} = (0.5,1) \times (0,0.5), \tag{5.32}$$

$$\Omega_0^{(3)} = (0,0.5) \times (0.5,1), \qquad \Omega_0^{(4)} = (0.5,1) \times (0.5,1), \tag{5.33}$$

whereby the temporal and spatial dimensions are given in the units [s] and [m] throughout this section. With regard to the heat conduction problem, the material parameters are specified by $\rho_0 = 1\,\mathrm{kg/m^3}$, $c_\mathrm{p} = 1\,\mathrm{J/(kg{\cdot}K)}$, $\lambda = 1\,\mathrm{W/(m{\cdot}K)}$, initial- and boundary conditions are defined through

$$T(\boldsymbol{X},0) = 270, \quad \boldsymbol{X} \in \Omega_0, \quad T(\boldsymbol{X},t) = 270, \quad (\boldsymbol{X},t) \in \Gamma_\mathrm{e} \times I, \quad \Gamma_\mathrm{e} := \partial\Omega_0, \tag{5.34}$$

and the heat source $R\colon \Omega_0 \times I \to \mathbb{R}$ is manufactured such that the analytical solution of the initial boundary value problem (5.17), (5.18) is given by[†]

$$T_a\colon \Omega_0 \times I \to \mathbb{R}, \quad T_a(\boldsymbol{X},t) = \sin(2\pi t)\sin(\pi X_1)\sin(\pi X_2) + 270, \tag{5.35}$$

see Figure 5.1 for illustration. It should be noted, that due to the essential boundary

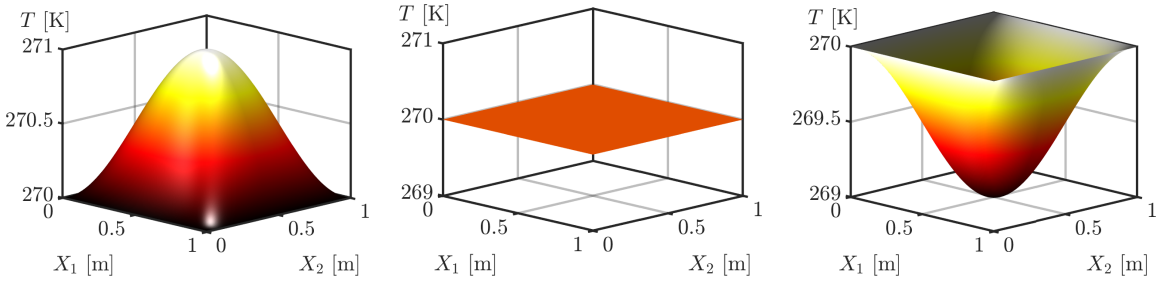

Figure 5.1: *Thermal conduction 2D.* Solution (5.35) at time $t = 0.25\,\mathrm{s}$, $0.5\,\mathrm{s}$, $0.75\,\mathrm{s}$ (from left to right).

conditions, in the multi-patch case four crosspoints occur on the boundary $\partial\Omega_0$ in addition to the centre of Ω_0, so that a total of five crosspoints

$$\mathfrak{C} = \left\{ \begin{pmatrix} 0 \\ 0.5 \end{pmatrix}, \begin{pmatrix} 0.5 \\ 0 \end{pmatrix}, \begin{pmatrix} 0.5 \\ 1 \end{pmatrix}, \begin{pmatrix} 1 \\ 0.5 \end{pmatrix}, \begin{pmatrix} 0.5 \\ 0.5 \end{pmatrix} \right\}, \tag{5.36}$$

have to be considered accordingly. Regarding the discretisation, we use a constant step-size of $0.005\,\mathrm{s}$ in the time-stepping scheme and for the spatial discretisation we use globally C^2-continuous bicubic, $\boldsymbol{p} = (3,3)$, shape functions, so that in the 1-patch system ($P1$) the domain is resolved into 20×20 elements and in the 4-patch systems the individual patches are resolved into 10×10 and 9×9 elements, respectively. The computational meshes, the numbering of the patches, the respective resolution and the definition of the master and slave sides are shown in Figure 5.2. In order to investigate the influence of

[†]To obtain the solution (5.35), R must take the form:

$$R(\boldsymbol{X},t) = \left[2\pi\cos(2\pi t) + 2\pi^2\sin(2\pi t)\right]\sin(\pi X_1)\sin(\pi X_2), \quad (\boldsymbol{X},t) \in \Omega_0 \times I.$$

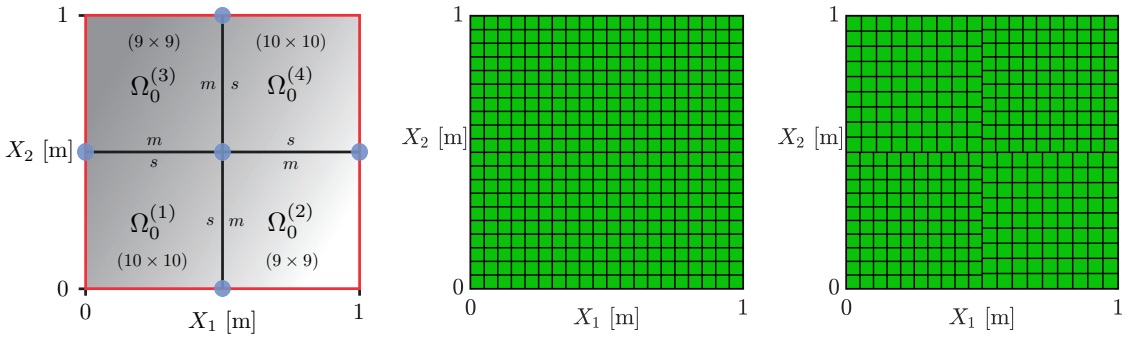

Figure 5.2: *Thermal conduction 2D.* Left: subdivision of Ω_0 into the four patches. The boundary Γ_e is marked in red, the five crosspoints are marked with blue bullets, the resolutions are given in the brackets and the master and slave sides of the interfaces are indicated by m/s. Middle: computational mesh of the 1-patch system. Right: computational mesh of the 4-patch systems.

the coupling-continuity, we consider in addition to $P1$ three different 4-patch systems in which we implement C^n-continuous couplings with $n = 0, 1, 2$. To distinguish between them, we will refer to them briefly as $P4C^0$, $P4C^1$ and $P4C^2$ in the following.

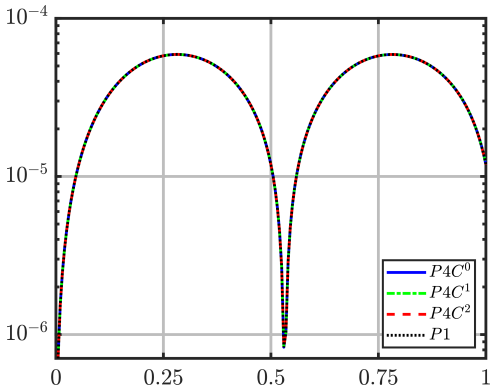

t [s]	$P4C^n$, $n = 0, 1, 2$, vs. $P1$		
	d_0^{gl} [K]	d_1^{gl} [K]	d_2^{gl} [K]
0.25	$5.353 \cdot 10^{-11}$	$6.821 \cdot 10^{-11}$	$7.755 \cdot 10^{-11}$
0.5	$9.882 \cdot 10^{-11}$	$1.257 \cdot 10^{-10}$	$1.431 \cdot 10^{-10}$
0.75	$1.379 \cdot 10^{-10}$	$1.754 \cdot 10^{-10}$	$1.996 \cdot 10^{-10}$
1	$1.724 \cdot 10^{-10}$	$2.192 \cdot 10^{-10}$	$2.496 \cdot 10^{-10}$

Figure 5.3: *Thermal conduction 2D.* Left: global L^2 errors err_{P1}^{gl} and $err_{P4C^n}^{gl}$, $n = 0, 1, 2$, as functions in time. Right: differences d_n^{gl}, $n = 0, 1, 2$, evaluated at different points in time.

First, we examine the influence of the multi-patch formulation on the approximation quality of the IGA framework. To this end, we introduce for each system a global L^2 error defined by $err_{P1}^{gl}(t) = \|[T_{\mathrm{h},P1} - T_a](\bullet, t)\|_{L^2(\Omega_0)}$ for the 1-patch setting and

$$err_{P4C^n}^{gl}(t) = \left(\sum_{k=1}^{4} \|[T_{\mathrm{h},P4C^n}^{(k)} - T_a](\bullet, t)\|_{L^2(\Omega_0^{(k)})}^2 \right)^{\frac{1}{2}}, \quad n = 0, 1, 2, \tag{5.37}$$

for the three 4-patch settings, where $T_{\mathrm{h},P1}$ denotes the numerical solution belonging to $P1$ and $T_{\mathrm{h},P4C^n}^{(k)}$ the numerical solution on the kth patch belonging to $P4C^n$. Figure 5.3

provides the temporal evolution of the four errors. As can be seen in the left picture, the corresponding error curves are essentially congruent, indicating that the approximation quality of the 4-patch systems is equal to that of $P1$, regardless of the order of the coupling-continuity. For a more detailed comparison of the 4-patch systems with $P1$, the table on the right hand side of Figure 5.3 contains the differences

$$d_n^{gl}(t) = err_{P4C^n}^{gl}(t) - err_{P1}^{gl}(t), \quad n = 0, 1, 2, \tag{5.38}$$

evaluated at several points in time. Note that by definition the sign of d_n^{gl} indicates whether the error in the respective 4-patch system has increased or decreased compared to $P1$. Here, also, no reduction in the approximation quality can be observed. Although an increase in the error can be noted in each case, it ranges between $5.353 \cdot 10^{-11}$ and $2.496 \cdot 10^{-10}$, corresponding to a maximum increase of 0.0021 % of the global L^2 error.

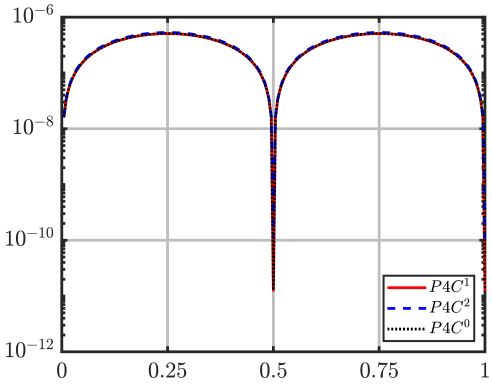

t [s]	$P4C^k$, $k = 1, 2$, vs. $P4C^0$	
	d_1^{if} [K]	d_2^{if} [K]
0.25	$-1.677 \cdot 10^{-9}$	$2.151 \cdot 10^{-8}$
0.5	$-1.803 \cdot 10^{-13}$	$9.293 \cdot 10^{-11}$
0.75	$-1.677 \cdot 10^{-9}$	$2.151 \cdot 10^{-8}$
1	$-1.685 \cdot 10^{-13}$	$9.294 \cdot 10^{-11}$

Figure 5.4: *Thermal conduction 2D.* Left: measures $err_{P4C^n}^{if}$ of the temperature jump on the skeleton as functions in time. Right: differences d_n^{if}, $n = 1, 2$, evaluated at different points in time.

Eventually, we consider the realisation of the temperature coupling on the skeleton and compare the two systems $P4C^1$, $P4C^2$ with $P4C^0$. The left picture in Figure 5.4 shows the temporal evolution of the errors

$$err_{P4C^n}^{if}(t) = \frac{1}{2}\left(\sum_{k=1}^{4} \|[T_{\mathrm{h},P4C^n}^{(s(k))} - T_{\mathrm{h},P4C^n}^{(m(k))}](\bullet, t)\|_{L^2(\Gamma_k)}^2\right)^{\frac{1}{2}}, \quad n = 0, 1, 2, \tag{5.39}$$

measuring the temperature jump on the entire skeleton, whereby the length of the skeleton is taken into account by the factor 1/2. It can be observed that the corresponding error curves are almost congruent, with the curve of $P4C^2$ deviating slightly from the curves of $P4C^0$ and $P4C^1$. Consequently, the temperature coupling is only marginally influenced by the additional coupling conditions in $P4C^1$ and $P4C^2$. For a more detailed comparison, the differences

$$d_n^{if}(t) = err_{P4C^n}^{if}(t) - err_{P4C^n}^{if}(t), \quad n = 1, 2, \tag{5.40}$$

at several points in time are listed in the table on the right-hand side in Figure 5.4. As in the case of the global error, the sign of d_n^{if} indicates whether the error of the systems

$P4C^1$ and $P4C^2$ has increased or decreased compared to $P4C^0$. It can be observed that the results differ only slightly from each other, with the absolute values of the differences in the order of $1.685 \cdot 10^{-13}$ and $2.151 \cdot 10^{-8}$. In addition, it is worth noting that in system $P4C^1$ a decrease in the error occurs, while the error in system $P4C^2$ increases.

5.3.2 Diffusion 2D

In our first diffusion example, we consider a two-dimensional 4-patch system describing spinodal decomposition in a tin-lead alloy. The mechanism of spinodal decomposition is observed when mixtures of metals or polymers separate into two co-existing phases, each rich in one species and poor in the other, cf. Gennes [81]. When the two phases emerge in approximately equal proportion, characteristic intertwined structures are formed that gradually coarsen. In the study of such phenomena, it is often useful to consider only a small section of a larger system, since it can be assumed that the process is essentially the same in the adjacent areas. For this purpose, it is reasonable to replace the boundary conditions in Eq. (5.29) by periodic ones. Due to the higher continuity requirements resulting from the Cahn-Hilliard equation (5.28), it must be ensured that besides the mole fraction, their gradients also match at the affected boundaries. In the single-patch case, this can be achieved in a strong sense by using a periodic NURBS basis and identifying the corresponding degrees of freedom with each other, cf. Gómez at al. [82]. This approach can be adapted for the multi-patch case but requires the conformity of the meshes. Formulating suitable generalized coupling conditions as introduced in Section 3.1.3, the periodic boundaries can be easily realised in the framework of the extended mortar method, as shown below.

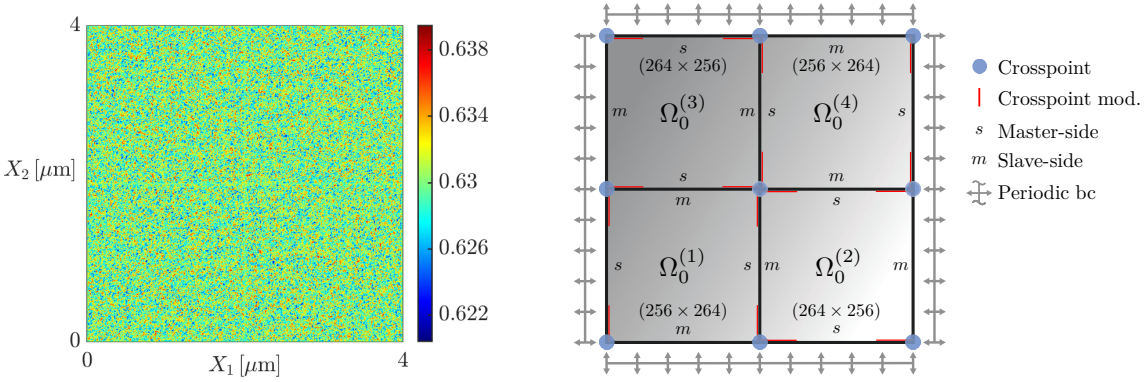

Figure 5.5: *Diffusion 2D.* Left: Initial configuration $\bar{c}(\boldsymbol{X})$, $\boldsymbol{X} \in \Omega_0$. Right: summary of the setting including patch numbering, choice of master and slave side, resolutions of the patches, crosspoints and boundary conditions.

The segregation phenomenon is studied in the time period $I = [0, 10^5]$ on the computational domain $\Omega_0 = (0, 4)^2$ which is subdivided into the four parts

$$\Omega_0^{(1)} = (0, 2) \times (0, 2), \qquad \Omega_0^{(2)} = (2, 4) \times (0, 2), \tag{5.41}$$

$$\Omega_0^{(3)} = (0,2) \times (2,4), \qquad \Omega_0^{(4)} = (2,4) \times (2,4), \tag{5.42}$$

whereby the temporal and spatial dimensions are given in the units [s] and [μm] throughout this section. The material data, such as the free energy and the mobilities for the tin-lead mixture are specified according to Appendix B through a constant temperature and a nearly homogeneous initial mole fraction given by

$$T(\boldsymbol{X}, t) = 423.15\,\mathrm{K}, \quad \bar{c}(\boldsymbol{X}) = 0.63 + \mathfrak{r}(\boldsymbol{X}), \qquad (\boldsymbol{X}, t) \in \Omega_0 \times I, \tag{5.43}$$

where $\mathfrak{r}$ is a random variable modelling slight inhomogeneities of the material within a range of $\pm 1\%$. For simplicity, we omit the fluctuations $\mathfrak{r}$ in the definition of the molar volume of the system and assume the volume to be constant $V_m = 9905/(582 \cdot 10^6)\,\mathrm{m^3 mol^{-1}}$, corresponding to a homogeneous initial state of $\bar{c} = 0.63$. Furthermore, a homogeneous distribution is also assumed at the boundaries of each patch to ensure a consistent initial configuration, i.e. to achieve that the coupling conditions are fulfilled at time $t = 0$, see Figure 5.5 for illustration. We point out that this also serves the purpose of simplification, since otherwise the random variable would have to be constructed in such a way that the mole fraction and the corresponding gradients of the individual patches at the interfaces coincide, which is contrary to the definition of a random variable.

In order to realise the periodic boundaries, we define, in addition to the four real interfaces within Ω_0, four virtual interfaces $(\gamma_1, \phi_1), \ldots, (\gamma_4, \phi_4)$ through

$$\Omega_0^{(1)}/\Omega_0^{(2)} : \ \gamma_1 = \{0\} \times (0,2), \quad \phi_1(\boldsymbol{X}) = \boldsymbol{X} + (4,0)^{\mathrm{T}}, \tag{5.44}$$

$$\Omega_0^{(3)}/\Omega_0^{(4)} : \ \gamma_2 = \{4\} \times (2,4), \quad \phi_2(\boldsymbol{X}) = \boldsymbol{X} - (4,0)^{\mathrm{T}}, \tag{5.45}$$

$$\Omega_0^{(1)}/\Omega_0^{(3)} : \ \gamma_3 = (0,2) \times \{4\}, \quad \phi_3(\boldsymbol{X}) = \boldsymbol{X} - (0,4)^{\mathrm{T}}, \tag{5.46}$$

$$\Omega_0^{(2)}/\Omega_0^{(4)} : \ \gamma_4 = (2,4) \times \{0\}, \quad \phi_4(\boldsymbol{X}) = \boldsymbol{X} + (0,4)^{\mathrm{T}}, \tag{5.47}$$

which respectively couple the left/right edges of $\Omega_0^{(1)}/\Omega_0^{(2)}$ and $\Omega_0^{(3)}/\Omega_0^{(4)}$ as well as the lower/upper edges of $\Omega_0^{(1)}/\Omega_0^{(3)}$ and $\Omega_0^{(2)}/\Omega_0^{(4)}$. Here, the diffeomorphisms ϕ_k, $k = 1, \ldots, 4$, are simple translations that move slave resp. the affected boundary part to the corresponding side adjacent to master. E.g. for $\Omega^{(1)}/\Omega^{(2)}$ one gets

$$\phi_1(\Omega_0^{(1)}) = (4,6) \times (0,2), \quad \gamma_1^{\phi_1} = \phi_1(\gamma_1) = \{4\} \times (0,2). \tag{5.48}$$

I.e. $\Omega_0^{(1)}$ is shifted under ϕ_1 to the right of $\Omega_0^{(2)}$ so that the left boundary of $\Omega_0^{(1)}$ and the right boundary of $\Omega_0^{(2)}$ are congruent. It should be noted that due to the virtual interfaces, there are 8 additional crosspoints on the boundary of Ω_0, cf. Figure 5.5.

For the simulations, we employ globally C^1-continuous shape functions of order $\boldsymbol{p} = (2,2)$, such that $\Omega_0^{(1)}$, $\Omega_0^{(4)}$ are resolved by 256×264 elements and $\Omega_0^{(2)}$, $\Omega_0^{(3)}$ by 264×256 elements, respectively, resulting in non-conforming meshes at each interface. Accordingly, we use weak C^1 couplings and a segment-based integration scheme for the evaluation of the mortar-integrals. We point out, that the patch numbering, the choice of master and slave side, the resolutions of the patches, the crosspoints and the boundary conditions are summarized in the right picture in Figure 5.5.

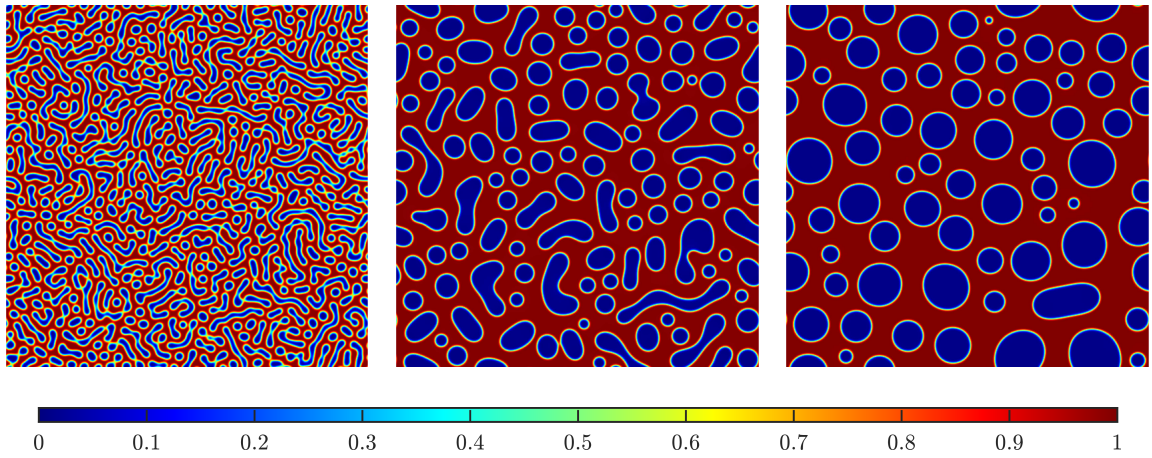

Figure 5.6: *Diffusion 2D.* Mole fraction c_h at time $t = 250.01\,\mathrm{s}$, $10000.01\,\mathrm{s}$, $100000.01\,\mathrm{s}$ (from left to right). The red areas represent the tin-rich phase and the blue areas indicate the lead-rich phase.

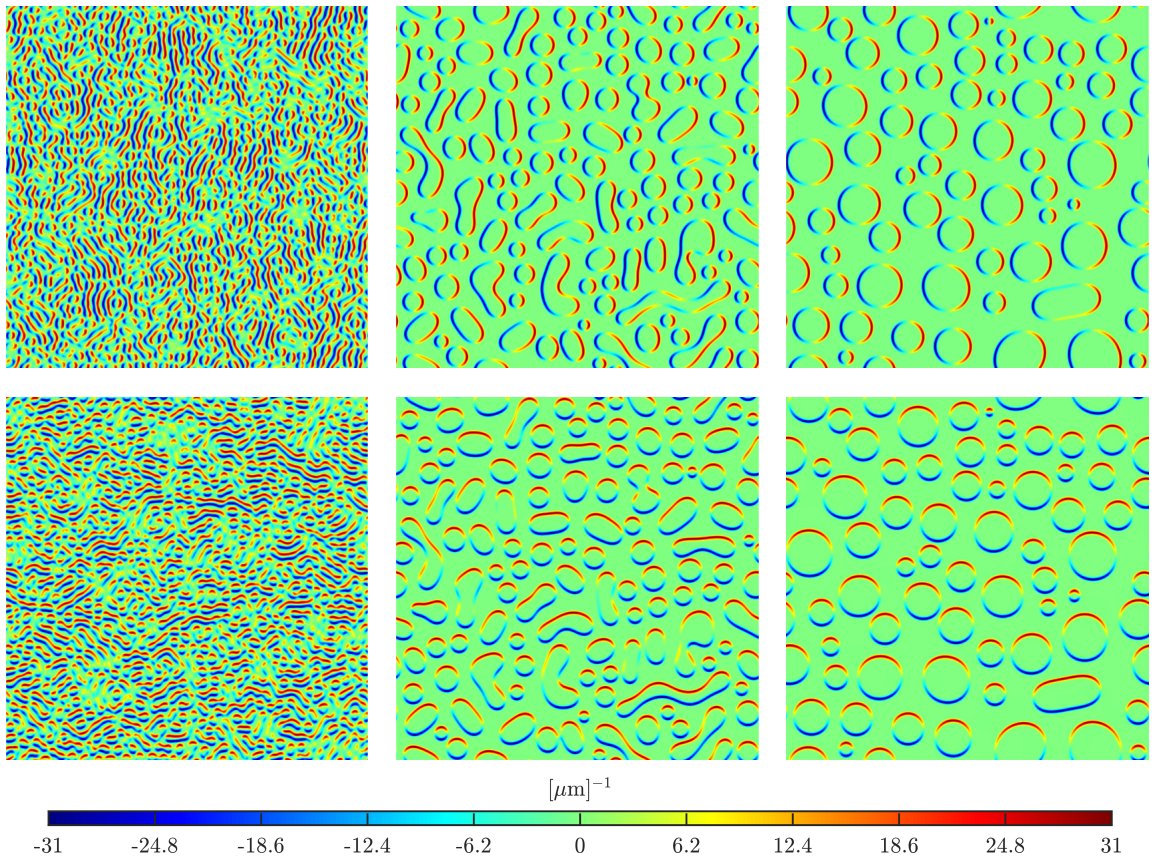

Figure 5.7: *Diffusion 2D.* Partial derivatives $\partial_{X_1} c_\mathrm{h}$ (upper row) and $\partial_{X_2} c_\mathrm{h}$ (lower row) at time $t = 250.01\,\mathrm{s}$, $10000.01\,\mathrm{s}$, $100000.01\,\mathrm{s}$ (from left to right).

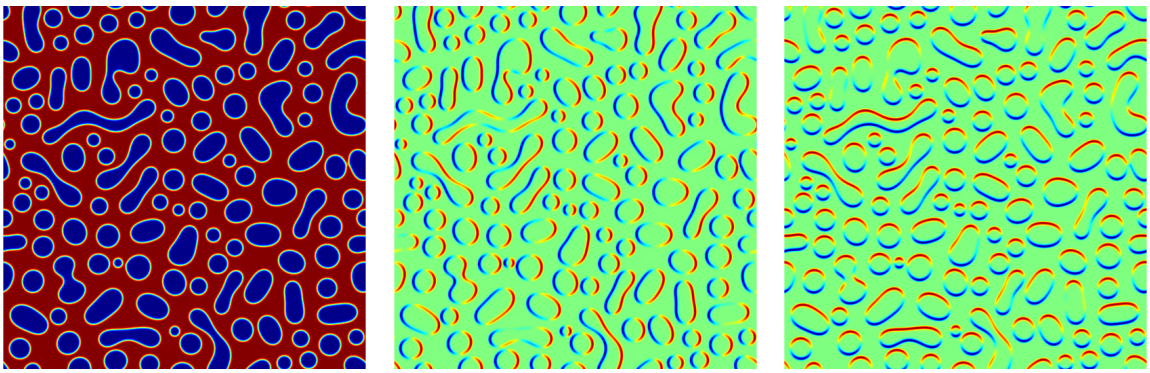

Figure 5.8: *Diffusion 2D.* Reordered patches $\Omega^{(1)} \leftrightarrow \Omega^{(4)}$ and $\Omega^{(2)} \leftrightarrow \Omega^{(3)}$. From left to right: c_h, $\partial_{X_1} c_\mathrm{h}$ and $\partial_{X_2} c_\mathrm{h}$ at time $t = 10000.01\,\mathrm{s}$.

With regard to the temporal discretisation, we use a time-dependent step-size $h_\nu \colon I \to \mathbb{R}_{\geq 0}$,

$$h_\nu = h_\nu(t_{\nu-1}) = \begin{cases} 0.005, & \text{if } t_{\nu-1} \in [0,3], \\ 0.1, & \text{if } t_{\nu-1} \in (3,10], \\ 1, & \text{if } t_{\nu-1} \in (10,1000], \\ 10, & \text{if } t_{\nu-1} \in (10000,100000], \end{cases} \tag{5.49}$$

whereby the step-size control is designed to take into account the different stages of the spinodal decomposition.

The simulation results for c_h are shown in Figure 5.6 and Figure 5.7 illustrates the corresponding results for $\nabla_{\boldsymbol{X}} c_\mathrm{h}$. As can be seen in Figure 5.6, a rapid phase decomposition takes place in the first seconds and a branched pattern forms from the two phases. In the further course, the structure becomes increasingly coarse, with lead-rich islands forming in a tin-rich environment. In particular, it can be observed that in all cases the patches merge C^1-continuously, so that the interfaces are not visible in the illustrations. The same holds true for the periodic boundaries. Figure 5.8 shows as an example the results at time $t = 10000.01\,\mathrm{s}$, with the positions of the patches in the images swapped according to $\Omega^{(1)} \leftrightarrow \Omega^{(4)}$ and $\Omega^{(2)} \leftrightarrow \Omega^{(3)}$. To quantify these observations, we consider in the left picture in Figure 5.9 the evolution of the two relative coupling errors

$$err_0^{if}(t) := \frac{1}{16} \left(\sum_{k=1}^{4} \| c_\mathrm{h}^{(s(k))} - c_\mathrm{h}^{(m(k))} \|_{L^2(\Gamma_k)}^2 + \| c_\mathrm{h}^{(s(k))} - c_\mathrm{h}^{(m(k))} \circ \phi_k \|_{L^2(\gamma_k)}^2 \right)^{\frac{1}{2}}, \tag{5.50}$$

$$err_1^{if}(t) := \frac{1}{16} \left(\sum_{k=1}^{4} \| \nabla_{\boldsymbol{X}} (c_\mathrm{h}^{(s(k))} - c_\mathrm{h}^{(m(k))}) \|_{L^2(\Gamma_k)}^2 + \| \nabla_{\boldsymbol{X}} c_\mathrm{h}^{(s(k))} - (\nabla_{\boldsymbol{X}} c_\mathrm{h}^{(m(k))}) \circ \phi_k \|_{L^2(\gamma_k)}^2 \right)^{\frac{1}{2}}, \tag{5.51}$$

where err_0^{if} and err_1^{if} assess the coupling of the function values and derivatives, respectively, while the factor $1/16$ takes into account the length of the skeleton. It can be observed that err_0^{if} lies between $2.5 \cdot 10^{-7}$ and $1.9 \cdot 10^{-4}$, while err_1^{if} is greater at each

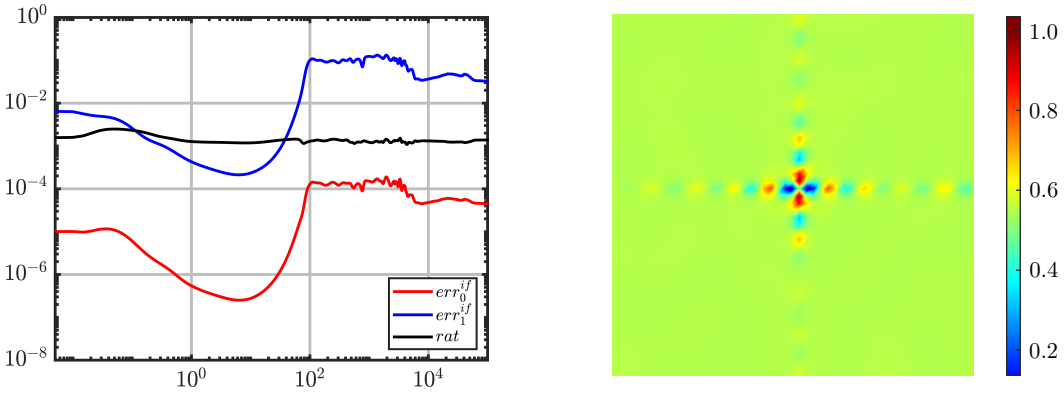

Figure 5.9: *Diffusion 2D.* Left: interface errors err_0^{if}, err_1^{if} and ratio rat as functions in time. Right: Solution c_h on $[1.85, 2.15]^2 \subset \Omega_0$ at time $t = 2.8\,\mathrm{s}$ using weak C^0 couplings.

point in time and is in the range $(1.9 \cdot 10^{-4}, 2.1 \cdot 10^{-4})$. Furthermore, it is noticeable that the two errors behave synchronously in time and differ by an almost constant factor $rat(t) := err_0^{if}(t)/err_1^{if}(t)$, whose evolution is also shown in Figure 5.9. Thereby it can be seen that $rat(I) \subset (2.5 \cdot 10^{-4}, 10^{-3})$ and the two errors thus differ by a maximum factor of 0.001 at each time.

Eventually, to demonstrate the necessity of C^1 couplings in the Cahn-Hilliard framework, the right picture in Figure 5.9 shows simulation results corresponding to $t = 2.8\,\mathrm{s}$ in which weak C^0 coupling conditions are used instead of the C^1 conditions, whereby only the small section $[1.85, 2.15] \times [1.85, 2.15]$ around the central crosspoint is shown. As can be seen, non-physical oscillations occur in the area of the interfaces, whose amplitude increases in the vicinity of the crosspoint. In particular, the mole fraction becomes greater than 1 and thus leaves its co-domain $[0, 1]$, leading to an immediate termination of the simulation.

5.3.3 Diffusion 3D

In this last application example on diffusion, we again consider spinodal decomposition in a tin alloy, this time based on a three-dimensional model consisting of two patches with a curved interface. The shape of the computational domain is motivated by a widely used semiconductor mounting technique, the so-called controlled collapse chip connection or flip chip technique. In this process, solder bumps are applied to the conductive traces of a chip. To connect the chip to an external circuit (e.g. a printed circuit board or another chip), it is turned face down and aligned so that the solder bumps match the corresponding traces of the external circuit. Finally, the solder is reflowed to complete the joint. Figure 5.10 schematically shows a section of a flip chip module. With the ongoing quest for increasingly smaller dimensions and higher functionality in a variety of devices, there is also an increasing interest in ever-finer bump sizes. As a result, the bumps become more susceptible to segregation phenomena.

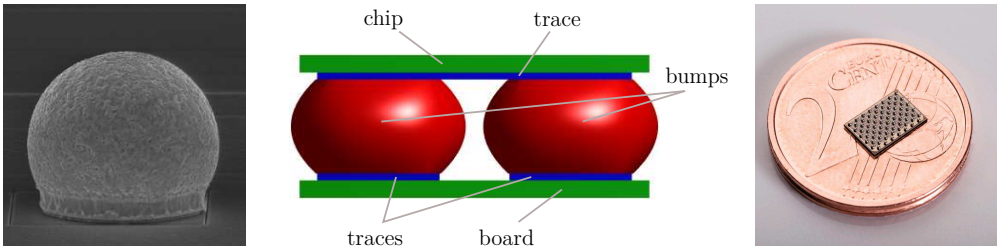

Figure 5.10: Left: single solder bump with a diameter of 25 μm, [1]. Middle: schematic diagram of a part of a flip chip package. Right: gallium nitrite power transistor with Sn-Pb solder bumps for flip chip mounting, [2].

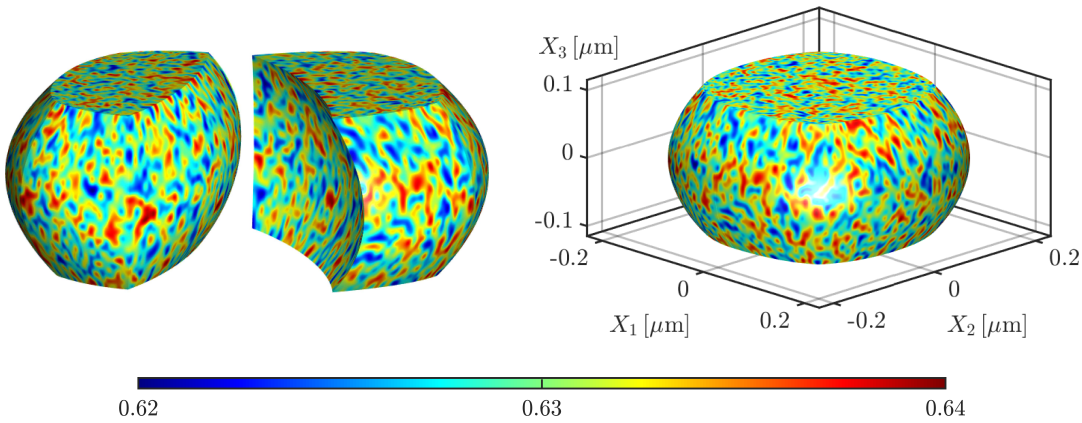

Figure 5.11: *Diffusion 3D.* Initial configuration $\bar{c}(\boldsymbol{X})$, $\boldsymbol{X} \in \Omega_0$. Left: illustration of the two patches. Right: computational domain.

We consider the spinodal decomposition in the period $I = [0, 1.64{\cdot}10^5]$ on a computational domain Ω_0 representing a tin-lead solder bump with a height of 0.2 and a maximum diameter of 0.4 in the plane $X_3 = 0$, see Figure 5.11 for illustration. As before, the temporal and spatial dimensions are given in the units $[s]$ and $[\mu\text{m}]$ throughout this example and we continue to use the material data from Section 5.3.2. With respect to the X_1-axes, Ω_0 consists of a left part $\Omega_0^{(1)}$ and a right part $\Omega_0^{(2)}$ with a curved interface so that $\Omega_0^{(1)}$ is convex, while $\Omega_0^{(2)}$ represents a non-convex set. Moreover, in contrast to the previous example, we use the boundary conditions (5.29).

For the temporal discretisation, we use the step-size control specified in Eq. (5.49) and for the spatial discretisation, we employ globally C^1-continuous shape functions of order $\boldsymbol{p} = (2, 2, 2)$, such that $\Omega_0^{(1)}$ and $\Omega_0^{(2)}$ are resolved by $24 \times 50 \times 26$ and $24 \times 48 \times 24$ elements, respectively. Accordingly, we use a weak C^1 coupling with an element-based integration scheme involving 64-point Gaussian integration, where $\Omega_0^{(1)}$ is defined as slave and $\Omega_0^{(2)}$ as master. Since this example is primarily a proof of concept, we refrain from modifying the Lagrangian multipliers at the wirebasket arising from the intersection of the interface with Γ_e for simplicity. Motivated by the results in Section 3.2.2, we instead use a constrained basis for the implementation of the coupling to reduce the condition

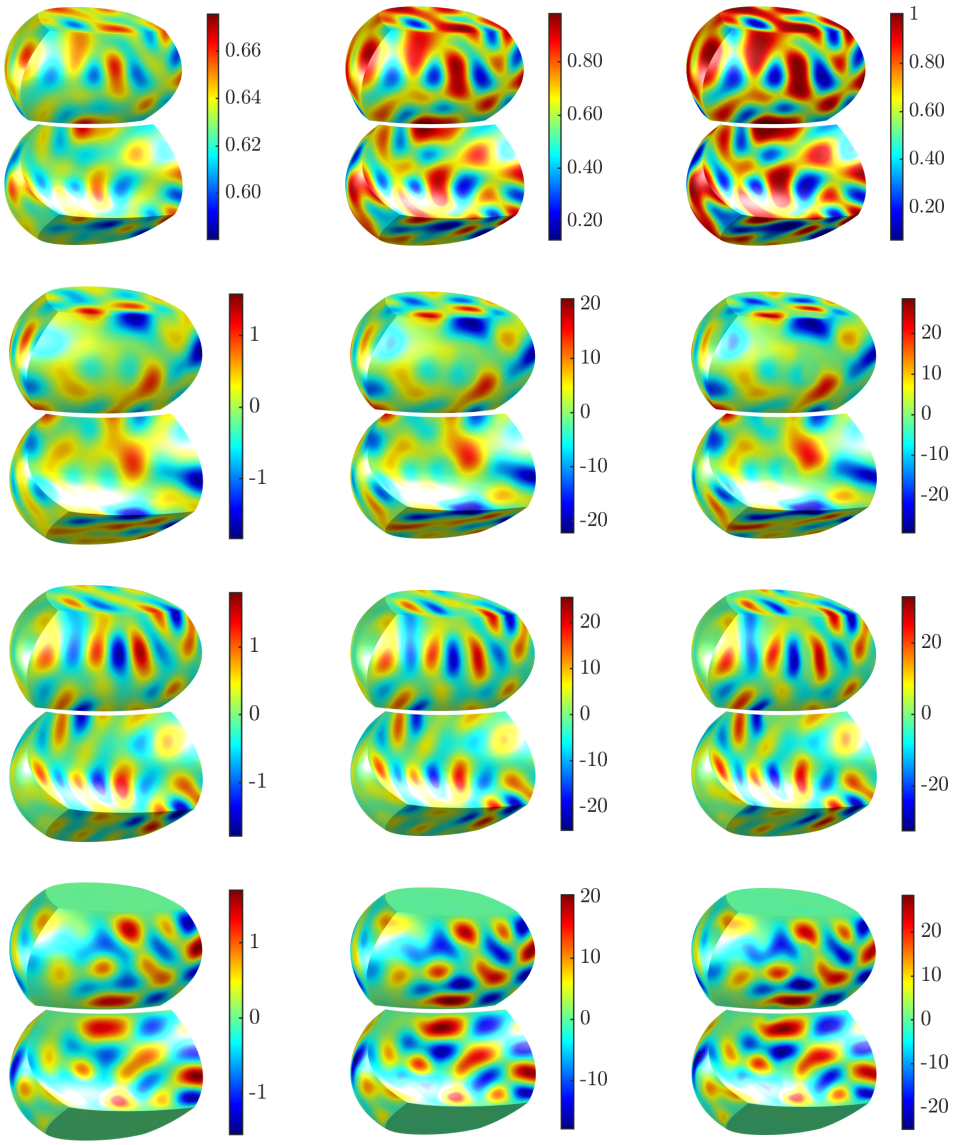

Figure 5.12: *Diffusion 3D.* Temporal evolution. Molar fraction and partial derivatives at time t=82003.002 s, 151503.002 s, 164003.002 s (from left to right). First row: c_h, second row: $\partial_{X_1} c_\mathrm{h}$, third row: $\partial_{X_2} c_\mathrm{h}$, fourth row: $\partial_{X_3} c_\mathrm{h}$.

number of the linear system during the simulation.

The results for c_h and $\nabla_{\boldsymbol{X}} c_\mathrm{h}$ are shown in Figure 5.12. As in the two-dimensional example, a branched pattern forms from the two phases which gradually coarsens. We point out that when comparing with the results of the 2D simulations, it should be noted that the geometry considered here is much smaller. Furthermore, we note that in the illustrations the values of $\boldsymbol{c}_\mathrm{h}^{(1)}$ resp. $\boldsymbol{c}_\mathrm{h}^{(2)}$ and $\nabla_{\boldsymbol{X}} \boldsymbol{c}_\mathrm{h}^{(1)}$ resp. $\nabla_{\boldsymbol{X}} \boldsymbol{c}_\mathrm{h}^{(2)}$ appear identical at the interface. To verify this observation, Figure 5.13 shows the temporal evolution of the two relative coupling errors

$$err_0^{if}(t) := A^{-1} \| c_\mathrm{h}^{(1)} - c_\mathrm{h}^{(2)} \|_{L^2(\Gamma)}, \quad err_1^{if}(t) := A^{-1} \| \nabla_{\boldsymbol{X}} (c_\mathrm{h}^{(1)} - c_\mathrm{h}^{(2)}) \|_{L^2(\Gamma)}, \tag{5.52}$$

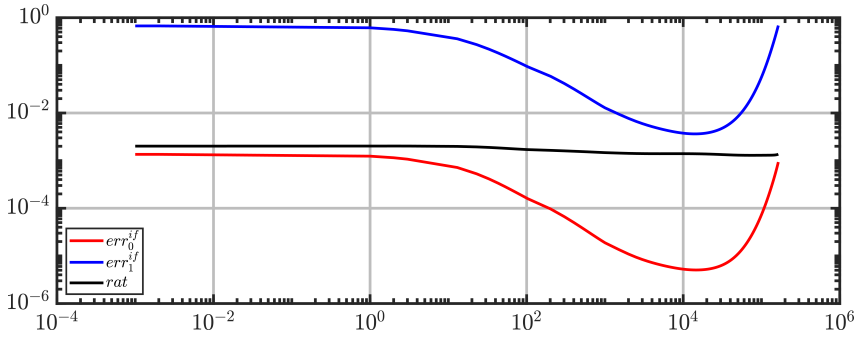

Figure 5.13: *Diffusion 3D.* Interface errors err_i^{if}, $i = 0, 1$, and ratio rat as functions in time.

where $A = 0.125406642792534\,\mu\text{m}^2$ is the surface area of the interface, together with the temporal evolution of $rat(t) := err_0^{if}(t)/err_1^{if}(t)$. It can be observed that err_0^{if} ranges in $(5.1 \cdot 10^{-6}, 1.4 \cdot 10^{-3})$ and err_1^{if} is located in $(3.6 \cdot 10^{-3}, 6.8 \cdot 10^{-1})$. Moreover, it is noticeable that the two errors behave synchronously in time and the factor rat is almost constant with $rat(I) \subset (1.3 \cdot 10^{-3}, 2 \cdot 10^{-3})$. Overall, it can be noted that the coupling in this example tends to be realised slightly worse than in the 2D example. However, compared to the previous example, simplifications were made here to reduce the numerical effort. While we have used a segment-based method to evaluate the mortar integrals in Section 5.3.2, we have resorted to an element-based method here and have refrained from modifying the multipliers in the vicinity of the wirebasket.

6 Phase-Field-Crystal modelling

Pattern formation can be observed in nature from microscopic to cosmological scales. Non-equilibrium systems in physics, chemistry, biology, mathematics, cosmology and other fields produce an amazing variety of spatio-temporal behaviour. Therefore, the formation of patterns and the associated nonlinear dynamics have attracted the attention of statistical physics in recent decades. In this context, the Phase-Field-Crystal model (PFC) has emerged as an efficient tool for studying crystalline self-organisation/pattern formation on an atomistic scale. The method is based on results from the density functional theory (DFT), which postulates that the particle density and thus the behaviour of the system is characterised by a grand canonical free energy functional. Since this functional is usually not known, it must be approximated accordingly. This is done by an incomplete functional Taylor expansion, which means that the functional Taylor series is truncated above a certain order. The level of the order determines the accuracy of the model, but also the level of the derivative orders that occur. I.e. the more accurately the model approximates the grand canonical free energy functional, the higher the derivatives in the resulting evolution equation. Consequently, isogeometric analysis appears to be a well-suited tool within the PFC framework.

In the following, we outline the derivation of a PFC model on the basis of DFT and formulate the associated multi-patch framework. For this purpose, we provide the necessary results of the density functional theory in Section 6.1. Building on this, we construct a free energy functional in Section 6.2, where we truncate the functional Taylor expansion at 2nd order. The resulting evolution equation for the particle density of the system contains spatial derivatives up to 6th order and, in the variational statements, derivatives up to 3rd order. Consequently, a C^2-continuous basis is required in the IGA framework and correspondingly C^2-continuous couplings in the multi-patch case. Finally, these relationships are examined in more detail by means of numerical examples in Section 6.3. For a detailed overview concerning PFC and its applications, we recommend the work of Emmerich et al. [71].

6.1 Density Functional Theory

In this section, the most important results of DFT are summarised, which are needed to derive the PFC model in Section 6.2. For this purpose, the grand canonical free-energy functional is introduced in the framework of static DFT in Section 6.1.1 and its approximation by a functional Taylor expansion is discussed. Based on the approximation,

the dynamic DFT (DDFT) yields an evolution equation for the particle density of the system, which is subsequently given Section 6.1.2.

6.1.1 Static Density Functional Theory

We consider an N-particle system contained in a domain Ω_0, where the centre-of-mass positions and the momenta of the particles are defined in a Cartesian coordinate system through the vectors $\boldsymbol{R}_i$ and $\boldsymbol{P}_i$, respectively. At a given temperature T and chemical potential μ, we assume that the particle interaction is governed by a symmetric pairwise potential $U_{\text{int}}\colon \Omega_0 \times \Omega_0 \to \mathbb{R}$ and that the system is exposed to an external potential $U_{\text{ext}}\colon \Omega_0 \to \mathbb{R}$, describing, e.g., gravity or system boundaries. Thus, the Hamiltonian can be represented in the form

$$H_N = \sum_{i=1}^{N} \frac{\boldsymbol{P}_i \cdot \boldsymbol{P}_i}{2m_i} + \sum_{i=1}^{N} U_{\text{ext}}(\boldsymbol{R}_i) + \frac{1}{2} \sum_{\substack{i,j=1 \\ i \neq j}}^{N} U_{\text{int}}(\boldsymbol{R}_i, \boldsymbol{R}_j), \tag{6.1}$$

where m_i denotes the mass of particle i and we have taken into account $U_{\text{int}}(\boldsymbol{R}_i, \boldsymbol{R}_i) = 0$ and the symmetry property $U_{\text{int}}(\boldsymbol{R}_i, \boldsymbol{R}_j) = U_{\text{int}}(\boldsymbol{R}_j, \boldsymbol{R}_i)$. In addition, we define the equilibrium probability density f_{eq}^N as

$$f_{\text{eq}}^N = \Xi_{\text{g}}^{-1} \exp(-\beta[H_N - \mu N]), \quad \Xi_{\text{g}} := \sum_{N=0}^{\infty} \operatorname{Tr}_N(\exp(-\beta[H_N - \mu N])), \tag{6.2}$$

where Ξ_{g} is the grand partition function, $\beta := (k_{\text{B}}T)^{-1}$, k_{B} denotes the Boltzmann constant and the trace of a suitable function $f\colon \prod_{i=1}^{2N} \Omega_0 \to \mathbb{R}$ is, with the Planck constant h, defined by

$$\operatorname{Tr}_N(f) = \frac{1}{N! h^{3N}} \int_{\Omega_0} \dots \int_{\Omega_0} f \, \mathrm{d}\boldsymbol{R}_1 \dots \mathrm{d}\boldsymbol{R}_N \, \mathrm{d}\boldsymbol{P}_1 \dots \mathrm{d}\boldsymbol{P}_N. \tag{6.3}$$

According to [71, 73] the equilibrium density of the system is given by a one-particle density $\bar{\rho}$, which provides the probability to find a particle at position $\boldsymbol{X} \in \Omega_0$. Its microscopic definition is

$$\bar{\rho}(\boldsymbol{X}) = \left\langle \sum_{i=1}^{N} \delta\left(\boldsymbol{X} - \boldsymbol{R}_i\right) \right\rangle_{\text{gc}}, \tag{6.4}$$

where δ denotes the delta Dirac function and the grand canonical ensemble average is defined as $\langle \bullet \rangle_{\text{gc}} = \sum_{N=0}^{\infty} \operatorname{Tr}_N(f_{\text{eq}}^N \bullet)$, see Chaikin & Lubensky [35] and Evans [73] for a detailed review of ensembles and thermodynamic averages used in statistical mechanics. The density functional theory is based on the following Hohenberg–Kohn theorems, [71, 96, 146]:

There exists a unique grand canonical free energy functional $\mathcal{E} = \mathcal{E}(T, \mu, \rho)$ of the system's particle density, which becomes minimal for the equilibrium one-particle density $\bar{\rho}$:

$$\frac{\delta \mathcal{E}(T, \mu, \bar{\rho})}{\delta \rho} = 0. \tag{6.5}$$

If $\mathcal{E}$ is evaluated at $\bar{\rho}$, it is the real equilibrium grand canonical free energy of the inhomogeneous system.

The DFT thus provides a basis for determining the equilibrium one-particle density field (6.4) and the free energy of any many-body system. In practice, however, the exact form of the grand canonical free energy is not known and one has to rely on approximations. Via a Legendre transform, $\mathcal{E}$ can be expressed by an equivalent Helmholtz free energy functional $\mathcal{F} = \mathcal{F}(T, \rho)$,

$$\mathcal{E}(T, \mu, \rho) = \mathcal{F}(T, \rho) - \mu \int_{\Omega_0} \rho \, \mathrm{d}V, \tag{6.6}$$

which is conveniently divided into three additive contributions as follows

$$\mathcal{F}(T, \rho) = \mathcal{F}_{\mathrm{id}}(T, \rho) + \mathcal{F}_{\mathrm{ext}}(\rho) + \mathcal{F}_{\mathrm{exc}}(T, \rho). \tag{6.7}$$

In Eq. (6.7), $\mathcal{F}_{\mathrm{id}}$ is the ideal gas free energy functional, which, according to Evans [73], is given by

$$\mathcal{F}_{\mathrm{id}}(T, \rho) = k_{\mathrm{B}} T \int_{\Omega_0} \rho \left[\ln(\Lambda^3 \rho) - 1 \right] \, \mathrm{d}V, \tag{6.8}$$

where Λ is the thermal de Broglie wavelength. The second contribution $\mathcal{F}_{\mathrm{ext}}$ is the external free energy functional, taking into account external influences and is defined as

$$\mathcal{F}_{\mathrm{ext}}(\rho) = \int_{\Omega_0} \rho \, U_{\mathrm{ext}} \, \mathrm{d}V. \tag{6.9}$$

Eventually, the third term $\mathcal{F}_{\mathrm{exc}}$ denotes the excess free energy functional. It includes all the correlations due to the pair interactions between particles. In general, it is not known explicitly and must therefore be approximated appropriately. A formally exact expression for $\mathcal{F}_{\mathrm{exc}}$ is gained by a functional Taylor expansion* in $\Delta\rho = \bar{\rho} - \rho_{\mathrm{ref}}$ around a homogeneous reference density ρ_{ref}. In the simplest nontrivial approach, the Taylor expansion is truncated at second order, leading to the Ramakrishnan-Yussouff theory [136],

$$\mathcal{F}_{\mathrm{exc}}(T, \rho) = -\frac{k_{\mathrm{B}} T}{2} \int_{\Omega_0} \int_{\Omega_0} c(\boldsymbol{X}_1, \boldsymbol{X}_2) \Delta\rho(\boldsymbol{X}_1) \Delta\rho(\boldsymbol{X}_2) \, \mathrm{d}\boldsymbol{X}_1 \, \mathrm{d}\boldsymbol{X}_2. \tag{6.10}$$

*For details concerning higher order functional derivatives and functional Taylor expansions we refer to the textbook of Engel & Dreizler [72]

The Ramakrishnan-Yussouff approximation needs the direct pair-correlation function c as an input. Well known analytic approximations for c are, e.g., the second order virial expression,

$$c(\boldsymbol{X}_1, \boldsymbol{X}_2) = \exp\left(-\frac{U_{\text{int}}(\boldsymbol{X}_1, \boldsymbol{X}_2)}{k_{\text{B}}T}\right) - 1, \tag{6.11}$$

cf. van Roij et al. [163], and the random-phase or mean-field approximation

$$c(\boldsymbol{X}_1, \boldsymbol{X}_2) = -\frac{U_{\text{int}}(\boldsymbol{X}_1, \boldsymbol{X}_2)}{k_{\text{B}}T}, \tag{6.12}$$

where the latter approach becomes in the case of a bounded potential asymptotically exact at high densities, cf. [118, 117, 164].

6.1.2 Dynamic Density Functional Theory

Dynamic density functional theory is the time-dependent analogue of static DFT. It can be derived from the Smoluchowski equation, [139, 149], by postulating that the correlations between the particles when the system is out of equilibrium are equivalent to those of an equilibrium system with the same one particle density profile. In the following, we provide the main results of the theory and refer to Archer & Evans [6] for a detailed discussion.

In its basic form, DDFT describes the slow dissipative non-equilibrium relaxation dynamics of a system of N Brownian particles close to thermodynamical equilibrium or the behaviour in a time-dependent external potential $U_{\text{ext}} = U_{\text{ext}}(\boldsymbol{X}, t)$. Here we define a one-particle density field via

$$\bar{\rho}(\boldsymbol{X}, t) = \left\langle \sum_{i=1}^{N} \delta\left(\boldsymbol{X} - \boldsymbol{R}_i(t)\right) \right\rangle_{\text{c}}, \tag{6.13}$$

where t is the time variable and the classical canonical ensemble average is given by $\langle \bullet \rangle_{\text{c}} = \text{Tr}_N(f^N \bullet)$ with the probability density and partition function

$$f^N = \Xi^{-1} \exp(-\beta H_N), \quad \Xi = \text{Tr}_N(-\beta H_N). \tag{6.14}$$

Note that the densities (6.4) and (6.13) differ, apart from the time-dependence, in the choice of the respective ensemble. A comparison of the canonical and the grand canonical ensemble can be found in Chaikin & Lubensky [35]. According to Marconi & Tarazona [120], a characteristic evolution equation for the density is obtained within the framework of Brownian motions, using the Langevin equations and the Smoluchowski picture. Assuming that $\bar{\rho}$ is conserved and dissipative, the DDFT equation reads

$$\dot{\bar{\rho}} = \frac{D_{\text{T}}}{k_{\text{B}}T} \nabla_{\boldsymbol{X}} \cdot \left(\bar{\rho}\, \nabla_{\boldsymbol{X}} \frac{\delta \mathcal{F}(T, \bar{\rho})}{\delta \rho}\right), \quad \text{in } \Omega_0 \times I, \tag{6.15}$$

where D_{T} is the translational diffusion coefficient of the system and I is a real interval representing the timespan under consideration. Note that the functional derivative in

Eq. (6.15) can be interpreted as an inhomogeneous chemical potential, [6], such that the DDFT equation corresponds to a generalized Fick's law of particle diffusion, cf. also Section 5.

We point out that the use of the particle density (6.13) is one of several options to describe the dynamics of the system. Since $\bar{\rho}$ results from taking an ensemble average over the stochastic noise, it is uniquely valued at time t; consequently, Eq. (6.15) is deterministic. This is the approach, e.g., in [6, 120, 121]. The time evolution equation for the instantaneous particle density $\hat{\rho}(\boldsymbol{X}, t) = \sum_{i=1}^{N} \delta(\boldsymbol{X} - \boldsymbol{R}_i(t))$ is discussed, e.g., in [58, 78, 106], and for Brownian particles this is a stochastic equation. A further approach is to use a coarse-grained density given by a time integral of the product of the instantaneous particle density and an experimental resolution function, also resulting in a stochastic equation for the time evolution, [106, 128]. For a detailed discussion of the several approaches, we recommend the work of Archer & Rauscher [7].

6.2 Phase-field crystal model

Using appropriate approximations, the phase-field crystal (PFC) model can be justified from DFT respectively DDFT. The free energy used in the PFC model was first derived from DFT by Elder et al. [69], while the corresponding dynamics were derived from DDFT by van Teeffelen et al. [164]. In this section, we outline the basic ideas of these works and formulate the corresponding variational problem for the dynamical Phase-field Crystal Equation.

6.2.1 Free energy functional

To derive the free energy functional for the PFC model, we first of all define a dimensionless density deviation ψ of the one-particle density from a reference density by

$$\bar{\rho}(\boldsymbol{X}, t) = \rho_{\mathrm{ref}}(1 + \psi(\boldsymbol{X}, t)), \quad (\boldsymbol{X}, t) \in \Omega_0 \times I. \tag{6.16}$$

This relative density deviation is considered to be small, $|\psi| \ll 1$, and slowly varying in space (on the microscale). The basic steps to derive the PFC free energy functional are threefold: 1) insert (6.16) into the free energy functional (6.7), 2) Taylor-expand systematically in terms of powers of ψ, 3) perform a gradient expansion of the correlation functions. Here, in accordance with the assumption that the density deviation is small, we use the Ramakrishnan-Yussouff approximation (6.10) as a convenient approximation for the excess free energy functional.

Substituting Eq. (6.16) into Eq. (6.8) and Taylor expansion of the logarithm up to fourth

order yields the PFC ideal gas free functional[†]

$$\mathcal{F}_{\mathrm{id}}(T,\psi) = \rho_{\mathrm{ref}} k_{\mathrm{B}} T \int\limits_{\Omega_0} \frac{\psi^2}{2} - \frac{\psi^3}{6} + \frac{\psi^4}{12} \,\mathrm{d}V, \tag{6.17}$$

whereby substituting Eq. (6.16) into Eq. (6.9) simply leads to the PFC external free energy functional

$$\mathcal{F}_{\mathrm{ext}}(\psi) = \rho_{\mathrm{ref}} \int\limits_{\Omega_0} \psi U_{\mathrm{ext}} \,\mathrm{d}V. \tag{6.18}$$

For the approximation of the excess free energy functional the direct pair-correlation function c in the Ramakrishnan-Yussouff approximation (6.10) is gradient expanded[‡]. up to fourth order. Therefore, it is important to note that c has the same symmetry as the particle interaction potential U_{int}, cf. Eqs. (6.11), (6.12). In the PFC model, radially symmetric interactions are assumed, i.e.

$$c(\boldsymbol{X}_1, \boldsymbol{X}_2) = c(X) \tag{6.19}$$

with the distance $X = \|\boldsymbol{X}_1 - \boldsymbol{X}_2\|$. Consequently, we obtain the following excess free energy functional

$$\mathcal{F}_{\mathrm{exc}}(T,\psi) = -\frac{\rho_{\mathrm{ref}} k_{\mathrm{B}} T}{2} \int\limits_{\Omega_0} A_1' \psi^2 + A_2' \psi \Delta_{\boldsymbol{X}} \psi + A_3' \psi \Delta_{\boldsymbol{X}}^2 \psi \,\mathrm{d}V, \tag{6.20}$$

where the coefficients are given by

$$A_1' = 4\pi\rho_{\mathrm{ref}} \int\limits_0^\infty X^2 c(X) \,\mathrm{d}X,\; A_2' = \frac{2\pi\rho_{\mathrm{ref}}}{3} \int\limits_0^\infty X^4 c(X) \,\mathrm{d}X,\; A_3' = \frac{\pi\rho_{\mathrm{ref}}}{30} \int\limits_0^\infty X^6 c(X) \,\mathrm{d}X. \tag{6.21}$$

Following Provatas & Elders [134], we additionally introduce two constant model parameters A_4, A_5 to control the contribution of the cubic and quartic term in Eq. (6.17). Altogether, we finally obtain the general form of the Helmholtz free energy functional for the PFC model:

$$\mathcal{F}(T,\psi) = \rho_{\mathrm{ref}} k_{\mathrm{B}} T \int\limits_{\Omega_0} \frac{A_1}{2}\psi^2 + \frac{A_2}{2}\psi\Delta_{\boldsymbol{X}}\psi + \frac{A_3}{2}\psi\Delta_{\boldsymbol{X}}^2\psi + \frac{A_4}{3}\psi^3 + \frac{A_5}{4}\psi^4 \,\mathrm{d}V + \mathcal{F}_{\mathrm{ext}}(\psi), \tag{6.22}$$

where A_1, A_2, A_3 are related to the coefficients in Eq. (6.20) via $A_1 = 1 - A_1'$, $A_2 = -A_2'$, $A_3 = -A_3'$.

[†]In the following approximations we omit a priori constant terms which are irrelevant for the model. Moreover, we neglect integrals of ψ over Ω_0 justified by the assumption $|\psi| \ll 1$.

[‡]For details concerning the gradient expansion of correlation functions we refer to Leeuwen [162].

6.2.2 The Phase-field Crystal Equation and multi-patch framework

The dynamics of the PFC model can now be deduced from DDFT in a straight-forward manner. Inserting the representation (6.16) for the one-particle density field into the DDFT equation (6.15), using the PFC Helmholtz free energy functional (6.22) and assuming a uniform temperature distribution, we obtain for the temporal evolution of the density deviation the following relation

$$\dot{\psi} = \nabla_{\boldsymbol{X}} \cdot (M(\psi)\nabla_{\boldsymbol{X}}\mu(\psi)), \quad \text{in } \Omega_0 \times I, \tag{6.23}$$

where $M(\psi) := D_{\mathrm{T}}(1+\psi)$ denotes the diffusivity of the system and the scaled chemical potential is given by

$$\mu = (\rho_{\mathrm{ref}} k_{\mathrm{B}} T)^{-1} \frac{\delta \mathcal{F}(T,\psi)}{\delta \psi} = A_1\psi + A_2\Delta_{\boldsymbol{X}}\psi + A_3\Delta_{\boldsymbol{X}}^2\psi + A_4\psi^2 + A_5\psi^3 + \frac{U_{\mathrm{ext}}}{k_{\mathrm{B}}T}. \tag{6.24}$$

As in the case of the Cahn-Hilliard equation introduced in Section 5.2.2, we consider a closed system and exclude effects at the external boundary which leads here to the boundary conditions[§]

$$M\nabla_{\boldsymbol{X}}\mu \cdot \boldsymbol{N} = 0, \quad \nabla_{\boldsymbol{X}}\psi \cdot \boldsymbol{N} = 0, \quad \nabla_{\boldsymbol{X}}\Delta_{\boldsymbol{X}}\psi \cdot \boldsymbol{N} = 0, \quad \text{on } \partial\Omega_0 \times I, \tag{6.25}$$

with the unit outward normal $\boldsymbol{N}$ on $\partial\Omega_0$. The first condition in Eq. (6.25) ensures conservation of ψ whereas the second and third condition exclude effects at the boundary. To complete the initial boundary value problem we further specify an initial condition as $\psi = \bar{\psi}$ in $\Omega_0 \times \{0\}$, where $\bar{\psi}$ is a prescribed initial density deviation.

The derivation of a multi-patch framework is analogous to Sections 4.5, 5.2.1 and 5.2.2. After applying the time-stepping procedure from Appendix A and transferring the resulting boundary value problems into corresponding weak forms, the result for each patch is a sequence of variational problems of the form: given $\psi_0^{(i)} = \bar{\psi}^{(i)}$, for $\nu = 1, \ldots, M$, find $\psi_\nu^{(i)} \in \mathcal{S}^{(i)}$ such that

$$\begin{aligned}
\mathrm{V}_\nu^{(i)}(\psi_\nu^{(i)}, \delta\psi^{(i)}) := {} & h_\nu^{-1}\langle \psi_\nu^{(i)} - \psi_{\nu-1}^{(i)}, \delta\psi^{(i)}\rangle_{\Omega_0} + \langle M(k_{\mathrm{B}}T)^{-1}\nabla_{\boldsymbol{X}} U_{\mathrm{ext},\nu-\frac{1}{2}}, \nabla_{\boldsymbol{X}}\delta\psi^{(i)}\rangle_{\Omega_0} \\
& + \langle [(M[A_1 + 2A_4\psi^{(i)} + 3A_5(\psi^{(i)})^2] - A_2 D_{\mathrm{T}}\Delta_{\boldsymbol{X}}\psi^{(i)})\nabla_{\boldsymbol{X}}\psi^{(i)}]_{\nu-\frac{1}{2}}, \nabla_{\boldsymbol{X}}\delta\psi^{(i)}\rangle_{\Omega_0} \\
& + \langle A_3 D_{\mathrm{T}}(\nabla_{\boldsymbol{X}} \otimes \nabla_{\boldsymbol{X}}\psi^{(i)})\nabla_{\boldsymbol{X}}\Delta_{\boldsymbol{X}}\psi^{(i)}]_{\nu-\frac{1}{2}}, \nabla_{\boldsymbol{X}}\delta\psi^{(i)}\rangle_{\Omega_0} \\
& + \langle [-A_2 M\Delta_{\boldsymbol{X}}\psi^{(i)} + A_3 D_{\mathrm{T}}\nabla_{\boldsymbol{X}}\psi^{(i)} \cdot \nabla_{\boldsymbol{X}}\Delta_{\boldsymbol{X}}\psi^{(i)}]_{\nu-\frac{1}{2}}, \Delta_{\boldsymbol{X}}\delta\psi^{(i)}\rangle_{\Omega_0} \\
& + \langle A_3 D_{\mathrm{T}}\nabla_{\boldsymbol{X}}\psi_{\nu-\frac{1}{2}}^{(i)}, (\nabla_{\boldsymbol{X}} \otimes \nabla_{\boldsymbol{X}}\delta\psi^{(i)})\nabla_{\boldsymbol{X}}\Delta_{\boldsymbol{X}}\psi_{\nu-\frac{1}{2}}^{(i)}\rangle_{\Omega_0} \\
& + \langle A_3 M\nabla_{\boldsymbol{X}}\Delta_{\boldsymbol{X}}\psi_{\nu-\frac{1}{2}}^{(i)}, \nabla_{\boldsymbol{X}}\Delta_{\boldsymbol{X}}\delta\psi^{(i)}\rangle_{\Omega_0} = 0
\end{aligned} \tag{6.26}$$

for all $\delta\psi^{(i)} \in \mathcal{V}^{(i)}$, which can further be treated with the methods from Chapter 3. When deriving the weak forms, note that in the strong form 6.23 the expression corresponding to the coefficients A_2 and A_3 contains derivatives up to the 4th and 6th order, respectively, so

[§]The first and third condition are natural whereas the second one is essential.

that in the first case partial integration has to be performed twice and in the second case three times. The resulting boundary integrals vanish due to the homogeneous boundary conditions (6.25). Furthermore, it should be noted that in the integrals of the weak form, derivatives up to the 3rd order occur for both the solution functions and the test functions. I.e. to ensure that the expressions in (6.26) are defined and the essential boundary condition is fulfilled, we require spaces so that

$$\mathcal{S}^{(i)} = \mathcal{V}^{(i)} \subset \left\{ \psi \in H^3(\Omega_0^{(i)}) \,|\, \nabla_{\boldsymbol{X}} \psi \cdot \boldsymbol{N} = 0 \text{ on } \Gamma_{\mathrm{e}}^{(i)} \right\}, \tag{6.27}$$

where $\Gamma_{\mathrm{e}}^{(i)} := \partial\Omega_0^{(i)} \cap \partial\Omega_0$. As with the Cahn-Hilliard equation in Section 5.2.2, the spaces of the admissible solution and test functions are identical at each time step since the essential boundary conditions are homogeneous.

6.3 Numerical studies

Finally, we present the results of PFC simulations in the framework of multi-patch IGA using the extended mortar method. In the first example, we consider a two-dimensional system describing the nucleation and growth of crystals, formulated as a 4-patch system. Instead of the boundary conditions given in Eq. (6.25), periodic boundaries are used there. In the PFC context, this corresponds to a C^2 coupling with spatially separated interfaces and is treated with generalised coupling conditions according to Section 3.1.3. The second example serves as proof of concept and is the three-dimensional analogue of the first example, where we consider a two-patch system with a curved interface.

6.3.1 Crystal growth 2D

In this example, we consider nucleation and growth of crystals from a pure supercooled liquid in a two-dimensional domain consisting of four patches. In such a process, small (heterogeneous or homogeneous) crystallites nucleate and grow at different locations and in different directions. Eventually, the crystallites collide and grain boundaries are formed. Further growth is then determined by the development of the grain boundaries. In such scenarios, it is often useful to consider only a part of a larger system, as the process is similar in the adjacent areas. Therefore we replace the boundary conditions (6.25) by periodic ones, analogous to the diffusion example in Section 5.3.2. Due to the continuity requirements of the PFC framework, the values of the derivatives up to the 2nd order must match for this purpose in addition to the conditions for the value of the density deviation at the corresponding boundaries. To this end, generalised C^2-continuous coupling conditions according to Section 3.1.3 are formulated at the corresponding edges. For details on the configuration used here (area size, material parameters etc.), we refer to the work of Elder et al. [70] and Praetorius & Voigt [131], on which the example is based.

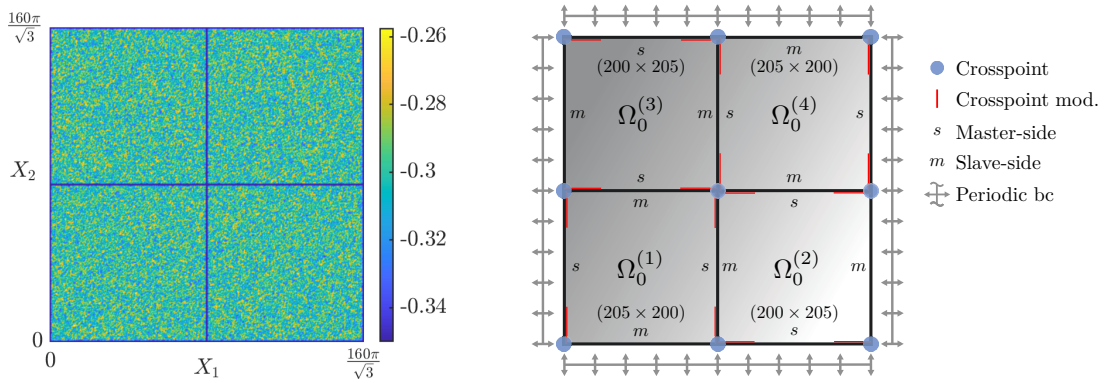

Figure 6.1: *Crystal growth 2D.* Left: Initial configuration $\bar{\psi}(\boldsymbol{X})$, $\boldsymbol{X} \in \Omega_0$. Right: setting summary including patch numbering, choice of master and slave side, resolutions of the patches, crosspoints and boundary conditions.

We consider the crystallisation process in the period $I = [0, 4994.6]$ on the domain $\Omega_0 = (0, 160\pi/\sqrt{3})^2$ consisting of the four parts

$$\Omega_0^{(1)} = \left(0, \frac{80\pi}{\sqrt{3}}\right) \times \left(0, \frac{80\pi}{\sqrt{3}}\right), \qquad \Omega_0^{(2)} = \left(\frac{80\pi}{\sqrt{3}}, \frac{160\pi}{\sqrt{3}}\right) \times \left(0, \frac{80\pi}{\sqrt{3}}\right), \tag{6.28}$$

$$\Omega_0^{(3)} = \left(0, \frac{80\pi}{\sqrt{3}}\right) \times \left(\frac{80\pi}{\sqrt{3}}, \frac{160\pi}{\sqrt{3}}\right), \qquad \Omega_0^{(4)} = \left(\frac{80\pi}{\sqrt{3}}, \frac{160\pi}{\sqrt{3}}\right) \times \left(\frac{80\pi}{\sqrt{3}}, \frac{160\pi}{\sqrt{3}}\right), \tag{6.29}$$

whereby, following the examples in [70, 131], both the temporal and spatial dimensions are unitless. The material is defined through the parameter

$$D_{\mathrm{T}} = 1, \quad A_1 = 0.65, \quad A_2 = 2, \quad A_3 = 1, \quad A_4 = 0, \quad A_5 = 1 \tag{6.30}$$

and the initial configuration $\bar{\psi}\colon \Omega_0 \to \mathbb{R}$ is given by $\bar{\psi}(\boldsymbol{X}) = -0.35 + \mathfrak{r}(\boldsymbol{X})$, where $\mathfrak{r}$ is a random variable modelling slight inhomogeneities in the system within a range of $\pm 1\%$ to trigger nucleation. As in the diffusion example 5.3.2, a homogeneous density deviation of $\bar{\psi} = -0.35$ is assumed at the boundaries of the patches to ensure that the coupling conditions are fulfilled at time $t = 0$, see Figure 6.1 for illustration.

For the implementation of the periodic boundaries, we define, in addition to the four real interfaces within Ω_0, four virtual interfaces $(\gamma_1, \phi_1), \ldots, (\gamma_4, \phi_4)$ through

$$\Omega_0^{(1)}/\Omega_0^{(2)} : \ \gamma_1 = \{0\} \times \left(0, \frac{80\pi}{\sqrt{3}}\right), \qquad \phi_1(\boldsymbol{X}) = \boldsymbol{X} + \left(\frac{160\pi}{\sqrt{3}}, 0\right)^{\mathrm{T}}, \tag{6.31}$$

$$\Omega_0^{(3)}/\Omega_0^{(4)} : \ \gamma_2 = \left\{\frac{160\pi}{\sqrt{3}}\right\} \times \left(\frac{80\pi}{\sqrt{3}}, \frac{160\pi}{\sqrt{3}}\right), \qquad \phi_2(\boldsymbol{X}) = \boldsymbol{X} - \left(\frac{160\pi}{\sqrt{3}}, 0\right)^{\mathrm{T}}, \tag{6.32}$$

$$\Omega_0^{(1)}/\Omega_0^{(3)} : \ \gamma_3 = \left(0, \frac{80\pi}{\sqrt{3}}\right) \times \left\{\frac{160\pi}{\sqrt{3}}\right\}, \qquad \phi_3(\boldsymbol{X}) = \boldsymbol{X} - \left(0, \frac{160\pi}{\sqrt{3}}\right)^{\mathrm{T}}, \tag{6.33}$$

$$\Omega_0^{(2)}/\Omega_0^{(4)} : \ \gamma_4 = \left(\frac{80\pi}{\sqrt{3}}, \frac{160\pi}{\sqrt{3}}\right) \times \{0\}, \qquad \phi_4(\boldsymbol{X}) = \boldsymbol{X} + \left(0, \frac{160\pi}{\sqrt{3}}\right)^{\mathrm{T}}, \tag{6.34}$$

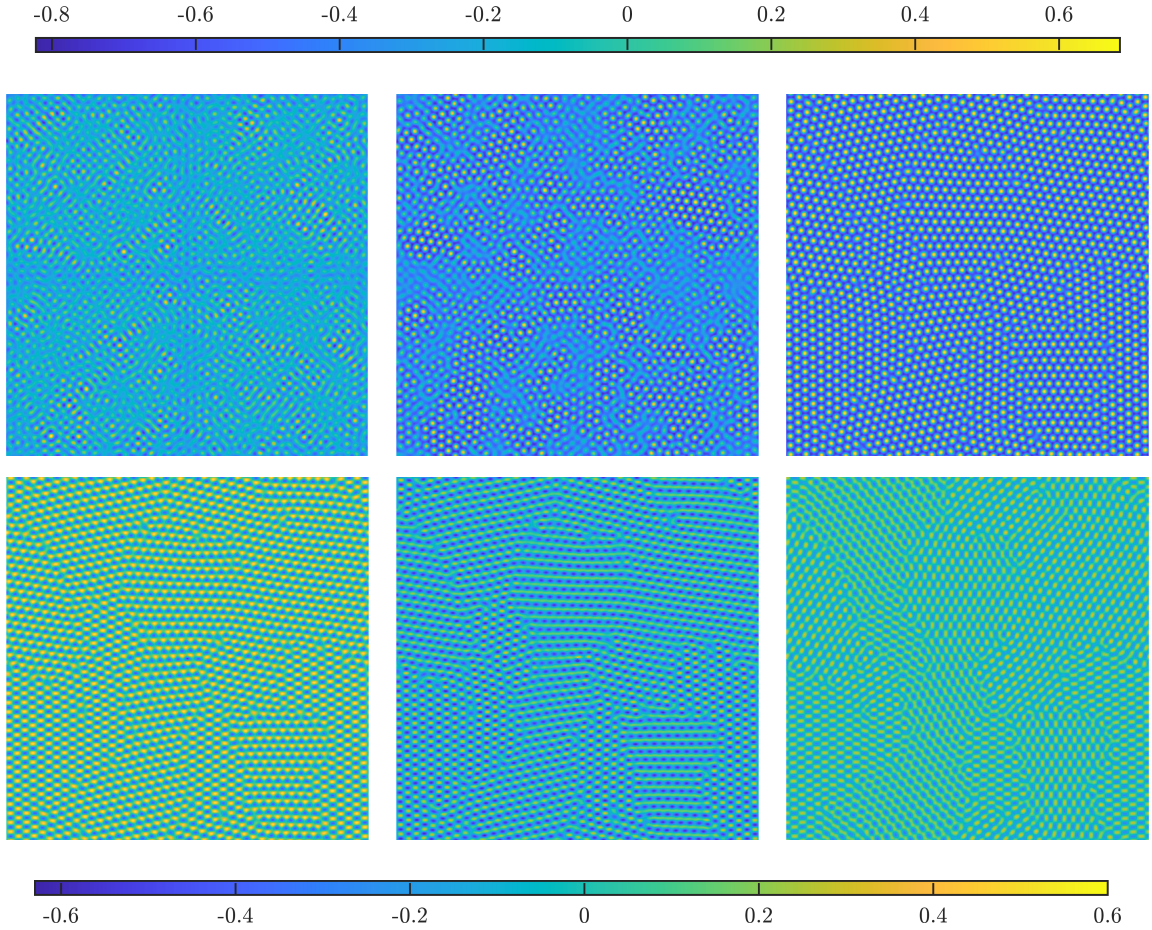

Figure 6.2: *Crystal growth 2D.* Simulation results. Upper row: density deviation ψ_h at time $t = 49.6, 99.06, 4994.6$ (from left to right). Lower row: derivatives $\partial_{X_2}\psi_\mathrm{h}$, $\partial^2_{X_2}\psi_\mathrm{h}$, $\partial_{X_1}\partial_2\psi_\mathrm{h}$ (from left to right) at time $t = 4994.6$. The upper colour bar belongs to the density deviation and the lower one to the partial derivatives.

which respectively couple the left/right edges of $\Omega_0^{(1)}/\Omega_0^{(2)}$ and $\Omega_0^{(3)}/\Omega_0^{(4)}$ as well as the lower/upper edges of $\Omega_0^{(1)}/\Omega_0^{(3)}$ and $\Omega_0^{(2)}/\Omega_0^{(4)}$.

Furthermore, for the simulations we employ globally C^2-continuous shape functions of order $\boldsymbol{p} = (3, 3)$, such that $\Omega_0^{(1)}$, $\Omega_0^{(4)}$ are resolved by 205×200 elements and $\Omega_0^{(2)}$, $\Omega_0^{(3)}$ by 200×205 elements, respectively, resulting in non-conforming meshes at each interface. Accordingly, we use weak C^2 couplings and a segment-based integration scheme for the evaluation of the mortar-integrals. Note that the patch numbering, the choice of master and slave side, the resolutions of the patches, the crosspoints and the boundary conditions are summarized in the right picture in Figure 6.1. With regard to the temporal discretisation, we use a time-dependent step-size $h_\nu \colon I \to \mathbb{R}_{\geq 0}$,

$$h_\nu = h_\nu(t) = \begin{cases} 0.1, & \text{if } t \in [0, 0.5], \\ 1, & \text{if } t \in (0.5, 4994.6]. \end{cases} \tag{6.35}$$

The small step-size at the beginning of the simulation takes into account a rapid change of the system, while the crystallisation process proceeds significantly slower in the further course. The simulation results for the density deviation ψ_h and several partial derivatives are shown in Figure 6.2. It can be observed, that due to the inhomogeneous density distribution modelled by the random variable $\mathfrak{r}$, nucleation occurs throughout the whole domain. As time progresses, the small crystallites grow from the initial seeds until impingement. Eventually, the entire system is filled with crystallites arranged hexagonally to each other (each crystallite is surrounded by 6 nearest neighbours), and further evolution continues by motion at grain boundaries. In particular, it should be noted that in all cases the patches merge seamlessly and the interfaces are not recognisable in the illustrations. The same holds true for the periodic boundaries. Figure 6.3 shows as an

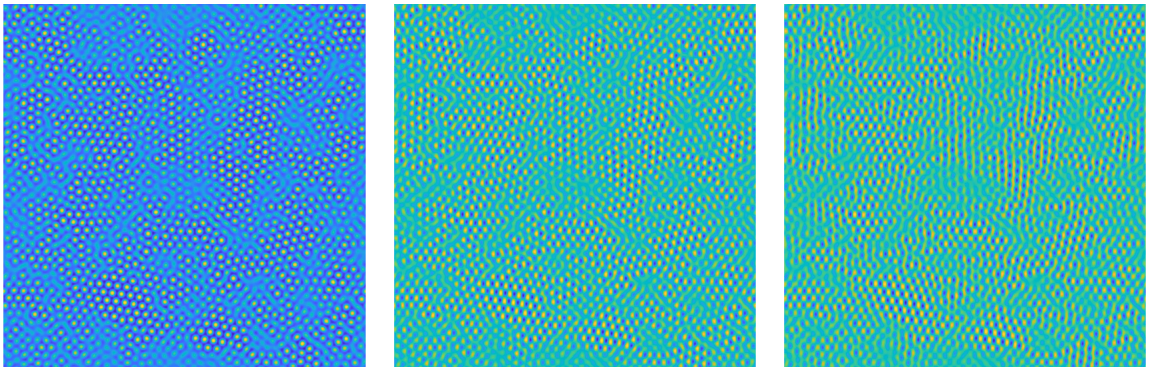

Figure 6.3: *Crystal growth 2D.* Reordered patches $\Omega^{(1)} \leftrightarrow \Omega^{(4)}$ and $\Omega^{(2)} \leftrightarrow \Omega^{(3)}$. From left to right: ψ_h, $\partial_1\psi_\mathrm{h}$ and $\partial_1^2\psi_\mathrm{h}$ at time $t = 99.6$.

example the results at time $t = 99.6$, with the positions of the patches in the images swapped according to $\Omega^{(1)} \leftrightarrow \Omega^{(4)}$ and $\Omega^{(2)} \leftrightarrow \Omega^{(3)}$. To quantify these observations, the

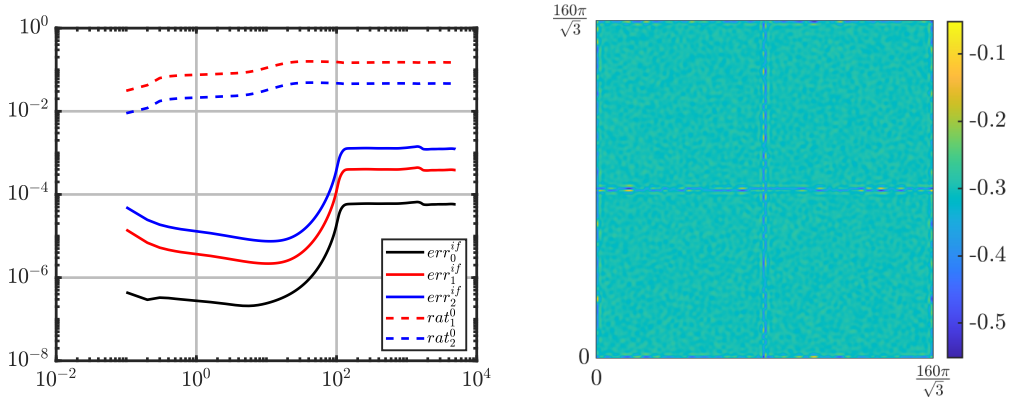

Figure 6.4: *Crystal growth 2D.* Left: interface errors err_0^{if}, err_1^{if}, err_2^{if} and ratios rat_1^0, rat_1^0 as functions in time. Right: ψ_h on Ω_0 using weak C^1 couplings.

evolution of the three relative coupling errors

$$err_0^{if}(t) = \frac{1}{L}\left(\sum_{k=1}^{4} \|\psi_{\mathrm{h}}^{(s(k))} - \psi_{\mathrm{h}}^{(m(k))}\|_{L^2(\Gamma_k)}^2 + \|\psi_{\mathrm{h}}^{(s(k))} - \psi_{\mathrm{h}}^{(m(k))} \circ \phi_k\|_{L^2(\gamma_k)}^2\right)^{\frac{1}{2}}, \tag{6.36}$$

$$err_1^{if}(t) = \frac{1}{L}\left(\sum_{k=1}^{4} \|\nabla_{\boldsymbol{X}}(\psi_{\mathrm{h}}^{(s(k))} - \psi_{\mathrm{h}}^{(m(k))})\|_{L^2(\Gamma_k)}^2 + \|\nabla_{\boldsymbol{X}}\psi_{\mathrm{h}}^{(s(k))} - (\nabla_{\boldsymbol{X}}\psi_{\mathrm{h}}^{(m(k))}) \circ \phi_k\|_{L^2(\gamma_k)}^2\right)^{\frac{1}{2}}, \tag{6.37}$$

$$err_2^{if}(t) = \frac{1}{L}\left(\sum_{k=1}^{4} \|\mathrm{D}^2(\psi_{\mathrm{h}}^{(s(k))} - \psi_{\mathrm{h}}^{(m(k))})\|_{L^2(\Gamma_k)}^2 + \|\mathrm{D}^2\psi_{\mathrm{h}}^{(s(k))} - (\mathrm{D}^2\psi_{\mathrm{h}}^{(m(k))}) \circ \phi_k\|_{L^2(\gamma_k)}^2\right)^{\frac{1}{2}}, \tag{6.38}$$

is provided in Figure 6.4. Here, D^2 is a linear operator summarizing the second partial derivatives according to $\mathrm{D}^2\psi_{\mathrm{h}} = (\partial_{X_1}^2\psi_{\mathrm{h}}, \partial_{X_2}^2\psi_{\mathrm{h}}, \partial_{X_1}\partial_{X_2}\psi_{\mathrm{h}})^{\mathrm{T}}$ and $L = 640\pi/\sqrt{3}$ is the sum of the interface lengths. It can be seen that $err_0^{if}(I) \subset (2 \cdot 10^{-7}, 6.6 \cdot 10^{-5})$, $err_1^{if}(I) \subset (2.1 \cdot 10^{-7}, 4.5 \cdot 10^{-4})$ and $err_2^{if}(I) \subset (7.4 \cdot 10^{-6}, 1.5 \cdot 10^{-3})$, whereby the error increases with increasing order of the derivatives. Furthermore, it can be observed that the three errors behave synchronously in time. The dashed lines show the evolution over time of the two ratios

$$rat_1^0(t) := \frac{err_0^{if}(t)}{err_1^{if}(t)}, \quad rat_2^0(t) := \frac{err_0^{if}(t)}{err_2^{if}(t)} \tag{6.39}$$

quantifying the difference of the two derivative errors err_i^{if}, $i = 1, 2$, with respect to the density deviation error err_0^{if}. For these two quantities, it holds $rat_1^0(I) \subset (3.1 \cdot 10^{-2}, 1.6 \cdot 10^{-1})$ and $err_2^0(I) \subset (8.9 \cdot 10^{-3}, 4.9 \cdot 10^{-2})$, such that err_1^{if} is at most 32.1 times greater than err_0^{if} and err_2^{if} is at most 111.3 times greater than err_0^{if}.

Eventually, to demonstrate the necessity of C^2 couplings in the PFC framework, the right picture in Figure 6.4 shows simulation results employing weak C^1 coupling conditions instead of C^2 conditions. In this case, non-physical fluctuations of the density deviation occur in the area of the interfaces, which leads to the termination of the simulation after a few time steps.

6.3.2 Crystal growth 3D

This final example serves as a proof of concept and is the three-dimensional analogue of the previous example. Instead of a 4-patch system, however, we study here a 2-patch system with a curved interface.

We consider the crystallisation process in the period $I = [0, 3655]$ on a cube-shaped area $\Omega_0 = (0, 20\pi/\sqrt{3})^3$ decomposed into two patches $\Omega_0^{(1)}$ (slave), $\Omega_0^{(2)}$ (master) with a curved interface, see the left picture in Figure 6.5 for illustration. As in the two-dimensional example, the material parameters and initial configuration are given by

$$D_{\mathrm{T}} = 1, \quad A_1 = 0.65, \quad A_2 = 2, \quad A_3 = 1, \quad A_4 = 0, \quad A_5 = 1 \tag{6.40}$$

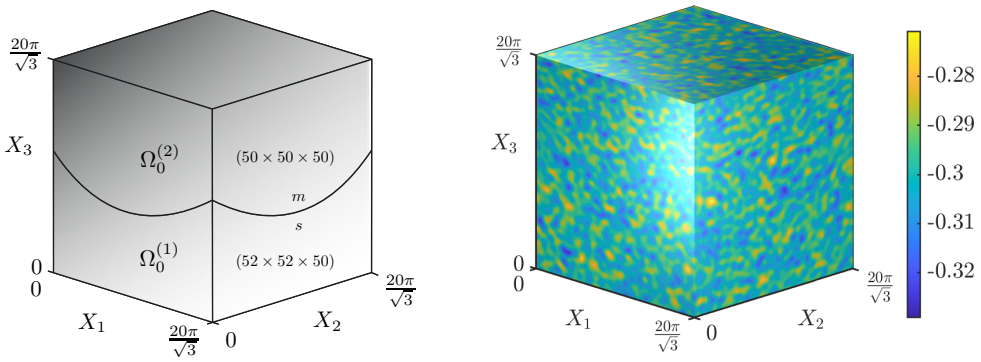

Figure 6.5: *Crystal growth 3D.* Left: subdivision of Ω_0 into the two patches. The master and slave sides of the interface are indicated by m/s and the resolutions are given in the brackets. Right: initial configuration $\bar{\psi}(\boldsymbol{X})$, $\boldsymbol{X} \in \Omega_0$.

and $\bar{\psi}\colon \Omega_0 \to \mathbb{R}$, $\bar{\psi}(\boldsymbol{X}) = -0.35 + \mathfrak{r}(\boldsymbol{X})$, where here the random variable $\mathfrak{r}$ is constructed in such a way that inhomogeneities also occur at the interface and the patches still C^2-continuously merge at $t = 0$, see the right picture in Figure 6.5.

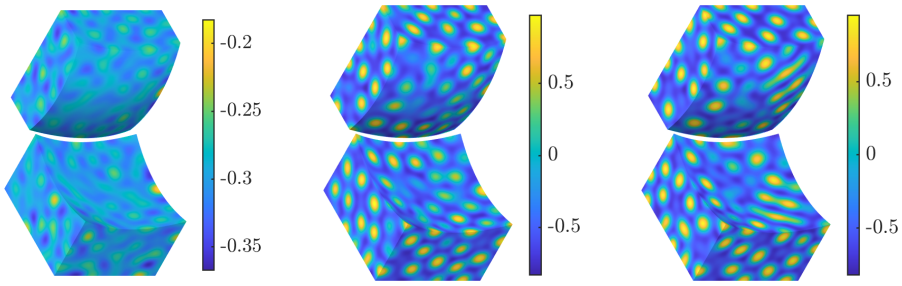

Figure 6.6: *Crystal growth 3D.* Temporal evolution. ψ_h at times t=50.5001, 100.5001, 3655.5001.

For the time-stepping scheme, we use the step-size control specified in Eq. (6.35) and for the spatial discretisation, we employ globally C^2-continuous shape functions of order $\boldsymbol{p} = (3, 3, 3)$, such that $\Omega_0^{(1)}$ and $\Omega_0^{(2)}$ are resolved by $52 \times 52 \times 50$ and $50 \times 50 \times 50$ elements, respectively. Accordingly, we use a weak C^2 coupling with an element-based integration scheme involving 64-point Gaussian integration. Furthermore, for simplicity, we refrain from modifying the Lagrangian multipliers at the wirebasket arising from the intersection of the interface with Γ_e.

Snapshots of the simulation results for ψ_h are shown in Figure 6.6 and Figure 6.7 illustrates the corresponding results for the partial derivatives of ψ_h up to the 2nd order. As in the two-dimensional example, nucleation occurs throughout the whole domain until the entire system is filled with hexagonally arranged crystallites. In particular, it can be noted that no irregularities at the interface are recognisable in the illustrations.

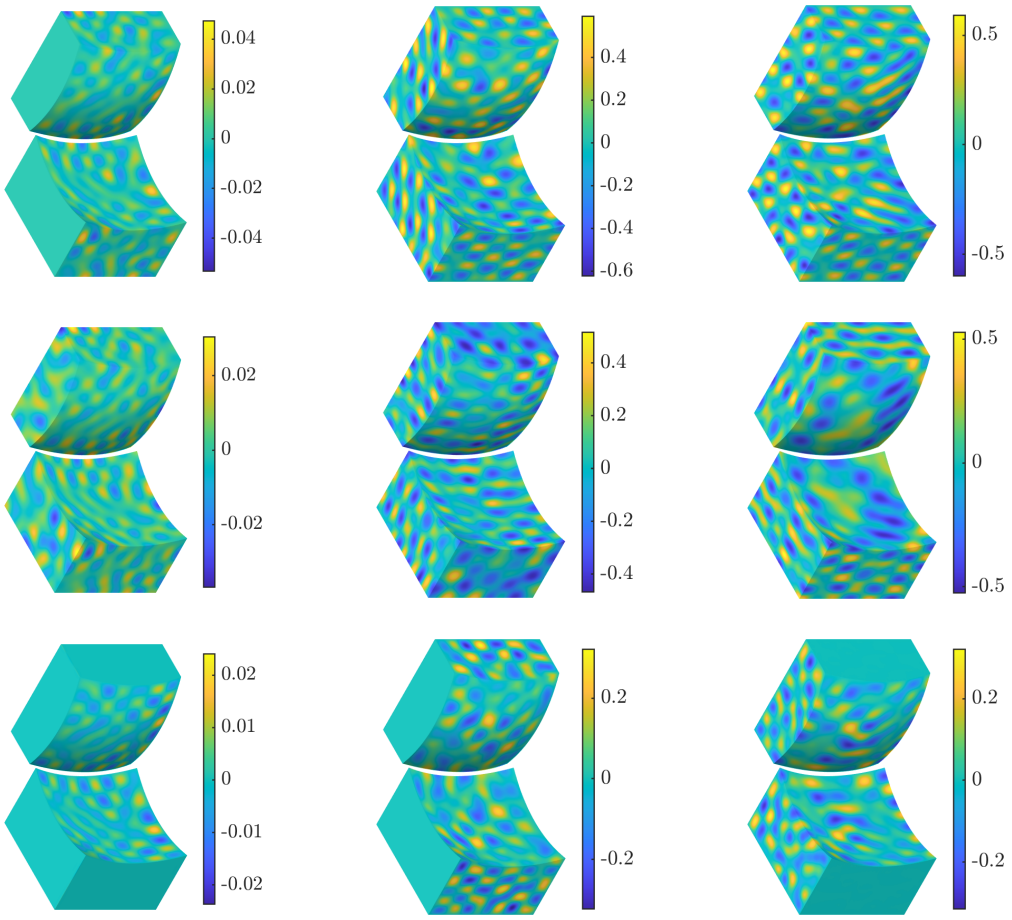

Figure 6.7: *Crystal growth 3D.* Temporal evolution. From left to right and top to bottom: $\partial_{X_1}\psi_{\mathrm{h}}(\bullet,t_1)$, $\partial_{X_2}\psi_{\mathrm{h}}(\bullet,t_2)$, $\partial_{X_3}\psi_{\mathrm{h}}(\bullet,t_3)$, $\partial^2_{X_1}\psi_{\mathrm{h}}(\bullet,t_1)$, $\partial^2_{X_2}\psi_{\mathrm{h}}(\bullet,t_2)$, $\partial^2_{X_3}\psi_{\mathrm{h}}(\bullet,t_3)$, $\partial_{X_1}\partial_{X_2}\psi_{\mathrm{h}}(\bullet,t_1)$, $\partial_{X_1}\partial_{X_3}\psi_{\mathrm{h}}(\bullet,t_2)$, $\partial_{X_2}\partial_{X_3}\psi_{\mathrm{h}}(\bullet,t_3)$, where $t_1 = 50.5001$, $t_2 = 100.5001$, $t_3 = 3655.5001$.

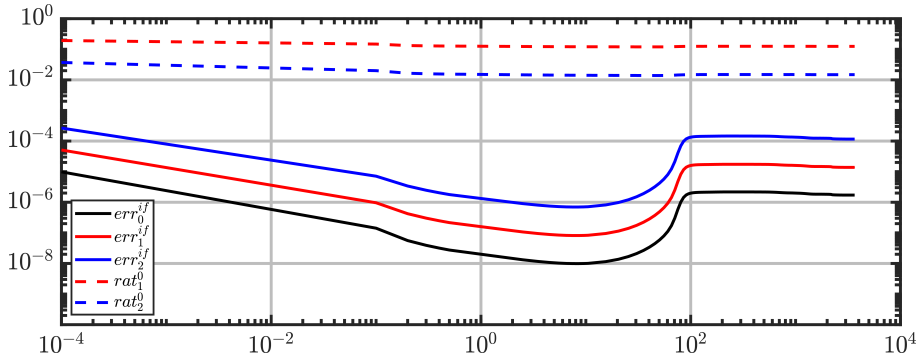

Figure 6.8: *Crystal growth 3D.* Interface errors err_0^{if}, err_1^{if}, err_2^{if} and ratios rat_1^0, rat_2^0 as functions in time.

To verify this observation, Figure 6.8 shows the temporal evolution of the three relative coupling errors

$$err_0^{if}(t) := A^{-1}\|\psi_{\mathrm{h}}^{(1)} - \psi_{\mathrm{h}}^{(2)}\|_{L^2(\Gamma)}, \quad err_i^{if}(t) := A^{-1}\|\mathrm{D}^i(\psi_{\mathrm{h}}^{(1)} - \psi_{\mathrm{h}}^{(2)})\|_{L^2(\Gamma)}, \tag{6.41}$$

$i = 1, 2$, where D^i summarize the ith partial derivatives according to $\mathrm{D}^1\psi_{\mathrm{h}} := \nabla_{\boldsymbol{X}}\psi_{\mathrm{h}}$, $\mathrm{D}^2\psi_{\mathrm{h}} := (\partial^2_{X_1}\psi_{\mathrm{h}}, \partial^2_{X_2}\psi_{\mathrm{h}}, \partial^2_{X_3}\psi_{\mathrm{h}}\partial_{X_1}\partial_{X_2}\psi_{\mathrm{h}}, \partial_{X_1}\partial_{X_3}\psi_{\mathrm{h}}, \partial_{X_2}\partial_{X_3}\psi_{\mathrm{h}})^{\mathrm{T}}$ and $A = 1375.750066027$ is the surface area of the interface. Additional, Figure 6.8 provides the temporal evolution of the two quantities $rat_1^0(t) := err_0^{if}(t)/err_1^{if}(t)$, $rat_2^0(t) := err_0^{if}(t)/err_2^{if}(t)$ showing the ratio between the two derivative errors err_i^{if}, $i = 1, 2$, and density deviation error err_0^{if}. It can be observed, that $err_0^{if}(I) \subset (9.89{\cdot}10^{-9}, 9.85{\cdot}10^{-6})$, $err_1^{if}(I) \subset (8.18{\cdot}10^{-8}, 5.11{\cdot}10^{-5})$ and $err_2^{if}(I) \subset (6.99{\cdot}10^{-7}, 2.67{\cdot}10^{-4})$ which shows that the error increases with increasing derivative order. Furthermore it can be seen $rat_1^0(I) \subset (1.19 \cdot 10^{-1}, 1.93 \cdot 10^{-1})$ and $rat_1^0(I) \subset (1.38 \cdot 10^{-2}, 3.7 \cdot 10^{-2})$, so that over time err_1^{if} is at most 8.37 times as large as err_0^{if} and err_2^{if} is at most 72.1 times as large as err_0^{if}.

7 Summary and outlook

In this work, a novel mortar method was introduced that realises weak C^n- and G^1-continuous domain couplings in the context of IGA. The implementation of the coupling conditions was discussed on the basis of an abstract variational problem without further restrictions, which allows the method to be easily transferred to a wide range of problems. Within this framework, couplings of real interfaces as well as generalised couplings were considered, which can be used, e.g., for the implementation of periodic boundary conditions in higher-order differential equations.

For the coupled variational framework, two equivalent formulations were provided. One formulation utilized constrained spaces that satisfy the coupling conditions, while the other was formulated as a saddle point system in which the couplings were implemented using Lagrange multipliers. The discretisation of the problem was discussed within the context of IGA, with the discrete space of Lagrange multipliers defined as the trace space on the slave side, eliminating the need to evaluate additional shape functions for the multiplier space. To avoid over-constrained situations in the vicinity of crosspoints or wirebaskets, a new method for modifying the multiplier space was introduced extending a known method for C^0 couplings to higher-order coupling conditions. This involved removing basis functions to prevent excessive multipliers' influence on the crosspoints or wirebaskets, while modifying the remaining basis functions to preserve the partition of unity and the ability to reproduce polynomials with reduced degrees in that region. Furthermore, a novel method for implementing coupling conditions without explicitly using Lagrange multipliers was devised. This approach allowed for the construction of isogeometric approximation spaces that inherently respected the coupling conditions. While the number of unknowns increases with a saddle point formulation, the number is reduced to the same extent when using these constrained approximation spaces.

The application of the higher-order couplings was explored through a diverse range of engineering problems, including polyharmonic equations, elasticity, Kirchhoff-Love shells, heat conduction, diffusion problems, and the phase-field crystal method. During these investigations, coupling conditions up to the second order were successfully implemented. Through numerous comparisons with corresponding 1-patch systems, it was demonstrated that the high approximation quality of the IGA framework is preserved in a multi-patch environment using the extended mortar method.

Let us now discuss the possible perspectives to this work. One important point of an isogeometric mortar method is the choice of the Lagrange multipliers. From the classical mortar theory, two abstract requirements are given. One is the sufficient approximation order, the other is the requirement of an inf-sup stability. Here we have used the trace

space of the slave side, which has the consequence that the basis functions of the primary and the dual space are of the same order. Other pairings are conceivable. For C^0 couplings, several constellations have been investigated in the framework of IGA with respect to inf-sup stability and convergence rate, Brivadis et al. [31]. Analogous investigations for general C^n couplings are still pending. Another interesting approach in the choice of the multiplier space is the use of global polynomials, Hansbo et al. [87]. This has the advantage that in an element-based integration scheme the mortar integrals are evaluated exactly if the quadrature formula is of sufficient order. A transfer of the approach to C^n couplings could be an interesting subject. Another worthwhile investigation also concerns the element-based integration scheme. The patch test in Section 4.7.1 has shown that in the case of a curved interface, a simple midpoint rule is superior to Gaussian quadrature. Based on this result, it seems interesting to investigate further alternatives.

A Temporal discretisation

Most of the examples considered in this work are dynamic problems, i.e. the solutions sought to the problems are functions in space and time. To solve such problems numerically, it is common practice to first discretise them in time, resulting in a sequence of boundary value problems which can further be treated in the context of isogeometric analysis. In this section, we briefly present the temporal discretisation schemes used in this work. For more details concerning this topic, we refer to the textbook of Reinhardt [138] and the work of Simo & Tarnow [147].

We consider abstract initial value problems stated as follows: find $\boldsymbol{v}\colon \Omega_0 \times I \to \mathbb{R}^d$ such that

$$\partial_t^s \boldsymbol{v} - \mathcal{P}(\boldsymbol{x}, t, \boldsymbol{v}) = \boldsymbol{0}, \qquad \text{in } \Omega_0 \times I, \tag{A.1}$$

where $s \in \{1, 2\}$, ∂_t^s denotes the s times partial derivative w.r.t. t, Ω_0 is a suitable open and bounded subset of $\mathbb{R}^{d_p}$ with $d_p \leq d$, $I = [0, \tau] \subset \mathbb{R}$, $\tau > 0$ and the operator $\mathcal{P}$ represents the problem and incorporates any spatial derivative. Furthermore, we assume that the solution and, in case $s = 2$, its partial derivative w.r.t. t at time $t = 0$ are known and given by the functions $\boldsymbol{v}_0\colon \Omega_0 \to \mathbb{R}^d$, $\bar{\boldsymbol{v}}_0\colon \Omega_0 \to \mathbb{R}^d$.

Let $t_0, \ldots, t_N \in I$ be a sequence of points in time such that $t_0 = 0$, $t_N = \tau$ and $t_\nu < t_{\nu+1}$. In case $s = 1$, we use for the temporal discretization the midpoint rule, resulting in the sequence of spatial problems: for $\nu = 1, \ldots, N$ find $\boldsymbol{v}_\nu\colon \Omega_0 \to \mathbb{R}^d$ such that

$$(\boldsymbol{v}_\nu - \boldsymbol{v}_{\nu-1}) h_\nu^{-1} - \mathcal{P}(\boldsymbol{x}, t_{\nu-1/2}, \boldsymbol{v}_{\nu-1/2}) = \boldsymbol{0}, \quad \text{in } \Omega_0, \tag{A.2}$$

where $\boldsymbol{v}_\nu$ denotes the evaluation of $\boldsymbol{v}$ at time t_ν, $\boldsymbol{v}_{\nu-1/2}$ the evaluation at time $t_{\nu-1/2} := (t_\nu + t_{\nu-1})/2$ and $h_\nu := t_\nu - t_{\nu-1}$ the step-size. In case $s = 2$, the temporal discretization is performed using a two-step midpoint rule, resulting in the problem sequence: for $\nu = 1, \ldots, N$ find $\boldsymbol{v}_\nu\colon \Omega_0 \to \mathbb{R}^d$ such that

$$(\bar{\boldsymbol{v}}_\nu - \bar{\boldsymbol{v}}_{\nu-1}) h_\nu^{-1} - \mathcal{P}(\boldsymbol{x}, t_{\nu-1/2}, \boldsymbol{v}_{\nu-1/2}) = \boldsymbol{0}, \quad \bar{\boldsymbol{v}}_\nu = 2h_\nu^{-1}(\boldsymbol{v}_\nu - \boldsymbol{v}_{\nu-1}) - \bar{\boldsymbol{v}}_{\nu-1}, \quad \text{in } \Omega_0. \tag{A.3}$$

We finally note that the two integration schemes are in $\mathcal{O}(h^2)$, where $h = \max_{\nu=1,\ldots,N} h_\nu$. The first scheme is used in this work for problems in heat conduction and diffusion (Chapter 5) and for Phase-Field-Crystal modeling (Chapter 6), whereas the second one is applied to problems in elasticity introduced in Chapter 4.

Remark A.0.1. *In particular, problems of elasticity require structure-preserving time integration schemes such that the linear momentum, angular momentum and total energy are preserved. Applied to the equation of motion in the form* (4.37) *the scheme* (A.3)

algorithmically preserves the linear and angular momentum. To additionally ensure the conservation of total energy, the equation of motion has first to be rewritten in terms of the second Piola-Kirchhoff stress tensor $\boldsymbol{S}$*, such that* (4.37) *becomes*

$$\rho_0(\boldsymbol{X})\ddot{\boldsymbol{\varphi}}(\boldsymbol{X},t) = \nabla_{\boldsymbol{X}} \cdot [\boldsymbol{F}(\boldsymbol{X},t)\, \boldsymbol{S}(\boldsymbol{X},t)] + \boldsymbol{B}(\boldsymbol{X},t) \quad \forall (\boldsymbol{X},t) \in \Omega_0 \times I. \tag{A.4}$$

Using the algorithmically consistent discrete version

$$\boldsymbol{S}_{\mathrm{h},\nu-1/2} = 2\left[\frac{\partial \mathrm{W}_{\nu-1/2}}{\partial\, \boldsymbol{C}_{\mathrm{h}}} + \frac{\mathrm{W}_{\nu} - \mathrm{W}_{\nu-1} - \partial \mathrm{W}_{\nu-1/2} / \partial\, \boldsymbol{C}_{\mathrm{h}} : \Delta\, \boldsymbol{C}_{\mathrm{h}}}{\Delta\, \boldsymbol{C}_{\mathrm{h}} : \Delta\, \boldsymbol{C}_{\mathrm{h}}}\, \Delta\, \boldsymbol{C}_{\mathrm{h}}\right] \tag{A.5}$$

of $\boldsymbol{S}$ *when applying scheme* (A.3)*, total energy as well as the linear and angular momentum are conserved. For more details and the proof of the algorithmic conservation properties, we refer to the works of Gonzalez & Simo [83] and Betsch & Steinmann [24]. For the application on thermomechanical problems see furthermore Hesch et al. [91] and for the application on phase-field methods to fracture see Hesch & Weinberg [93].*

Examples: As a first example we consider the parabolic initial boundary value problem stated as follows: find $v\colon \bar{\Omega}_0 \times I \to \mathbb{R}$ such that

$$\dot{v} - \Delta v = 0 \text{ in } \Omega_0 \times I, \qquad v = g \text{ on } \Gamma_{\mathrm{e}} \times I, \tag{A.6a}$$

$$\nabla v \cdot \boldsymbol{N} = h \text{ on } \Gamma_{\mathrm{n}} \times I, \qquad v = v_0 \text{ on } \Omega_0 \times \{0\}, \tag{A.6b}$$

where Γ_{e}, $\Gamma_{\mathrm{n}} \subset \partial\Omega_0$ with $\Gamma_{\mathrm{e}} \cap \Gamma_{\mathrm{n}} = \emptyset$ and $\bar{\Gamma}_e \cap \bar{\Gamma}_n = \partial\Omega_0$, $g, h\colon \Gamma_{\mathrm{e}} \to \mathbb{R}$, $v_0\colon \Omega_0 \to \mathbb{R}$ are prescribed functions and $\boldsymbol{N}$ denotes the unit outward normal on $\partial\Omega_0$. Application of the midpoint rule (A.2) yields the following sequence of boundary value problems: for given v_0 find for $\nu = 1, \ldots, N$ a function $v_\nu\colon \bar{\Omega}_0 \to \mathbb{R}$ such that

$$(v_\nu - v_{\nu-1})h_\nu^{-1} - \Delta v_{\nu-1/2} = 0 \qquad \text{in } \Omega_0, \tag{A.7a}$$

$$v_\nu = g_\nu \qquad \text{on } \Gamma_{\mathrm{e}}, \tag{A.7b}$$

$$\nabla v_{\nu-1/2} \cdot \boldsymbol{N} = h_{\nu-1/2} \qquad \text{on } \Gamma_{\mathrm{n}}. \tag{A.7c}$$

As a second example we apply the following hyperbolic initial boundary value problem: find $v\colon \bar{\Omega}_0 \times I \to \mathbb{R}$ such that

$$\ddot{v} - \Delta v = 0 \text{ in } \Omega_0 \times I, \qquad v = g \text{ on } \Gamma_{\mathrm{e}} \times I, \tag{A.8a}$$

$$\nabla v \cdot \boldsymbol{N} = h \text{ on } \Gamma_{\mathrm{n}} \times I, \qquad v = v_0,\ \dot{v} = \bar{v}_0 \text{ on } \Omega_0 \times \{0\}, \tag{A.8b}$$

where we use the same notation as in the first example and the prescribed function $\bar{v}_0\colon \Omega_0 \to \mathbb{R}$ determines the first derivative of v w.r.t. t at $t = 0$. Application of the two-step midpoint rule (A.4) yields the sequence of boundary value problems: for given v_0, $\bar{v}_0$ find for $\nu = 1, \ldots, N$ a function $v_\nu\colon \bar{\Omega}_0 \to \mathbb{R}$ such that

$$2[(v_\nu - v_{\nu-1})h_\nu^{-1} - \bar{v}_{\nu-1}]h_\nu^{-1} - \Delta v_{\nu-1/2} = 0 \qquad \text{in } \Omega_0, \tag{A.9a}$$

$$v_\nu = g_\nu \qquad \text{on } \Gamma_{\mathrm{e}}, \tag{A.9b}$$

$$\nabla v_{\nu-1/2} \cdot \boldsymbol{N} = h_{\nu-1/2} \qquad \text{on } \Gamma_{\mathrm{n}}, \tag{A.9c}$$

with $\bar{v}_{\nu-1} = 2h_{\nu-1}^{-1}(v_{\nu-1} - v_{\nu-2}) - \bar{v}_{\nu-2}$ for $\nu = 2, \ldots, N$.

B Material data for tin-lead alloys

The following is a summary of the material data for tin-lead alloys used in the examples in Section 5.3. For details on the derivation of the quantities, we refer to Schuß et al. [142].

Free energy. The configurational part of the free energy of a tin-lead system valid within the temperature range $250\,\mathrm{K} < T < 505\,\mathrm{K}$ is represented by the mole fraction and temperature-dependent function

$$\Psi^{\mathrm{con}}(c,T) = g_1 c + g_2(1-c) + g_3 c\,\ln(c) + g_4(1-c)\ln(1-c) + g_5 c(1-c), \tag{B.1}$$

where the field variable c denotes the mole fraction of tin*. The coefficients g_i are temperature-dependent functions obtained from fits to experimental data as

$$g_k(T) = A_k + B_k T + C_k T\ln(T) + D_k T^2 + E_k T^3 + \frac{F_k}{T}, \quad k = 1,...,4, \tag{B.2}$$

$$g_5(T) = A_5 + B_5 T, \quad \text{in } \left[\mathrm{Jm}^{-3}\right], \tag{B.3}$$

where the numerical values of the fit parameters are listed in Table B.1. Moreover, the gradient energy coefficient κ is calculated from the lattice structure of the equilibrium phases and is related to the surface energy density $\tilde{\kappa}$ and the interfacial thickness l between the tin- and lead-rich phases via

$$\kappa(T) = \frac{3\tilde{\kappa} l}{(c_{\mathrm{Sn}}(T) - c_{\mathrm{Pb}}(T))^2}, \quad \text{in } \left[\mathrm{Jm}^{-1}\right], \tag{B.4}$$

where $\tilde{\kappa} = 1.5\,\mathrm{Jm}^{-2}$, $l = 25\,\mathrm{nm}$ and $c_{\mathrm{Sn/Pb}}$, are the temperature-dependent equilibrium mole fractions determined by the polynomials

$$c_{\mathrm{Sn/Pb}}(T) = c_3^{\mathrm{Sn/Pb}} T^3 + c_2^{\mathrm{Sn/Pb}} T^2 + c_1^{\mathrm{Sn/Pb}} T^1 + c_0^{\mathrm{Sn/Pb}}, \tag{B.5}$$

see also Table B.2. Thus, the interface part of the free energy density reads

$$\Psi^{\mathrm{int}}(c,T) = \frac{75\cdot 10^{-9}}{2(c_{\mathrm{Pb}}(T) - c_{\mathrm{Sn}}(T))^2} \|\nabla_{\boldsymbol{X}} c\|^2. \tag{B.6}$$

*I.e. we specify lead as component a and tin as component b, cf. Section 5.2.2.

Table B.1: Fit parameter for the functions g_i introduced in Eqs. (B.2), (B.3).

	$A_i\left[\frac{\mathrm{MJ}}{\mathrm{m}^3}\right]$	$B_i\left[\frac{\mathrm{MJ}}{\mathrm{m}^3\mathrm{K}}\right]$	$C_i\left[\frac{\mathrm{MJ}}{\mathrm{m}^3\mathrm{K}}\right]$	$D_i\left[\frac{\mathrm{J}}{\mathrm{m}^3\mathrm{K}^2}\right]$	$E_i\left[\frac{\mathrm{J}}{\mathrm{m}^3\mathrm{K}^3}\right]$	$F_i\left[\frac{\mathrm{GJK}}{\mathrm{m}^3}\right]$
$i=1$	-355.77	3.9628	-0.96695	-1146	0.1898	-3.7692
$i=2$	-405.42	5.5101	-1.3286	-191.5847	-0.0153	0.027891
$i=3$	275.05	1.338	-0.18453	389.8139	-0.1331	1.9559
$i=4$	-85.964	1.3153	-0.13691	244.7001	-0.0888	1.274
$i=5$	1224.9	-0.49161	-	-	-	-

Table B.2: Coefficients of the equilibrium mole fractions introduced in Eq. (B.5).

	$c_0^i\,[\quad]$	$c_1^i\left[\mathrm{K}^{-1}\right]$	$c_2^i\left[\mathrm{K}^{-2}\right]$	$c_3^i\left[\mathrm{K}^{-3}\right]$
$i=\mathrm{Sn}$	1.03418	$-3.867\cdot10^{-4}$	$1.4722\cdot10^{-6}$	$-1.8897\cdot10^{-9}$
$i=\mathrm{Pb}$	$-1.2076\cdot10^{-2}$	$2.4223\cdot10^{-4}$	$-5.5931\cdot10^{-7}$	$1.1125\cdot10^{-9}$

Mobilities. The atomic mobilities of tin in lead and lead in tin, respectively, are represented by the functions

$$M_{\mathrm{Sn/Pb}}(T)=\frac{463}{5\cdot10^4V_m}\left(\frac{\partial^2\Psi^{\mathrm{con}}(c_{\mathrm{Pb/Sn}}(T),T)}{\partial c^2}\right)^{-1}D_{\mathrm{Sn/Pb}}(T), \tag{B.7}$$

in $[\mathrm{m^2molJ^{-1}s^{-1}}]$, where the molar volume of the alloy is given by the weighted sum $V_m=\bar{c}V_m^{\mathrm{Sn}}+(1-\bar{c})V_m^{\mathrm{Pb}}$, in $[\mathrm{m^3mol^{-1}}]$. Thereby, $V_m^{\mathrm{Sn}}=16.29\cdot10^{-6}\,\mathrm{m^3mol^{-1}}$ is the molar volume of tin, $V_m^{\mathrm{Pb}}=18.26\cdot10^{-6}\,\mathrm{m^3mol^{-1}}$ the molar volume of lead and the scalar field $\bar{c}\colon\Omega_0\to[0,1]$ determines the initial state of the system, cf. Section 5.2.2.[†] The diffusivities $D_{\mathrm{Sn/Pb}}$ of tin/lead are obtained from an Arrhenius relationship

$$D_{\mathrm{Sn/Pb}}(T)=D^0_{\mathrm{Sn/Pb}}\exp\left(-\frac{Q_{\mathrm{Sn/Pb}}}{RT}\right), \tag{B.8}$$

where $R=8.31451\,\mathrm{Jmol^{-1}K^{-1}}$ denotes the universal gas constant and the frequency factors $D^0_{\mathrm{Sn/Pb}}$ and the activation energies $Q_{\mathrm{Sn/Pb}}$ are given by

$$D^0_{\mathrm{Sn}}=4.1\cdot10^{-5}\,\mathrm{m^2s^{-1}},\qquad Q_{\mathrm{Sn}}=94400\,\mathrm{Jmol^{-1}}, \tag{B.9}$$

$$D^0_{\mathrm{Pb}}=3.533\cdot10^{-6}\,\mathrm{m^2s^{-1}},\quad Q_{\mathrm{Pb}}=61370\,\mathrm{Jmol^{-1}}. \tag{B.10}$$

Using the data presented in Eqs. (B.9), (B.10), it turns out that diffusion within the tin-rich regions is considerably faster than in the lead-rich regions. Consequently, neglecting the atomic mobility of tin in lead, the mobility of the alloy is approximately given by

$$M(c,T)=c(1-c)M_{\mathrm{Pb}}(T),\quad\text{in }\left[\mathrm{m^2molJ^{-1}s^{-1}}\right]. \tag{B.11}$$

[†]In our numerical investigations, we always assume a constant initial configuration $\bar{c}(\boldsymbol{X})=0.63$, $\boldsymbol{X}\in\Omega_0$, so that in this case the molar volume of the system is constant and given by $V_m=9905/(582\cdot10^6)\,\mathrm{m^3mol^{-1}}$.

Bibliography

[1] photo source: http://aliceinfo.cern.ch/public/en/chapter2/chap2_spd.html, 2011.

[2] photo source: http://www.fbh-berlin.com/press/download-center, 2011.

[3] D. Anders, M. Dittmann, and K. Weinberg. A higher-order finite element approach to the Kuramoto-Sivashinsky equation. *Journal of Applied Mathematics and Mechanics*, 92(8):599–607, 2012.

[4] D. Anders, C. Hesch, and K. Weinberg. Computational modeling of phase separation and coarsening in solder alloys. *International Journal of Solids and Structures*, 49: 1557–1572, 2012.

[5] A. Apostolatos, R. Schmidt, R. Wüchner, and K. U. Bletzinger. A Nitsche-type formulation and comparison of the most common domain decomposition methods in isogeometric analysis. *International Journal for Numerical Methods in Engineering*, 97:473–504, 2014.

[6] A. J. Archer and R. Evans. Dynamical density functional theory and its application to spinodal decomposition. *Journal of Chemical Physics*, 121(9):4246–4254, 2004.

[7] A. J. Archer and M. Rauscher. Dynamical density functional theory for interacting Brownian particles: stochastic or deterministic? *Journal of Physics A: Mathematical and General*, 37:9325–9333, 2004.

[8] J. H. Argyris and S. Kelsey. *Energy Theorems and Structural Analysis*. Springer New York, NY, 1960.

[9] J. H. Argyris, I. Fried, and D. W. Scharpf. The TUBA Family of Plate Elements for the Matrix Displacement Method. *The Aeronautical Journal*, 72(692):701–709, 1968.

[10] Y. Başar and Y. Ding. Shear deformation models for large-strain shell analysis. *International Journal of Solids and Structures*, 34(14):1687–1708, 1997.

[11] Y. Başar and M. Itskov. Finite element formulation of the Ogden material model with application to rubber-like shells. *International Journal for Numerical Methods in Engineering*, 42(7):1279–1305, 1998.

[12] Y. Başar and D. Weichert. *Nonlinear Continuum Mechanics of solids*. Springer-Verlag Berlin, Heidelberg, New York, 2000.

[13] Y. Bazilevs, L. Beirao da Veiga, J. A. Cottrell, T. J. R Hughes, and G. Sangalli. Isogeometric analysis: approximation, stability and error estimates for h-refined meshes. *Mathematical Models and Methods in Applied Sciences*, 16(07):1031–1090, 2006.

[14] L. Beirão da Veiga, A. Buffa, G. Snagalli, and R. Vázquez. Mathematical analysis of variational isogeometric methods. *Acta Numerica*, pages 157–287, 2014.

[15] F. B. Belgacem. The Mortar finite element method with Lagrange multipliers. *Numerische Mathematik*, 84(2):173–197, Dec 1999.

[16] F. B. Belgacem and Y. Maday. The Mortar finite element method for three dimensional finite elements. *Mathematical Modelling and Numerical Analysis*, 31(2): 289–302, 1997.

[17] F. B. Belgacem, P. Hild, and P. Laborde. Extension of the mortar finite element method to a variational inequality modeling unilateral contact. *Mathematical Models and Methods in Applied Sciences*, 9(02):287–303, 1999.

[18] K. Bell. A refined triangular plate bending finite element. *International Journal for Numerical Methods in Engineering*, 1(1):101–122, 1969.

[19] D. J. Benson, Y. Bazilevs, M. C. Hsu, and T. J. R. Hughes. Isogeometric shell analysis: The Reissner–Mindlin shell. *Computer Methods in Applied Mechanics and Engineering*, 199:276–289, 2010.

[20] D. J. Benson, Y. Bazilevs, M.C. Hsu, and T. J. R. Hughes. A large deformation, rotation-free, isogeometric shell. *Computer Methods in Applied Mechanics and Engineering*, 200:1367–1378, 2011.

[21] C. Bernardi, Y. Maday, and A. T. Patera. *Domain Decomposition by the Mortar Element Method*, pages 269–286. Springer Netherlands, 1993.

[22] C. Bernardi, Y. Maday, and A. T. Patera. A new nonconforming approach to domain decomposition: the mortar element method. *Nonlinear Partial Differential Equations and their Applications, Collège de France Seminar*, XI:13–51, 1994.

[23] C. Bernardi, Y. Mayday, and A. T. Patera. A new nonconforming approach to domain decomposition: the mortar element method. *Nonlinear partial differential equations and their applications*, pages 13–51, 1994.

[24] P. Betsch and P. Steinmann. Conserving properties of a time FE method - Part II: Time-stepping schemes for non-linear elastodynamics. *International Journal for Numerical Methods in Engineering*, 50:1931–1955, 2001.

[25] J. Betten. *Kontinuumsmechanik*. Springer-Verlag Berlin, Heidelberg, New York, 2001.

[26] A. Blidia, B. Mourrain, and N. Villamizar. G1-smooth splines on quad meshes with 4-split macropatch elements. *Computer Aided Geometric Design*, 52–53:106–125, 2017.

[27] J. F. Blowey and C. M. Elliott. The Cahn–Hilliard gradient theory for phase separation with non-smooth free energy Part I: Mathematical analysis. *European Journal of Applied Mathematics*, 2(3):233–280, 1991.

[28] J. F. Blowey and C. M. Elliott. The Cahn–Hilliard gradient theory for phase separation with non-smooth free energy Part II: Numerical analysis. *European Journal of Applied Mathematics*, 3(2):147–179, 1992.

[29] M. J. Borden, T. J. R. Hughes, C. M. Landis, and C. V. Verhoosel. A higher-order phase-field model for brittle fracture: Formulation and analysis within the isogeometric analysis framework. *Computer Methods in Applied Mechanics and Engineering*, 273:100–118, 2014.

[30] E. Brivadis. *Isogeometric mortar methods with applications in contact mechanics*. PhD thesis, Scuola Universitaria Superiore IUSS Pavia, 2016.

[31] E. Brivadis, A. Buffa, B. Wohlmuth, and L. Wunderlich. Isogeometric mortar methods. *Computer Methods in Applied Mechanics and Engineering*, 284:292–319, 2015. Isogeometric Analysis Special Issue.

[32] E. Brivadis, A. Buffa, B. Wohlmuth, and L. Wunderlich. The Influence of Quadrature Errors on Isogeometric Mortar Methods. *Isogeometric Analysis and Applications 2014. Lecture Notes in Computational Science and Engineering*, 107, 2015.

[33] J. W. Cahn. Phase separation by spinodal decomposition in isotropic systems. *Journal of Chemical Physics*, 42(1):93–99, 1964.

[34] J. W. Cahn and J. E. Hilliard. Free energy of a nonuniform system. I. Interfacial free energy. *Journal of Chemical Physics*, 28:258–267, 1958.

[35] P. M. Chaikin and T. C. Lubensky. *Principles of condensed matter physics*. Cambridge University Press, 1st edition.

[36] C. L. Chan, Anitescu C., and T. Rabczuk. Strong multipatch C1-coupling for isogeometric analysis on 2D and 3D domains. *Computer Methods in Applied Mechanics and Engineering*, 357:112599, 2019.

[37] P. G. Ciarlet. *Mathematical elasticity*, volume I: Three-dimensional elasticity. Elsevier Science Publishers B.V., 1988.

[38] P. G. Ciarlet. *Mathematical Elasticity*, volume III: Theory of Shells. Elsevier Science Publishers B.V., 2000.

[39] P. G. Ciarlet. *An Introduction to Differential Geometry with Aplications to Elasticity*. Springer, 2005.

[40] R. W. Clough. *The Finite Element Method in Plane Stress Analysis*. American Society of Civil Engineers, 1960.

[41] R. W. Clough and J. L. Tochter. Finite element stiffness matrices for analysis of plates in bending. In *Conference on Matrix Methods in Structural Mechanics*. Wright-Patterson A.F.B.

[42] E. Cohen, T. Lyche, and L. L. Schumaker. Algorithms for degree-raising of splines. *ACM Transaction on Graphics*, 4(3):171–181, 1985.

[43] J. A. Cottrell, T. J. R. Hughes, and A. Reali. Studies of refinement and continuity in isogeometric structural analysis. *Computer Methods in Applied Mechanics and Engineering*, 196(41–44):4160–4183, 2007.

[44] J. A. Cottrell, T. J. R. Hughes, and Y. Bazilevs. *Isogeometric Analysis: Toward Integration of CAD and FEA*. Wiley, 2009.

[45] R. Courant. Variational methods for the solution of problems of equilibrium and vibrations. *Bulletin of the American Mathematical Society*, 49(1):1–23, 1943.

[46] S. Court and K. Kunisch. Almost global existence of weak solutions for the nonlinear elastodynamics system for a class of strain energies. *arXiv preprint arXiv:1607.03282*, 2016.

[47] G. R. Cowper. Gaussian quadrature formulas for triangles. *International Journal for Numerical Methods in Engineering*, 7(3):405–408, 1973.

[48] M. G. Cox. The numerical evaluation of B-splines. *IMA Journal of Applied Mathematics*, 10(2):134–149, 1972.

[49] H. B. Curry and I. J. Schoenberg. *On Pólya Frequency Functions IV: The Fundamental Spline Functions and their Limits*, pages 347–383. Birkhäuser Boston, Boston, MA, 1988.

[50] M. de Berg, O. Cheong, M. van Kreveld, and M. Overmars. *Computational Geometry*. Springer, Berlin, Heidelberg, 2008.

[51] C. De Boor. On calculating with B-splines. *Journal of Approximation Theory*, 6 (1):50–62, 1972.

[52] C. De Boor. *A Practical Guide to Splines*. Springer New York, 1st edition, 1978.

[53] S. R. de Groot and P. Mazur. *Non-Equilibrium Thermodynamics*. Dover Publications, 1984.

[54] J. De Loera, J. Rambau, and F. Stantos. *Triangulations, Structures for Algorithms and Applications*. Springer, Berlin, Heidelberg, 2010.

[55] L. De Lorenzis, İ. Temizer, P. Wriggers, and G. Zavarise. A large deformation frictional contact formulation using NURBS-based isogeometric analysis. *International Journal for Numerical Methods in Engineering*, 87(13):1278–1300, 2011.

[56] L. De Lorenzis, P. Wriggers, and G. Zavarise. A mortar formulation for 3D large deformation contact using NURBS-based isogeometric analysis and the augmented Lagrangian method. *Computational Mechanics*, 49(1):1–20, 2012.

[57] B. F. de Veubeke and G. Sander. An equilibrium model for plate bending. *International Journal of Solids and Structures*, 4(4):447–468, 1968.

[58] D. S. Dean. Langevin equation for the density of a system of interacting Langevin processes. *Journal of Physics A: Mathematical and General*, 29:L613–L617, 1996.

[59] T. D. DeRose. *Geometric Continuity: A Parametrization Independent Measure of Continuity for Computer Aided Geometric Design.* PhD thesis, University of California, 1985.

[60] T. D. DeRose and B. A. Barsky. An Intuitive Approach to Geometric Continuity for Parametric Curves and Surfaces. In N. Magnenat-Thalmann and D. Thalmann, editors, *Computer-Generated Images.* Springer, Tokyo, 1985.

[61] M. Dittmann. *Isogeometric analysis and hierarchical refinement for multi-field contact problems.* PhD thesis, University of Siegen, 2017.

[62] M. Dittmann, M. Franke, İ. Temizer, and C. Hesch. Isogeometric Analysis and thermomechanical Mortar contact problems. *Computer Methods in Applied Mechanics and Engineering*, 274:192–212, 2014.

[63] M. Dittmann, F. Aldakheel, J. Schulte, P. Wriggers, and C. Hesch. Variational Phase-Field Formulation of Non-Linear Ductile Fracture. *Computer Methods in Applied Mechanics and Engineering*, 342:71–94, 2018.

[64] M. Dittmann, S. Schuß, B. Wohlmuth, and C. Hesch. Weak C^n coupling for multi-patch isogeometric analysis in solid mechanics. *International Journal for Numerical Methods in Engineering*, 118(11):678–699, 2019.

[65] M. Dittmann, S. Schuß, B. I. Wohlmuth, and C. Hesch. Crosspoint modification for multi-patch isogeometric analysis. *Computer Methods in Applied Mechanics and Engineering*, 360:112768, 2020.

[66] W. Dornisch, S. Klinkel, and B. Simeon. Isogeometric Reissner–Mindlin shell analysis with exactly calculated director vectors. *Computer Methods in Applied Mechanics and Engineering*, 253:491–504, 2013.

[67] R. Echter, B. Oesterle, and M. Bischoff. A hierarchic family of isogeometric shell finite elements. *Computer Methods in Applied Mechanics and Engineering*, 254: 170–180, 2013.

[68] A. Eden, V. K. Kalantarov, and S. V. Zelik. Global solvability and blow up for the convective Cahn-Hilliard equations with concave potentials. *Journal of Mathematical Physics*, 54(4), 2013.

[69] K. R. Elder, N. Provatas, J. Berry, P. Stefanovic, and M. Grant. Phase-field crystal modeling and classical density functional theory of freezing. *Physical Review B*, 75: 064107, 2007.

[70] K.R. Elder, M. Katakowski, M. Haataja, and M. Grant. Modeling Elasticity in Crystal Growth. *Physical Review Letters*, 88:245701, 2002.

[71] H. Emmerich, H. Löwen, R. Wittkowski, T. Gruhn, G. Tóth, G. Tegze, and L. Gránásy. Phase-field-crystal models for condensed matter dynamics on atomic length and diffusive time scales: an overview. *Advances in Physics*, 61(6):665–743, 2012.

[72] E. Engel and R. M. Dreizler. *Density Functional Theory*. Springer, 2011.

[73] R. Evans. The nature of the liquid-vapour interface and other topics in the statistical mechanics of non-uniform, classical fluids. *Advances in Physics*, 28(2):143–200, 1979.

[74] P. Farah, A. Popp, and W. A. Wall. Segment-based vs. element-based integration for mortar methods in computational contact mechanics. *Computational Mechanics*, 55(1):209–228, 2015.

[75] G. Farin. *NURBS Curves and Surfaces: From Projective Geometry to Practical Use*. Computer science and scientific computing. Elsevier Science, 2014.

[76] G. Farin. *Curves and Surfaces for Computer-Aided Geometric Design: A Practical Guide*. Computer science and scientific computing. Elsevier Science, 2014.

[77] P. Fischer, M. Klassen, J. Mergheim, P. Steinmann, and R. Müller. Isogeometric analysis of 2D gradient elasticity. *Computational Mechanics*, 47(3):325–334, 2011.

[78] H. Frusawa and R. Hayakawa. On the controversy over the stochastic density functional equations. *Journal of Physics A: Mathematical and General*, 33:L155–L160, 2000.

[79] B. G. Galerkin. Series solution of some problems of elastic equilibrium of rods and plates. *Vestnik inzhenerov i tekhnikov*, 19(7):897–908, 1915.

[80] T. Garrity and J. Warren. Geometric continuity. *Computer Aided Geometric Design*, 8:51–65, 1991.

[81] P. G. Gennes. *Scaling Concepts in Polymer Physics.* Cornell University Press, Ithaca.

[82] H. Gomez, V. M. Calo, Y. Bazilevs, and T. J. R. Hughes. Isogeometric analysis of the Cahn–Hilliard phase-field model. *Computer Methods in Applied Mechanics and Engineering*, 197:4333–4352, 2008.

[83] O. Gonzalez and J. C. Simo. On the stability of symplectic and energy-momentum algorithms for non-linear Hamiltonian systems with symmetry. *Computer Methods in Applied Mechanics and Engineering*, 134:197–222, 1996.

[84] A. E. Green and W. Zerna. *Theoretical Elasticity*. Dover Publications, Inc., 1968.

[85] Y. Guo and M. Ruess. Nitsche's method for a coupling of isogeometric thin shells and blended shell structures. *Computer Methods in Applied Mechanics and Engineering*, 284:881–905, 2015.

[86] Y. Guo, J. Heller, T. J. R. Hughes, M. Ruess, and D. Schillinger. Variationally consistent isogeometric analysis of trimmed thin shells at finite deformations, based on the STEP exchange format. *Computer Methods in Applied Mechanics and Engineering*, 336:39–79, 2018.

[87] P. Hansbo, C. Lovadina, I. Perugia, and G. Sangalli. A lagrange multiplier method for the finite element solution of elliptic interface problems using non-matching meshes. *Numerische Mathematik*, 100:91–115, 2005.

[88] T. J. Healey. Existence of weak solutions for non-simple elastic surface models. *Journal of Elasticity*, 151:32–55, 2022.

[89] A. J. Herrema, E. L. Johnson, D. Prosperio, J. Kiendl, and M. C. Hsu. Penalty coupling of non-matching isogeometric Kirchhoff-Love shell patches with application to composite wind turbine blades. *Computer Methods in Applied Mechanics and Engineering*, submitted, 2018.

[90] C. Hesch and P. Betsch. Transient 3D Domain Decomposition Problems: Frame-indifferent mortar constraints and conserving integration. *International Journal for Numerical Methods in Engineering*, 82:329–358, 2010.

[91] C. Hesch and P. Betsch. Energy-momentum consistent algorithms for dynamic thermomechanical problems–Application to mortar domain decomposition problems. *International Journal for Numerical Methods in Engineering*, 86(11):1277–1302, 2011.

[92] C. Hesch and P. Betsch. Isogeometric analysis and domain decomposition methods. *Computer Methods in Applied Mechanics and Engineering*, 213–216:104–112, 2012.

[93] C. Hesch and K. Weinberg. Thermodynamically consistent algorithms for a finite-deformation phase-field approach to fracture. *International Journal for Numerical Methods in Engineering*, 99(12):906–924, 2014.

[94] C. Hesch, M. Franke, M. Dittmann, and İ. Temizer. Hierarchical NURBS and a higher-order phase-field approach to fracture for finite-deformation contact problems. *Computer Methods in Applied Mechanics and Engineering*, 301:242–258, 2016.

[95] C. Hesch, S. Schuß, M. Dittmann, M. Franke, and K. Weinberg. Isogeometric analysis and hierarchical refinement for higher-order phase-field models. *Computer Methods in Applied Mechanics and Engineering*, 303:185–207, 2016.

[96] P. Hohenberg and W. Kohn. Inhomogeneous electron gas. *Physical Reciew*, 136(3 B):864–871, 1964.

[97] G. A. Holzapfel. *Nonlinear Solid Mechanics*. John Wiley & Sons, 2001.

[98] T. Horger, A. Reali, B. I. Wohlmuth, and L. Wunderlich. A hybrid isogeometric approach on multi-patches with applications to Kirchhoff plates and eigenvalue problems. *Computer Methods in Applied Mechanics and Engineering*, 348:396–408, 2019.

[99] R. E. Howard and A. B. Lidiard. Matter transport in solids. *Reports on Progress in Physics*, 27:161–240, 1964.

[100] T. J. R. Hughes, J. A. Cottrell, and Y. Bazilevs. Isogeometric analysis: CAD, finite elements, NURBS, exact geometry and mesh refinement. *Computer Methods in Applied Mechanics and Engineering*, 194(39–41):4135–4195, 2005.

[101] B. M. Irons. Engineering applications of numerical integration in stiffness methods. *Journal of the American Institute of Aeronautics and Astronautics*, 4(11):2035–2037, 1966.

[102] M. Kapl, V. Vitrih, B. Juttler, and K. Birner. Isogeometric analysis with geometrically continuous functions on two-patch geometries. *Computers and Mathematics with Applications*, 70(7):1518–1538, 2015.

[103] M. Kapl, G. Sangalli, and T. Takacs. Construction of analysis-suitable G^1 planar multi-patch parameterizations. *Computer Aided Geometric Design*, 97:41–55, 2018.

[104] V. V. Karachik. About solvability of boundary value problems for the nonhomogeneous polyharmonic equation in a ball. *Differential Equations*, 50:1449–1456, 2014.

[105] V. V. Karachik. Solution of the dirichlet problem with polynomial data for the polyharmonic equation in a ball. *Differential Equations*, 8:1033–1042, 2015.

[106] K. Kawasaki. Irreducible memory function for dissipative stochastic systems with detailed balance. *Physica A: Statistical Mechanics and its Applications*, 215:61–74, 1994.

[107] J. Kiendl, K. U. Bletzinger, J. Linhard, and R. Wüchner. Isogeometric shell analysis with Kirchhoff–Love elements. *Computer Methods in Applied Mechanics and Engineering*, 198:3902–3914, 2009.

[108] J. Kiendl, Y. Bazilevs, M.-C. Hsu, R. Wüchner, and K.-U. Bletzinger. The bending strip method for isogeometric analysis of Kirchhoff–Love shell structures comprised of multiple patches. *Computer Methods in Applied Mechanics and Engineering*, 199: 2403–2416, 2010.

[109] J. Kiendl, M. C. Hsu, M. C. H. Whu, and A. Reali. Isogeometric Kirchhoff-Love shell formulations for general hyperelastic materials. *Computer Methods in Applied Mechanics and Engineering*, 291:280–303, July 2015.

[110] J. Y. Kim and S. K. Youn. Isogeometric contact analysis using mortar method. *International Journal for Numerical Methods in Engineering*, 89(12):1559–1581, 2012.

[111] S. K. Kleiss, C. Pechstein, B. Jüttler, and S. Tomar. IETI – Isogeometric Tearing and Interconnecting. *Computer Methods in Applied Mechanics and Engineering*, 247-248:201–215, 2012.

[112] K. Königsberger. *Analysis 2*. Springer-Verlag Berlin, Heidelberg, New York, 2004.

[113] B. D. Koshanov. About solvability of boundary value problems for the nonhomogeneous polyharmonic equation in a ball. *Advances in Pure and Applied Mathematics*, 4:351–373, 2013.

[114] C. Lacour, Y. Maday, and L. Cazabeau. Numerical quadratures and mortar methods. In G. Etgen W. Fitzgibbon J.-L. Lions J. Périaux M.-O. Bristeau and M. F. Wheeler, editors, *Conference in honor of Professor Roland Glowinski on the occasion of his 60th birthday*, pages 119–128. John Wiley & Sons, 1997.

[115] B. P. Lamichhane and B. I. Wohlmuth. Biorthogonal Bases with Local Support and Approximation Properties. *Mathematics of Computation*, 76(257):233–249, 2007.

[116] G. Liang and J. He. The non-conforming domain decomposition method for elliptic problems with lagrangian multipliers. *Chinese Journal of Numerical Mathematics and Applications*, 15:8–19, 1993.

[117] C. N. Likos, A. Lang, M. Watzlawek, and H. Löwen. Criterion for determining clustering versus reentrant melting behavior for bounded interaction potentials. *Physical Review E*, 63(3):031206, 2001.

[118] C. N. Likos, N. Hoffmann, H. Löwen, and A. A. Louis. Exotic fluids and crystals of soft polymeric colloids. *Journal of Physics: Condensed Matter*, 14(33):7681, 2002.

[119] Y. Maday, F. Rapetti, and B. I. Wohlmuth. The Influence of Quadrature Formulas in 2D and 3D Mortar Element Methods. *Recent Developments in Domain Decomposition Methods. Lecture Notes in Computational Science and Engineering*, 23, 2002.

[120] U. M. B. Marconi and P. Tarazona. Dynamic density functional theory of fluids. *Journal of Chemical Physics*, 110(16):8032–8044, 1998.

[121] U. M. B. Marconi and P. Tarazona. Dynamic density functional theory of fluids. *Journal of Physics: Condensed Matter*, 12:A413–A418, 2000.

[122] J. E. Marsden and T. J. R. Hughes. *Mathematical Foundations of Elasticity*. Prentice-Hall, INC, 1983.

[123] P. M. Naghdi. The Theory of Shells and Plates. In C. Truesdell, editor, *Mechanics of Solids*, volume 2, chapter 5. Springer-Verlag Berlin, Heidelberg, 1972.

[124] V. P. Nguyen, P. Kerfriden, M. Brino, S. P. A. Bordas, and E. Bonisoli. Nitsche's method for two and three dimensional NURBS patch coupling. *Computational Mechanics*, 53(6):1163–1182, 2014.

[125] R. W. Ogden. *Non-Linear Elastic Deformations*. Ellis Horwood Limited, 1984.

[126] A. N. Palazotto and S. T. Dennis. *Nonlinear Analysis of Shell Structures*. American Institute of Aeronautics and Astronautics, Inc., 1992.

[127] T. Pavlidis. *Polygon Clipping*, pages 337–357. Springer Berlin Heidelberg, 1982.

[128] A. Pérez-Madrid, D. Reguera, and J. M. Rubí. A mesoscopic approach to the slow dynamics of supercooled liquids and colloidal systems. *Journal of Physics: Condensed Matter*, 14:1651–1657, 2002.

[129] L. Piegl. On nurbs: a survey. *IEEE Computer Graphics and Applications*, 11(01): 55–71, 1991.

[130] L. Piegl and W. Tiller. *The NURBS Book*. Springer, 2nd edition, 2010.

[131] S. Praetorius and A. Voigt. Development and Analysis of a Block-Preconditioner for the Phase-Field Crystal Equation. *SIAM Journal on Scientific Computing*, 37 (3):B425–B451, 2015.

[132] H. Prautzsch. Degree elevation of b-spline curves. *Computer Aided Geometric Design*, 1(2):193–198, 1984.

[133] H. Prautzsch and B. Piper. A fast algorithm to raise the degree of spline curves. *Computer Aided Geometric Design*, 8(4):253–265, 1991.

[134] N. Provatas and K. Elder. *Phase-Field Methods in Materials Science and Engineering*. Wiley-VCH, 2009.

[135] M. A. Puso. A 3D mortar method for solid mechanics. *International Journal for Numerical Methods in Engineering*, 59:315–336, 2004.

[136] T. V. Ramakrishnan and M. Yussouff. First-principles order-parameter theory of freezing. *Physical Reciew B*, 19(5):2775–2794, 1977.

[137] A. Reali and H. Gomez. An isogeometric collocation approach for Bernoulli–Euler beams and Kirchhoff plates. *Computer Methods in Applied Mechanics and Engineering*, 284:623–636, 2015.

[138] H. J. Reinhardt. *Numerik gewöhnlicher Differentialgleichungen*. De Gruyter, 2008.

[139] H. Risken. *The Fokker-Planck Equation: Methods of Solution and Applications*. Springer, 2nd edition, 1989.

[140] N. Roidos and E. Schrohe. The Cahn-Hilliard equation and the Allen-Cahn equation on manifolds with conical singularities. *Communications in Partial Differential Equations*, 38(5):925–943, 2013.

[141] M. Ruess, D. Schillinger, A. I. Özcan, and E. Rank. Weak coupling for isogeometric analysis of non-matching and trimmed multi-patch geometries. *Computer Methods in Applied Mechanics and Engineering*, 269:46–71, 2014.

[142] S. Schuß, K. Weinberg, and C. Hesch. Thermomigration in SnPb solders: Material model. *Mechanics of Materials*, 121:31–49, 2018.

[143] S. Schuß, M. Dittmann, S. Klinkel, B. Wohlmuth, and C. Hesch. Multi-patch isogeometric analysis for Kirchhoff-Love shell elements. *Computer Methods in Applied Mechanics and Engineering*, 349:91–116, 2019.

[144] S. Schuß, S. Glas, and C. Hesch. Non-linear space-time elasticity. *International Journal for Numerical Methods in Engineering*, 124(9):1965–1990, 2023.

[145] A. Seitz, P. Farah, J. Kremheller, B.I. Wohlmuth, W.A. Wall, and A. Popp. Isogeometric dual mortar methods for computational contact mechanics. *Computer Methods in Applied Mechanics and Engineering*, 301:259–280, 2016.

[146] D. S. Sholl and J. A. Steckel. *Density Functional Theory: a practical introduction*. Wiley & Sons, 2009.

[147] J. C. Simo and N. Tarnow. The Discrete Energy-Momentum Method. Conserving Algorithms for Nonlinear Elastodynamics. *Applied Mathematics and Physics (ZAMP)*, 43:757–792, 1992.

[148] M. Slater, A. Steed, and Y. Chrysanthou. *Computer graphics and virtual environments: from realism to real-time*. Addison-Wesley, 2002.

[149] M. v. Smoluchowski. Über Brownsche Molekularbewegung unter Einwirkung äußerer Kräfte und deren Zusammenhang mit der verallgemeinerten Diffusionsgleichung. *Annalen der Physik*, 353(24):1103–1112, 1916.

[150] E. Stein and F.-J. Barthold. *Elatizitätstheorie*. Ernst & Sohn, Berlin, 1996.

[151] P. Su and R. L. S. Drysdale. A comparison of sequential delaunay triangulation algorithms. *Computational Geometry*, 7(5):361–385, 1997.

[152] I. E. Sutherland and G. W. Hodgman. Reentrant polygon clipping. *Communications of the ACM*, 17:32–42, 1974.

[153] H. Swann. On the use of lagrange multipliers in domain decomposition for solving elliptic problems. *Mathematics of Computation*, 60:49–78, 1993.

[154] T. Takacs and B. Jüttler. Existence of stiffness matrix integrals for singularly parameterized domains in isogeometric analysis. *Computer Methods in Applied Mechanics and Engineering*, 200(49):3568–3582, 2011.

[155] T. Takacs and B. Jüttler. H^2 regularity properties of singular parameterizations in isogeometric analysis. *Graphical Models*, 74(6):361–372, 2012.

[156] İ. Temizer, P. Wriggers, and T. J. R. Hughes. Three-dimensional mortar-based frictional contact treatment in isogeometric analysis with NURBS. *Computer Methods in Applied Mechanics and Engineering*, 209–212:115–128, 2012.

[157] W. Tiller. Rational b-splines for curve and surface representation. *IEEE Computer Graphics and Applications*, 3(06):61–69, 1983.

[158] S. Triebenbacher, M. Kaltenbacher, B. Wohlmuth, and B. I. Flemisch. Applications of the mortar finite element method in vibroacoustics and flow induced noise computations. *Acta Acustica united with Acustica*, 96(3):536–553, 2010.

[159] C. Truesdell and W. Noll. *The Non-Linear Field Theories of Mechanics*. Springer, 3rd edition, 2004.

[160] B. K. Turmetov and R. R. Ashurov. On solvability of the neumann boundary value problem for a non-homogeneous polyharmonic equation in a ball. *Boundary Value Problems*, 2013:1–15, 2013.

[161] M. J. Turner, R. W. Clough, H. C. Martin, and L. J. Topp. Stiffness and Deflection Analysis of Complex Structures. *Journal of the Aeronautical Sciences*, 23:805–823, 1956.

[162] R. van Leeuwen. The density gradient expansion of correlation functions. *Physical Review B*, 87:155142, 2013.

[163] R. van Roij, P. Bolhuis, B. Mulder, and D. Frenkel. Transverse interlayer order in lyotropic smectic liquid crystals. *Physical Review E*, 52:R1277–R1280, 1995.

[164] S. van Teeffelen, R. Backofen, A. Voigt, and H. Löwen. Derivation of the phase-field-crystal model for colloidal solidification. *Physical Review E*, 79:051404, 2009.

[165] V. Volpert and V. Vougalter. On the solvability conditions for a linearized Cahn-Hilliard equation. *Rendiconti dell'Istituto di Matematica dell'Università di Trieste*, 43:1–9, 2011.

[166] K. Washizu. *Variational Methods in Elasticity & Plasticity*. Pergamon Press, 3rd edition, 1982.

[167] K. Weinberg and C. Hesch. A high-order finite deformation phase-field approach to fracture. *Continuum Mechanics and Thermodynamics*, pages 1–11, 2015.

[168] K. Willner. *Kontinuums- und Kontaktmechanik*. Springer-Verlag Berlin, Heidelberg, New York, 2003.

[169] B. I. Wohlmuth. *Discretization Methods and Iterative Solvers based on Domain Decomposition*. Springer, 2000.

[170] B. I. Wohlmuth. *Iterative Solvers Based on Domain Decomposition*, pages 85–176. Springer Berlin Heidelberg, Berlin, Heidelberg, 2001.

[171] B. I. Wohlmuth. Variationally consistent discretization schemes and numerical algorithms for contact problems. *Acta Numerica*, 20:569–734, 2011.

[172] B. I. Wohlmuth, A. Popp, M. W. Gee, and W. A. Wall. An abstract framework for a priori estimates for contact problems in 3D with quadratic finite elements. *Computational Mechanics*, 49:735–747, 2012.

[173] P. Wriggers. *Computational contact mechanics*. John Wiley & Sons, Ltd., 2002.

[174] O. C. Zienkiewicz and Y. K. Cheung. *The Finite Element Method in Structural and Continuum Mechanics*. McGraw-Hill, 1968.

[175] O. C. Zienkiewicz, R. L. Taylor, and J. Z. Zhu. *The Finite Element Method. Its Basis and Fundamentals*. Butterworth Heinemann, 6th edition, 2005.

Vol. 1

Publication series of the Chair of Computational Mechanics

Editor: Prof. Dr. habil. Christian Hesch

Abstract

This work presents an innovative approach to tackle the challenge of implementing general non-conforming weak C^n-continuous domain couplings in isogeometric analysis. Building on the established mortar method, the approach extends it by introducing additional constraints on derivatives up to a specified order. The study comprehensively elucidates the method within an abstract variational framework, covering aspects such as discretisation in isogeometric analysis, dual space selection, efficient handling of crosspoints and wirebaskets, and the evaluation of mortar integrals. Special attention is given to constructing isogeometric approximation spaces that inherently satisfy higher-order coupling conditions. The performance and applicability of the method are explored in diverse engineering problems, including elasticity, heat conduction, diffusion, and Phase-Field-Crystal modelling. Through a series of simulations, the study demonstrates the efficiency and applicability of the approach in various technical domains.

ISBN 978-3-96182-169-3